2019-2023
China National Report on Geodesy

For

The 28th IUGG General Assembly

Berlin, Germany, July 11-20, 2023

Prepared by Chinese National Committee for

International Association of Geodesy (CNC-IAG)

June 25 2023

Preface

This report presents the progress of research and development on geodesy in China during the time period from January 2019 to June 2023. It is to be submitted, on behalf of the Chinese National Committee for International Association of Geodesy (CNC-IAG), to the IAG General Assembly at the 28th IUGG General Assembly to be held in Berlin, Germany, July 11-20, 2023.

It is hoped that this national report would be of help for Chinese scientists in exchanging the results and ideas in the research, development and application of geodesy with scientists all over the world.

Colleagues listed below made their contribution for this national report (sorted alphabetically by last name):

Lifeng Bao, Yachuan Bao, Jinzhong Bei, Bin Chen, Peng Chen, Qiujie Chen, Ruizhi Chen, Shi Chen, Xiaodong Chen, Zhaohui Chen, Yingyan Cheng, Yonghai Chu, Xiaoming Cui, Xiaolei Dai, Yamin Dang, Mingli Deng, Zhongliang Deng, Wei Feng, Haiqiang Fu, Haiyang Fu, Yanguang Fu, Zhouzheng Gao, Jianghui Geng, Shengfeng Gu, Chunxi Guo, Jing Guo, Jinyun Guo, Xiang Guo, Xinwei Guo, Zehua Guo, Houzeng Han, Jiancheng Han, Changyong He, Lin He, Qianqian He, Pengyu Hou, Andong Hu, Jun Hu, Minzhang Hu, Zhigang Hu, Tong Hua, Lu Huang, Xingliang Huo, Haonan Jia, Lulu Jia, Yongjun Jia, Guangwei Jiang, Haitao Jiang, Tao Jiang, Weiping Jiang, Taoyong Jin, Baogui Ke, Xiange Lei, Ang Li, Bijun Li, Bofeng Li, Dehai Li, Hang Li, Honglei Li, Min Li, Min Li, Pan Li, Qianqian Li, Qiong Li, Shuang Li, Tao Li, Tuan Li, Wang Li, Xin Li, Xingxing Li, Yongbo Li, Zhao Li, Zishen Li, Wei Liang, Jianchi Liao, Ang Liu, Chun Liu, Lin Liu, Qi Liu, Sulan Liu, Teng Liu, Xiaogang Liu, Yanxiong Liu, Ziwei Liu, Yidong Lou, Feng Lu, Hongyan Lu, Zhicai Luo, Jie Lv, Xiaoji Niu, Ming Ou, Yuanjin Pan, Zongpeng Pan, Ling Pei, Fukai Peng, Xianping Qin, Xia Ren, Xiaodong Ren, Yingying Ren, Yunzhong Shen, Chuang Shi, Wen Shi, Yong Su, Fuping Sun, Heping Sun, Zhongmiao Sun, Chengpan Tang, Xiaoyun Wan, Cheng Wang, Hu Wang, Jian Wang, Lei Wang, Leyang Wang, Liang Wang, Linhai Wang, Ningbo Wang, Wei Wang, Yunjia Wang, Zhengtao Wang, Na Wei, Weisong Wen, Lin Wu, Yihao Wu, Yunlong Wu, Longwei Xiang, Yun Xiao, Guodong Xu, Jianqiao Xu, Qiaozhuang Xu, Tianhe Xu, Weimin Xu, Xinyu Xu, Shuqiang Xue, Cheng Yang, Fan Yang, Heng Yang, Jinling Yang, Lianjun Yang, Qiang Yang, Yuanxi Yang, Yibin Yao, Shuang Yi, Wei You, Baoguo Yu, Fangwen Yu, Wenxian Yu, Yunbin Yuan, Jiuping Zha, Baocheng Zhang, Bei Zhang, Chuanyin Zhang, Hongjuan Zhang, Miaomiao Zhang, Qiang Zhang, Quan Zhang, Xiaohong Zhang, Dongsheng Zhao, Qile Zhao, Qiuyue Zheng, Bo Zhong, Jiahao Zhong, Yulong Zhong, Hao Zhou, Jiangcun Zhou, Feng Zhu, Jianjun Zhu, Xinhui Zhu, Yiqing Zhu, Jiancang Zhuang, Xiancai Zou.

Prof. Yamin Dang
President of CNC-IAG

Contents

Development of Comprehensive PNT and Resilient PNT

Xia Ren[1,2], *Yuanxi Yang*[1,2]

[1] *State Key Laboratory of Geo-Information Engineering, Xian, China*

[2] *Xi'an Research Institute of Surveying and Mapping, Xian, China*

Any single positioning, navigation and timing (PNT) technology has its vulnerability and limits, even powerful Global Navigation Satellite System (GNSS) is no exception. To provide continuous and reliable PNT information to users, the theory and technique of comprehensive PNT information system and resilient PNT application system have attracted great attention from Chinese scholars. We try to summarize the progress and development of the synthetic PNT system, including the proposal, the modification and the improvement of the comprehensive PNT, as well as the follow-up resilient PNT. The frame of China's comprehensive PNT system consisted of comprehensive PNT infrastructure and comprehensive PNT application system is initially described; the achievements on some main PNT technologies are introduced; the conceptual models of resilient PNT are given; besides, existing researches on resilient function models and stochastic models are summarized according to different user scenarios.

1 Introduction

Satellite navigation system have advantages in high precision, global coverage and real-time service, making it the most wildly used positioning, navigation and timing (PNT) technology in the world. However, Global Navigation Satellite System (GNSS) signals are vulnerable with low landing power and poor penetrating, that cannot serve non-exposed spaces or easy to be inferred. With the explosion of the weaknesses of GNSS, it is realized that only relying on GNSS or any single PNT technology may bring potential risks, and a new PNT system needs to be built to guarantee the safety of core PNT users (Yang et al., 2023). Published in Nov. 2022,"China's BeiDou Navigation Satellite System in the New Era" by the State Council Information O ffice of the People's Republic of China says that a more extensive, more integrated, and more intelligent comprehensive spatiotemporal system with BDS as the core is going to be created in the coming years (State Council Information Office of the People's Republic of China, 2022).

In 2016, the concept of comprehensive PNT system was proposed, namely a PNT information source frame covering from deep space to deep sea providing seamless PNT information for users in any environments (Yang, 2016). Correspondingly, in 2017 and 2019, the thinking of micro-PNT terminal system and resilient PNT application system were proposed for the resilient application of multiple PNT information (Yang and Li, 2017; Yang, 2018). Since then, the key technologies on the construction of comprehensive PNT information sources and study on resilient PNT methods and algorithms became a research highlight in China. With deeper study, intelligent PNT concept was proposed as a more advanced PNT application mode catering to the requirement of intelligent society (Yang et al., 2021, Liu et al., 2022). Then, a secure PNT system is formed with comprehensive PNT information sources, resilient PNT application mode and intelligent PNT service mode (Yang et al., 2023).

In the following sections, the frame of Comprehensive PNT system consisted of comprehensive PNT infrastructures and comprehensive PNT application system is presented; then, the significant achievements are introduced on the aspects of navigation satellite constellation at Lagrange points, BeiDou global navigation system (BDS-3), Low Earth Orbit Satellite (LEO) Augmentation System, and various ground-based PNT systems; besides, the resilient PNT concept and its key elements are described, and the study progress on resilient methods and algorithms in underwater scenario, indoor scenario and urban scenario are presented.

2 Comprehensive PNT system

The concept of Comprehensive PNT system described a PNT information source system without distinguishing the comprehensive PNT infrastructure and the comprehensive application system at the initial description (Yang, 2016; Yang and Li, 2017). By a series discussion, it is realized that the comprehensive PNT system should be divided into comprehensive PNT infrastructure system and comprehensive PNT application system (as shown in Figure 1.) (Yang et al., 2023). Comprehensive PNT infrastructure system contains all the large artificial PNT information sources covering from deep space to deep sea, and the comprehensive PNT application system is various PNT terminal sensors receiving artificial and natural PNT signals or self-sensing the state of motion of the carriers.

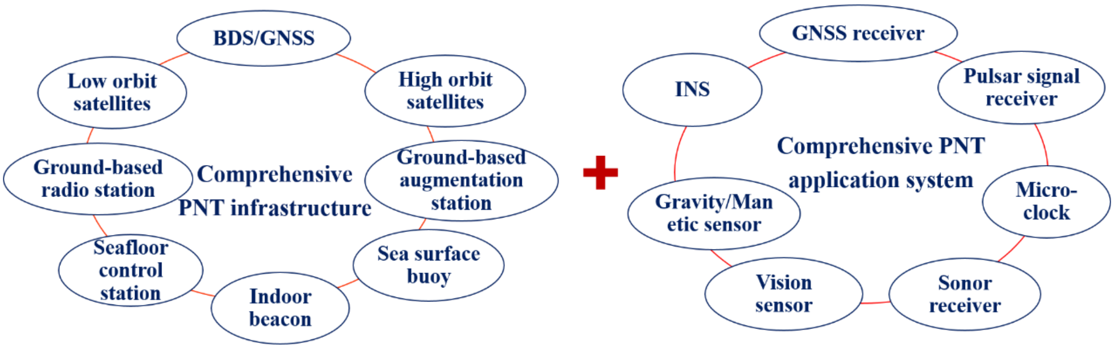

Figure 1. Comprehensive PNT system

As an important part of national comprehensive PNT system, the comprehensive PNT infrastructure system is a seamless PNT main information source frame which should be designed and constructed based on different PNT information sources. In the exposed space from deep space to the ground, the artificial PNT information source frame includes navigation satellite constellation at Lagrange points connecting the PNT service from ground to deep space; the existing or improved BeiDou navigation satellites at high and medium earth orbits, serving for the exposed ground users, ships and low orbit vehicles; the low orbit navigation satellite constellation, augmenting the BeiDou navigation system; the ground-based radio stations such as the ground-based radio navigation stations “Changhe”, ground-based augmentation stations of BDS/GNSS and mobile base stations, augmenting or compensating satellite navigation systems. In non-exposure spaces, beacons such as WiFi, infrared and radio frequency and Ultra Wide Band are also important PNT information sources. In under water environments, sea surface buoys and seafloor beacons are all main PNT infrastructures providing PNT information and transmitting time-space datum.

Also, the integrated PNT sensors like INS and micro clock, as well as the natural PNT information sources like matching information (magnetism, gravity and image) and pulsar signals, could be applied as compensation methods in many scenarios. Besides, scene-based augmentation systems (SceneBAS) for comprehensive PNT should also be included in the comprehensive PNT application system, for example, the geo-graphic scene in three dimension could be important PNT augmentation information (Zhang et al., 2023).

Navigation satellite at Lagrange points

The navigation satellite constellation at Lagrange points of Sun-Earth and Earth-Moon system is still under demonstration. A feasible thinking on navigation satellite at Lagrange points is making it not only the navigation method for cisluar spaces, but also navigation relay station from the surface of the earth to deep space. The navigation signal should follow the same structure as BeiDou/GNSS signals to realize the compatibility and interoperability with BeiDou/GNSS. Besides, the satellites should carry upward and downward antennas directing to the deep space and the earth respectively. The upward antenna is to broadcast navigation signal for deep space users, and the downward antenna is to receiving the signal of GNSS to realize the transferring of the space and time datum (Yang et al., 2023).

Satellite navigation technology

BDS-3 was accomplished in June 2020, and officially opened service in July 2022. Series of creative designs are used such as the hybrid constellation, the whole constellation inter-satellite links, and Asymmetric Constant Envelope Binary Offset Carrier (ACE-BoC) signal modulation mode (Yang et al., 2020a, 2022; Xie and Kang, 2021). These creative designs strongly support not only the PNT performance but also six featured services namely Regional Short Message Communication Service (RSMCS), Precise Point Positioning Service via B2b signal (PPP-B2b), Global Short Message Communication Service (GSMCS), International Search & Rescue Service (MEOSAR) and Satellite Based Augmentation Service (SBAS).

The performance of BDS-3 is evaluated and assessed by academies and organizations (Yang et al., 2022; Guo et al., 2019; Cai et al., 2021). The international GNSS monitoring and assessment (iGMAS) evaluated the performances of BDS-3 signal and the basic PNT service in 2022, and the results showed that each item could fill the requirement of design index (as shown in Table 1). The SBAS service could broadcast GPS/BDS single- and dual-frequency augmentation information through BDS GEO satellites achieving APV-I and the CAT-I precision. The PPP-B2b performance for real-time positioning is about 0.1-0.2 m which is at the same level of PPP with IGS real-time products, and the convergence time is about 20-30 min (Yang et al., 2021, 2022; Yu et al., 2022; Song et al., 2021).

Table 1. performance of BDS-3 signal and system service

	SISRE (m)	Orbit (m)	Clock (ns)	BDGIM (m)

Signal accuracy	B1I /B3I	IGSO	MEO	IGSO	MEO	day	night
	1.13	1.81	1.24	2.13	1.78	0.89	0.59

System perfor-mance	Positioning (m)								Timing (ns)	PDOP availability
	B1I		B3I		B1C		B2a			
	H	V	H	V	H	V	H	V		
	3.50	5.45	4.66	7.04	2.99	4.22	4.06	7.28	13.01	100%

On the aspect of further development, demonstrations are made on the inter-satellite links and the IGSOs to improve the service performance (Yang et al., 2020a, 2023). A space-based autonomous time keeping method was proposed using Hydrogen maser as the reference clock, and the predicted clock bias is 0.1 ns in 1 h (Yang Y F et al., 2021). IGSOs are suggested to increase the inclination angle to support PNT service in polar region, and involve in RSMCS, BDSBAS and PPP-B2b to overcome “South Wall” effect (Yang et al., 2020a).

Low Earth Orbit Satellite (LEO) augmentation system

Low earth orbit (LEO) satellite augmented space-based PNT is a research highlight in recent years and progresses have been made on both technology development and LEO constellation construction. With stronger received signal power and better special geometry, LEO constellation becomes a key component of comprehensive PNT system (Ma et al., 2019). China now has many commercial LEO navigation augmentation constellation projects, such as “Hongyan” constellation, “Hongyun” constellation, and “Centispace” (Meng et al., 2018). In Oct. 2022, the Beijing Future Navigation Technology Co., Ltd launched the S5 and S6 satellites of “Centispace” for the demonstration of the LEO navigation augmentation system (http://www.beidou.gov.cn/yw/xwzx/202210/t20221026_24755.html). The whole constellation is planned to be hundreds of satellites and will help to realize rapid kinematic positioning and navigation at centimeter level. The system is designed to be highly compatible with BDS and users may directly use it through software update.

The related key technologies on LEO augmentation system have been researched, such as constellation design, broadcast ephemeris design, the combined orbit determination of LEO and GNSS satellites and rapid PPP augmented with LEO etc. (Ma et al., 2020; Hou et al., 2019; Zhang et al., 2020, Meng et al., 2021). A confirmed conclusion is that the PPP accuracy and convergence time could be significantly improved by LEO constellation (Ge et al., 2018; Li et al., 2019, Meng et al., 2018).

Ground-based augmentation system

As an important support of BDS, the Network ground stations of ground-based augmentation system have been built across China, with the guidance of the government and efforts from Central Enterprise and related departments (State Council Information Office of the People’s Republic of China, 2022). Until 2020, over 25000 stations were built or under construction with over 10,000,000 high precision receivers, chips and cards (Jiang and Wang, 2021). Also, a series of National Standards were published on the technologies of station construction, communication network, data processing center, broadcasting interface etc. The system could provide real-time meter-level, decimeter-level, centimeter-level, and post processing millimeter-level positioning augmentation service, which has been applied in many fields such as transportation and electric power industry (Zhao et al., 2021; Jia, 2020).

Land-based radio navigation system

Land-based radio navigation system at very-low frequency is planned to be updated with the re-awareness of its advantages on better anti-inference. Chinese “Changhe 2” system is still on operation with 6 navigation stations, 3 monitoring stations and 1 control center. The system can serve the South China Sea, East China Sea and North China Sea. More navigation stations is going to be built to expand the coverage of the system, and improve the service accuracy, continuity and integrity through the improvement of signal structure etc. (Hu, 2018; Zhen, 2018).

Ground-based communication base stations

Recently, ground-based communication base stations are engaged in PNT service. With more than 4.8 million communication base stations and 500 thousand 5G stations, China has the largest 5G network and user group in the world. The positioning pattern integrated with 5G and BDS is developed rapidly and the largest high-precision positioning system based on it is published by China Mobile in Oct. 2020. The system is able to provide sub-meter, centimeter, and millimeter level positioning service through 5G network which has good application prospect in areas like vehicle management, autonomous driving and vehicle-road cooperation (Yin et al., 2020).

Seafloor and underwater bacon positioning system

The start of Chinese seafloor PNT infrastructure construction is relatively late and facing many difficulties not only in device development but also the positioning theory and methods. With the support of “Maritime Power Policy”, some progresses have been made in both device development and seafloor geodetic network establishment. Following the criteria of long-term working ability, and better pressure-resistant, anti-corrosive, anti-dragging and anti-flow, the seafloor geodetic station shelter in deep sea is developed with an overflow structure and a stable foundation bed; the shallow-sea shelter is developed with an overflow-type anti-dragging structure and a penetrating design (Sun et al., 2019; Yang et al., 2020b). The seafloor geodetic network is realized by extending and densifying the basic configuration with one master station located in the center of a square, and four auxiliary stations distributed on the four vertexes of the square. Successfully verified the performance of geodetic station devices in shallow sea, long-term seafloor geodetic stations were initially established in the deep-sea area of 3000 m in 2019. The internal positioning accuracy of the seafloor station is turned out to be better than 0.05 m, and the navigation accuracy within the geodetic network coverage of 10 km with acoustic/INS/gravity is better than 10 m (Yang et al., 2020b).

3 Resilient PNT technology

With so many PNT information sources provided by comprehensive PNT infrastructure and nature PNT information, the coming problem for PNT users is how to use multiple information optimally according to the scenario and requirements of the users. Resilient PNT concept was then proposed to provide a PNT application pattern with full use of available information in comprehensive PNT to generate continuous, robust and reliable PNT results (Yang, 2018). Following up, the connotation and characteristic of resilient PNT is discussed (Ming et al., 2023; Bian et al., 2021).

On the aspect of sensor integration, the PNT terminal should resiliently integrate available PNT sensors based on the optimal, available, compatible and interoperable principles; on the aspect of model building, resilient algorithms should be applied to adjust and optimize the basic functional model and stochastic model making them more suitable for the scenario (Yang, 2018).

Resilient model modification should take both functional model and stochastic model into account (Yang, 2018). The common expression of resilient observation model at time t_k can be given as (Yang, 2018)

$$L_i(t_k) = A_i\hat{X}\left(t_k\right) + \mathrm{F}_i(\Delta_{t_{k-m},t_{k-m}}) + e_i$$

where, $\hat{X}\left(t_k\right)$ is the estimating parameter vector at time t_k, L_i is the observation measured by sensor i, A_i and e_i are the corresponding design matrix and observation random error vector, and $\mathrm{F}_i(\Delta_{t_{k-m},t_{k-m}})$ is the modification function related with observation error series $\Delta_{t_{k-m},t_{k-m}}$ from time t_{k-m} to t_k. If extended Kalman filtering (EKF) algorithm is used, resilient dynamic function model is also needed, whose common expression at time t_k can be given as (Yang, 2018)

$$\bar{X}\left(t_k\right) = \Phi_{k,k-1}\hat{X}\left(t_{k-1}\right) + G_i(\Delta_{\bar{X}t_{k-m},t_{k-m}}) + W_i$$

where $\bar{X}\left(t_k\right)$ is the prediction parameter vector at t_k, $G_i(\Delta_{\bar{X}t_{k-m},t_{k-m}})$ is the modification function related with dynamic model error series $\Delta_{t_{k-m},t_{k-m}}$ from time t_{k-m} to t_k, W_i is the processing noise matrix.

Resilient stochastic model is to adjust the stochastic model of observation information and dynamic information according to their uncertainty in parameter estimation. Existing variance component estimation, robust estimation and adaptive estimation are typical resilient stochastic models (Yang et al., 2001ab, 2004ab, 2005), and the common expression for EKF can be used as:

$$\hat{X}_k = \left(\bar{P}_{\bar{X}_k} + A_1^T\bar{P}_1A_1 + \cdots + A_r^T\bar{P}_rA_r\right)^{-1}\left(\bar{P}_{\bar{X}_k}\bar{X}_k + A_1^T\bar{P}_1L_1 + \cdots + A_r^T\bar{P}_rL_r\right)$$

where $\bar{P}_{\bar{X}_k}$ and $\bar{P}_j$ are the adjusted weight matrix of predicted vector and observation vector L_i.

Absolutely, resilient PNT is the development trend of PNT application, and relevant researches have already started based on different application scenarios.

Resilient PNT application in urban scenarios

In urban area, GNSS signals are easy to be sheltered by buildings and interfered by other signals. The cellular net and ground-based navigation stations can be the backup of GNSS, and ground-based GNSS augmentation system, pseudo-satellites and magnetic/image matching can be the compensation. In urban environment, multipath and non-line-of-sight (NLOS) signals are one of the main errors affecting the final PNT results. To increase the signal reception classification and control the effect of NLOS and multipath on final results, some machine learning methods are applied. With advanced study on the sample observations, a gradient boosting decision tree (GBDT)-based method and adaptive neuro-fuzzy inference system are applied in multipath/NLOS signal classification in specific areas (Sun et al., 2019, 2020). Without a priori information, K-means++, Gaussian mixed model (GMM) and fuzzy C-means (FCM) clustering methods are employed to separate LOS, multipath and NLOS signals (Zhu et al., 2021). Based on the predicted multipath value, adaptive filtering is applied to adjust the weight of the multipath signals (Sun et al., 2022). On the aspect of multi-source data fusion, a GNSS/INS-integrated system is formed enabling to calibrate INS autonomously based on a robust motion mode self-recognition technique (Mu et al., 2019a); a GNSS/INS/Odometer-integrated system is formed enabling the real-time calibration and compensation of odometer error based on environment information (Mu et al., 2019b, 2021).

Resilient PNT application in indoor/underground scenario

Indoor and underground PNT system are mainly relay on radio frequency positioning technologies such as WiFi, Bluetooth, UWB and compensated with autonomous positioning methods such as INS, pseudo-satellites, cellular and magnetic matching. Deep learning and machine learning methods such as convolutional neural network are applied in 5G positioning models (Xiong et al., 2022) to achieve better accuracy. Robust estimation and robust Bayesian estimation are used to control the effect of observation outliers, and covariance component estimation is applied to adjust the contribution of different observations (Zhang et al., 2022a, b). Although GNSS can barely serve non-exposed spaces, the 5G/GNSS positioning mode and the integration of 5G and GNSS are also studied to realize the seamless positioning from outdoor to indoor (Shi et al., 2019; Yin et al., 2020; Hong et al., 2020).

4 Summary

Comprehensive PNT is to provide seamless and redundant information, and resilient PNT is to use the information to provide optimal multi-source PNT application strategies. For users in complex environment with secure PNT requirement, the collaborative utilization of comprehensive PNT system and resilient PNT system are of great significance for the continuous, robust and reliable PNT services. China scholars pay highly attention to comprehensive PNT infrastructure design and resilient PNT application research, progresses and achievements have been made on the construction of comprehensive infrastructures, as well as the theoretical and experimental study of resilient PNT methods.

(1) Comprehensive PNT infrastructure is the prerequisite for resilient PNT applications, and resilient PNT provides important support for comprehensive PNT. Without comprehensive PNT, resilient PNT is impossible to realize; without resilient PNT, comprehensive PNT is nothing but individual PNT information.

(2) Comprehensive PNT system is consisted of comprehensive PNT infrastructure and comprehensive PNT system. There is no doubt that BDS has been and will always be the core of China's comprehensive PNT system.

(3) The development schedule of comprehensive PNT system in different area is unbalanced, with advancing in satellite-based PNT technology, and relatively falling behind in that of deep space and deep sea.

(4) Resilient PNT includes resilient integration of multiple PNT sensors, resilient function models and resilient stochastic models. Initiated by Chinese scholars, the resilient PNT system design and resilient model establishment have become research focuses in PNT field. Although some achievements are made, the realization and application of a relatively complete resilient PNT system is still on the way.

Bibliography

Bian H W, Xu J N, He H Y et al (2021) The concept of resilience of national comprehensive PNT system (in Chinese). Geomatics and Information Science of Wuhan University, 46:1265-1272

Cai H L, Meng Y N, Geng C J (2021) BDS-e performance assessment: PNT, SBAS, PPP, SMC and SAR (in Chinese). Acta Geodaetica et Cartographica Sinica 50: 427-435

Chen G X, Liu Y, Liu Y X et al (2019) Adjustment of transceiver lever arm offset and sound speed bias for GNSS-Acoustic positioning. Remote Sensening 11: 1606

Deng Y F (2019) Application research of railway GBAS based on BeiDou satellite. Railway signaling & communication engineering 16: 37-41

Ge H B, Li B F, Ge M R et al (2018) Initial assessment of precise point positioning with LEO enhanced global navigation satellite systems (LeGNSS). Remote Sensing 10: 984

Guo S R, Cai H L, Meng Y N (2019) BDS-3 RNSS technical Charactoeristics and service performance. Acta Geodactica et Cartographica Sinica 48: 810-821

Hong X M, Xu X T, Peng A et al (2021) Key technologies and system architecture evolution of fusion positioning based on 5G mobile communication systems (in Chinese). Xiamen Univ Nat Sci 60: 571-585

Hu A P (2018) Research on the development of land-based ultra-long-range radio navigation (in Chinese). Navigation Positioning & Timing 5: 1-6

Hou Z, Yi X, Zhang Y et al (2019) Satellite-ground link planning for LEO satellite navigation augmentation networks. IEEE Access 7: 98715-98724

Jia Y (2020) Development and Application Overview of GBAS in Civil Aviation. Modern Navigation 11: 272-276

Jiang K, Jiao W H, Hao X L et al (2023) Scientific experiments and achievements of XPNAV-1 (in Chinese). Acta Aeronautica et Astronautica Sinica. Acta Aeronautica et Astronautica Sinica 44: 97-106

Jiang L J, Wang T S (2021) Present and development thinking of BDS ground-based augmentation system (in Chinese). Satellite Application 11:8-12

Li X X, Ma F J, Li X et al (2019) LEO constellation-augmented multi-GNSS for rapid PPP convergence. Journal of Geodesy 93: 749-764

Liu J N, Luo Y R, Guo C et al (2022) PNT intelligence and intelligent PNT (in Chinese). Acta Geodaetica et Cartographica Sinica, 51: 811-828

Liu Q, Wang Y, Liu Y et al (2019) Automatic radio environment measurement system for QTT site (in Chinese). Sci Sin-Phys Mech Astron 49: 099512

Ma F, Zhang X, Li X et al (2020) Hybrid constellation design using a genetic algorithm for a LEO-based navigation augmentation system. GPS solutions 24: 1-14

Meng L, Chen J, Wang J, et al (2021) Broadcast ephemerides for LEO augmentation satellites based on nonsingular elements. GPS Solutions 25: 129

Meng Y S, Bian L, Wang Y et al (2018) Global navigation augmentation system based on Hongyan satellite constellation. Space International 10: 20-27

Ming F, Yang Y X, Zeng A M et al (2023) The conceptual connotation, characteristics and discrimination of resilient PNT. Bulletin of surveying and mapping 4: 79-86

Mu M X, Zhao L (2019a) A GNSS/INS-integrated system for an arbitrarily mounted land vehicle navigation device. GPS solutions 23:112-13

Mu M X, Zhao L (2019b) Improved decentralized GNSS/SINS/odometer fusion system for land vehicle navigation applications. Meas. Sci. Technol 34: 035117-13

Mu M X, Zhao L (2021) A Data Fusion Algorithm of GNSS/INS/ Odometer Integrated System In Consideration of Total Odometer Errors. 2021 The 21st International Conference on Control, Automation and Systems (ICCAS 2021) Ramada Plaza Hotel, Jeju, Korea, Oct. 12~15, 2021:1093-1098

Qi K, Qu G Q, Xue S Q et al (2019) Analytical optimization on GNSS buoy array for underwater positioning, Acta Oceanologica Sinica 38: 137–143

Shi C, Gu S F, Jing G F et al (2019) Fog positioning and its applications (in Chinese). GNSS World of China 44: 1-9

Shuai P, Liu Q, Huang L et al (2019) Pulsar navigation test satellite XPNAV-1 and its observation results (in Chinese). Journal of Chinese Inertial Technology 27: 281-287

Song W W, Zhao X K, Lou Y D et al (2023) Performance Evaluation of BDS-3 PPP-B2b Service (in Chinese). Geomatics and Information Science of Wuhan University 48: 408-415

State Council Information Office of the People’s Republic of China (2022) China’s BeiDou Navigation Satellite System in the New Era [2022-11-04]. http://www.scio.gov.cn/zfbps/32832/Document/1732795/1732795.html

Sun D J, Zheng C E, Zhang J C (2019) Development and prospect for underwater acoustic positioning and navigation technology (in Chinese). Bull Chin Acad Sci 34: 331–338

Sun R, Hsu L T, Xue D B (2019) GPS signal reception classification using adaptive Neuro-Fuzzy inference system. Journal of Navigation 72: 685-701

Sun R, Wang G Y, Cheng Q (2020) Improving GPS code phase positioning accuracy in urban environments using machine learning. IEEE Internet of Thing Journal 8: 7065-7078

Sun R, Zhang Z, Cheng Q (2022) Pseudorange error prediction for adaptive tightly coupled GNSS/IMU navigation in urban areas. GPS solutions 26, 1-13

Wang J T, Xu T H, Liu Y F et al (2021a) Kalman filter based acoustic positioning of deep seafloor datum point with two-step systematic error estimation. Applied Ocean Research 114: 102817

Wang J T, Xu T H, Liu Y F et al (2023) Augmented Underwater Acoustic Navigation with Systematic Error Modeling Based on Seafloor Datum Network. Marine Geodesy 46: 129-148

Wang J T, Xu T H, Zhang B S et al (2021b) Underwater acoustic positioning based on the robust zero-difference Kalman filter. Journal of Marine Science and Technology 26: 734-749

Wang W, Meng F C, Kan B X (2022) Multi-source autonomous navigation system technology under national comprehensive PNT system (in Chinese). Navigation and Control 21: 10

Xie J, Kang C B (2021) Engineering Innovation and the Development of the BDS-3 Navigation Constellation (in Chinese). Engineering 7: 558–563

Xiong X Y, He D, He Z J et al (2022) Wireless Localization Method Based on Convolutional Neural Network Using 5G Cellular Networks. Journal of Data Acquisition and Processing 37: 1228-1245

Yang Y F, Yang Y X, Chen J P et al Pseudo-stable constellation bias error of BDS-3 and its high-precision prediction. Acta Geodaetica et Cartographica Sinica 50: 1728-1737

Yang Y X (2016) Concept of comprehensive PNT and related key technologies. Acta Geodaetica et Cartographica Sinica 45: 505-510

Yang Y X (2017) Resilient PNT concept frame. Acta Geodaetica et Cartographica Sinica,2018,47: 893-898

Yang Y X, Cui X Q, Gao W G (2004a) Adaptive Integrated Navigation for Multi-sensor Adjustment Outputs. The Journal of Navigation 57: 287-295

Yang Y X, Ding Q, Gao W G (2022) Principle and performance of BDSBAS and PPP-B2b of BDS-3. Satell Navig 3: 1-9

Yang Y X, Gao W G (2004b) Integrated Navigation by Using Variance component estimates of Multi-sensor measurements and Adaptive Weights of Dynamic Model information (in Chinese). Acta Geodaetica et Cartographica Sinica 33: 22-26

Yang Y X, He H B, Xu G C (2001a) Adaptively Robust Filering for Kinematic Geodetic Positioning. Journal of Geodesy 75:109-116

Yang Y X, He H B, Xu T H (2001b) Adaptive Robust Filtering for Kinematic GPS Positioning (in Chinese). Acta Geodaetica et Cartographica Sinica 30: 293-298

Yang Y X, Mao Y, Sun B J (2020a) Basic performance and future developments of BeiDou global navigation satellite system. Satell Navig 1: 1-8

Yang Y X, Li X Y (2017) Micro-PNT and comprehensive PNT. Acta Geodaetica et Cartographica Sinica 46(10):1249-1254

Yang Y X, Liu L, Li J L et al (2021d) Featured services and performance of BDS-3. Chin Sci Bull, 66: 2135-2143

Yang Y X, Liu Y X, Sun D J et al (2020b) Seafloor geodetic network establishment and key technologies. Science China Earth Science 50: -DOI:10.1360/SSTe-2019-0242

Yang Y X, Qin X P (2021) Resilient observation models for seafloor geodetic positioning, Journal of Geodesy 95: 79

Yang Y X, Xu T H, Song L J (2005) Robust Estimation of Variance Components with Application in Global Positioning System Network Adjustment. Journal of Surveying Engineering 131:107-112

Yin L, Ma Y Z, Li G W et al (2020) Research Progress of Communication-Positioning Integrated Technology. Navigation Positioning & Timing 7: 64-76

Yu d Y, Jin J H, Liu Y et al (2022) Marine precise positioning experimental analysis based on BeiDou-3 PPP-B2b signal (in Chinese). Hydrographic Surveying and Charting 42: 51-55, 64

Zhang H C, Yu B G, Bi J Z et al (2023) A survey of scene-based augmentation systems for comprehensive PNT. Geomatics and Information Science of Wuhan University 48: 491-505

Zhang W, Yang Y X, Zeng A M et al (2022a) A GNSS/5G integrated three-dimensional positioning scheme based on D2D communication. Remote Sensing, 14: 1517

Zhang W, Yang Y X, Zeng A M et al (2022b) Robust BDS/5G integrated positioning based on resilient observation model. Advances in Space Research 71: 4006-4017

Zhang X H, Ma F J (2019) Review of the development of LEO navigation-augmented GNSS (in Chinese). Acta Geodaetica et Cartographica Sinica 48:1073-1087

Zhang Y, Li Z, Li R et al (2020) Orbital design of LEO navigation constellations and assessment of their augmentation to BDS. Advances in Space Research 66: 1911-1923

Zhao W, Wang Q, Shang K Y (2021) Electric Power Industry Precise Time-Space Service Network

Based on BD Navigation System (in Chinese). ELECTRIC POWER ICT 29: 75-82

Zhen W, Ding C (2019) Development status and trend of land-based radio navigation system (in Chinese). GNSS would of China 44: 10-15

Zhou Q Y，WEI Z Q，LEI Y H et al (2023) X-ray telescope for pulsar deep space reference and its development vision (in Chinese). Acta Aeronautica et Astronautica Sinica 44: 526608

Zhou Q Y, Wei Z Q, Yan L L et al (2021) Space/ground based pulsar timescale for comprehensive PNT system. Acta Phys 70: 471-483

Zhu B, Yang C, Liu Y. 2021. Analysis and comparison of three unsupervised learning clustering methods for GNSS multipath signals (in Chinese). Acta Geodaet Cartograph Sin, 50: 1762-1771

Maintenance of mm-level Geodetic Reference Framework

Yamin Dang [1], Hu Wang [1], Fuping Sun [2], Yingyan Cheng [1], Guangwei Jiang [3], Xinhui Zhu [2], Qiang Yang [1], Yingying Ren [1]

[1] *Chinese Academy of Surveying and Mapping, Beijing, China*

[2] *Institute of Geospatial Information, Information Engineering University, Zhengzhou, China*

[3] *College of Geology Engineering and Geomatics, Chang'an University, Xi' an, China*

1 Introduction

The high-precision regional reference frame is the basis of the air-space-earth geodetic observation system and the national major infrastructure. A long-term and stable high-precision Earth reference framework is not only of great significance for national economic development and national defense construction, but also plays a significant role in fields such as Earth science research, disaster reduction and prevention. A high-precision maintenance method is the key to maintain the accuracy and stability of the terrestrial reference frame. Up to Date, the coordinate precisions of ITRF reference stations have already reached to mm level, even submilimeters, at reference epoch, but the coordinate maintenance precision of these stations are still at cm level due to non-linear movements related with geophysical phenomena.

Extensive observation collection, unified and rigorous data processing, and accurate construction of the station motion model are the three essential elements for the accuracy and reliability of the Global Navigation Satellite System (GNSS) velocity field. Based on the GNSS observation data from continuous observation data of the Crustal Movement Observation Network of China (CMONOC) and IGS stations over the past thirty years, more Chinese geodesy scientists devoted more efforts to themMaintenance of mm-level geodetic reference framework. The main contributions of this work included the followings.

- The Research Progress on the Method of Maintenance of Regional Reference Frame based on GNSS.
- The Dynamic maintenance of mm-level terrestrial reference frame
- The Reprocessing and Reanalysis of Two-Decade GNSS Observation in Continental China
- The Refinement of Provincial Plate and Establishment of Horizontal Relative Motion Velocity Field Model in Chinese Mainland
- The Distribution characteristics of crustal Deformation in Chinese Mainland and its relationship with strong earthquakes
- The progress of CGCS2000 frame maintenance in millimeter level accuracy
- The Preliminary Realization and Evaluation of CTRF2020

2 Methods of Maintenance of Regional Reference Frame based on GNSS

The high-precision regional reference frame is the basis of the air-space-earth geodetic observation system and the national major infrastructure. Due to frequent regional tectonics activities in China, continuous elastic changes in the surface morphology, multiple nonlinear signals superimposed on the base station, and internal relative movements between plates, various factors make it difficult to maintain the regional reference frame. GNSS technology has the advantages of high precision, all-weather, real-time, etc., so it is necessary to carry out the maintenance of regional reference frame based on GNSS technology.

From 2014 to 2022, China successively carried out the Modern Surveying and Mapping Datum Construction and Maintenance Project and the National Satellite Navigation and Positioning Datum Station Network Adjustment Project, and conducted regular monitoring and analysis of China's geodetic datum and updating of local coordinate frame, achieving millimeter level monitoring of the national coordinate frame. At the same time, it also monitors and maintains the reference station network in multiple provinces and cities across the country, providing important guarantees for railway construction, water conservancy and hydropower projects, mineral resource development, earthquake prevention and disaster reduction, and ecological environment governance. At present, many provinces and cities of China have basically completed the upgrading and transformation of provincial reference stations, and the scale of the national reference station network has reached a super large scale of 3000 stations, of which about 2400 support BDS services, accounting for about 89% of the total number in the country. Related studies have shown that BDS-3 is equivalent to GPS in building high-precision reference frame. By using IGS station stability indicators as constraints and jointly maintaining coordinate frames with multiple GNSS, the maximum deviation of three-dimensional coordinates of stable points is better than 2mm, and the RMS is better than 1mm. Using long-term data from national large-scale GNSS reference stations to maintain regional frame in China will be an important means of frame maintenance and monitoring. In response to the complex terrain and mountainous areas in China, a rapid monitoring algorithm for the GNSS network solution of mountainous frame points with additional ground point tropospheric delay information correction is proposed, and a GNSS based regional reference frame maintenance software is developed to achieve high-precision dynamic monitoring and maintenance of regional reference frames in complex mountainous environments.

The research on the maintenance methods of regional reference frame based on GNSS has partly promoted the role of GNSS technology in dynamic monitoring and maintenance of regional reference frame and datum services, improved the theory and methods of regional reference frame maintenance, and provided technical support for the maintenance and use of regional reference frame. Relevant methods and technologies have played an important role in multiple national and provincial projects.

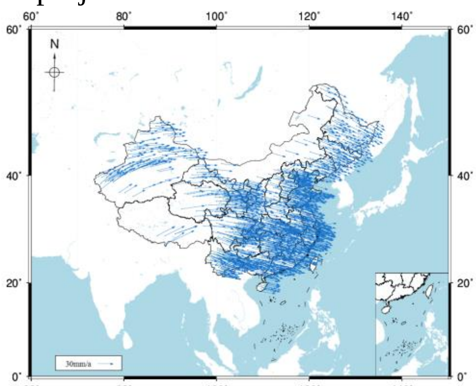

Figure 1. ITRF2014 Horizontal Velocity Field of GNSS Reference Station in Chinese Mainland

3 Dynamic maintenance of mm-level terrestrial reference frame

A long-term and stable high-precision Earth reference framework is not only of great significance for national economic development and national defense construction, but also plays a significant role in fields such as Earth science research, disaster reduction and prevention. A high-precision maintenance method is the key to maintain the accuracy and stability of the terrestrial reference frame.

At present, the accuracy of the measured velocity field of the terrestrial reference frame can reach within 1 mm/a, which can accurately and linearly maintain the reference frame, ensuring its millimeter level accuracy on a long-term scale. However, under the influence of nonlinear motion of the reference station and geocentric motion, the maintenance method based solely on linear velocity makes the accuracy of the reference frame only at the centimeter level on a seasonal scale, which cannot meet the needs of millimeter level Earth change monitoring and research. Therefore, considering the linear motion, nonlinear motion and geocentric motion of the reference station, the comprehensive maintenance of the reference frame is the development trend of the dynamic maintenance technology of the millimeter-level terrestrial reference frames (Sun et al., 2022).

Linear maintenance refers to the maintenance of a reference frame based on the linear (or long-term) changes in the position of the reference station. Linear maintenance relies on the linear speed of the reference station. There are two sources of linear velocity at reference stations, namely crustal motion models and measured velocity fields. Zhu et al (2014) proposed to use SLR data to establish a globally unified reference datum for vertical crustal movement; Zhu et al (2009, 2010) established a current plate motion model by using the results of space geodesy and ITRF velocity field. Compared with the methods of geology and geophysics, the accuracy has been greatly improved.

The nonlinear maintenance of the terrestrial reference frame can be divided into two categories. One is the modeling of nonlinear changes based on geophysical influence mechanisms. The main factors causing nonlinear motion of the reference station include environmental loads, thermal expansion effects, tidal deformation, and post-earthquake deformation (Zhu et al., 2020). Sun et al (2012) confirmed that there is a strong positive correlation between temperature changes and station annual displacement changes through correlation analysis.

And the other of nonlinear change modeling is based on coordinate time series. The methods for modeling nonlinear changes in coordinates include harmonic models, SSA, ARIMA models, and global statistical correction models. Dai et al (2021) proposed a nonlinear motion modeling method that combines wavelet multi-scale decomposition and singular spectrum analysis, and demonstrated that its modeling accuracy can be improved by about 26% compared to the SSA method. Jia et al (2023) extracted the time-varying amplitude of the annual term in the GNSS vertical coordinate time series, and conducted a thorough analysis of the time-varying characteristics of the annual term amplitude at global stations. It was found that the average consistency of the weekly amplitude changes between environmental loads, thermal expansion displacement, and GNSS vertical coordinates was around 60%, Moreover, after both corrections, 68% and 76% of the stations showed a decrease in the amplitude fluctuations of the annual term amplitude (as shown in Figure 1), indicating that environmental loads and thermal expansion effects are important reasons for the amplitude changes of the annual term.

In addition to the above aspects, the dynamic maintenance of the millimeter level terrestrial reference frame still needs to consider the following issues: firstly, further improve the spatial observation data processing technology, weaken the impact of system errors, and obtain more accurate reference station coordinates, which is the foundation for improving the dynamic maintenance accuracy of the terrestrial reference frame; Secondly, the accuracy of nonlinear motion modeling of reference stations based on geophysical influence mechanisms and coordinate time series needs to be further improved; Thirdly, we need to further improve the implementation accuracy and stability of the epoch reference frame.

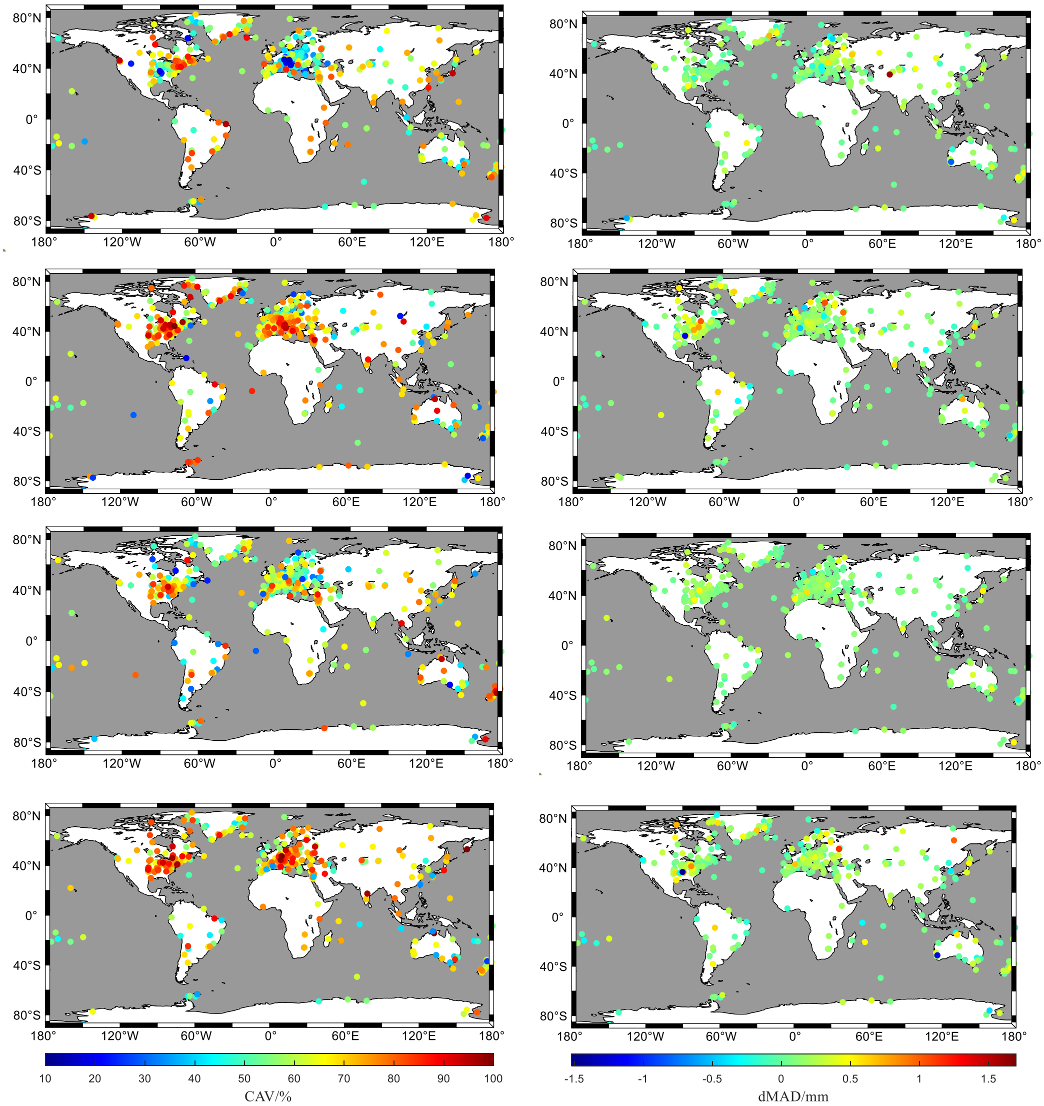

Figure 2. Spatial distribution of CAV (consistency of amplitude variation) of the annual signals between the environmental loading and coordinate time series (left) and the change of MAD (mean absolute deviation) (right). From top to bottom are ATML, CWSL, NTOL and total environmental loading

4 Reprocessing and Reanalysis of Two-Decade GNSS Observation in Continental China

Extensive observation collection, unified and rigorous data processing, and accurate construction of the station motion model are the three essential elements for the accuracy and reliability of the Global Navigation Satellite System (GNSS) velocity field. GNSS data reprocessing not only can weaken the influence of untrue nonlinear site signals caused by imperfect models but also can eliminate the displacement offset caused by frame transformation, solution strategy, and model change. Based on the new repro3 criteria of the International GNSS Service (IGS), we process rigorously GNSS observations of continental China from the period 2000 to 2020 to refine GNSS station secular velocities and analyze the present-day crustal deformation in continental China. The main contributions of this work included the followings. Firstly, the repro3 algorithm and model are used to uniformly and rigorously process the two-decade GNSS historical observations to obtain more reliable GNSS coordinate time series with mm-level precision. Combined with the historical records of major earthquakes in continental China, we build a GNSS time series model considering nonlinear factors (velocity, offset, period, co-seismic/post-seismic deformation) to extract GNSS horizontal velocity field whose root mean square (RMS) mean is 0.1 mm/a.

To ensure the accuracy and consistency of the GNSS coordinate solutions, we use the updated convention and processing settings of repro3 to reprocess the two-decade GNSS observations of continental China in an entirely consistent way. The offsets caused by receiver fault, antenna replacement, earthquake, and other factors can be detected using station logs, while the offsets caused by frame transformation, solution strategy, and model change need to be eliminated by data reprocessing. The basic input GNSS sites of this research are shown in Figure 2. The CMONOC comprises 260 continuous operation reference stations (daily observation) and more than 2000 regional stations (irregular observation). It has preliminarily realized the dynamic monitoring of the primary and secondary tectonic blocks, main active fault zones, and key seismic risk areas in continental China. These GNSS stations have laid a foundation for describing the detailed characteristics of crustal movement in continental China. In addition, IGS stations around China and other continuous observation stations are collected.

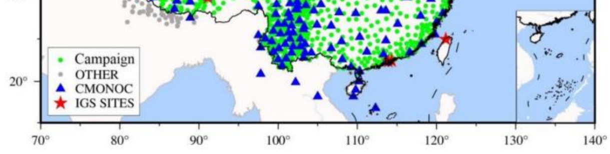

Figure 3. GNSS sites in continental China

A GNSS coordinate time series usually contains the secular trend (linear velocity), seasonal variation (annual and semi-annual signals), offsets caused by non-seismic factors (equipment replacement, antenna height measurement error, phase center modeling error, or other human and software errors) or seismic factors (co-seismic deformation), post-seismic deformation, and other unmodeled errors. For theses errors, an Integrated Time Series Method (ITSM) concerning the effect of seismic deformation was proposed to model the station's nonlinear motion accurately. Distinguished with existing studies, all parameters including seismic relaxation time can be simultaneously estimated by ITSM, which improves the accuracy and reliability of GNSS station velocity significantly. After analysis of the time series for all sites, we can obtain the ITRF2014 GNSS horizontal velocity field of continental China. As shown in Figure 4, there is a clockwise rotation movement from southwest to southeast in continental China, especially in the western region. The velocity field in the eastern region points from northwest to southeast.

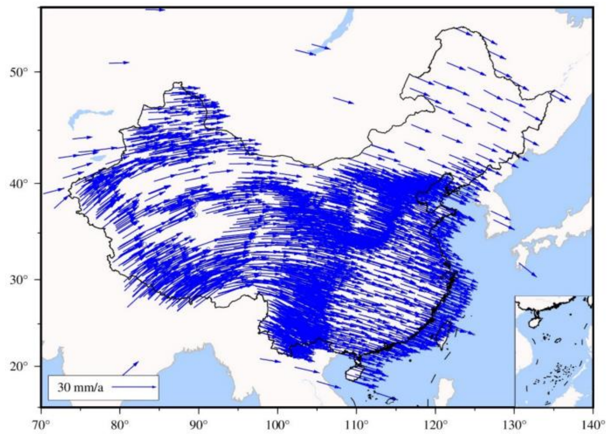

Figure 4. GNSS horizontal velocity field of ITRF2014 in continental China

In general, the emergence and development of GNSS technology in the 1990s significantly promoted the research of tectonic movement and deformation monitoring into a new stage. With over 30 years of research, horizontal tectonic movement and main deformation characteristics in continental China have been clear, and the tectonic deformation in most areas has been accurately quantified. In the future, it is necessary to intensify the continuous GNSS observation further to obtain the three-dimensional tectonic movement information and its evolution characteristics with time. At the same time, it is necessary to strengthen the integration of GNSS and different geodetic technologies, and interdisciplinary research.

5 Refinement of Provincial Plate and Establishment of Horizontal Relative Motion Velocity Field Model in Chinese Mainland

Provincial CORS system is an important part of modern city digitization, informatization and intellectualization, which is easy to obtain the spatiotemporal information of various objects and their related dynamic changes. In order to further realize the modernization and autonomy of the regional framework benchmark, improve the comprehensive service level and emergency support capacity of the modern surveying benchmark, upgrade the accuracy of the regional velocity field and accurately depict its own local motion characteristics in the mainland of China, the velocity field is derived from continuous observation data of the Crustal Movement Observation Network of China (CMONOC).

Both high precise coordinate and velocity of these CMONOC stations have been calculated with GAMIT/GLOBK software. In addition, the Euler vector of the whole Chinese continent and two-stage plates in the China mainland are reanalyzed based on the above velocity field. On the basis of the Euler vectors of the abovementioned, i. e. the whole Chinese continent, two-stage plates, provincial plates, sub-blocks in some provinces' interior, as well as that of Eurasia plate derived from NNR-NUVEL1A plate motion model, the contribution of the average movement of each block to the horizontal velocity field could be available and then the residual velocity fields in Mainland China are further analyzed and compared.

The results show that the NNR-NUVEL1A model only deducts the partial movement trend of the velocity field in Mainland China. In contrast, the overall movement model of Mainland China plate can better reflect the overall movement trend. The movement model of two-stage plates and provincial plates in Chinese mainland, both of whose inner and outer average precision is less than 2 mm.a(-1) and 3 mm.a(-1), respectively, can both depict the local movement characteristics of Mainland China more precisely, and the only difference between them is that the former is easier to understand in the sense of physics while the latter is simpler in using. However, both of them is not perfect for researching the relative motion of some regions such as Xinjiang, Tibetan Plateau, Sichuan, Yunnan where exist complex crustal movement. Hence, through cluster analysis with K-Means++ on horizontal velocity field in these complex areas, these provincial blocks are further decomposed into some sub-blocks quickly and accurately. Our results are in accordance with those of present-day blocks of second order. Consideration to the impact of complex geological structure, topography and geomorphology in these provinces and the physical significance in respect to each corresponding provincial plate, we also give the Euler vectors of these sub-blocks in some provinces' interior. The result can be concluded that not only the average error and mean square error are less than 2 mm.a(-1) in Mainland China but also the precision of horizontal velocity fields can reach 2 mm.a(-1) in some complex regions, that is Xinjiang, Tibet, Sichuan, Yunnan. Obviously, the scheme of the sub-block demarcation in some provinces' interior by the method of K-Means++ is effective and feasible in terms of high precision and convenience.

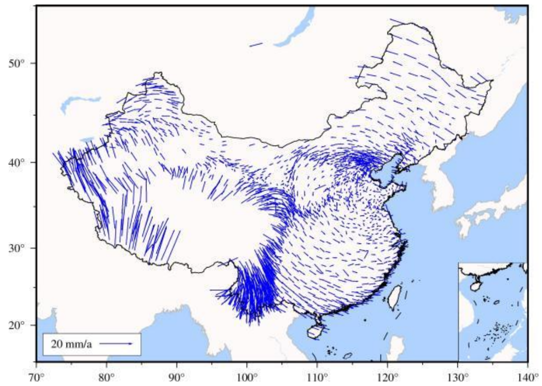

(a)

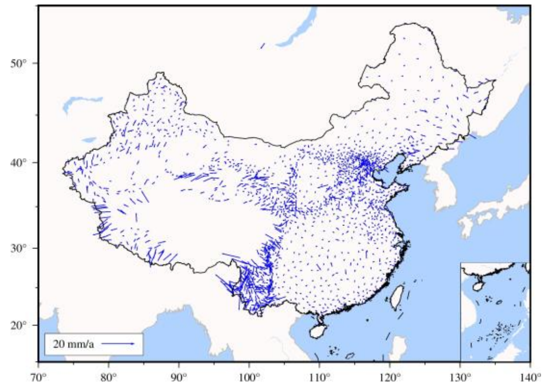

(b)

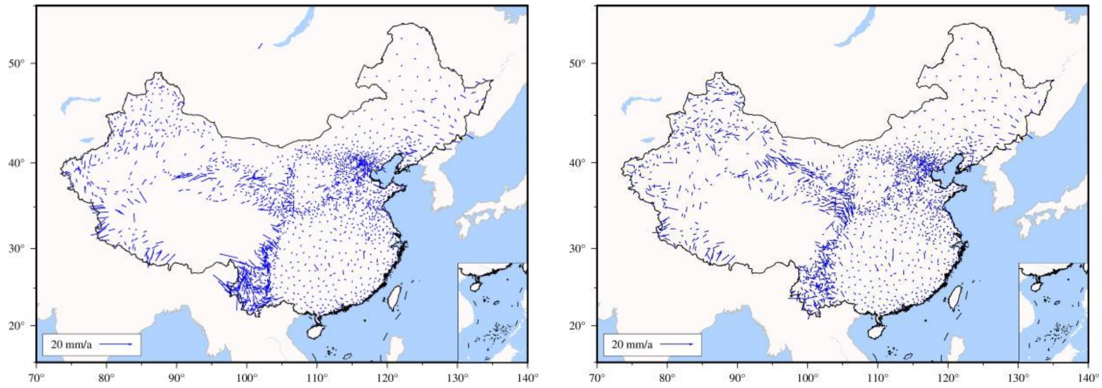

(c) (d)

Figure 5. The horizontal relative velocity field of Chinese Mainland: (a) relative to Chinese mainland ; (b) relative to the secondary block; (c) relative to provincial blocks; (d) relative to sub blocks within the province

6 Distribution characteristics of crustal Deformation in Chinese Mainland and its relationship with strong earthquakes

GNSS velocity field can directly reflect the characteristics of crustal movement in the study area under a certain reference frame, and its spatial distribution characteristics will vary with the change of datum. While the crustal strain field is not limited by datum, and it can reflect the dynamic mechanism of crustal deformation. This section estimates the GNSS horizontal crustal strain rate field in continental China using the GNSS horizontal velocity field of more than 2000 sites from the above solution to analyze the characteristics of the current crustal strain rate field in continental China. And we obtained the horizontal grid velocity field (1◦ ×1◦) of continental China, as shown in Figure 6. The red arrow is raw velocity, and the blue arrow is interpolation velocity.

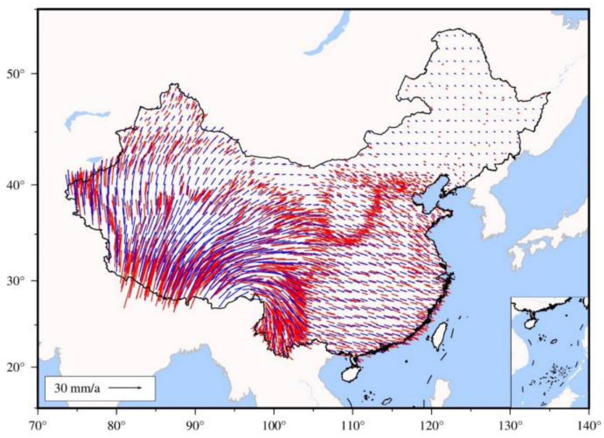

Figure 6. The horizontal grid velocity field (1◦×1◦) of continental China (The red arrow is the known velocity, and the blue arrow is the grid velocity).

The principal strain rate field of continental China can be estimated using the horizontal grid velocity field . The overall pattern of tectonic deformation in continental China in the past two decades is shown in Figure 7. The principal strain rate in West China is much higher than that in East China. Among them, the principal strain rate in the west is large, and the strain distribution is complex, indicating that the crustal deformation in this area is intense and the geological tectonic movement is more complex. The high-strain areas in continental China are mainly located in the Qinghai Tibet Plateau and Tianshan Mountains. The principal compressive strain rates of the Himalayas and Tianshan orogenic belts are perpendicular to the orogenic belt trend, and the other principal strain rate is much lower than the principal compressive strain rate, revealing the northward pushing of the Indian plate. In contrast, the total amount of principal strain rates in the east is small. The principal strain rates of several active blocks in the east are less than 5 nstrain/year, and the principal strain rate field has no significant regional distribution characteristics.

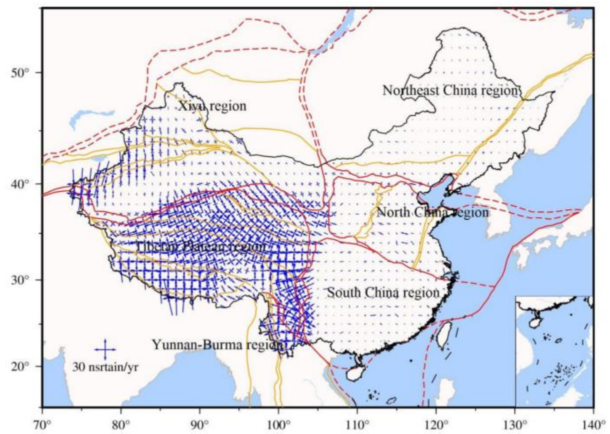

Figure 7. The principal strain rate field in continental China (The red and yellow lines are block boundaries).

Figure 8 shows the relationship between a strong earthquake and the second strain invariant field in the Chinese mainland. Similarly, we find that there is a strong correlation between the distribution of strong earthquakes and the second strain invariant field, that is, most strong earthquakes are concentrated in yellow and red areas where the second strain invariant is greater than 20 nstrain/year. It can be seen that the second strain rate invariance of the Tianshan, Qinghai, Tibet Plateau, and Sichuan-Yunnan regions is large, and the second strain rate invariance changes greatly. The range of the second strain rate in Sichuan Yunnan, Qinghai Tibet Plateau, and Tianshan region are 5~40, 10~60, and 10~45 nstrain/year respectively. In fact, strong earthquakes occur widely in the Qinghai, Tibet Plateau, Sichuan Yunnan, and Tianshan regions, while there are relatively few strong earthquake activities in other regions. From this, we can infer that the occurrence of strong earthquakes is closely related to the magnitude and change rate of the second strain rate invariant field.

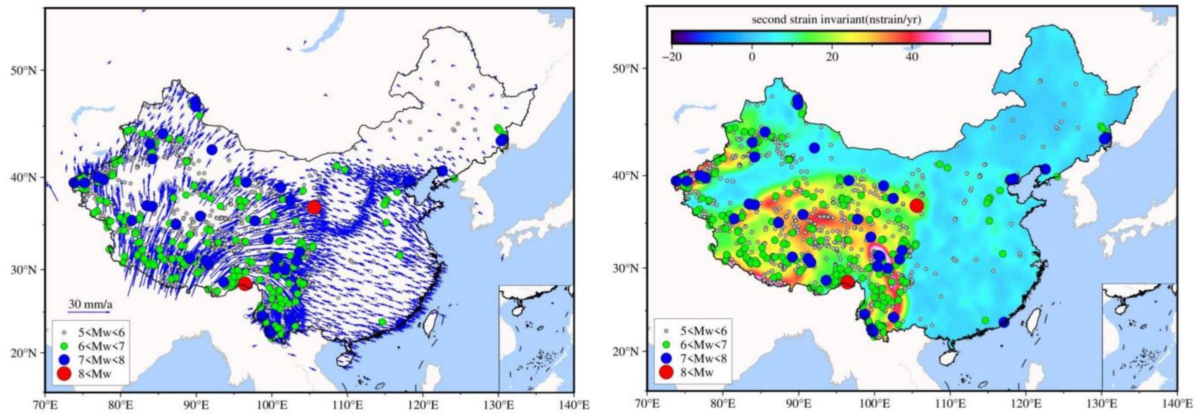

Figure 8. The distribution of strong earthquake and deformation strain field

According to the relationship between the above strong earthquake distribution and GNSS velocity field and the second strain invariant field, we can draw the following conclusions. First, strong earthquakes occur when the magnitude and direction of the GNSS velocity field change greatly. The change of velocity field is caused by the mutual compression of crustal structures of different active blocks. The stronger the regional velocity change, the higher the frequency of strong earthquakes. Secondly, strong earthquakes usually occur in areas with large strain rates and large changes in strain rates. All strong earthquakes with > 7 are distributed in the region where the second strain rate invariance is greater than 20 nstrain/year.

7 The progress of CGCS2000 frame maintenance in millimeter level accuracy

Up to Date, the coordinate precisions of ITRF reference stations have already reached to mm level, even submilimeters, at reference epoch, but the coordinate maintenance precision of these stations are still at cm level due to non-linear movements related with geophysical phenomena. To enhance the accuracy of site location expressed, an enhanced method known as SSA-PD (Singular spectrum analysis with pseudo data) to address the phase shift issue of SSA and another method named SSA-P (Singular spectrum analysis for prediction) for predicting the coordinates of GPS sites at any specific time are proposed and put into use. For this purpose, the coordinate time series of China continuous operating reference stations spanning of ten years are used. After interpolation for missing data and gross data detection, all position time series were modeled with SSA-PD. Here only stations located in the plate of the South China subplate were taken as an example, the modeling results in U directions are shown in Figure 9.

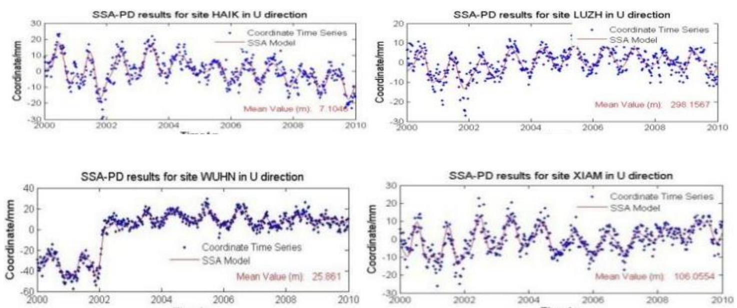

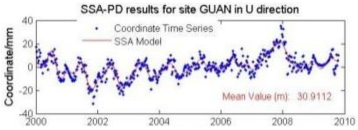

Figure 9. Modeling results for station nonlinear movements in the U directions in the South China subplate.

From the results analyzed, the original signals and modeled signals at most stations agreed well, and their differences - which were in fact the accuracies of the model results - were better than 3 mm, 2 mm, and 5 mm in the E, N, and U directions, respectively. Figure 9 also shows that similar trends and oscillation terms exist at the sites located in the same subplate, especially in the horizontal directions. Thus, it is possible for us to model the nonlinear movement at sites with a long period of time series and expand the nonlinear movement to the sites with a short period of observations, and then transform its position from the current epoch to any epoch needed.

The time series of two stations with a distance of under 500 km had approximately the same amplitude and phase. If the distance between two stations was greater, both the amplitude and the phase drift at the two stations were not synchronized. It seems that only the nonlinear movement at two stations within a 500 km distance can be replaced in this way.

This another expanded method called SSA for prediction (SSA-P), for predicting the coordinates of GPS sites at any specific time was proposed. Its performance was assessed using 10-year GPS time series of weekly coordinates of 32 national GPS sites. The first 468 weekly samples were used to reconstruct the signals; the reconstructed model was then used to predict the next 52 weekly samples to validate the model's prediction results.

As vertical movements are much more complicated due to co-seismic and post-seismic deformations, global geophysical fluid dynamics, and so forth. It was found to be typical that the characteristic of the modeling based on earlier years could not be expanded forward to following years or had poor accuracy; thus, the accuracy of the modeling for the vertical component was usually poorer than that of the horizontal components, even though the accuracy of the modeling in the vertical direction was better than 5 mm.

In general, the results shown in Figure 10 indicate insignificant differences between the predicted signals and the real signals; the accuracy of the predicted results is quite stable, with an accuracy of about 3 mm at most stations.

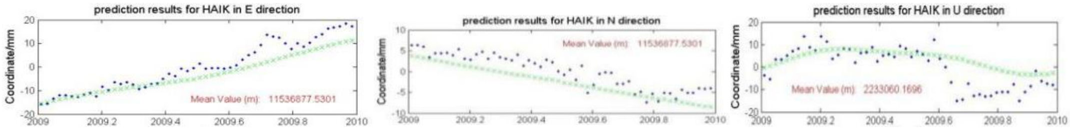

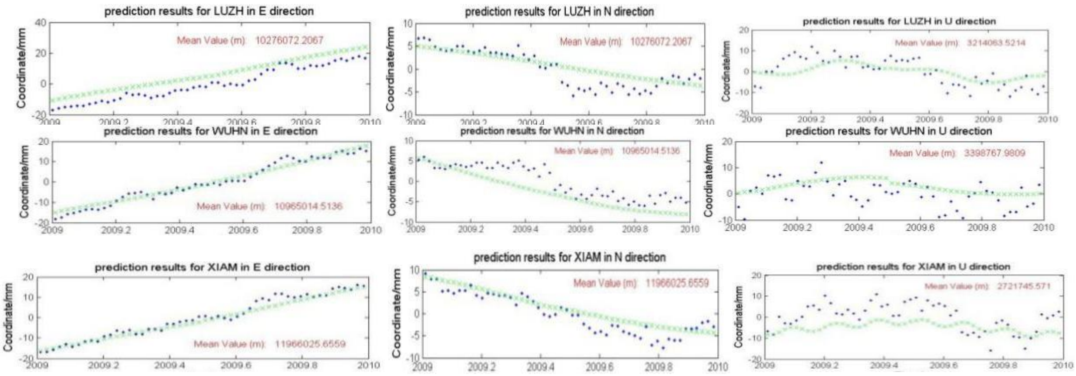

Figure 10. Prediction results for station nonlinear movements in the N, E, and U directions in the South China subplate.

The results for the performance assessment of SSA-P indicate that it is possible to obtain a high accuracy even when the noise level is larger than the oscillatory components.

The accuracy of the SSA-P used to predict the coordinates of the GPS sites in the horizontal and vertical directions was better than 5 mm and 1 cm, respectively, for most GPS sites, even though annual and semiannual signals in amplitude exist in the time series. However, the prediction results for the stations in the Lhasa and ChuanDian plates were poor, compared with those for the stations in other plates, resulting in the same conclusion as the fitted error from the plates.

8 The Preliminary Realization and Evaluation of CTRF2020

The current research of the international and regional coordinate reference framework is mainly realized by GPS technology. The launch of the last BDS3 satellite on June 23 of 2020 marked the completion of the global deployment of BDS. Therefore, it is urgent to study and establish the corresponding coordinate reference framework. We aim to preliminarily realize and evaluate the BDS3/COMPASS terrestrial reference framework (CTRF2020). CTRF2020 reference epoch is 2020.0, and it can be expressed with the coordinates and velocities of a series of reference sites at the epoch of 2020.0.

Firstly, the evaluation of the actual service performance of BDS in the global region reflects the high visibility and change trend of BDS satellite in recent three years, which provides basic input data for CTRF2020. Then, the BDS observations of about 100 global stations in the recent three years are calculated by PPP and NET solution, to obtain the global high-precision BDS coordinate time series. Then, the BDS time series of the two solutions are fitted and compared with the IGS14 velocity field. The results show that the series accuracy of PPP-BDS and NET-BDS solutions is equivalent, and there is an mm-level systematic deviation with IGS14 solutions. The horizontal series fitting accuracy of PPP-BDS and NET-BDS solutions is better than that of the vertical direction, the accuracy of NET-BDS solution is slightly better than PPP-BDS, and the difference of fitting accuracy is 0.12, 0.13, and 0.50 mm in the NEU direction. The velocity field accuracy of PPP-BDS and NET-BDS solution is the same, and the overall three-dimensional velocity difference is less than 0.2 mm/a. The velocity fields of PPP-BDS and NET-BDS solution have little difference from IGS14, and the overall difference is less than 0.5 mm/a. Finally, we give the limitations and improvement direction of CTRF2020. The preliminary realization and evaluation of CTRF2020 may be expected to provide a reference for the future realization of a comprehensive terrestrial reference framework dominated by BDS3 technology and supplemented by multi-source space geodetic technology.

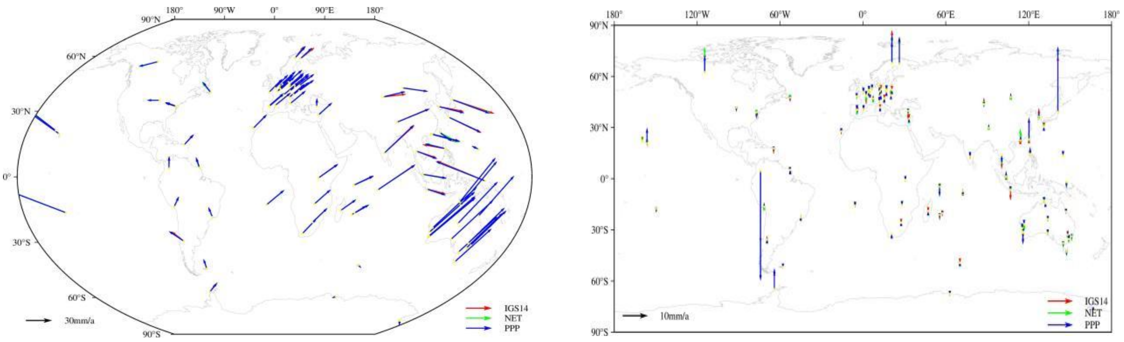

(a) (b)

Figure 11. CTRF2020 horizontal and vertical velocity field.

We aim to preliminarily realize and evaluate the terrestrial reference framework based on BDS technology. The main research work includes three aspects:

(1) We evaluate the global actual service performance of BDS in recent years. By 2021, a total of 59 BDS satellites have been launched, the number of available BDS satellites in orbit has exceeded 40, and the number of visible BDS satellites in the global region has exceeded 10, which indicates that the high visibility of BDS satellites in the global region in recent three years. This provides the necessary input conditions for CTRF2020, that is, long-term and reliable global BDS observation data.

(2) We fit and analyze the global BDS time series based on PPP-BDS and NET-BDS, respectively, and compare them with IGS14 velocity field. The results show that the series accuracy of PPP-BDS and NET-BDS solutions is equivalent, and there is a systematic error from IGS14 solution. The velocity parameters in BDS time series are not sensitive to periodic parameters, and whether the difference of velocity fitting solution of the periodic term is considered is within 0.1 mm/a. The BDS time series of the two modes can accurately reflect the station's linear motion rate and periodic change trend, and the periodic change trend in the vertical direction is usually more obvious than that in the horizontal direction. The horizontal series fitting accuracy of PPP-BDS and NET-BDS solutions is better than the vertical direction, and the series fitting accuracy of NET-BDS mode is slightly better than PPP-BDS. The difference in the NEU direction fitting accuracy between them is 0.12, 0.13, and 0.50 mm.

(3) We analyze and evaluate the accuracy and reliability of two kinds of velocity field models (PPP-BDS and NET-BDS) of CTRF2020. The results show that the three-dimensional velocity fields of PPP-BDS and NET-BDS are roughly the same in both numerical and direction, and the horizontal direction of CTRF2020 is close to IGS14 in both numerical and direction. However, there are some differences in the vertical direction. The velocity field accuracy of PPP-BDS and NET-BDS solution modes is the same, and the overall three-dimensional velocity difference is less than 0.2 mm/a. The velocity field of PPP-BDS and NET-BDS solution has little difference from that of IGS14, and the overall difference is less than 0.5 mm/a.

This research is limited to the processing and analysis of global BDS observations in the recent three years (2019–2021), and there are still several jobs to be developed and improved. First, at present, the number of global BDS continuous observation stations is still small, the spatial distribution is uneven, and the cumulative observation time is short, which also affects the accuracy and reliability of the preliminary velocity field product of CTFR2020 to a certain extent. Second, there is still a lack of integrated satellite orbit and clock error products of BDS, which leads to some inconsistency in the coordinates calculated by different analysis centers. Third, the integrated multi-source space geodetic technology is expected to further improve the stability and reliability of the framework. Fourth, although CTRF2020 adopts the analysis and evaluation technology of long-term time coordinate series of stations considering nonlinear factors, its results do not fully reflect the nonlinear variation parameters.

9 Summary

The research on the maintenance methods of regional reference frame based on GNSS has partly promoted the role of GNSS technology in dynamic monitoring and maintenance of regional reference frame and datum services, improved the theory and methods of regional reference frame maintenance, and provided technical support for the maintenance and use of regional reference frame. Relevant methods and technologies have played an important role in multiple national and provincial projects.

The current research of the international and regional coordinate reference framework is mainly realized by GPS technology. CTRF2020 aim to preliminarily realize and evaluate the BDS3/COMPASS terrestrial reference framework (CTRF2020). CTRF2020 reference epoch is 2020.0, and it can be expressed with the coordinates and velocities of a series of reference sites at the epoch of 2020.0.

In general, the emergence and development of GNSS technology in the 1990s significantly promoted the research of tectonic movement and deformation monitoring into a new stage. With over 30 years of research, horizontal tectonic movement and main deformation characteristics in continental China have been clear, and the tectonic deformation in most areas has been accurately quantified. In the future, it is necessary to intensify the continuous GNSS observation further to obtain the three-dimensional tectonic movement information and its evolution characteristics with time. At the same time, it is necessary to strengthen the integration of GNSS and different geodetic technologies, and interdisciplinary research.

In addition, the dynamic maintenance of the millimeter level terrestrial reference frame still needs to consider the following issues: firstly, further improve the spatial observation data processing technology, weaken the impact of system errors, and obtain more accurate reference station coordinates, which is the foundation for improving the dynamic maintenance accuracy of the terrestrial reference frame; Secondly, the accuracy of nonlinear motion modeling of reference stations based on geophysical influence mechanisms and coordinate time series needs to be further improved; Thirdly, we need to further improve the implementation accuracy and stability of the epoch reference frame.

Bibliography

DANG Yamin, CHENG Chuanlu, YANG Qiang, et al. (2022) Vertical Deformation Characteristics Affected by Strong Earthquakes in Mount Qomolangma and Surrounding Areas.Geomatics and Information Science of Wuhan University, 2022, 47(1).

DANG Yamin, GUO Chunxi, JIANG Tao, et al. (2021) 2020 height measurement and determination of Mount Qomolangma. Acta Geodaetica et Cartographica Sinica , 50(4).

DANG Yamin, Yang Qiang, WANG Wei, et al. (2022) Analysis on 3D crustal deformation of Qinghai-Tibet Plateau and its surrounding areas based on block model. Acta Geodaetica et Cartographica Sinica, 2022,51(7) : 1192-1205. DOI: 10.11947/j. AGCS.2022.20220123.

DANG Yamin,JIANG Tao, CHEN Junyong.(2022) Review on Research Progress of the Global Height Datum.Geomatics and Infor mation Science of Wuhan University, 47(10):1576-1586.

Guangwei, J. I. A. N. G., Panlong, W. A. N. G., Chunxi, G. U. O., Bin, W. A. N. G., & Yuanxi, Y. A. N. G. Short-term GNSS network solution and performance in large height difference region with tropospheric delay constraint. Acta Geodaetica et Cartographica Sinica, 51(11), 2255.

Hou, Y., Wang, H., Wang, J., Ma, H., Ren, Y., Li, P., & Wang, Y. (2022). Studies and Analysis of Combining BDS-3/GNSS Ultra-Rapid Orbit Products from Different IGS Analysis Centers. Remote Sensing, 14(23), 6122.

Hu, W. A. N. G., Yamin, D. A. N. G., Yangfei, H. O. U., Jinzhong, B. E. I., Jiexian, W. A. N. G., Guixia, B. A. I., ... & Shoujian, Z. H. A. N. G. (2020). Rapid and precise solution of the whole network of thousands of stations in China based on PPP network solution by UPD fixed technology. Acta Geodaetica et Cartographica Sinica, 49(3), 278.

JIANG, G. W., WANG, B., WANG, Y. W., LI, K., & SUN, Y. Y. (2020). Establishment of regional terrestrial refference frame considering coordinate characteristic and stability. Progress in Geophysics, 35(1), 8-15.

Jiang, G., Wang, P. , Guo C., Wang, B. , Yang Y. (2022). Short-term GNSS network solution and performance in large height difference region with tropospheric delay constraint. Acta Geodaetica et Cartographica Sinica. 51(11): 2255-2264.

Pengfei Cheng a, Yingyan Cheng, Xiaoming Wang, Suqin Wu, Yantian Xu. Realization of an Optimal Dynamic Geodetic Reference Frame in China: Methodology and Applications[J]. Engineering,2020,6(08):879-917

REN, Y., WANG, J., WANG, H., LIAN, L., HOU, Y., & WANG, Y. (2021). Construction of Velocity Field in Chinese Mainland Based on Local Seamless Delaunay Triangulation with Inverse Distance Weighting Method. Geomatics and Information Science of Wuhan University, 46(7), 1071-1080.

Ren, Y., Lian, L., & Wang, J. (2021). Analysis of seismic deformation from global three-decade GNSS displacements: implications for a three-dimensional earth GNSS velocity field. Remote Sensing, 13(17), 3369.

Ren, Y., Wang, H., Hou, Y., Wang, J., Cheng, Y., & Li, P. (2022, May). The Preliminary Realization and Evaluation of CTRF2020 Based on New BDS3 Technology. In China Satellite Navigation Conference (CSNC 2022) Proceedings: Volume I (pp. 57-69). Singapore: Springer Nature Singapore.

Ren, Y., Wang, H., Lian, L., Wang, J., Cheng, Y., Zhang, Y., ... & Zhang, S. (2021). A method based on MTLS and ILSP for GNSS coordinate time series analysis with missing data. Advances in Space Research, 68(9), 3546-3561.

Ren, Y., Wang, H., Wang, J., Lian, Li., Zhu, W., Wang, Y., & Zhang, S. (2020). The sub-block demarcation with K-Means plus plus in each province's interior and establishment analysis of the relative horizontal velocity field model in Mainland China. CHINESE JOURNAL OF GEOPHYSICS-CHINESE EDITION, 63(7), 2516-2533.

Sun Fuping, Jia Yanfeng, Zhu Xinhui, Xiao Kai, Liu Jing. (2022). Advances in dynamic maintenance technology of mm-level terrestrial reference frame. Geomatics and Information Science of Wuhan University, 47(10): 1688-1700.

Wang B., Jiang G., Sun Y., Hu W., Ma X.(2022). Regional reference frame maintenance considering anisotropy of plate motion. Science of Surveying and Mapping, 47(12):16-22.

Wang X, Cheng Y, Wu S, Zhang K. An effective toolkit for the interpolation and gross error detection of GPS time series. Surv Rev 2015;48(348):202–11.

Wang XM, Cheng YY, Wu SQ, Zhang KF. An enhanced singular spectrum analysis method for constructing nonsecular model of GPS site movement. J Geophys Res Solid Earth 2016;121(3):2193–211.

Wang, H., Hou, Y., Dang, Y., Bei, J., Zhang, Y., Wang, J., ... & Gu, S. (2021). Long-term time-varying characteristics of UPD products generated by a global and regional network and their interoperable application in PPP. Advances in Space Research, 67(2), 883-901.

Wang, H., Li, P., Wang, J., Ma, H., Hou, Y., & Ren, Y. (2022). Analysis of BDS-3 Real-Time Satellite Clock Offset Estimated in Global and Asia-Pacific and the Corresponding PPP Performances. Remote Sensing, 14(24), 6206.

Wang, H., Ren, Y., Hou, Y., Wang, J., Zhang, Y., Cheng, Y., ... & Fang, S. (2022). The refinement of reprocessed GNSS three-decade displacement trajectory model with spectral analysis and hypothesis test. Advances in Space Research, 70(7), 1810-1829.

Wang, H., Ren, Y., Wang, A., Wang, J., Cheng, Y., Fang, S., & Yang, Q. (2022). Two-Decade GNSS Observation Processing and Analysis with the New IGS Repro3 Criteria: Implications for the Refinement of Velocity Field and Deformation Field in Continental China. Remote Sensing, 14(15), 3719.

Zhu Xinhui, Sun Fuping, Wang Ren. (2009). GIobal plate motion models based on ITRF2005. Progress in Geophysics, 24(3):859-865.

Zhu Xinhui, Sun Fuping, Wang Ren. (2010). Development and comparison of current plate motion. Journal of Geomatics Science and Technology, 27(3): 184-188

Zhu Xinhui, Sun Fuping. (2014). Establishment methods of modern crustal motion reference datum. Beijing: Sino Maps Press.

Zhu Xinhui, Yang Li, Sun Fuping, Wang Ren. (2014). Study on Reference Datum of Global Vertical Crustal Motion by SLR Techniques. Acta Geodaetica et Cartographica Sinica, 43(3): 240-247.

The Progress of IGS Analysis Center and Data Center of Wuhan university

Weiping Jiang[1], Qile Zhao[1], Min Li[1], Jing Guo[1], Jianghui Geng[1], Zhao Li[1], Shengfeng Gu[1], Qiang Zhang[1], Zhigang Hu[1], Na Wei[1]

[1] *GNSS Research Center, Wuhan University, Wuhan, China*

1 Introduction

GNSS Research Center of Wuhan University（WHU） was established in January 1998. Its main focus is on the basic theoretical research and methods of satellite positioning navigation and related fields, the promotion and application of new technologies, and the cultivation of "high-precision and cutting-edge" talents. It is not only the National Engineering Research Center for Satellite Navigation System, but also one of the analysis centers (ACs) and data centers (DCs) of IGS. Additionally, it is designated by the Ministry of Science and Technology of China as a pilot unit for the navigation and positioning service industry in the country, and serves as the analysis center for both the International GNSS Monitoring and Assessment System (iGMAS) and the BeiDou data center and analysis center. The GNSS research center of WHU is now an internationally influential research and innovation platform and talent cultivation base in the field of satellite navigation.

2 WHU Analysis Center

As one of the ACs of the IGS, WHU has been contributing to the IGS for providing ultra-rapid as well as rapid orbit and clock solutions of the established GPS and GLONASS since 2012. In the same year, the IGS initiated the Multi-GNSS Experiment (MGEX) to support the analysis of the emerging GNSS systems and prepare the IGS for Multi-GNSS, which includes GPS, GLONASS, the European Galileo system, the Chinese BeiDou Navigation Satellite System (BDS), the Japanese Quasi-Zenith Satellite System and the Indian Regional Navigation Satellite System (IRNSS/NaVIC). The major products, i.e., orbits, Earth Orientation Parameters (EOPs), and satellite clock as well as attitude have also been provided by WHU since 2013. Besides, WHU has engaged the third reprocess of IGS for generating the high accurate station coordinates as the inputs for establishment of International Terrestrial Reference Frame (ITRF) during 2019-2020. The products provided by WHU are summarized in Table 1.

Table 1． List of products provided by WHU

WHU final GNSS produtcts	
WUM0MGXFIN_YYYYDDDHH _01D_05M_ORB.SP3	5-min orbits for GPS/GLONASS/Galileo/BDS satellites
WUM0MGXFIN_ YYYYDDDHH_01D _30S_CLK.CLK	30-second clocks for GPS/GLONASS/Galileo/BDS satellites
WUM0MGXFIN_ YYYYDDDHH _01D_30S_ATT.OBX	30-second attitudes for GPS/GLONASS/Galileo/BDS satellites
WUM0MGXFIN_ YYYYDDDHH_01D_01D_ERP.ERP	Earth Rotation Parameters
WHU rapid GNSS products	
WHU0OPSRAP_YYYYDDDHH_01D_15M_ORB.SP3	15-min orbits for GPS/GLONASS/Galileo satellites
WHU0OPSRAP_YYYYDDDHH_01D_05M _CLK.CLK	5-min clocks for stations and GPS/GLONASS/Galileo satellites
WHU0OPSRAP_YYYYDDDHH_01D_01D_ERP.ERP	Earth Rotation Parameters
WHU ultra-rapid GNSS products	
WHU0OPSULT_YYYYDDDHH_02D_15M_ORB.SP3	15-min orbits for GPS/GLONASS/Galileo satellites, provided to IGS every 6 hours
WHU0OPSULT_YYYYDDDHH_02D_01D_ERP.ERP	Observed and predicted ERPs provided to IGS every 6 hours
WHU Ionosphere products	
whugDDD0.YYi	Final GIM with 3-d GPS/GLONASS observations
whrgDDD0.YYi	Rapid GIM with 1-d GPS/GLONASS observations
WUM0MGXRAP_YYYYDDD0000_01D_01D_ABS.BIA	Rapid OSB with 1-d multi-GNSS observations
IONO00WHU0	Real time GIM with 5-min GPS observations

WUM final products

Initially, the focus of WHU's MGEX-related activity was on the analysis of the BDS performance. With the support of the BeiDou Experimental Tracking Network (BETN) established by WHU, the orbit and clock solutions for BDS-2 satellites have been determined and submitted to IGS MGEX since 2012. 2013 was the first year when quad-constellation, i.e., GPS, GLONASS, Galileo, and BDS, was included in WHU's MGEX (WUM) solution by using the BETN and increasing MGEX network. Later, the QZSS Michibiki satellite has been incorporated into the WUM solution since 2015. With the development of the BDS-3 constellation, the tracking networks from the International GNSS Monitoring and Assessment System (iGMAS) and IGS have been upgraded gradually to track BDS-3 signals. This laid the fundament for the analysis of BDS-3. Hence, since Day of Year (DOY) 1, 2019, BDS-3 satellites have been incorporated in WUM routine analysis. The frequencies used for BDS data processing were switched from B1I/B2I to B1I/B3I. Considering that no more than 30 stations are available with ability of tracking the signals from the three IGSO satellites as well as the MEO satellites with PRN beyond C37 in 2019, they have not been included for analysis until DOY 279, 2020. Besides, the GEO satellites, i.e., C59, C60 and C61, are not analyzed due to poor tracking geometry as well as deficiencies in orbit modeling. Meanwhile, the QZSS-2 satellites have been also included for analysis since DOY 1, 2019.

There are some important development steps for the final products since 2022. The first one is that the ITRF2020 frame has been adopted since GPS week 2238. At the same time, the recommendation for the third reprocess of IGS have been implemented, including the long-term mean pole, high-frequency EOP, ocean tidal loading corrections for station deformation and gravitational effect on satellite orbits based on FES2014b, and more. Besides the model updates, the undifferenced ambiguity resolution was implemented for orbit and clock determination instead of the double-difference ambiguity resolution used previously. The following figure show the workflow. Generally, the processing is accomplished in two analysis steps. First, the orbit and clock are estimated based on zero-difference measurements with the double-difference ambiguity resolution. Subsequently, the undifferenced ambiguities are fixed based on the daily wide-lane and 15min narrow-lane FCB. Finally, the satellite orbit and clock corrections are re-estimated based on a zero-difference analysis including undifferenced ambiguity resolution for GPS, Galileo, and BDS. As the improvement of successful ambiguity fixing rate, the orbit quality has been improved. All of the updates have been active since GPS week 2238.

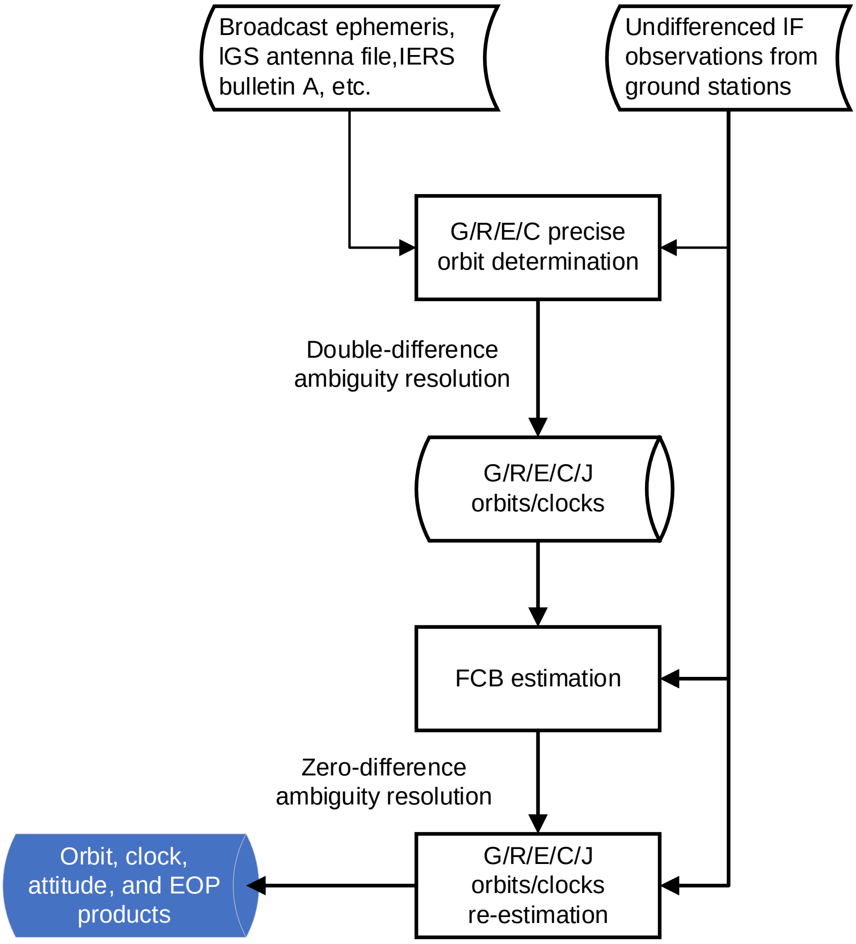

Figure 1. The workflow for generation of WUM final products since GPS week 2238.

In summary, the WUM orbit and clock solution has seen significant improvements in the recent years. It turned out to be a good testbed for the more complex multi-GNSS environment of the future. The products are made available for public use via the IGS data center WHU (ftp://igs.gnsswhu.cn).

BDS products

Besides these operational changes the modelling has improved as well. Considerable progress was made in the orbit modelling, in particular for the BDS satellites. In order to overcome the deficiency of Extended CODE Orbit Model (ECOM) under orbit normal (ON) attitude, a constrained constant acceleration in along-track has been used (Guo et al. 2016). Wang et al. (2019) confirmed that the perturbation caused by the communication antenna generates the Sun-elongation-angle-dependent variation and the bias for BDS GEO satellites, and an empirical a priori SRP model was established to enhance the ECOM-1 model. By using this enhanced SRP model, the SLR validation achieve around 10 cm. This approach has also been used to establish an a priori SRP model for BDS-3 MEO satellites (Guo et al. 2023). The prior models have been active since November 2017 and June 2020, respectively. At the beginning of 2015, the SRP model proposed by Montenbruck et al. (2015) has been used to enhance the ECOM1 to reduce the Sun-elongation angle dependent orbit errors due to the elongated satellite bodies of Galileo. Similar model has been proposed for QZSS-1 Michibiki satellite (Montenbruck et al. 2017), it has been used in June,2017, and is quickly switched to Zhao et al. (2018). Besides SRP, models for Earth albedo and transmit antenna thrust were implemented and activated for GPS, GLONASS, and Galileo in October 2017. The box- wing models used for the albedo modelling are based on the meta data disclosed by the GSA (2016), CAO (2017) as well as the guessed value from Rodrigues-Solano (2009). The transmit power used for the antenna thrust modelling is based on a study performed by Steigenberger et al. (2018) for GPS, GLONASS, and Galileo as well as the disclosed values from CAO (2017) for QZSS. In June 2020, the earth albedo as well as thrust antenna were also active for BDS-2 IGSO and MEO as well as BDS-3 MEO satellites. Based on that Wang et al. (2022) analyzed the impact of the spacecraft’s thermal re-radiation, a model covering this effect has been introduced in June 2020.

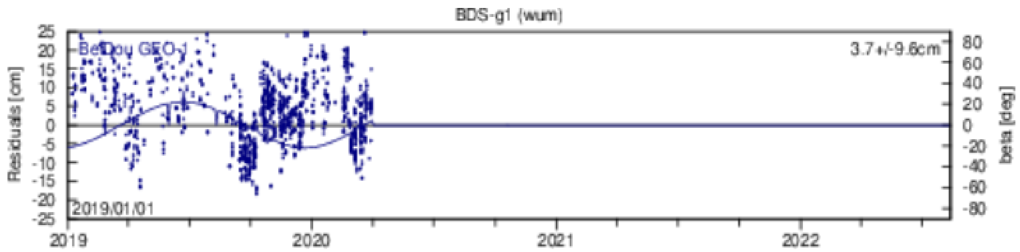

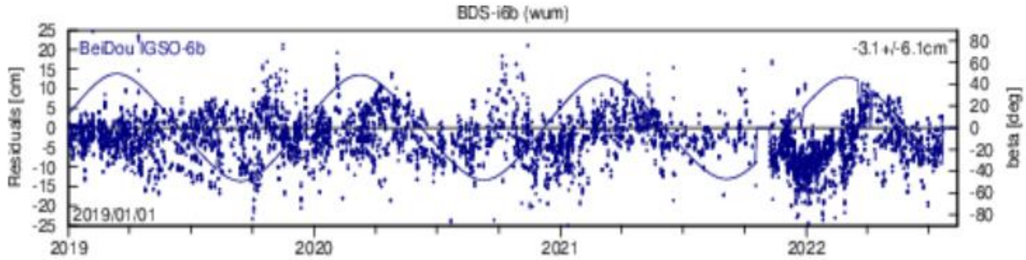

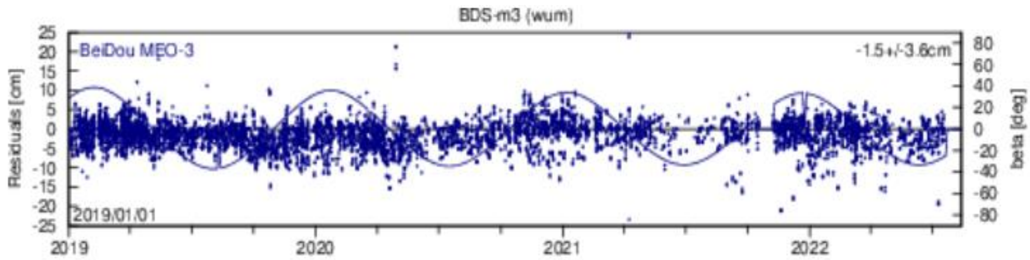

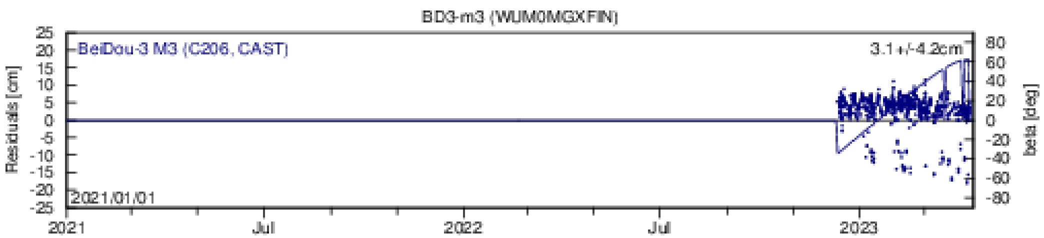

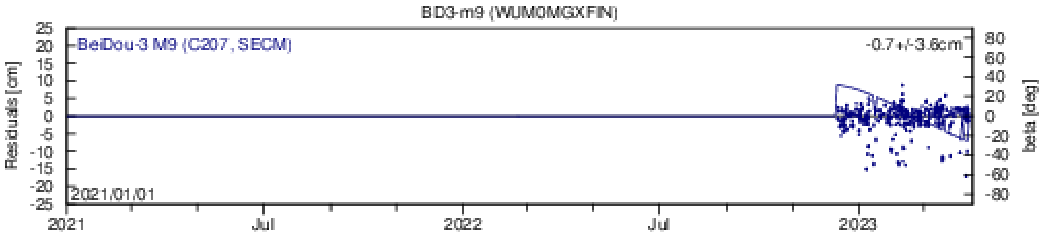

Figure 2. The SLR residuals for BDS-2 GEO, IGSO, MEO, and BDS-3 CAST as well as SECM MEO satellites (source https://igs.org/mgex/analysis).

The calibrated phase center corrections (PCCs) of BDS-2 from Guo (2016) as well as the satellite-specific PCO from CSNO (2019) for BDS-3 have been used until GPS week 2072, when the block-specific PCOs in the IGS official antenna file are used for all constellations. For receiver antenna corrections, as ground antenna calibrations covering all GNSS and all frequencies are not available to the IGS until the repro3, the PCCs for the new constellations are adopted from the GPS L1 and L2 frequencies when analyzing data from Galileo, BDS, and QZSS.

While yaw steering (YS) attitude was assumed for all GNSS satellites in the past, the eclipse attitude laws proposed by Kouba (2009) and Dilssner (2011) were activated for GPS and GLONASS. The eclipse attitude laws disclosed by the GSA (2016) were activated for Galileo IOV and FOC satellites. The yaw-steering and orbital-normal mode are used for BDS-2 IGSO and MEO as well as QZSS Michibiki satellites. All GEO satellites are assumed to obey the orbit-normal mode. The orientation of BDS-3 satellites in space follows the conventions in Montenbruck et al. (2015) considering eclipse yaw laws presented in Wang et al. (2018) and Yang et al. (2023) for BDS-3 CAST and SECM satellites, respectively.

The hourly updated WUM orbit and clock products are published since DOY 067, 2019, with the CSNO disclosed PCO and PCV values. Afterwards, they were switched to IGS values since Day of Year (DOY) 139, 2020. In addition, with the increase of the tracking stations, BDS-3 satellites with PRN beyond C37 were included at DOY 022, 2021. In order to be consistent with IGS, we switched the SRP from ECOM-1 to ECOM-2 for GPS in DOY 1, 2022. In addition, Earth albedo and antenna thrust model are considered for Galileo and BDS. We also provide the attitude file in ORBEX format to eliminate the disorientation effects on positioning.

Ionosphere products

WHU has studied the ionosphere using GNSS techniques for more than ten years in the field of ionospheric physics and space geodetic applications. In February 2016, the GNSS Research Center of Wuhan University was recognized as a new member of the IGS Ionosphere Associated Analysis Centers (IAACs). In the context of the IGS, WHU will benefit from the IGS ionosphere working group and will make more contributions to the global ionosphere mapping.

WHU use the spherical harmonic (SH) expansion model to map the global ionosphere in a solar-geomagnetic reference frame. Currently, both the GPS and the GLONASS data are used with the data sampling rate of 300 s. The maximum degree and order are 15, and the time resolution is 2 h. Considering the continuity of the SH expansion coefficients between consecutive days, 28-h (one day and two hours before and after the current day) observations are used. An inequality-constrained least squares method was proposed to eliminate the non-physical negative values in the VTEC maps (Zhang et al., 2013). The global ionosphere mapping methodology was implemented by a new GNSS Ionosphere Monitoring and Analysis Software (GIMAS) that was developed at the GNSS Research Center of Wuhan University (Zhang and Zhao 2018). The daily rapid and final GIM products have been generating with this new software since 21 June 2018.

The core modules of the GIMAS software were programmed by the C++ language and the automatic scripts were written by the Shell language. Figure 3 shows the flowchart of the software. The yellow rectangles represent the parallel computing with the OpenMP techniques. With this new high-performance software, we preprocessed the GIM products from 1998 to 2018 within about two solar cycles.

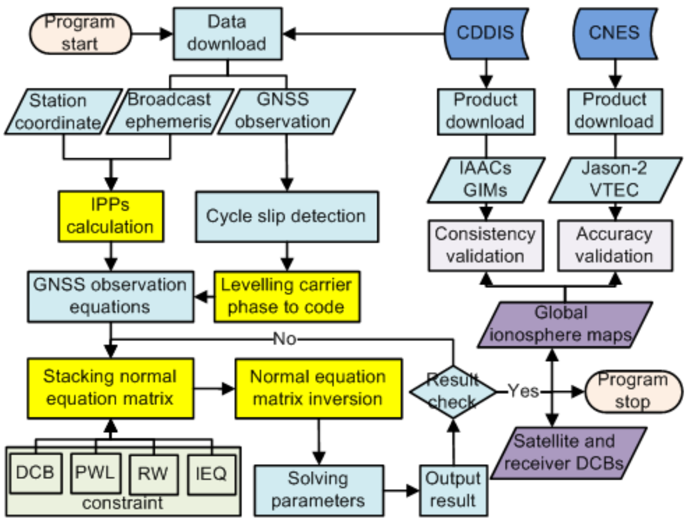

Figure 3. The GIMAS software flowchart.

The root mean square of WHU GIMs relative to the IGS final GIMs were computed and compared with that of the other six IAACs GIMs, as shown in Figure 4. This assessment demonstrated that the GIM products at WHU were consistent with other IAACs GIMs and had high accuracy and reliability for the global ionosphere monitoring and analysis.

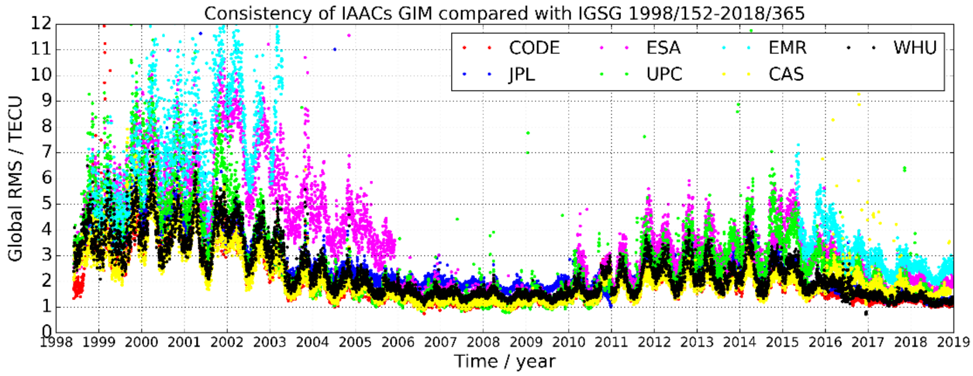

Figure 4. Consistency of the IAACs GIMs relative to the IGS final GIM.

At the end of year 2020, the GNSS Research Center of Wuhan University has published the RT GIM products and the very first products have been incorporated in the experimental combined RT-IGS GIM. During 2021, WHU updated their method and published the improved RT GIM products. The WHU RT GIM can be accessible via Wuhan Real Time Data Center (http://ntrip.gnsslab.cn) with Mountpoint IONO00WHU0 and Wuhan Data Center (ftp://igs.gnsswhu.cn/pub/whu/MGEX/ realtime-ionex) in IONEX format.

WHU use the Spherical Harmonic Expansion (SHE) model to map the global ionosphere in a solar-geomagnetic reference frame. Currently, only the GPS real-time data streams from about 120 globally distributed IGS stations are used. According to our experience, the real-time data is not enough to model the ionosphere precisely on a global scale when using the SHE technique. Considering the lack and the uneven distribution of the GPS-derived ionospheric data, external ionospheric information is also incorporated. In our method, we use the 2-day predicted GIM as background information. Specifically speaking, the real-time SHE coefficients are estimated using not only the real-time data but also the 2-day predicted SHE coefficients. It is very important to balance the weight between the real-time data and the background information, both the RT-GIM precision and the root mean square (RMS) map are influenced (Zhang and Zhao 2019).

The double frequency code and carrier phase observations with cut-off angle 10 degrees are used and the precise geometry-free ionospheric data is derived with the "Carrier-to-Code Leveling" method. To avoid the influence of satellite and receiver DCB on ionospheric parameters estimation, we directly use the previous estimated DCB from WHU rapid GIM product. We assume that the ionospheric TEC is condensed on a single layer with an altitude of about 450 km above the Earth. The global TEC is described by the SHE with a maximum degree and order 15. The WHU RT GIM is updated every 5 minutes and broadcasted every 1 minute.

In addition, we also published multi-GNSS and multi-frequency observable-specific signal bias (OSB) products. The products can be accessible via IGN FTP (ftp://igs.ensg.ign.fr) and WHU FTP (ftp://igs.gnsswhu.cn). The daily generated OSB products including GPS, GLONASS, Galileo, BDS and QZSS biases are computed using the MGEX data and several constrains or conditions are introduced in those computation.

3 BDS/GNSS Real-time prodcuts

Performance of RTS from IGS

Since mid-2008, the Real-Time Working Group (RTWG) of the International GNSS Service (IGS) has provided continuous BDS/GNSS orbit and clock products. There are 3 RTS ACs (Real-Time Service analysis centers) in China, i.e., CAS (Chinese Academy of Sciences), SHA (Shanghai Observatory) and WHU (Wuhan University), that are providing RT orbit and clock for BDS, GPS, GLONASS and Galileo in SSR format (Guo et al., 2022). Li et al. (2022) compared these RT products from different RTS ACs, and argued that CNES (Centre National D'Etudes Spatiales) and WHU (GNSS Research Center of Wuhan University) provides the most complete products with the best quality, with one-dimensional BDS orbit precision of MEO better than 10 cm, and clock precision better than 0.35 ns.

Real-Time Satellite clock filter model

White noise model is widely used for satellite clock estimation (Yang et al. 2019). It was validated oscillator noise model can benefit real-time satellite clock generation and prediction (Shi et al. 2019; Peng et al. 2019). As for satellite clock estimation constrained with oscillator noise model, the stochastic properties of the satellite clock model firstly could be determined by final product of IGS ACs. Then, they were applied to real-time satellite clock estimation to improve the stability of satellite clock time datum and accuracy of satellite clock in terms of data discontinuity. Figure 1 presents the overlapping HDEV of the different satellite clock products. It is interesting to note that the stabilities of estimated clock products with the clock model are improved more obviously for satellite clocks with outstanding stabilities such as clocks of GPS IIF/III, BDS-3, and Galileo satellites. To avoid filter divergence, an adapted online quality control procedure is developed to rapidly estimate Multi-GNSS real-time clocks (Fu et al., 2019). The identification is adapted properly for efficient computation, and identified measurements are removed from the estimation by adding the contribution of their observation equation to the normal equation but with opposite weights.

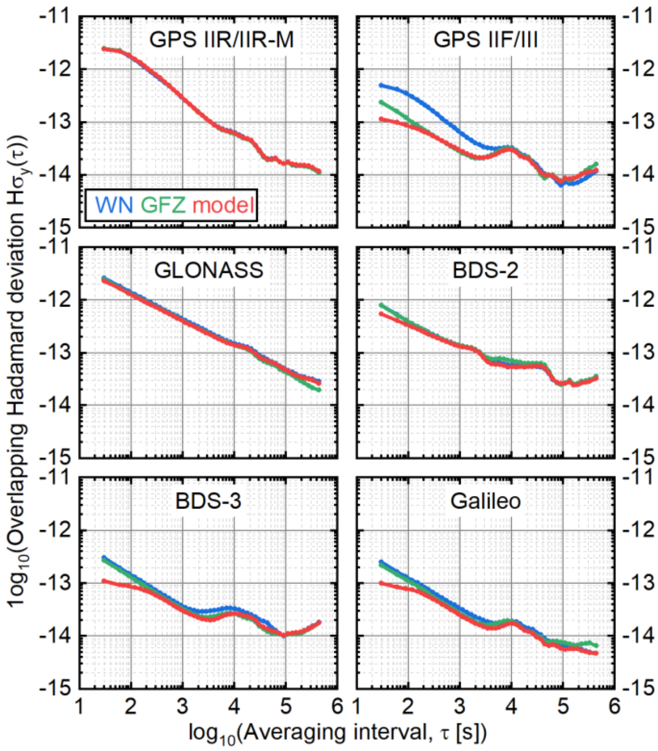

Figure 5. Overlapping HDEV of the estimated clock products with the WN (white noise) and model (clock model). Average values for different sets of clocks were calculated baed on products from GPS week 2177–2183. Also, the results of GFZ final multi-GNSS products (green) for the same period were shown as references

GLONASS IFB products for the real-time clock estimation

A new GLONASS pseudo ranges IFB correction strategy has been implemented in the real-time GLONASS satellite clock generation. In this strategy, the IFBs on each frequency of the GLONASS satellite-receiver pair were corrected in advance with the weekly averaged value of IFBs in advance. The IFB on each individual frequency of different satellite-receiver pairs was estimated based on the undifferenced and uncombined PPP. Figure 2 presented the IFB on each individual frequency of IGS for March 2017 with the PPP ionospheric delay modeling solution. As we can see, the PPP solution turned out to have an STD of about 1.0 ns and 1.17 ns (Zhang et al., 2021).

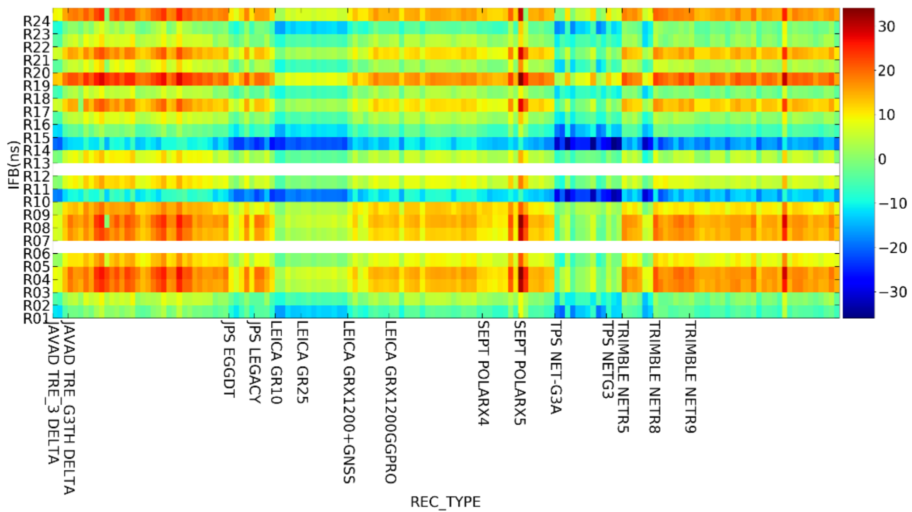
IFB(ns)
R24
R23
R22
R21
R20
R19
R18
R17
R16
R15
R14
R13
R12
R11
R10
R09
R08
R07
R06
R05
R04
R03
R02
R01
30
20
10
0
−10
−20
−30
JAVAD TRE_3 DELTA
JAVAD TRE_G3TH DELTA
JPS EGGDT
JPS LEGACY
LEICA GR10
LEICA GR25
LEICA GRX1200+GNSS
LEICA GRX1200GGPRO
SEPT POLARX4
SEPT POLARX5
TPS NET-G3A
TPS NETG3
TRIMBLE NETR5
TRIMBLE NETR8
TRIMBLE NETR9
REC_TYPE

(a1)

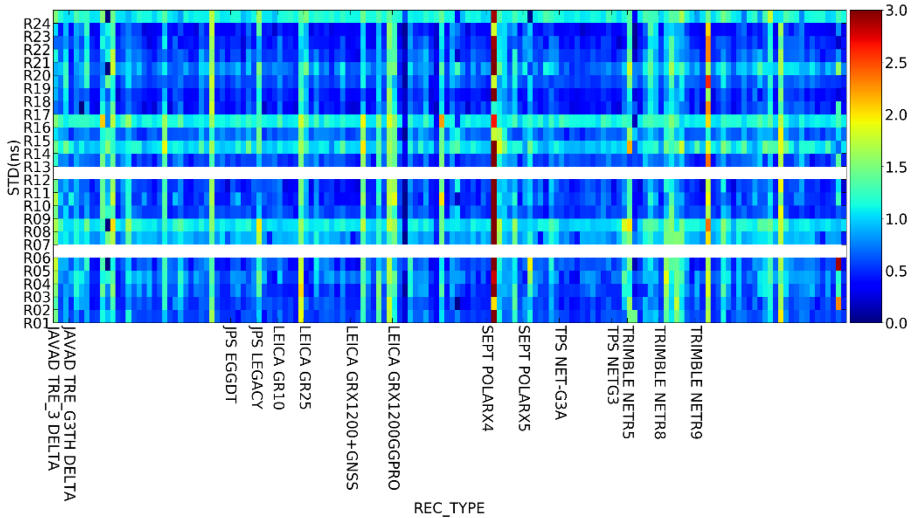
STD(ns)
R24
R23
R22
R21
R20
R19
R18
R17
R16
R15
R14
R13
R12
R11
R10
R09
R08
R07
R06
R05
R04
R03
R02
R01
3.0
2.5
2.0
1.5
1.0
0.5
0.0
JAVAD TRE_3 DELTA
JAVAD TRE_G3TH DELTA
JPS EGGDT
JPS LEGACY
LEICA GR10
LEICA GR25
LEICA GRX1200+GNSS
LEICA GRX1200GGPRO
SEPT POLARX4
SEPT POLARX5
TPS NET-G3A
TPS NETG3
TRIMBLE NETR5
TRIMBLE NETR8
TRIMBLE NETR9
REC_TYPE

(b1)

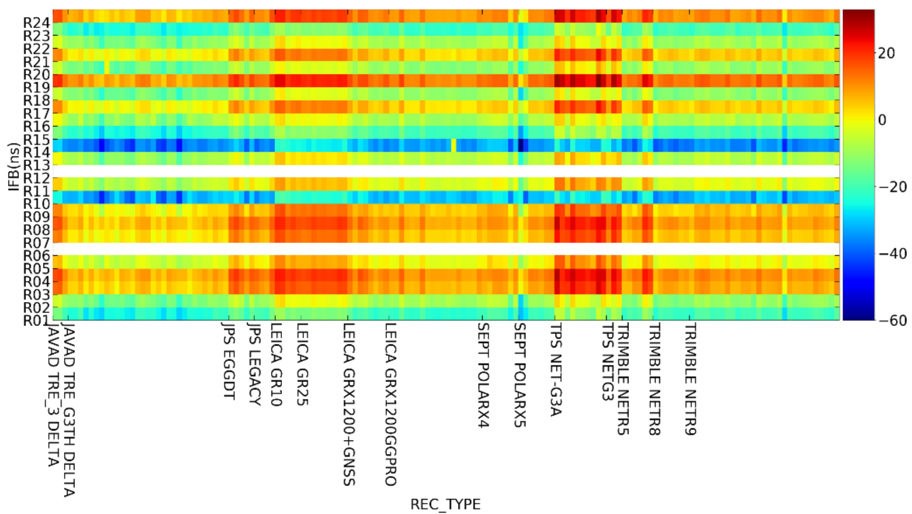
IFB(ns)
R24
R23
R22
R21
R20
R19
R18
R17
R16
R15
R14
R13
R12
R11
R10
R09
R08
R07
R06
R05
R04
R03
R02
R01
20
0
−20
−40
−60
JAVAD TRE_3 DELTA
JAVAD TRE_G3TH DELTA
JPS EGGDT
JPS LEGACY
LEICA GR10
LEICA GR25
LEICA GRX1200+GNSS
LEICA GRX1200GGPRO
SEPT POLARX4
SEPT POLARX5
TPS NET-G3A
TPS NETG3
TRIMBLE NETR5
TRIMBLE NETR8
TRIMBLE NETR9
REC_TYPE

(a2)

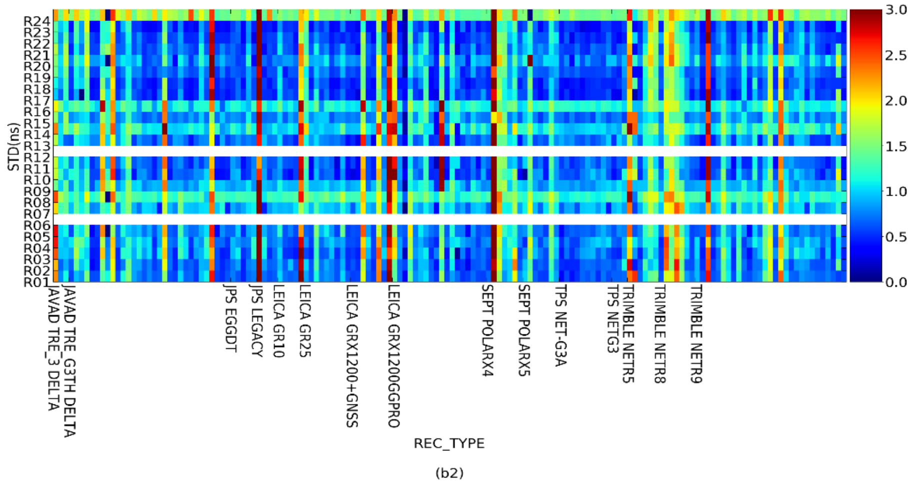

Figure 6. The mean value (a) and the STD (b) for GLONASS IFB (1: IFB_1; 2: IFB_2) of each receiver-satellite pair for IGS stations in March 2017 based on the undifferenced and uncombined PPP solution. The X-axis is grouped according to the receiver type. The color bar represents the STD value in ns, and the averaged STD is about 1.107 ns

4 Phase bias products

Precise point positioning with ambiguity resolution (PPP-AR) is a valuable tool for high-precision geodetic observations, which can achieve centimeter to millimeter positioning accuracy by utilizing precise satellite orbit, clock and phase bias products. Since phase bias products are critical to implementing GNSS PPP-AR, analysis centers (ACs) in International GNSS service (IGS) have begun to release the daily computed dual-frequency multi-GNSS rapid phase bias products to enable PPP-AR by GNSS users. Wuhan University is one of them and begins to release the phase bias products since 2020 which can be freely downloaded at (ftp://igs.gnsswhu.cn/pub/whu/ phasebias). The estimation strategy for phase bias products provided by Wuhan University refers to Geng et al. (2019a), where wide-lane and narrow-lane biases are computed by the Melbourne-Wübbena combination observables and ionosphere-free combination observables, respectively. Furthermore, satellite clock corrections are re-computed by fixing and holding integer ambiguities and narrow-lane phase biases with the goal of improving the accuracy of estimated satellite clocks. In this case, the satellite clock corrections will be aligned with high-precision carrier-phase measurements, instead of noisy pseudorange measurements, as accomplished in the integer clock model and the clocks are so called phase clocks. In order to make the phase biases easy to use, the wide-lane and narrow-lane phase biases are then transformed to observable-specific biases (OSBs) according to Bias SINEX (Solution Independent Exchange) format 1.0 released by IGS (Schaer et al., 2016). Following the rules in Bias SINEX format, all varieties of pseudorange and carrier-phase observables on different tracking channels are assigned with specific corrections and users can simply subtract them from raw measurements to realize GNSS PPP-AR. The OSB framework has good interoperability such that the phase biases from different AR methods can be accommodated. Besides, the rapid satellite orbit products and attitude products in ORBEX (Orbit Exchange Format) format are also computed and provided along with phase clock and phase bias products to users. The whole procedure of determining these products is described by Figure 7 (Geng et al., 2022a). In Figure 1, the blue boxes denote the final released precise satellite products.

To reconcile with the released WUM (Wuhan University MGEX) rapid phase bias products, the open-source software “PRIDE PPP-AR” which aiming at multi-GNSS PPP-AR for relevant research, application and development with GPS post-processing is also provided to users (Geng et al., 2019b). Throughout the third-party evaluation, “PRIDE PPP-AR” and the released phase bias products show a very good performance in positioning accuracy compared with other open-source software (see Vázquez-Ontiveros et al., 2023). And the single-system dual-frequency PPP-AR solutions based on WUM rapid products are depicted in Figure 7.

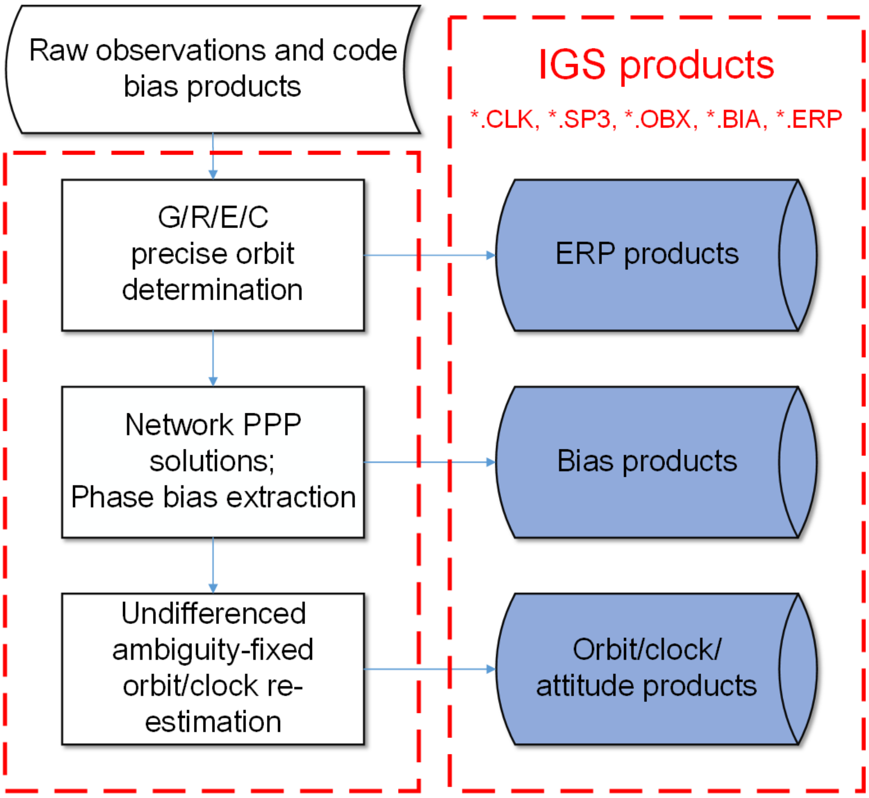

Figure 7. Flowchart of WUM rapid phase clock/bias and orbit products generation procedure. Blue boxes depict the estimated products. G, R, E, C represent GPS, GLONASS, Galileo, BDS respectively

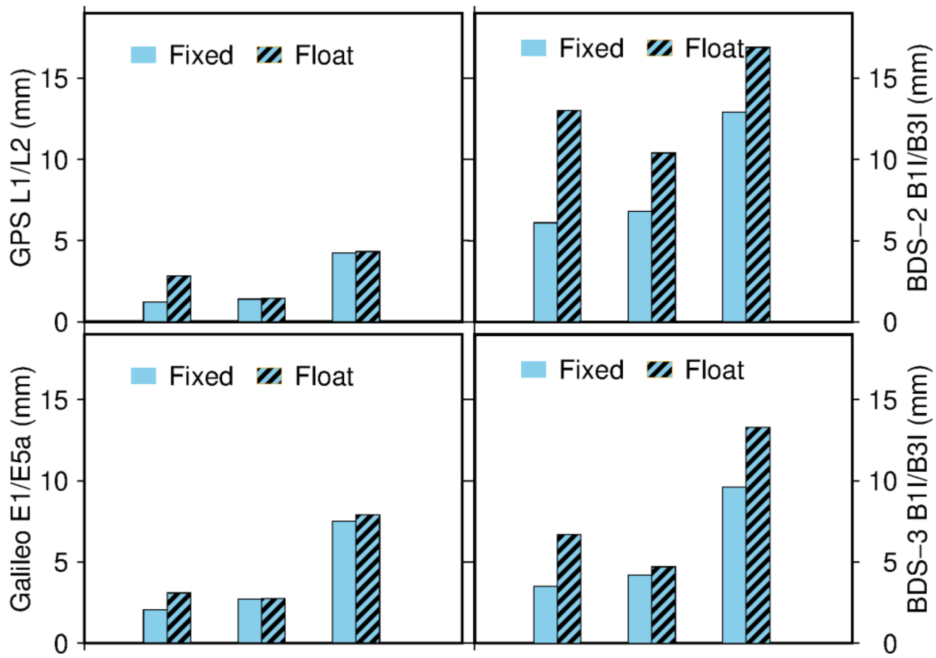

Figure 8. RMSE at E, N, and U directions of float and fixed solutions for single-system dual-frequency PPP-AR using WUM rapid phase bias products

Except for the daily rapid phase bias products, the combined satellite clock and phase bias products accomplished in IGS third reprocessing project from year 1995 to 2020 are also provided in the same FTP as above. Since 2019, the Analysis Centers (ACs) of IGS began to reprocess and reanalyze the full history of GPS, GLONASS and Galileo data collected by the IGS global network since 1994 in a fully consistent way using the latest models and methodology. Several ACs also provide phase bias products to enable PPP-AR for GPS and Galileo systems so that phase bias products combination is a new challenging task for IGS to handle. Wuhan University took on the work for satellite clock and phase bias combination to obtain more reliable and precise combined products and the job was well finished before June, 2022. Satellite clock and phase bias products from CODE、TUG、GRG、EMR、JPL、ESA、GFZ、MIT and WHU nine ACs were processed and combined. The final combined products for GPS and Galileo systems contain phase clocks and phase biases, respectively, while for GLONASS only legacy clocks were combined due to the lack of corresponding phase biases from ACs. The positioning accuracy based on combined products and individual AC products is described in Figure 9 and it can be concluded that combined products can provide more reliable and precise positions.

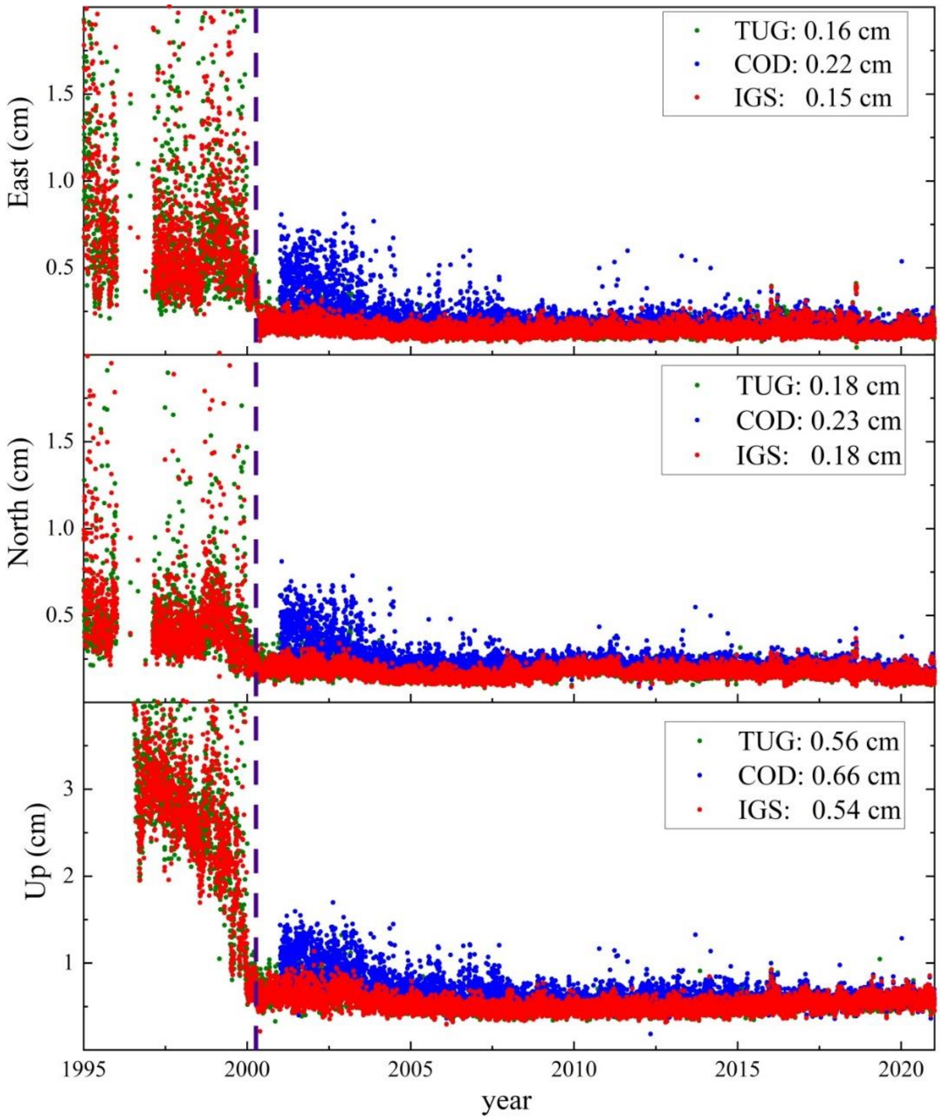

Figure 9. Positioning accuracy comparison between combined phase clock/bias products and individual AC products. The vertical dashed line in each subfigure denotes the date that GPS abandoned the "Selective Availability" policy.

Moreover, with the development of multi-frequency GNSS signals, a new concept that calling "all-frequency PPP-AR" is proposed and developed (Geng et al., 2022b). Meanwhile, the corresponding all-frequency phase bias products are nearly to be released by Wuhan University in this year. By utilizing all-frequency phase bias products, users can implement PPP-AR flexibly based on any GNSS frequency choices and observable combinations without restrictions.

5 GNSS Antenna Calibration

Wuhan University (WHU) has initiated studies about antenna calibration at 2013 (Hu et al., 2015) aiming at providing PCC models for high precision BDS/GNSS applications. At present, absolute field antenna calibration with industrial robot is available for multi-gnss signals including GPS/BDS/GAL/GLO/QZS, and corresponding PCC models has been submitted to research community like IGS/iGMAS and antenna manufacturers.

Method Detail

Methodologies of field absolute antenna calibration with high-precision industrial robot arm are adopted at WHU. Differentiations between station, epoch and satellite are sequentially performed to eliminate the large system errors, and information of PCC to be calibrated remains due to accurate and swift attitude motions with the robot, and correlations of the TD (triple differenced) observation is obtained through full covariance propagation. Here, PCC is represented through spherical harmonic (SH) expansion to degree 8 and order 8. Multi-GNSS signals of GPS(L1/L2/L5), BDS(B1I/B3I/B1C/B2a/B2b/B2), GLO(R1/R2), GAL (E1/E5a/E5b/E5/E6) and QZS(J1/J2/J5) are sampled at rate of 2 Hz. The elevation cut-off angle for data processing is lowered to -5 degree to improve the PCC estimation at low elevation angle. Typical data span for one calibration is 24 hours, while 4-6 hours is enough in fact. Considering the coupling of PCO and PCV, the procedure of calibration is divided into two steps: first, PCO are estimated with PCV ignored; second, PCV are estimated from the residuals with PCO derived in the first step re-introduced into the differential observation.

To advance the antenna calibration, novel attempts, such as stand-alone calibration, PCC fitting with Zernike polynomials, adaptive fitting order determination, are under validation, and details will be released in later work.

Calibration system

Antenna calibration system at WHU has been built and enhanced since 2013. Currently, a six-axis industrial robot arm is installed, and the robot motion are designed to make observation cover the antenna hemisphere as fully and evenly as possible. Besides, high precision geodetic receivers are equipped to track multi-gnss signals. A software for PCC Estimation of Multi-GNSS signals has been developed by CSharp (C#), which can be deployed in cross-platform. All the antenna calibration algorithm and function are implemented using object-oriented programming with high extensibility. High-performance matrix library is introduced to accelerate parameter estimation, which enables an iterated parallel PCC estimation for Multi-GNSS with multi methods.

Figure 10. Field antenna calibration system at Wuhan University. The system is built on a rooftop and includes a six-axis robot, a controller, an atomic clock, receivers and other auxiliary equipment.

Consistency accuracy verification with IGS

Based on the antenna calibration system at WHU, antennas of more than 10 types have been calibrated. According to our evaluation method (Zhou et al., 2022), the repeatability over different calibration sessions can reach 0.5 mm level, and accuracy can reach 1 mm level compared with PCC models released by IGS.

Specifically, average consistency (STD) between our calibration and IGS patterns for 12 geodetic is 0.68 mm. For short-baseline positioning, average accuracy of different signals can reach 1.7 mm using our PCC patterns. Calibration for low-cost and consumer antennas, such as vehicle antenna, have been performed, and baseline positioning accuracy can reach 5 mm after their PCC pattern applied.

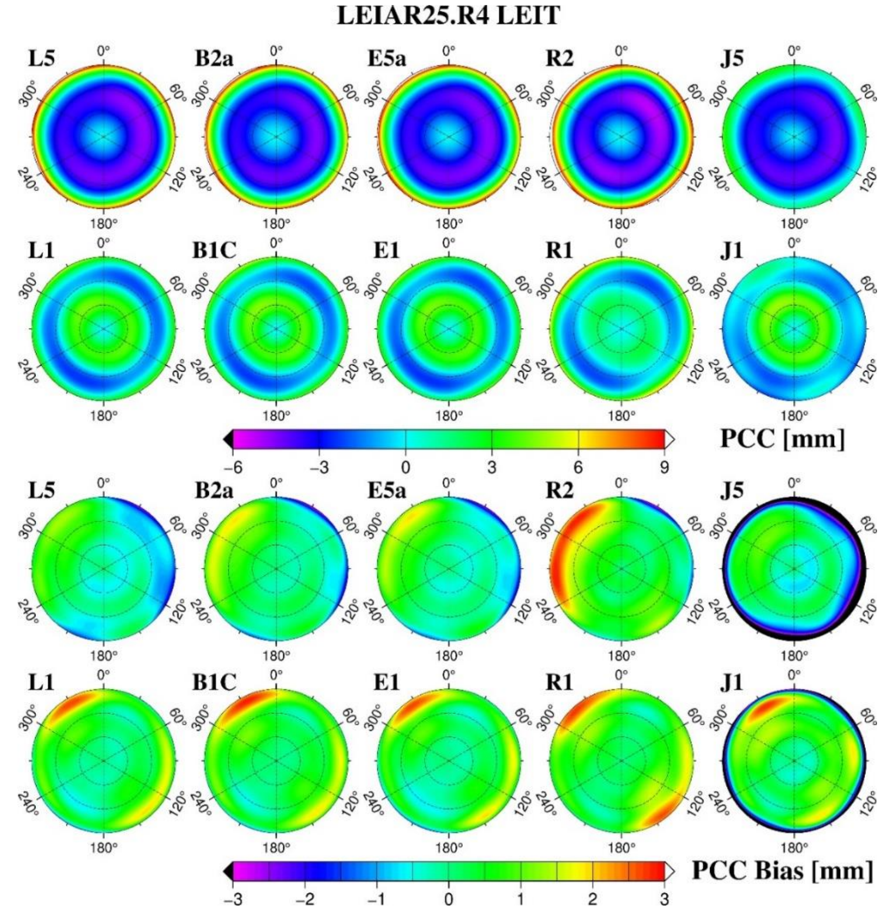

Figure 11. Calibration accuracy for different signals of LEIAR25.R4 LEIT, compared with igs14.atx. The differences are calculated in a grid format.

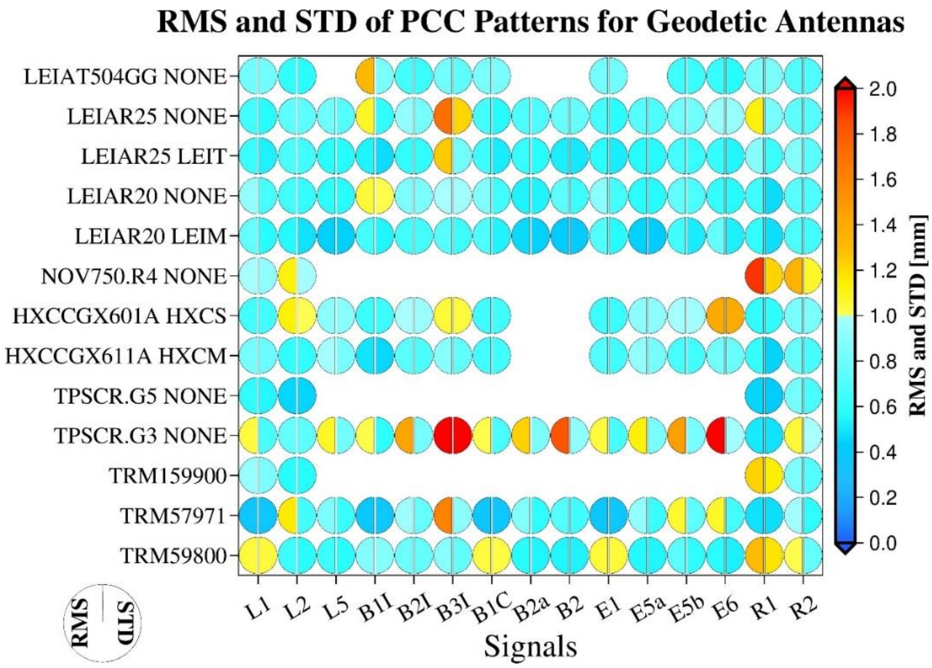

Figure 12． RMS Statistics of Antenna Phase Calibration for Different Antennas and Frequency Bands

International Cooperation between Wuhan University and IGS Antenna Group for Joint Calibration of GNSS Antennas

In November 2021, at the invitation of Dr. Arturo Villiger, Chairman of the IGS Antenna Working Group (AWG), Wuhan University was fortunate enough to participate in the AWG ring calibration project. For such a dedicated campaign, 6 GNSS receiver antennas have be selected for calibration and each contributing calibration facility would calibrate those antennas (see Table 2). The antenna would be sent around from participant to participant until each calibration facility had the chance to calibrate the antennas.

The current calibration work at Wuhan University is progressing very smoothly and is about to complete the antenna calibration task sent from NGS in the United States.

Table 2. International Antenna Calibration and Comparison Plan

Region	Method	Institution	TPSCR.G5C	TPSG5.A1	JAVRINGANT_DM	TRM57971.00	LEICA25.R3	HXCCGX601A
Australia	robot	GSA - Geoscience Autralia	9	9	1	1	9	9
China	robot	GNSS Research Center of Wuhan University (WHU-GNSSRC)	8	8	3	3	8	1
Europe	chamber	DLR German Aerospace Centre Institute of Communications and Navigation	5	5	9	9	4	5
		Uni Bonn	4	4	8	8	3	6
	robot	Geo++ GmbH	3	3	6	6	2	8
		TOPCON AGRICULTURE S.R.L.	1	1	4	4	5	4
		ETH Zurich	6	6	5	5	6	3
		LUH-IfE	2	2	7	7	1	7
USA	robot	NGS/NOAA	7	7	2	2	7	2

Legend

1:= last stop in rotation

antenna(s) not arrived/calibrated

antenna(s) under testing/calibration

waiting position for receiving antenna(s) as next

finished testings/calibration

In addition, antennas from International GNSS Monitoring & Assessment System (iGMAS) (Hu.2022) and antenna manufacturer have been calibrated in WHU. At present, service of antenna calibration is open to public and related communities.

6 Non-linear Motion for GNSS Reference Stations

GNSS reference stations exhibit significant non-linear motions, among which the strong annual signal observed at most sites is now known to be true physical site motion driven by environmental mass redistribution. However, the quantitative effect of environmental loading on GNSS height time series can be quite different from investigation to investigation. The variability depends on the environmental mass data used to determine the load at the sites, the loading model, and the GNSS coordinate time series used in the comparison. We used three different environmental loading methods to estimate surface displacements and correct nonlinear variations in a set of GPS weekly height time series. Loading data were provided by (1) Global Geophysical Fluid Center (GGFC), (2) Loading Model of Quasi-Observation Combination Analysis software (QLM) and (3) our own daily loading time series (we call it OMD for optimum model data), among which OMD has the smallest scatter in height across the selected 233 globally distributed GPS reference stations, GGFC has the next smallest variability, and QLM has the largest scatter. By removing the load-induced height changes from the GPS height time series, we are able to reduce the scatter on 74, 64 and 41 % of the stations using the OMD models, the GGFC model and QLM model respectively (Fig. 1). We demonstrate that the discrepancy between the center of earth (CE) and the center of figure (CF) reference frames can be ignored. The most important differences between the predicted models are caused by (1) differences in the hydrology data, (2) grid interpolation, and (3) whether the topographic effect is removed or not. Both QLM and GGFC are extremely convenient tools for non-specialists to use to calculate loading effects. GGFC dataset is much more suitable than QLM for applying environmental loading corrections to GPS height time series. However, loading results from QLM could be used as a complement to the GGFC product to model the load in Greenland. We find that the predicted loading from all three models cannot reduce the scatter of the height coordinate for some stations in Europe (Jiang et al., 2013).

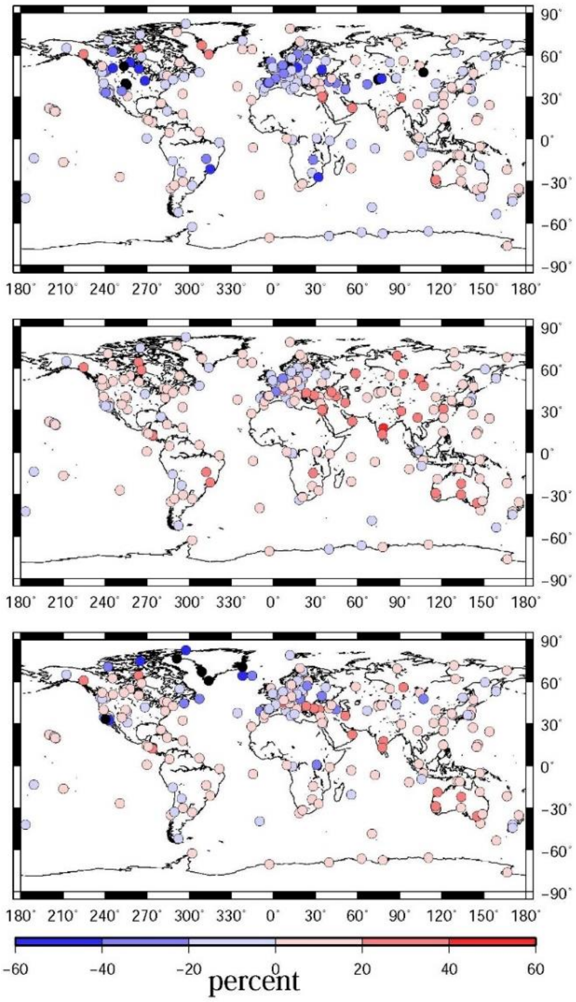

Figure 13. Spatial distribution of WRMS differences in percentage using the three loading corrections. Black circles indicate that a station's WRMS change exceeded the limits of the scale range. Unit of WRMS difference is %. Top panel shows the QLM model; the middle panel shows the OMD model; the bottom panel shows the GGFC model.

Besides, thermal expansion is also considered to be one of the potential geophysical contributors to the non-GNSS height time series. The displacements introduced by thermal expansion were usually derived without considering the annex height and underground part of the monument (e.g. located on roof or top of the buildings), which may bias the geophysical explanation of the seasonal oscillation. We derived the improved vertical displacements by a refined thermal expansion model, where the annex height and underground depth of the monument were taken into account (Fig. 2), and then 560 IGS stations were adopted to validate the modeled thermal expansion (MTE) displacements. The MTE displacements of 80 IGS stations with less data discontinuities were then selected to compare with their observed GPS vertical (OGV) displacements with the modeled surface loading (MSL) displacements removed in advance. We find that the maximum annual and semiannual amplitudes of the MTE are 6.65 mm (NOVJ) and 0.51 mm (IISC), respectively, and the maximum peak-to-peak oscillation of the MTE displacements can be 19.4 mm. The average annual amplitude reductions are 0.75 mm and 1.05 mm respectively after removing the MTE and MSL displacements from the OGV, indicating the seasonal oscillation induced by thermal expansion is equivalent to 75% of the impact of surface loadings. However, there are rarely significant reductions for the semiannual amplitude. Given the result in this study that thermal expansion can explain 17.3% of the annual amplitude in GPS heights on average, it must be precisely modeled both in GPS precise data processing and GPS time series analysis, especially for those stations located in the middle and high latitudes with larger annual temperature oscillation, or stations with higher monument (Wang et al., 2018).

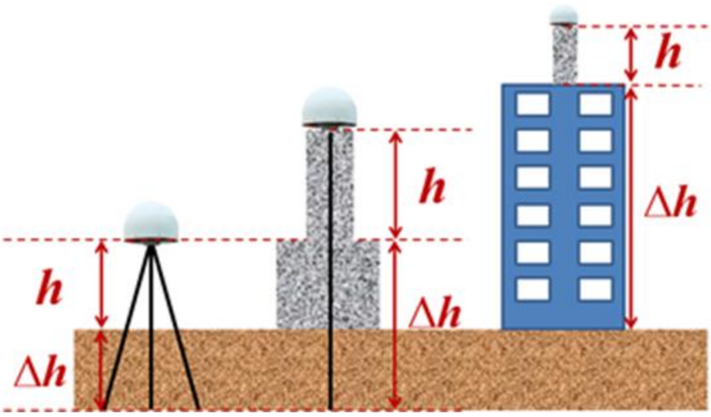

$$\boldsymbol{TEM(t) = (\alpha_1 \cdot h + \alpha_2 \cdot \Delta h) \cdot [T(t) - T']}$$

Figure 14. Refined monument thermal expansion model

With respect to terrestrial reference frame (TRF), each GNSS adopts its own TRF to produce broadcast ephemerides. However, inconsistencies in these ground-based TRFs can be ignored in multi-GNSS combined positioning, since the newest versions of WGS84, GTRF, and BDCS are aligned to the International TRF (ITRF) at an accuracy of 1 cm (https://www.unoosa.org/oosa/en/ ourwork/ icg/resources/Regl-ref.html). Nevertheless, only seven BDCS stations in China are constrained in the alignment of BDS-3 broadcast orbits to BDCS. Hence, it is necessary to validate whether the insufficient geodetic constraints induce systematic errors into BDS-3 broadcast orbits. We find that the BDS-3 broadcast orbits coincide with ITRF2014 at an accuracy of 10 cm, although the broadcast orbits are constrained to BDCS only on the positions of regional stations in China. Obvious systematic errors in z-translation and rotation parameters are found in BDS-3 broadcast orbits, resulting in positioning errors of up to 10 and 25 cm, respectively. By contrast, random errors dominate Galileo and GPS orbits, with an uncertainty of approximately 5 cm. The annual instability of z-translation for BDS-3 shows manufacturer- and orbit-plane-dependent characteristics, which are probably triggered by imperfect orbit models. We then propose a posterior model to calibrate the periodic errors in z-origin. The three translations over 2020 were fitted with the function $y=a\cdot\cos(2\pi\cdot dt)+b\cdot\sin(2\pi\cdot dt)$, where dt is the fractional year (i.e. dt=DOY/365.25). The coefficients of the fitting function are a=7.09 and b=-2.77 cm for the z-component (Fig. 3). Limited by the weekly update of earth orientation parameters prediction, the orientation stability of BDS-3 broadcast orbits degrade within one week, which may be amplified as no global geodetic constraints are applied. If these rotation errors are removed, the root mean square error of BDS-3 broadcast orbits can be reduced by 30%-50% in the along and cross direction.

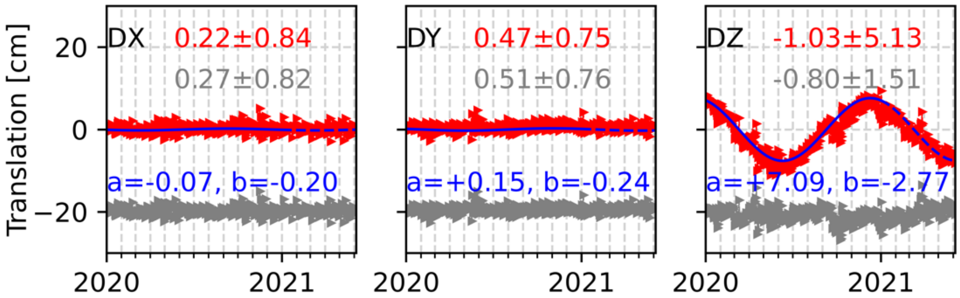

Figure 15. Translations between broadcast and precise orbits (red triangle), and their residuals (gray triangle, offset by -20 cm) with fitted/predicted annual harmonics (blue lines) removed from January 2020 to May 2021. The corresponding statistics of mean and SDs are shown in the same colors. Text in blue are the coefficients for the fitting function.

7 WHU Data Center

Wuhan University has joined as an IGS Global Data Center since 2015. The IGS Data Center from WHU has been established with the aim of providing services to global and especially Chinese users, for both post–processing and real-time applications. The GNSS observations of both IGS and MGEX from all the IGS network stations, as well as the IGS products are archived and accessible at WHU Data Center (WHU DC).

Access of WHU Data Center

In order to ensure a more reliable data flow and a better availability of the service, two identical configurations with the same data structure have been setup in Alibaba cloud and Data Server of Wuhan University. Each configuration has:

- FTP access to the GNSS observations and products (ftp://igs.gnsswhu.cn/).
- HTTP access to the GNSS observations and products (http://www.igs.gnsswhu.cn/).

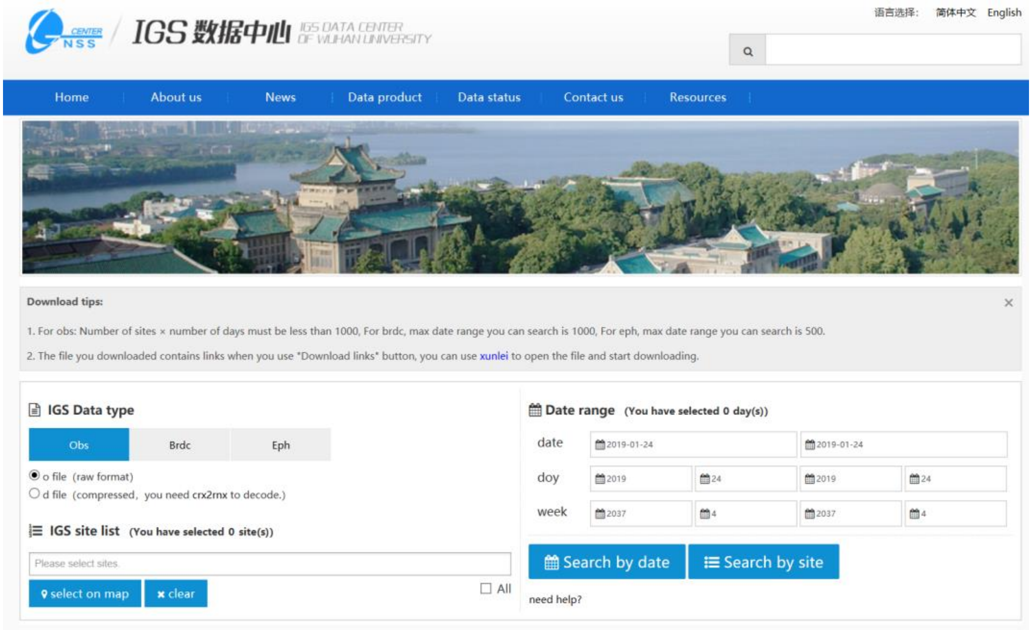

Figure 16. A snapshot of the website of WHU data center for data and products provision.

GNSS Data & Products of WHU Data Center

The WHU Data Center contains all the regular GNSS data and products, such as navigational data, meteorological data, observational data, and products, ready to accept GNSS data in the RINEX 4.00 format and Long Name Products.

- Navigational data: daily and hourly data (ftp://igs.gnsswhu.cn/pub/gps/data)
- Observational data: daily and hourly data (ftp://igs.gnsswhu.cn/pub/gps/data)
- Products: orbits, clocks, Earth Rotation Parameters (ERP), and station positions, ionosphere, troposphere (ftp://igs.gnsswhu.cn/pub/gps/products)

In addition to the IGS operational products, WHU data center has released ultra-rapid products updated every 1 hour and every 3 hours (ftp://igs.gnsswhu.cn/pub/whu/ MGEX/) from the beginning of June 2017. The ultra-rapid products include GPS/GLONASS/BDS/Galileo satellite orbits, satellite clocks, and ERP for a sliding 48-hr period, and the beginning/ending epochs are continuously shifted by 1 hour or 3 hours with each update. The faster updates and shorter latency should enable significant improvement of orbit predictions and error reduction for user applications.

WHU data center started to provide multi-GNSS rapid phase bias products in the bias-SINEX format along with self-consistent orbit, phase clock, code biases and attitude quaternion products since September 2021, and the products are traced back to the beginning of 2020 (ftp://igs.gnsswhu.cn/pub/whu/phasebias/). Five GNSS are included in our products: GPS, GLONASS, Galileo, BDS and QZSS.

The WHU RT GIMs also are accessible via Wuhan Real Time Data Center (http://ntrip.gnsslab.cn) with Mountpoint IONO00WHU0 and Wuhan Data Center (ftp://igs.gnsswhu.cn/pub/whu/MGEX/ realtime-ionex) in IONEX format.

Monitoring of WHU Data Center

WHU Data Center provides data monitoring function to display log information such as online user status, the arrival status of data and products, and the status of user downloading in real time. It can display real-time data downloading and data analysis related products graphically, with real-time information on online user status and product accuracy.

In order to ensure the integrity of the observation data and the products, we routinely compare the daily data, hourly data and products with those in CDDIS. If one data file is missing, we will redownload it from CDDISs. Figure 2 shows the status of daily observation.

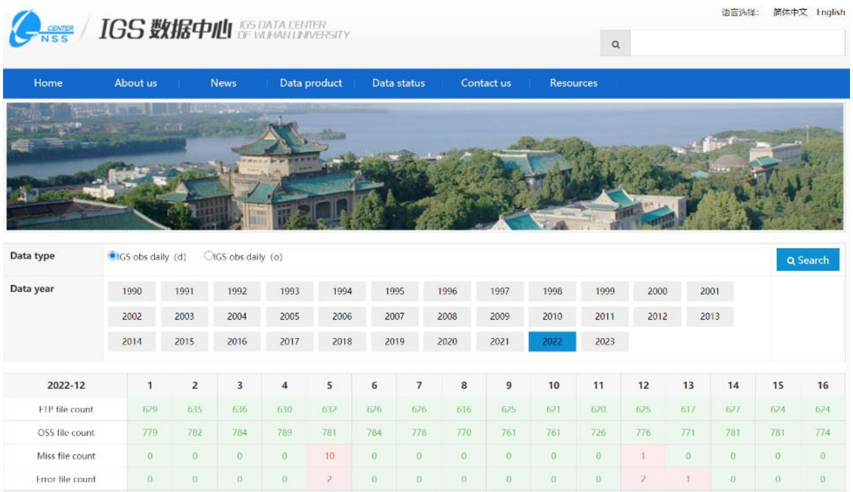

Figure 17. Data and products monitoring of WHU data center

Bibliography

Geng J, Shi C (2016) Rapid initialization of real-time PPP by resolving undifferenced GPS and GLONASS ambiguities simultaneously. Journal of Geodesy 91(4):1-14

Guo F, Zhang X, Wang J et al (2016) Modeling and assessment of triple-frequency BDS precise point positioning. J Geod 90(11):1223–1235

CAO (2019) Cabinet Office; The history information of QZS-1 operation.URL https://qzss.go.jp/en/technical/qzssinfo/khp0mf0000000wuf-att/ohi-qzs1_1_1.pdf

CSNO (2019) BeiDou satellite information file. URL:http://www.beidou.gov.cn/yw/gfgg/201912/W020191230559858089737.rar

Dilsner F, Springer T, Enderle W (2011a) GPS IIF yaw attitude control during eclipse season. AGU Fall Meeting, San Francisco 2011a:G54A-04. http://acc.igs.org/orbits/yaw-IIF_ESOC_agu11.pdf

GSA (2016) European GNSS Service Center; Galileo Satellite Metadata. URL https://www.gsc-europa.eu/support-to-developers/galileo-satellite-metadata

Chen K, Xu T, Chen G, Li J, Yu S (2015) The Orbit and Clock Combination of iGMAS Analysis Centers and the Analysis of Their Precision. In Proceedings of the China Satellite Navigation Conference (CSNC), Xian, China, 13–15 May 2015; Volume II, pp. 421–438.

Guo J, Xu X, Zhao Q, Liu J (2016) Precise orbit determination for quad-constellation satellites at Wuhan University: strategy, result validation, and comparison. J Geod 90:143–159. https://doi.org/10.1007/s00190-015-0862-9

Guo J, Zhao Q, Xu X, Tao J, Zhang Q, Qu Z, Chen G, Wang C (2018) Real-time orbit and clock products at Wuhan University to support Multi-GNSS applications. IGS Workshop 2018, 29 October to 2 November, Wuhan, China

Guo J, Wang C, Chen G, Xu X, Zhao Q (2023) BDS-3 precise orbit and clock solution at Wuhan University: status and improvement. J Geod 97:15. https://doi.org/10.1007/s00190-023-01705-5

Kouba J (2009) A simplified yaw-attitude model for eclipsing GPS satellites. GPS Solut 13(1):1–12. https://doi.org/10.1007/s10291-008-0092-1

Montenbruck O, Steigenberger P, Hugentobler U (2015). Enhanced solar radiation pressure modeling for Galileo satellites. Journal of Geodesy, 89(3), 283–297. https://doi.org/10.1007/s00190-014-0774-0.

Montenbruck O, Schmid R, Mercier F, Steigenberger P, Noll C, Fatkulin R, Kogure S, Ganeshan AS (2015) GNSS satellite geometry and attitude models. Adv Space Res 56(6):1015–1029. https://doi.org/10.1016/j.asr.2015.06.019

Montenbruck O, Steigenberger P, Darugna F (2017) Semi-analytical solar radiation pressure modeling for QZS-1 orbit-normal and yaw-steering attitude. Advances in Space Research, 59(8), 2088–2100. https://doi.org/10.1016/j.asr.2017.01.036.

Steigenberger P, Thoelert S, Montenbruck O (2018) GNSS satellite transmit power and its impact on orbit determination. Journal of Geodesy, 92, 609–624. DOI: https://doi.org/10.1007/s00190-017-1082-2

Steigenberger P, Deng Z, Guo J, Prange L, Song S, Montenbruck O (2022) BeiDou-3 orbit and clock quality of the IGS Multi-GNSS Pilot project. Advances in Space Research, 71(1), 355-368. https://doi.org/10.1016/j.asr.2022.08.058

Tan C, Chen G, Wei N, Cai H, Zhao Q (2016) Combined Satellite Orbits of the iGMAS Analysis Centers: Method and Precision. Geomat. Inf. Sci. Wuhan Univ., 41, 1439–1475.

Wang C, Guo J, Zhao Q, Liu J (2018). Yaw attitude modeling for BeiDou I06 and BeiDou-3 satellites. GPS Solutions, 22, 117. https://doi.org/10.1007/s10291-018-0783-1.

Wang C, Guo J, Zhao Q, Liu J (2019) Empirically derived model of solar radiation pressure for BeiDou GEO satellites. J Geod 93(8):1-17. https://doi.org/10.1007/s00190-018-1199-y

Wang C, Guo J, Zhao Q, Ge M (2022) Improving the orbits of BDS-2 IGSO and MEO satellites with compensating thermal radiation pressure parameters. Remote Sensing, 14(3), 641. https://doi.org/10.3390/rs14030641

Rodríguez-Solano, C. (2009). Impact of albedo modeling on GPS orbits. Master Thesis. Technische Universität München.

Yang C, Guo J, Zhao Q (2021). Yaw attitudes for BDS-3 IGSO and MEO satellites: Estimation, validation and modeling with inter-satellite link observations. Journal of Geodesy, 97, 6. https://doi.org/10.1007/s00190-022-01698-7

Zhao Q, Chen G, Guo J, Liu J, Liu X (2018) An a prior solar radiation pressure model for the QZSS Michibiki satellite. Journal of Geodesy 92, 109-121. https://doi.org/10.1007/s00190-017-1048-4

Yang X, Gu S, Gong X, Song W, Lou Y, Liu J. Regional BDS satellite clock estimation with triple-frequency ambiguity resolution based on undifferenced observation. GPS Solutions, 2019,23:33

Shi C, Guo S, Gu S, Yang X, Gong X, Deng Z, Ge M and Schuh H. Multi-GNSS satellite clock estimation constrained with oscillator noise model in the existence of data discontinuity. Journal of Geodesy, 2019, 93:515-528

Peng Y, Lou Y, Gong X, Wang Y, Dai X. Real-time clock prediction of multi-GNSS satellites and its application in precise point positioning. Advances in Space Research, 2019, 64:1445-1454

Fu, W. et al. Multi-GNSS real-time clock estimation using sequential least square adjustment with online quality control. Journal of Geodesy, 2019, 93, 963–976.

Zhang, Z., Lou, Y., Zheng, F. Gu, S. ON GLONASS pseudo-range inter-frequency bias solution with ionospheric delay modeling and the undifferenced uncombined PPP. Journal of Geodesy, 2021, 95, 32.

Zhang, H., Xu, P., Han, W., Ge, M., Shi, C. Eliminating negative VTEC in global ionosphere maps using inequality-constrained least squares. *Adv Space Res*, 51 (6), 988-1000, 2013.

Zhang, Q., Zhao, Q. Global ionosphere mapping and differential code bias estimation during low and high solar activity periods with GIMAS software. *Remote Sensing*, 10 (5), 705, 2018.

Zhang, Q., Zhao, Q. Analysis of the data processing strategies of spherical harmonic expansion model on global ionosphere mapping for moderate solar activity. *Adv Space Res*, 63 (3), 1214-1226, 2019.

Jiang WP*, Li Z, van Dam T, Ding WW (2013). Comparative analysis of different environmental loading methods and their impacts on the GPS height time series. Journal of Geodesy, 87(7), 687-703

Wang KH, Chen H, Jiang WP*; Li Z, Ma J; Deng LS. (2018). Improved vertical displacements induced by a refined thermal expansion model and its quantitative analysis in GPS height time series. Journal of Geophysics & Engineering, 15(2), 554-567

Chen, G., Wei, N. *, Li, M., Zhao, Q., Niu, Y., Cai, H., & Meng, Y. (2022). Assessment of BDS-3 terrestrial reference frame realized by broadcast ephemeris: comparison with GPS/Galileo. GPS Solutions, 26, 1-16.

Hu Z, Zhao Q, Chen G, Wang G, Dai Z, Li T (2015) First Results of Field Absolute Calibration of the GPS Receiver Antenna at Wuhan University Sensors 15:28717

Zhou R et al. (2022) Consistency Analysis of the GNSS Antenna Phase Center Correction Models Remote Sensing 14:540

Hu Z et al. Preliminary Results of iGMAS BDS/GNSS Absolute Antenna Phase Center Field Calibration. In, Singapore, 2022. China Satellite Navigation Conference (CSNC 2022) Proceedings. Springer Nature Singapore, pp 147-160

Research progress in Earth Gravity

Heping Sun[1,2], Lifeng Bao[1,2], Shi Chen[3], Xiaoming Cui[1], JianqiaoXu[1], Jiangcun Zhou[1], Minzhang Hu[4], Ziwei Liu[4], Yiqing Zhu[5], Xiaodong Chen[1], Qianqian Li[1], Lin Wu[1], Linhai Wang[3,6], Lulu Jia[3,6], Jiancheng Han[3,6], Miaomiao Zhang[1], Hang Li[1], Xiange Lei[1], Qianqian He[7], Mingli Deng[1], Hongyan Lu[3,6], Weimin Xu[3,6], Jinling Yang[8], Qiuyue Zheng[9], Zhaohui Chen[10], Longwei Xiang[11], Wen Shi[3,6], Honglei Li[3,6], Bei Zhang[3,6], Yongbo Li[3,6]， Jiancang Zhuang[12]

[1] *Innovation Academy for Precision Measurement Science and Technology, Chinese Academy of Sciences*

[2] *University of Chinese Academy of Sciences*

[3] *Institute of Geophysics， China Earthquake Administration*

[4] *Institute of Seismology， China Earthquake Administration*

[5] *Second Monitoring Center， China Earthquake Administration*

[6] *Beijing Baijiatuan Earth Sciences National Observation and Research Station*

[7] *East China University of Technology*

[8] *Fujian Earthquake Agency*

[9] *Yunnan Earthquake Agency*

[10] *The First Monitoring and Application Center, China Earthquake Administration*

[11] *School of Geosciences, Yangtze University*

[12] *The Institute of Statistical Mathematics, Research Organization of Information and Systems, Tokyo, Japan*

Gravity field is the most basic physical field generated by the material properties of the earth system. It reflects the spatial distribution, movement and change of materials determined by the interaction and dynamic process inside the Earth. Measuring gravity field is one of the three methods currently used to explore the internal structure of the Earth, including seismology and geomagnetism, and the gravity field provides a ’mirror’ reflecting the internal structure of the Earth. Over the years, a variety of technical means have been used to detect the Earth's gravity field, including gravimeter, superconducting gravimeter, sea and air gravimeter, satellite gravity, satellite altimetry and so on, and have obtained a large number of gravity data, supporting numerous studies on the global change, resource detection, geological structure movement, water resources change and other related fields of research. Here is part of the progress in Earth gravity obtained by Chinese geodesy scientists from 2019 to 2023 from the following aspects, including

(1) Continuous Gravity Network in Chinese Mainland

(2) Application of Superconducting gravity measurement

(3) Network adjustment for continental-scale gravity survey campaign and data quality control

(4) Regional time-variable gravity field and its application

(5) Research Progress on Novel Technologies for Gravity Inversion

(6) Research Progress on marine gravity field determination

(7) Application research on marine gravity field

1 Continuous Gravity Network in Chinese Mainland

Relative gravity measurement is an important technical means to study and explore global and regional geodynamic problems and the deep internal structure of the Earth. After decades of construction, China has built a comprehensive monitoring network of multi-source observation technology covering vast territory through major scientific projects according to the “Crustal Movement Observation Network of China” (CMONOC), the “China Digital Seismological Observation”, and the “China Seismic Background Field Detection Project”. The network comprehensively monitors crustal movement and the gravity field, atmosphere, ocean, and near-Earth space in the Chinese mainland and its adjacent area. to assist in earthquake prediction, national surveying and mapping, geoscience research, geodetic application and disaster weather prediction.

At present, China has established a continuous gravity network consisting of more than 80 stations that run various gravimeters including GWR superconducting gravimeter (SG), PET/gPhone, DZW, GS15 and TRG-1 types. The station distribution of more than 60 gPhone gravimeters and 7 SGs is listed in Figure 1 (Sun et al., 2022). As the gravity observation technology with the highest precision at present, China has invested huge efforts in the construction of SG network. Since 1985, when China's first SG was installed in the Institute of Geodesy and Geophysics in Wuhan, China has successively established seven SG stations until now. In 1997, Wuhan SG Station participated in the Global Geodynamics Program (GGP) implemented by Deep Earth Interior Committee of the International Union of Geodesy and Geophysics (IUGG) and the International Earth Tide Center (ICET) and the Asia-Pacific Space Geodynamics Program (APSG). Since then, Wuhan SG Station has been incorporated into the CMONOC and upgraded, and Lhasa and Lijiang SG stations have been successively established. At present, three SGs in Chinese Mainland including Wuhan, Lhasa, and Lijiang have participated in the International Geodynamics and Earth Tide Service (IGETS) implemented by the International Association of Geodesy (IAG) in 2016, and contributed to global geodynamics research joint with more than 40 SG stations around the world. In addition, the China SG Network also includes the instruments deployed in Wuhan, Lijiang and Beijing respectively by the China Earthquake Administration, Wuhan University and National Institute of Metrology. A series of subsequent SG stations are also under construction, which will provide more support for the research of time-varying gravity fields in the Chinese Mainland and global geodynamics in the future.

Since its establishment, continuous gravity network in in Chinese mainland has maintained a continuous and stable operation for a long time. It has accumulated a wealth of observation data and has played a very important role in exploring geodynamics and the internal structure of the Earth.

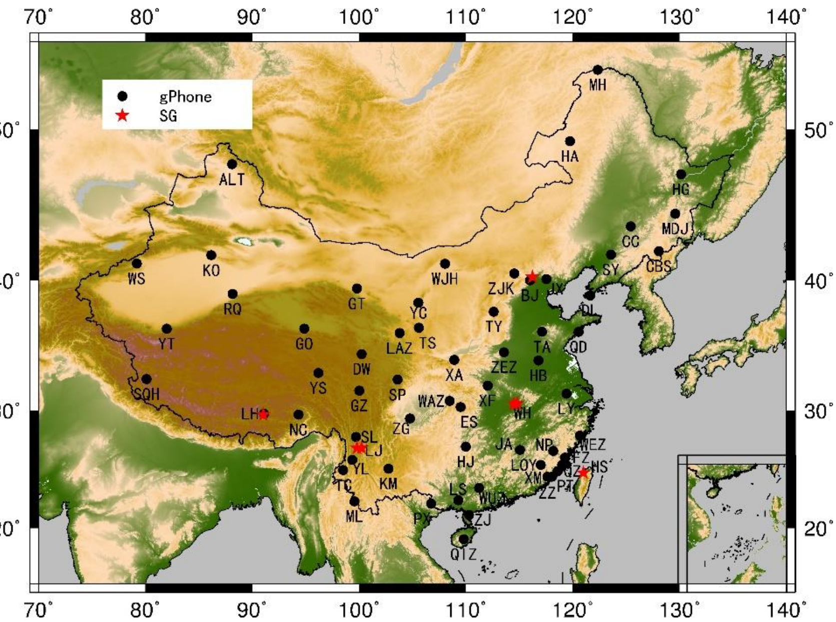

Figure 1. The distribution of 60 gPhone gravimeters and 7 Superconducting gravimeters (SGs: Wuhan (2), Lijiang (2), Lhasa (1), Beijing (1) and Hsinchu (1)) over China's mainland. gPhone stations are represented by the black solid circles while SG stations are represented by the red solid stars (Sun et al.， 2022).

2 Application of Superconducting gravity measurement

Application on Earth background noise

Based on the SG and gPhone gravity observations of the Crustal Movement Observation Network of China (CMONOC), the Innovation Academy for Precision Measurement Science and Technology (APM), Chinese Academy of Sciences, has carried out the application research of gravity technique in the study of Earth background noise. Earth background noise is some random waveform generated by non-seismic excitation sources recorded on the seismogram during seismically quiet periods. High-precision gravity technology is an effective method to detect weak signals from the Earth, so it has important application value in the study of Earth background noise.

The weak signal detection performance of gravimeter is closely related to the instrument noise level, which is determined by the observation performance of the instrument itself and the observation environment around the station. APM systematically evaluated noise levels of three IGETS SGs (OSG-065, OSG-057 and OSG-066) in Wuhan, Lhasa and Lijiang and 30 gPhone gravimeters covering mainland China belonging to the CMONOC, and the results are shown in Figure 2. Noise levels in the seismic and sub-seismic frequency bands were analyzed according to the power spectral density of the quietest period during seismically quiet periods (Figure 2). Compared with noise levels of other stations in the global SG network IGETS, the three SG stations in China all showed low noise and good observation quality in the seismic and sub-seismic frequency bands (Sun et al., 2019a; Li et al., 2020). Noise levels of 30 gPhone stations in mainland China were evaluated, and the results show that seismic noise magnitude (SNM) for most stations is in the range of 2~3, and attributed to complicated oceanic effects and active tectonic movement, noisier stations are mainly distributed along the coast and in the southeast of the Tibetan Plateau. This study also presents the Chinese low noise model (CLNM), which represents the best working conditions of gPhone in mainland China.

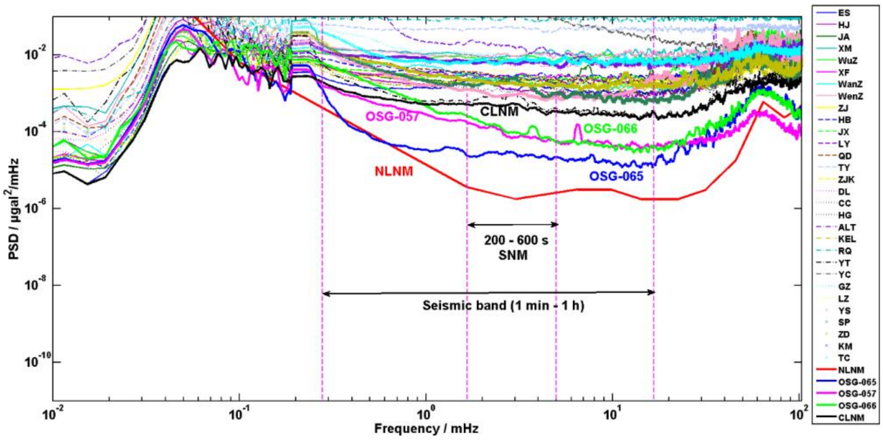

Figure 2. Power spectral densities of the quietest period for the 30 gPhone stations in the CMONOC network and three SG stations in the IGETS network. The black line (CLNM: Chinese Low Noise Model) is the lower envelope of the 30 gPhone stations, obtained similarly to the low noise model NLNM (red line) given by Peterson (1993). Figure 2 is quoted from Sun et al. (2022).

On this basis, we used SG stations of the global SG network IGETS to carry out the study of the Earth Hum signal, which is a very important type of the Earth background noise, including the long-period surface wave and background free oscillation signals that persist in the Earth even during seismically quiet periods. Using Lhasa, Canberra (Australia) and Syowa (Antarctica) stations, we extracted the background free oscillations from averaged power spectra between 0.3 and 5 mHz during seismically quiet periods. The spectral peaks of the background free oscillations are most clear at Canberra station, then at Lhasa station and finally at Syowa station which is very close to the coast and thus heavily affected by the ocean with high noise level. The excitation mechanism of background free oscillations has been controversial, with some early studies supporting the hypothesis of atmospheric excitation, but most later studies favoring the coupling between ocean infragravity waves and seafloor topography. Further analysis by the APM research team through four stations with low noise levels in Canberra (Australia), Bad Homburg (Germany), Kamioka (Japan) and Wuhan (China) showed that the excitation mechanism of background free oscillations below 5 mHz are associated with atmospheric and oceanic perturbations. In contrast to previous studies, the study found that the oceanic disturbance could play different roles in different periods (Sun et al., 2019a).

In the past two decades, the technique of surface wave signal extraction by seismic noise cross-correlation has been widely used in the study of crust and upper mantle structure. Broadband seismometer has the limitation of extracting long-period surface wave signals, so there are few studies on the deep interior structure of the Earth using this technique. In contrast, SG has high sensitivity, stability and observation accuracy, and can effectively record most kinds of seismic wave signals, which has incomparable advantages in the study of long-period seismology. The APM research team has selected the long-term observation data from stations of Canberra (CB), Black Forest (BF) and Sutherland (SU) from IGETS network. The three stations are also equipped with STS-1 seismometers. Long-period surface waves (2-7.5mHz, i.e. 133.3-500s) are successfully extracted by the noise auto-correlation method. The reliability of the results from SGs are verified by comparing with seismometers. It can be seen that both the SG and the STS-1 seismometer can clearly record the surface waves propagating around the Earth for one circle (R1+R2) and two circles (R3+R4). The results of this study can be extended to the two-station noise cross-correlation, which provides a new idea for the study of the deep structure and dynamics of the Earth by combining gravitational and seismic techniques (Li et al., 2020).

Application on Earth Tide and Geodynamics

The long-term observations of the continuous gravity network provide an important basis for studying the response characteristics of Earth tide and geodynamic phenomena in Chinese mainland. This report mainly introduces our research on the regional characteristics of the tidal response in the Qinghai-Tibet Plateau and the time-varying characteristics of the liquid core resonance in the diurnal tides based on the SG observations from IGETS network.

The tidal response in the Qinghai-Tibet Plateau

The SG stations in Wuhan and Lijiang are almost at the same latitude as Lhasa, thus their Earth tide observation are almost equally affected by rotation and ellipticity. This provides excellent conditions for studying the impact of special tectonic environment on regional tidal deformation in the Qinghai-Tibet Plateau and its adjacent areas. According to long term observation, APM has established high-precision regional gravity tide datum in the three stations, and carried out detailed research on the oceanic tide and atmospheric loading effect in the station area (Sun et al., 2019; Liang et al., 2020). The scale factors of three SGs were all evaluated with a strategy of co-site comparison between the SGs and the FG-5 absolute gravimeter. We carried out a comparison analysis using two-year continuous gravity measurements recorded by the three stations (Figure 3). The tidal parameters show that no significant differences existed in the amplitude factors measured in Lhasa and Lijiang, but a remarkable difference was found when compared with the factors measured in Wuhan. The mean gravimetric amplitude factors of waves O1, K1, and M2 were about 0.27, 0.34, and 0.42% larger, respectively, than those measured in Wuhan (Sun et al., 2019b). The tidal gravity anomaly was about 0.34%, which we regarded as a local phenomenon unique to the Tibetan Plateau. In the Qinghai Tibet Plateau, the biggest regional disturbance comes from changes in the Plateau glaciers. However, glacier melting itself and its accompanying "crustal rebound" is a long-term process, which has little impact on the Earth's tidal deformation. The relatively large difference between the gravity tide observations and the theoretical model at Lhasa and Lijiang stations possibly comes from the interference of regional tectonic anomalies and active tectonic movement (Sun et al., 2019b; Sun et al., 2022).

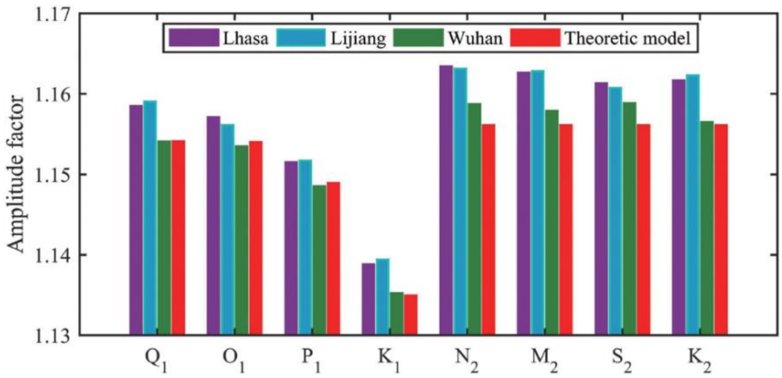

Figure 3. Comparison of the amplitude factors of diurnal and semidiurnal tidal waves observed in Lhasa, Lijiang, and Wuhan SG stations and the theoretical values from Mathews's (2001) model (Sun et al., 2019b).

The liquid core resonance in the diurnal Earth tides

The deep internal structure and internal dynamics of the Earth has always been the frontier hotspot in the field of geoscience research. The nearly diurnal free wobble (NDFW) of liquid core, also called free core nutation (FCN) in celestial frame, is a dynamic process originating from the core-mantle boundary. It involves a variety of geophysical information of the core-mantle couplings. The NDFW will lead to an obvious resonance enhancement in observations of diurnal tidal waves with near frequencies. The accurate separation of the tidal waves is an important means to detect this signal in the deep interior of the Earth. Previous research on NDFW parameters was limited to the low signal-to-noise ratio of ψ1 tidal wave which is most affected by the liquid core resonance. To explore whether NDFW has time-varying characteristics, we studied the reliability of liquid core resonance observed in different diurnal tidal waves under the current observation accuracy of SG. It is found that although K1 tidal wave is less affected by resonance compared with ψ1 tidal wave, it has higher observation signal-to-noise ratio due to its larger amplitude, which is more conducive to detecting the variation of liquid core resonance effect. We determined the accuracy limit of K1 tidal wave that can effectively detect the resonance change. On this basis, we analyzed the long-term observations from 20 SG stations of IGETS network and found a consistent temporal variation characteristics of liquid core resonance in the K1 wave tidal parameters from multiple stations that meet the accuracy limit. This variation was verified further by the results of VLBI observations. It is also found that the mechanism of this resonance change is closely related to the sudden change of geomagnetic field caused by the hydrodynamic phenomena of liquid core (Cui et al., 2020; Sun et al., 2022).

Application on regional gravity measurement

APM is committed to the application of gravity observation technology in regional geophysical research. This report mainly introduces the application of superconductive gravity technique in the quantitative separation of the local vadose zone water storage changes, the application of hybrid gravimetry in the surface subsidence of Wuhan city and the observation experiment of deep underground (-848m) gravity field.

Quantitative separation of the local vadose zone water storage changes

The vadose zone is the porous medium between the ground surface and the groundwater level in the first unconfined aquifer. Quantitative study of vadose zone water storage changes

(WSCVZ) is still a difficult problem. We proposed a new method for the quantitative separation of the local WSCVZ based on a single superconducting gravimeter (SG). This new method was verified through examples using the superconducting gravity observation data from Wuhan SG Station (May 2008 to April 2010) and groundwater level observation data. The quantitative separation results of the WSCVZ at Wuhan SG Station were compared with those obtained using the local hydrological modeling method and using the global GLDAS/Noah model. The results show good consistency, which indicates that the quantitative separation of the local WSCVZ can be achieved using the superconductive gravity technique and ground water level observations.

Application of hybrid gravimetry in the surface subsidence

Urban surface subsidence caused by groundwater exploitation, urban construction and other reasons is a potential hazard to public safety. We carried out experimental study of the surface subsidence in the city using the hybrid gravity measurement. We set up a gravity observation network in the area with relatively large surface subsidence observed by InSAR in Wuhan (Figure 4, left). Seven campaign mobile gravity and GPS measurements were carried out between 2016 and 2017. The absolute gravity observation is used to control the long-term gravity change of the whole observation area, and the GLDAS land water model data is used to calculate and eliminate the overall land water gravity impact of the observation area. The seventh campaign result of gravity change relative to the first is shown in Figure 4 (right). Compared with the vertical surface deformation observed by D-InSAR, the results show that the gravity observation technology can obtain high-precision regional gravity changes in the city, and the mobile gravity can clearly observe the urban surface subsidence. Compared with InSAR observation technology, the gravity changes caused by different factors such as surface subsidence, water volume of the Yangtze River and groundwater are analyzed in detail. Some regional gravity changes have good correlation with the seasonal changes of the Yangtze River water. The research results show that the combination of multi-source observation technology is an effective way to explain the mechanism of urban surface subsidence (Chen et al., 2020).

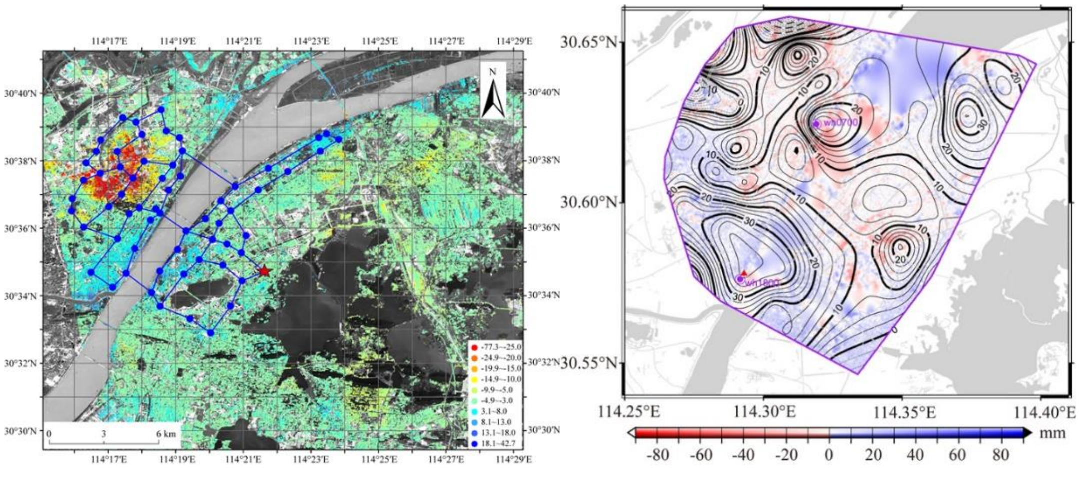

Figure 4. Left: Surface subsidence observed by InSAR and the mobile gravity observing network，Blue dots are gravity points. Red ★ point is the absolute gravity control point. Right: Comparison of the gravity change from the 1st campaign to the 7th covered on the vertical displacement observed by D-InSAR (Chen et al., 2020)

Gravity Observation experiment in Huainan 848 m deep underground

The deep underground environment is characterized by low background noise, low cosmic ray intensity, and low background radiation, and is an excellent platform for carrying out many major frontiers scientific experiment. The international deep underground laboratory has developed rapidly in recent years. APM and several research institutions in China have jointly carried out some preliminary observation experiments by relying on the space resources of underground coal mine tunnels in Huainan to build a deep multi-physical field observation and experiment platform. The experimental site, located at the junction of the southern source of the North China Craton and the lower Yangtze, is in Panyi Mine of Huainan Mining Group, about 15 km away from the urban area of Huainan (Figure 5_left). The deep space consists of an underground horizontal layer with an altitude of - 848 m and several vertical shafts as shown in Figure 5 (right). This experiment was conducted in the horizontal layer of - 848 m. The LaCoste-Lomberg ET and Burris spring gravimeter were respectively deployed on the surface and in the tunnel of horizontal layer on January 18, 2020. Comparison of the original gravity recordings between the surface and the −848 m tunnel showed that the continuous gravity observations are reliable, and the time-variant trends are consistent. The gravity noise underground and at the surface are analyzed with the power spectrum estimated from the quietest periods. The noise deep underground at the frequency band of 2–10 Hz is stronger than that at the surface, while the low-frequency band reverses and is more than 2 orders of magnitude lower than that at the surface. It fully demonstrates the low noise of underground environment at the deep geophysical experimental field in Huainan (Zhang et al., 2021; Wang et al., 2023).

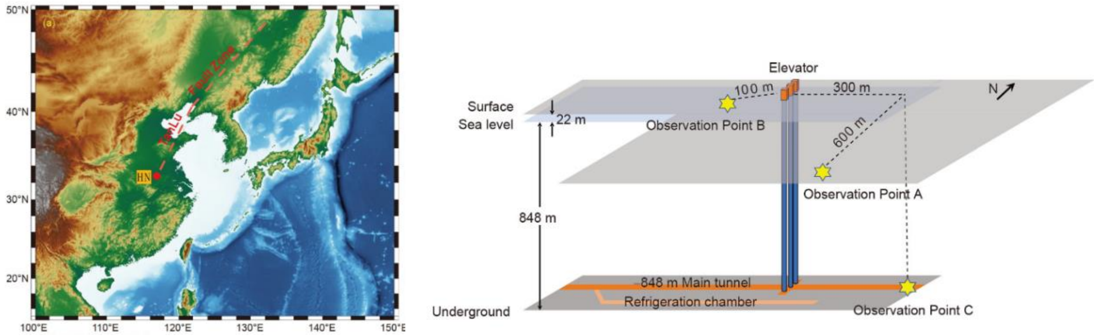

Figure 5. Huainan Deep Underground Lab. Left: the location of the lab; Right: layout of the observation system in the lab (Wang et al., 2023)

3 Network adjustment for continental-scale gravity survey campaign and data quality control

Spatiotemporal gravity signals from terrestrial hybrid repeated gravity observation have contributed to the understanding of the surface and subsurface mass redistribution, which reflects the crustal deformation and density changes. However, the disturbances of instrument performance and observation field source noise cause large uncertainty in the time-varying gravity signal. To quantify these uncertainties, based on the Bayesian principle and the Akaike's Bayesian information criterion (ABIC), Professor Chen's team has developed several advanced algorithms and models for the network adjustment, data quality control and multi-period gravity data assimilation. These methods can effectively determine the uncertainty in gravity observation data and obtain high-precision time-varying gravity signals.

To solve the problem of nonlinear drift of gravimeters in regional gravity measurements, Chen et al. (2019) proposed a new terrestrial scale gravity network adjustment method by means of objective Bayesian statistical inference. This method assumes that the variation of the drift rate is smooth function of lapsed time. We employed the ABIC to estimate these hyper-parameters. The drift rate change characteristics of each gravimeter can be obtained while estimating the gravity value, as shown in Figure 6. Compared with the linear drift model (Figure 6(b)), the residuals obtained by the Bayesian method using the nonlinear drift model exhibit the random characteristics of white noise (Figure 6(c)). On this basis, Wang et al. (2022) improved the Bayesian gravity adjustment method, using absolute and relative gravity observation data to estimate the scale factor of the relative gravimeter. As shown in Figure 6(d), compared with using the input scale factor, there is no correlation between the gravity difference and the mutual difference obtained by using the estimated scale factor. The improved method can effectively reduce the residual and is conducive to improving the accuracy of the gravity value. Further, a data quality assessment process of residual analysis, correlation analysis, and cross-validation of absolute gravity measurement has been formed (Zheng et al., 2022).

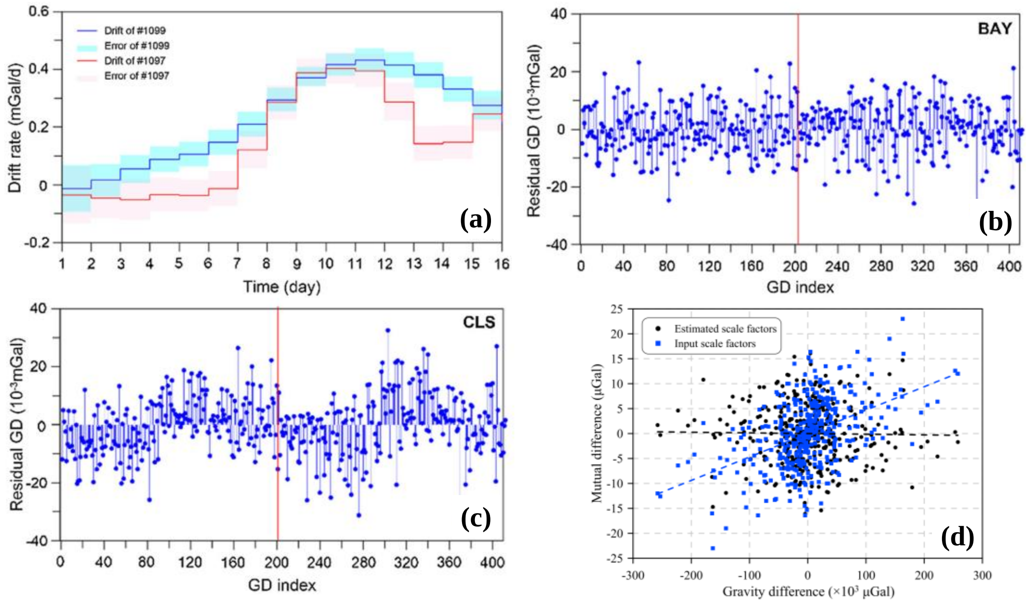

Figure 6. (a) The drift rate and uncertainty of two relative gravimeters estimated by Bayesian gravity adjustment. (b) and (c) the residuals obtained by Bayesian method and Classical adjustment respectively. (d) Comparison of the mutual difference between the estimated scale factors and the input scale factors.

The high-frequency features of the spatiotemporal gravity signals are related to near-surface field sources. Therefore, the low-frequency gravity changes potentially related to the deep source processes need to be extracted. Yang et al. (2021) and Chen et al. (2022) adopted a Bayesian apparent density source inversion (BADI) method with spatiotemporal smoothness constraints to effectively suppress the high-frequency fluctuations in the spatiotemporal gravity signals. The BADI method employs an equivalent apparent density model to build up a relationship between the deep field source body and the surface observed gravity changes. Then, the model-assimilated gravity changes can be derived from this apparent density model. We apply the method to the gravity observation data from 2014 to 2017 before the 2017 Jiuzhaigou

MS7.0 earthquake. As shown in Figure 7(a, c, e), there are the high-frequency components in the gravity changes without assimilation. The model-assimilated values gravity values (b, d, f) have a consistent and stable changing trend.

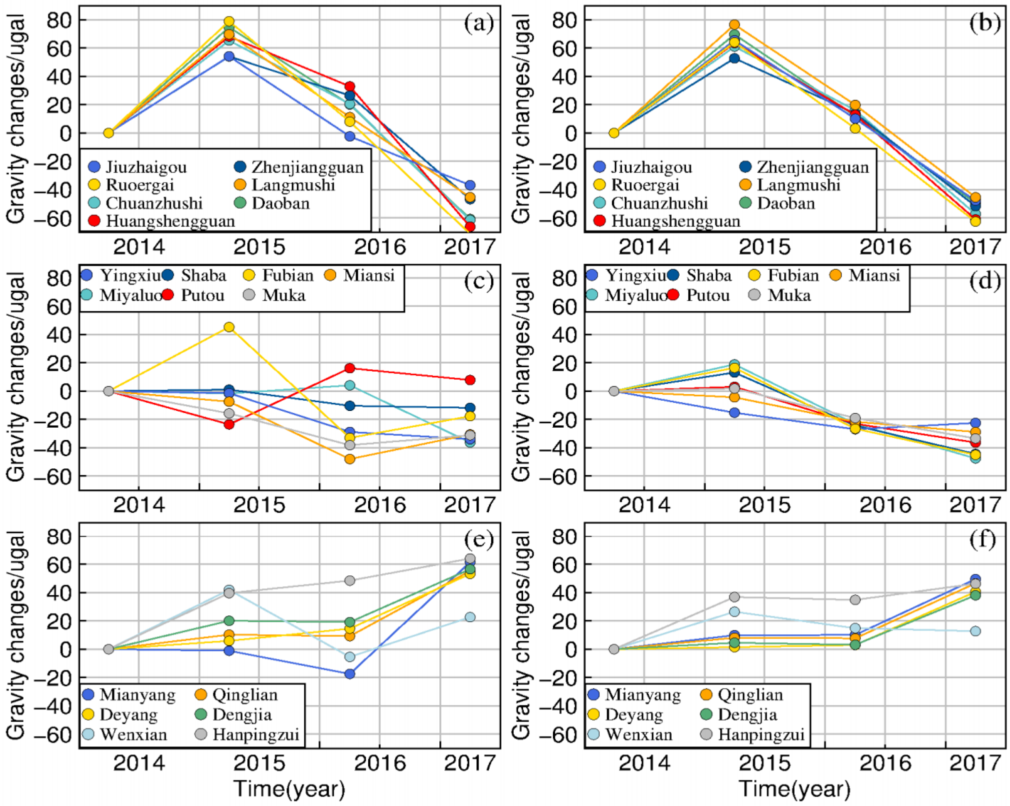

Figure 7. The time series of gravity value before and after processing by the Bayesian apparent density inversion method

4 Regional time-variable gravity field and its application

Measuring the small variations in the Earth's gravity field over time is an effective means to investigate issues related to mass changes, such as land subsidence, groundwater storage changes, and earthquake-induced mass migration. Terrestrial (ground-based) time-variable gravity measurement allows the detection and analysis of the regional and near-surface mass movement and migration because of its high accuracy and sensitivity to the sources of mass change in the Earth's crust. Since 2000, the quality of terrestrial time-variable gravity measurements has been greatly improved because of the rapid development of the geophysical infrastructure in the Chinese mainland, represented by the "Crustal Movement Observation Network of China" project. These high-quality gravity measurements provide valuable information for time-variable gravity field modeling in China.

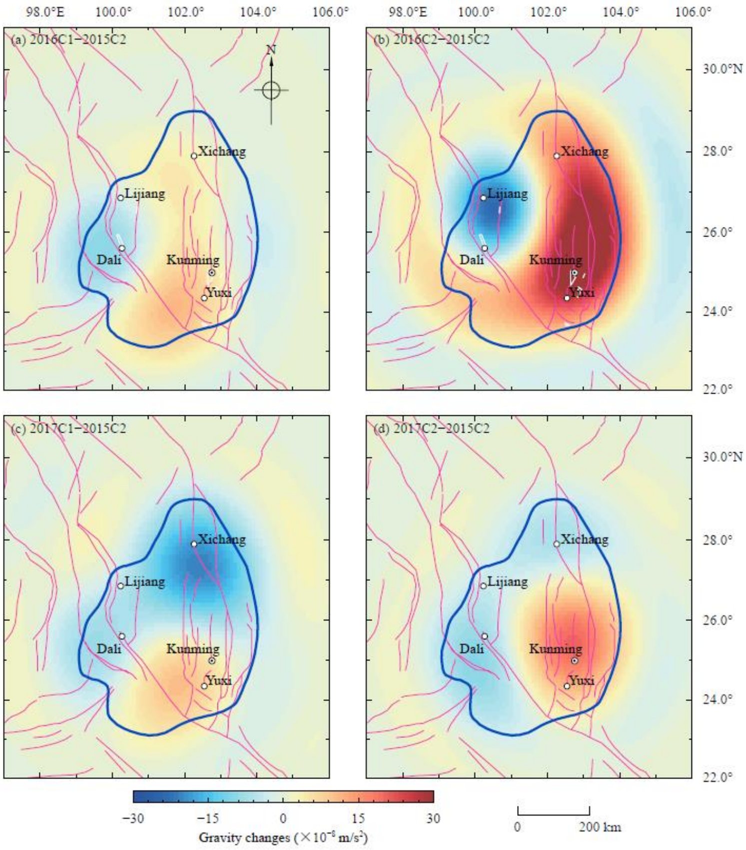

Figure 8. The spatial distribution of the degree 120 gravity field variations in the Sichuan-Yunnan region between 2016 and 2017 (with respect to 2015C2) determined using Slepian functions. The blue line indicates the boundary of the study area, and the magenta line indicates active faults.

Based on Slepian basis functions and terrestrial gravity measurements in the Sichuan-Yunnan region from 2015 to 2017, Han et al. (2021a) determined high-resolution (degree 120) time-variable gravity field (TVGF) solutions over this region (Figure 8). Figure 8a and Figure 8b show the gravity variations for 2016C1–2015C2 and 2016C2–2015C2 (C1 and C2 represent observations in the first half and second half of the year, respectively), while Figure 8c and Figure 8d show the cumulative gravity variations for 2017C1–2015C2 and 2017C2–2015C2, respectively. The spatial pattern in Figure 8b is correlated with the near-south tectonic structures along the Xichang-Yuxi line and the northwest-oriented Red River fault. This correlation indicates that the model results are tectonically sensitive. The gravity variations in Figure 8c shows that the increase around Xichang falls back, but the gravity increases around Kunming and Yuxi still exist. The results in Figure 8d show that the gravity increase around Xichang disappear while the gravity increases around Kunming and Yuxi continue to a larger extent. The degree 120 gravity solution in the Sichuan-Yunnan region will supplement the existing public geophysical models for the China Seismic Experimental Site, serving as a high-quality data product for regional crustal structure interpretation and seismic precursor identification.

Using a similar approach, Han et al. (2021b) determined high-resolution (degree 120) TVGF solutions in North China using Slepian functions and terrestrial gravity measurements from 2011 to 2013. Their comparison shows that the degree 120 results provide gravity variations with significantly higher spatial resolution and stronger signal strength compared with the GRACE-derived degree 60 results in the same region. The findings of this work could benefit regional gravity field modeling, and the derived high-resolution TVGF solution could support water storage monitoring, tectonic activity analysis, and seismic risk assessment in North China.

The preparation and development of large earthquakes may cause transient changes of regional gravity field. High-precision repeated absolute gravimetry can obtain time variable gravity signals of mass changes inside the crust, providing a unique perspective on seismotectonic feature of strong continental earthquakes. For example, before the 2008 Mw 7.9 Wenchuan earthquake, a significant absolute gravity increase of several μGal per year was observed near its epicenter (Zhang et al., 2020). However, due to the scarcity of absolute gravity data (lack of sufficient measurement stations), the mechanism behind this signal remains unknown.

Since 2010, the Crustal Movement Observation Network of China (CMONOC), a national network of crustal deformation monitoring originated from 1998, has expanded 25 absolute gravity stations to 101 (Han et al., 2020). These stations have been observed repeatedly every two or three years, greatly enriching high-precision absolute gravity data for earthquake research.

Based on absolute gravity observations by CMONOC for more than a decade in the northeastern Tibetan Plateau, an obvious and coincident gravity increase about 5 years before the 2022 Ms 6.9 Menyuan earthquake is observed at four stations around the epicenter, with the rate up to 3.94 μGal/yr at Minqin station (Jia et al., 2023). The observed gravity changes could not be reasonably explained by the land water storage change nor crustal vertical deformation and thus might be related to the processes in the crust. A disc-shaped equivalent source region is then modeled using MCMC method, based on the residual gravity rates. The disc has the radius of 174.9 ±31.7 km, thickness of 1.9 ±0.6 km, and depth of 10.2 ±1.2 km, with center (100.45°E, 39.18°N) located at about 172 km northwest of the epicenter of the Menyuan earthquake.

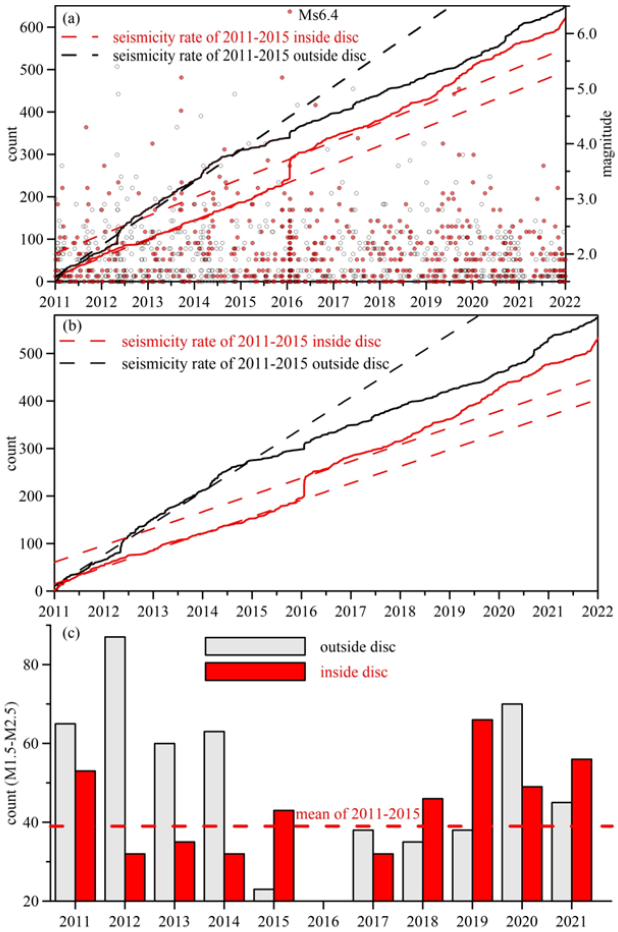

Figure 9. Seismicity in the modeled disc source region. (a) Cumulative curves for events with M⩾1.5. The dots denote magnitude of the events. (b) Cumulative curves for events with magnitude from 1.5 to 2.5. The red and black solid curves in (a) and (b) represent the seismicity cumulative curves inside and outside the modeled disc respectively. To align with the cumulative count after the 2016 Ms 6.4 Menyuan earthquake, the top red dashed lines in (a) and (b) are shifted, keeping the same slopes as the bottom red lines. (c) Number of earthquakes per year with magnitude from 1.5 to 2.5, the red dashed line shows mean value from 2011 to 2015 inside disc.

To investigate the mechanism of gravity changes in the disc source region, the historical earthquake data in this area are analyzed. After the 2016 Ms 6.4 Menyuan earthquake (close to epicenter of the 2022 earthquake), the seismic frequency in 2017–2021 is higher than that in 2011–2015 in the source region (Figure 9a). The earthquake frequency increases gradually especially for the events of magnitude from 1.5 to 2.5 (Figure 9b). This is similar to the behavior of deep fluids migration. The number of earthquakes per year in the source region has increased yearly since 2017 (Figure 9c). Furthermore, the spatiotemporal distribution of epicenters inside disc is consistent with the fluid diffusion model, indicating that gravity increase could be related to the redistribution of deep fluid mass. In contrast, the seismicity is decreased rather than increased outside the source region. On the other hand, there are many low-velocity zones in upper and middle crust around the source region, facilitating fluid mass transport.

In general, based on the analysis of gravity change, near-surface processes, regional crustal structure, and seismic activity, multiple lines of evidence consistently show that there are deep fluids migrations before the 2022 Menyuan earthquake. Upwelling and migration of deep fluids (usually accompanied by regional gravity increases according to finite element modeling (Liu et al., 2022)) promote rock rupture through reducing the effective normal stress and the friction coefficient. Then, this rupture leads to seismicity increases and potential triggering a large earthquake. Therefore, the observed gravity increases before the Menyuan earthquake could be related to fluid mass migration in the broad source region. Based on this explanation, a conceptual model for the fluid-driven seismicity and the simplified disc-shaped source is given in Figure 10. These results suggest that with the increasing availability of absolute gravimeters and the abundance of data, high-precision time-varying gravity observation may provide a geophysical method for monitoring regional crustal fluid environment and then determining the risk area with potential strong earthquakes.

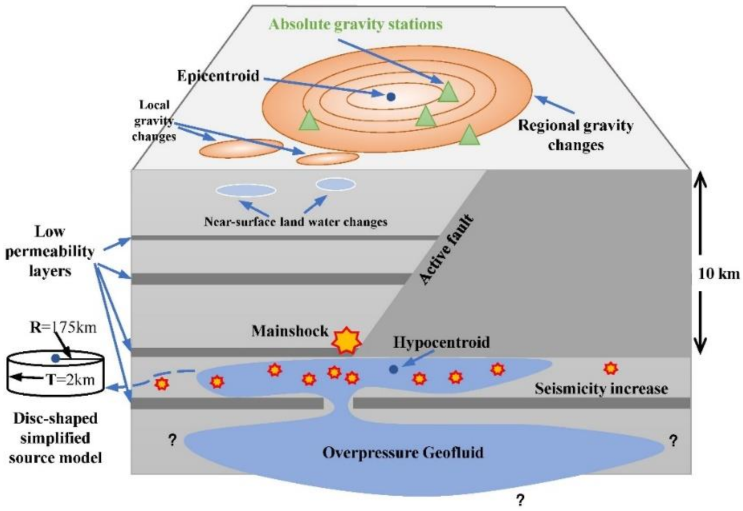

Figure 10. Sketch of deep mass transfer process and the disc-shaped source model of an earthquake. The hypocentroid is the center of mass of modeled disc and the epicentroid is surface projection of the hypocentroid.

5 Research Progress on Novel Technologies for Gravity Inversion

Gravity inversion, as one of the effective methods for studying the internal structure of the Earth, has the advantages of sensitivity to changes in subsurface material density, strong horizontal resolution, and low cost. However, it is also some drawbacks, such as low vertical resolution and strong non-uniqueness. Achieving high resolution, low non-uniqueness, and high reliability in detecting the Earth's internal structure are the main challenges for gravity inversion technology. The kernel issue for novel gravity inversion approach is how to address these problems by integrating the latest technological means. To address this issue, Chen Shi and his research team at the Institute of Geophysics of the China Earthquake Administration have developed advanced algorithms based on data assimilation and Bayesian uncertainty quantification theory. These algorithms have enabled the construction of finely detailed crustal density models for multiple seismic source regions in the Sichuan-Yunnan area, resulting in an improved level of understanding of these regions' structures.

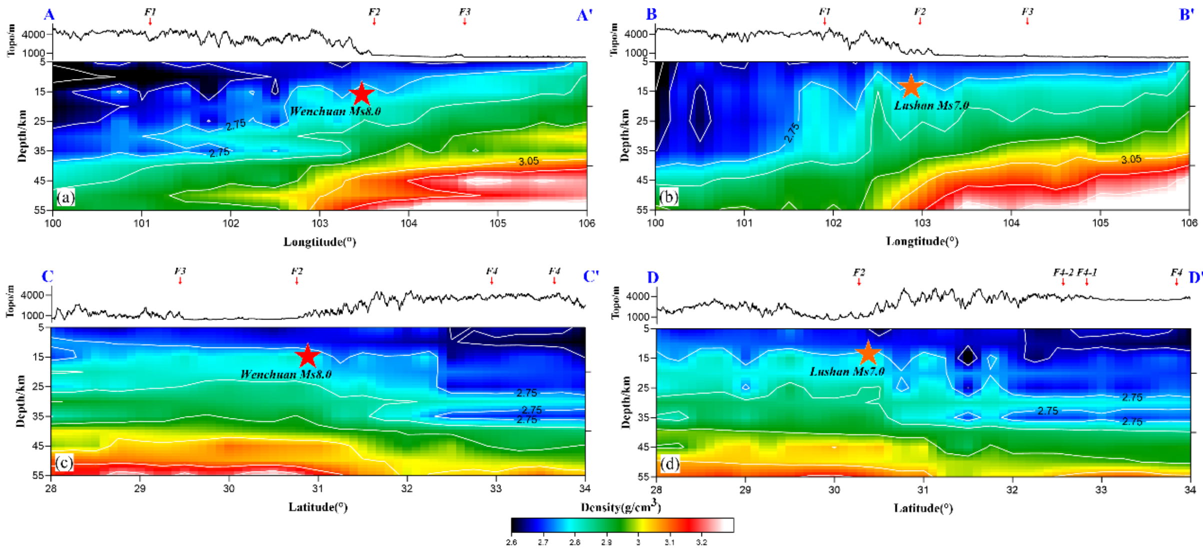

Figure 11. The density structure profiles below the epicenter area of Wenchuan earthquake and Lushan earthquake; (a) 31°N profile; (b) 30.3°N profile;(c) 103.4°E profile; (d) 103°E profile.

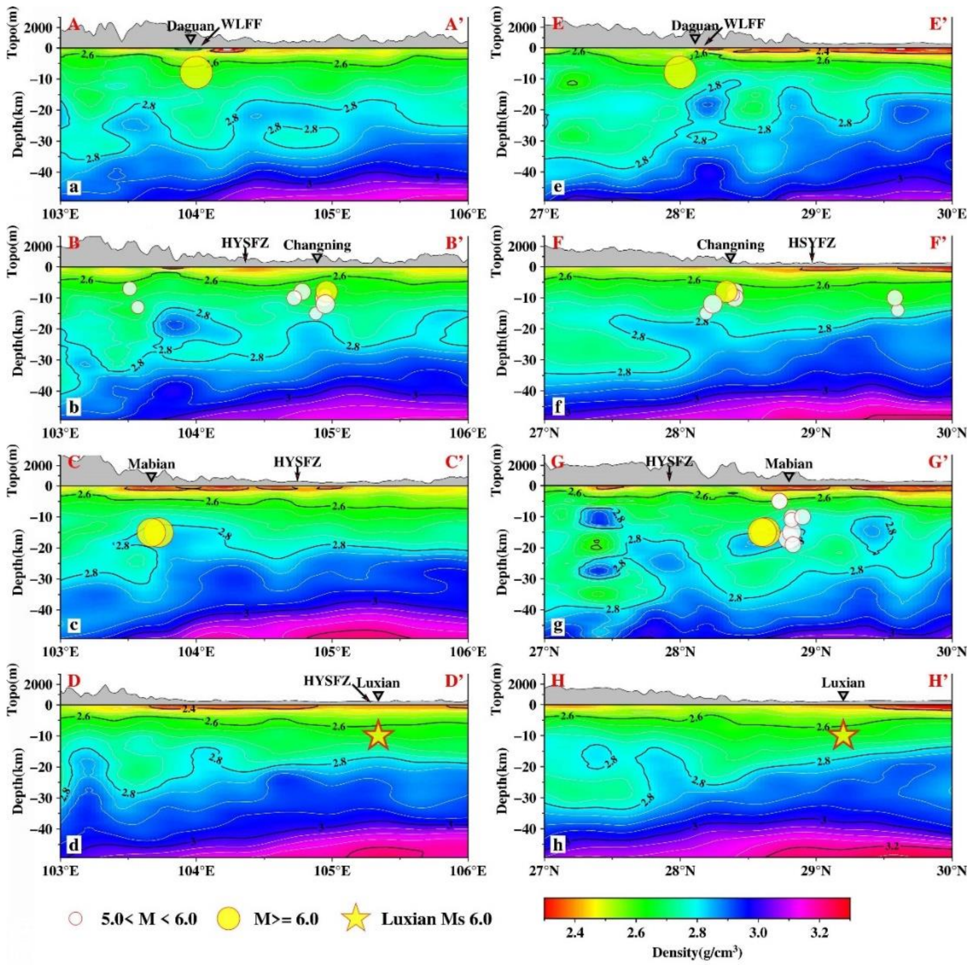

Figure 12. The density structure profiles below the epicenter area of Daguan earthquake, Changning earthquake, Maguan earthquake and Luxian earthquake; HYSFZ: Huaying Mountain Fault Zone; (a) 28.1°N profile; (b) 28.3°N profile; (c) 28.61°N profile; (d) 29.2°N profile; (e) 104°E profile; (f) 104.96°E profile; (g) 103.66°E profile; (h) 105.3°E profile.

Li et al. (2021) used the Bayesian assimilation gravity inversion method to construct the three-dimensional crustal density model for the strong earthquake source area in the Longmenshan region. This method effectively solves the classic problem of bias in knowledge introduced by single or subjective constraints in traditional gravity inversion algorithms by introducing Bayesian parameter optimization criteria. Figure 11 shows the density structure profiles below the Wenchuan earthquake and Lushan earthquake source areas. The steep variation of the middle and upper crustal density interface below the Wenchuan earthquake and Lushan strong earthquake source areas is significant. Comparing Figure 11a and Figure 11b, the low-density layer of the middle crust below the subduction front of the Wenchuan earthquake fault may be the main cause of the different seismic mechanisms compared with the Lushan earthquake. Li et al. (2022) used the MCMC inversion method to construct the three-dimensional crustal density model for the strong earthquake source area in southern Sichuan. This method ingeniously combines prior knowledge and observation data while quantifying the uncertainty characteristics of parameters. Figure 12 shows the density structure profile below the Daguan earthquake, Changning earthquake, Maguan earthquake, and Luxian earthquake source areas. Comparing Figure 12g, Figure 12h with Figure 12a-f, the deep density structure of the source areas of the Daguan earthquake, Changning earthquake, and Mabian earthquake has strong heterogeneity, showing the physical properties of tectonic earthquakes, while such features are not obvious in the Luxian earthquake. Both above research results can provide basic methods guarantee and effective deep constraints for the study of the crustal structure and physical properties of potential strong earthquake risk sources.

6 Research Progress on marine gravity field determination

Marine gravity field recovery from multi-source altimetry data

Satellite altimetry is the main means to rapidly acquire global high-precision and high-resolution marine gravity field. It mainly obtains sea surface height data by microwave ranging, and uses the theoretical relationship between the external shape of the Earth and the gravity field to calculate the marine gravity field by using the corresponding algorithm. After decades of development, the satellite altimetry technology has developed from radar altimeter to synthetic aperture altimeter and interferometric radar altimeter, the measurement band has developed from Ku to Ka, the sampling rate has developed from 20 Hz to 40 Hz, the observation mode has developed from nadir satellite to wide swath satellite, the acquired data has developed from one-dimensional sea surface height along the orbit to two-dimensional strip sea surface height, the range accuracy has been improved, and the spatial and temporal resolution of the acquired data have been improved too. Currently, the spatial resolution of altimetry-derived marine gravity field can reach 1'×1', and the accuracy reaches 1-2 mGal in the local sea area (Andersen OB, and Knudsen P, 2019; Sandwell et al., 2021). The APM has evaluated the accuracy of the advanced gravity field models DTU13, DTU10, V24.1, and V27.1 published by two major international agencies in the offshore region of the South China Sea using Chinese coastal ship measurements of gravity data (whose distribution is shown in Figure 13), and the results show that the accuracy of the gravity field models in the sea areas, which are less affected by ocean currents, can reach 2-3 mGal (Li et al., 2021).

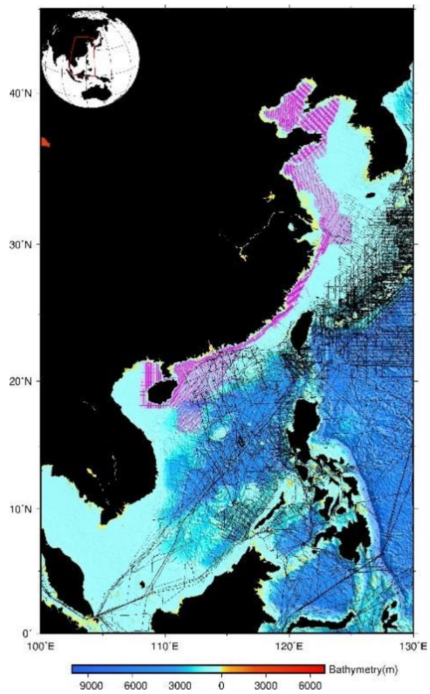

Figure 13. Geographic distribution of shipboard gravity measurements in the coastal region of China. The magenta lines are from the 908 Project, and the black lines are from the NCEI. The map was created by using GMT (http://gmt.soest.hawaii.edu). The background bathymetric data is from GEBCO (https://download.gebco.net/); its spatial resolution is resampled to 1′ × 1′.

The methods of marine gravity field recovery from satellite altimetry are mainly contain gravity anomaly recovery from the geoid height (inverse Stokes method), and from deflection of the vertical (inverse Vening-Meinesz method, Laplace equation method). In terms of data sources, considering the limitations of single altimetric satellite in spatial coverage and measurement period, combining multi-source and multi-generation altimetric satellite data to recover the marine gravity field is the main method. For a long time, Chinese scholars have conducted a lot of researches on the combined inversion of multi-source and multi-generation altimetry data and the refinement of marine gravity field. Sun et al. (2022) outlined the development history of marine microwave altimetry satellites briefly, focusing on the results of global marine gravity field and global seafloor topography modeling using satellite altimetry, and compared the classic marine gravity fields and seafloor topography models. Zhang et al. (2021) determined the marine gravity fields in four selected regions (Northwest Atlantic, Hawaiian Sea, Mariana Trench region, and Aegean Sea) based on sea surface height (SSH) and sea surface slope (SSS), respectively, using data from the CryoSat-2, Jason-1/2, and SARAL/Altika geodetic missions. The results were evaluated, and showed that the SSH-based method is advantageous in robustly estimating marine gravity anomalies in coastal areas. The SSS-based method has an advantage in the region of moderate ocean depths (2000-4000 m) with seamounts and ridges, but has a significant disadvantage in the case of currents flowing in a north-south direction (e.g., the Western Boundary Current) or topography with north-south oriented trenches. In the deep ocean with flat seafloor topography, both methods have similar accuracy. Based on multiple geodetic missions (GMs) and precise repetition missions such as CryoSat-2, Jason-1/2, SARAL/Altika and HY-2A, Zhu et al. (2021) innovatively used an iterative method to determine the sea surface heights (SSHs) of SARAL/Altika altimetry data with Ka band, and established the 1′×1′ gravity anomaly model SCSGA V1.0. Its accuracy was evaluated using ship-measured gravity data. The result showed that the accuracy of SCSGA V1.0 is comparable to that of international advanced models, which provides high-quality data support for seafloor topographic inversion, seafloor tectonic motion study, and underwater gravity-assisted navigation using marine gravity fields.

New altimetry satellite for marine gravity field recovery

The previous marine gravity field models are mainly from multi-source and multi-generation nadir altimetry satellite measurements. Since most of the altimetry satellites are polar orbiting satellites with large orbital inclination, the accuracy of the east-west component of the vertical deviation is significantly lower than that of the north-south component in most areas, and the time span of multi-source and multi-generation satellite data is affected by the time-varying information of the ocean, which limits the accuracy level of the ocean gravity field. In order to solve the above problems, scholars at home and abroad have proposed innovative altimetric satellite observation systems, such as SWOT (surface water ocean topography) and dual-satellite in tandem mode, aiming to achieve rapid acquisition of global coverage of two-dimensional sea surface height data, solving the high-precision vertical deviation north-south and east-west components simultaneity, so as to improve the resolution and accuracy of marine gravity field (Zhai et al., 2018; Bao and Xu, 2014). The successful launch of the SWOT satellite on December 16, 2022, kicked off the new system of altimetry satellites. Before acquiring the SWOT actual data, domestic and foreign scholars used simulated data to investigate the key techniques of marine gravity field recovery for the new altimetry data and achieved corresponding results. Jin et al. (2022) used the simulated single-period SWOT sea surface height data to calculate the vertical deviations in the South China Sea and parts of the Indian Ocean, and then compared with that calculated by one-year simulated sea surface height measurements from the Jason-1/GM (geodetic mission), Cryosat-2/LRM (low-rate mode), and SARAL/GM nadir altimeter missions. The results showed that the vertical deviation determined by single-period SWOT data is better than that determined by the combined dataset of Jason-1/GM, Cryosat-2/LRM and SARAL/GM data, which can significantly improve the accuracy of the east-west component of the vertical deviation. Yu et al. (2022) created a high-frequency SSH component using multibeam bathymetry data from the northern South China Sea, combined with mean sea level, to simulate SWOT surface height measurements. In addition, the SWOT SSH observation errors were simulated using the SWOT simulator to generate 19 21-day repetitive SWOT SSH observation periods (about 400 days), and two computational methods, the inverse Vening-Meinesz formula and the inverse Stokes integral, were used to calculate the marine gravity field in the South China Sea, and the results showed that the multi-period SWOT observations can provide high-quality marine gravity anomalies.

In terms of new satellite altimetry technology, APM has been conducting long-term research on related theories and key technologies. As early as 2014, APM took the lead in proposing a double-star companion altimetry satellite model, and gave a corresponding satellite orbit design scheme according to the basic requirements of satellite orbit design (Bao and Xu, 2014). Subsequent studies such as the demonstration of the calibration scheme of double-star altimetry and the demonstration of the ocean gravity field inversion scheme were carried out successively, which provided technical support for the new altimetry technology for marine gravity field inversion.

Marine and airborne gravity measurement

Marine and airborne gravity measurement is currently the main auxiliary method for obtaining the marine gravity field. This method primarily uses a gravimeter (or accelerometer) to measure the gravity acceleration of the sea surface while carried by a ship or aircraft. With high precision, it is suitable for measuring gravity information in wide ocean areas and inshore/reef regions where the precision of satellite altimetry for gravity field inversion is relatively low. The development of marine and airborne gravity measurement technology is closely related to the development of gravimeter equipment. In recent years, the successful development of new marine gravimeters and improvements in marine and airborne gravity data processing technology have led to the vigorous development of marine gravity measurement. Although the independent development of Chinese marine and airborne gravimeters started relatively late, significant achievements have been made in recent years with the investment of manpower and material resources. Currently, the marine and airborne gravimeter named CHZ-II developed by the APM and the SAG series gravimeters developed by the China Aerospace Science and Technology Corporation are gradually becoming practical.

With the development of marine gravity measurement technology, China's military oceanographic surveying and mapping department has carried out regular marine gravity measurement work using marine gravimeters. They have continuously conducted research on theoretical and technical methods for processing marine gravity measurement data, independently developed intelligent collection and processing equipment, constructed a complete and high-precision marine gravity measurement operation technology and equipment system, and formed a systematic and organized production operation capacity. With the development of independent marine gravimeters, domestic institutions have conducted multiple gravity measurement works and gravimeters platform comparison tests. In 2018, a multi-type marine gravity meter ship-to-ship comparison test was carried out in a partial area of the South China Sea on board the Xiangyanghong 6 research vessel (as shown in Figure 14). The marine and airborne gravimeter CHZ-II developed by the APM, together with six other gravimeters, including SAG-2M, SGA-WZ, ZL11, Russian GT-2M (No.39), and American LCR (No.S129), participated in the comparison, and six effective flight paths were obtained. By using methods such as repeat line comparison statistics, cross-point mismatch value statistics, and comparison of results from different gravimeters, the measurement accuracy of the six gravimeters was compared and analyzed. The results showed that all six gravity meters can meet the accuracy requirements of marine gravity measurement. The accuracy of domestic gravimeters is close to that of the GT-2M gravimeter and higher than that of the precision gravity meter LCR (Yuan et al., 2018).

Figure 14. Marine relative gravimeters: a CHZ-II; b ZL11; c SAG-2M; d SGA-WZ; e GT-2M; f LCR （Yuan et al., 2018）

Existing shipborne dynamic measurements are all relative gravity measurements, which measure the changes in gravity values of the moving carrier relative to fixed absolute gravity reference points. The problem of instrument zero drift during relative gravity measurement process affects the final measurement performance, and the lack of unified benchmarks between different measurement routes affects the fusion of shipborne data. The application of absolute gravimeters for dynamic measurement on moving carriers can provide same-site calibration for dynamic relative gravimeters, providing a new solution to the problems. With the development of cold atom interferometry technology, quantum dynamic absolute gravimeters have emerged, providing technical support for ocean dynamic absolute measurements.

In recent years, the APM, Zhejiang University of Technology, and China Shipbuilding Industry Group Co., Ltd. have respectively carried out research and development of quantum absolute gravimeters, track tests, lake tests, ocean mooring tests, and dynamic measurement experiments, solving a series of key technologies for cold atom dynamic absolute gravimeters and keeping up with the pace of foreign research. Among them, Zhejiang University has built a shipborne absolute gravity dynamic measurement system and conducted absolute gravity dynamic measurement experiments in a shipborne mooring state. According to the evaluation, the gravity measurement sensitivity in the shipborne mooring environment is 16.6 mGal/Hz-1/2, and the resolution of gravity measurement within 1000 s integration time can reach 0.7 mGal. The stability of the system was evaluated through two weeks of absolute gravity measurement (Cheng Bing et al., 2021). The APM and the Naval University of Engineering jointly built an absolute dynamic gravity measurement system based on a cold atom gravimeter and an inertial stabilization platform, and adopted a combination of cold atom gravimeter and traditional accelerometer measurement methods to conduct shipborne dynamic measurement experiments. According to the evaluation, the internal agreement accuracy of the four repeated measurement lines is 2.272 mGal, and the external agreement accuracy of the four voyages is 2.331, 1.837, 3.988, and 2.589 mGal, respectively (Che Hao et al., 2022).

7 Application research on marine gravity field

Application of marine gravity survey for seafloor topography inversion

The bathymetry reflects the variations in the topography of the sea floor, and it is a fundamental parameter for conducting marine investigations and research. It provides important basic data for the study of oceanography, marine geology, marine geophysics, and marine biology. A precise model of the bathymetry helps to understand the external shape of the Earth, the movement of seafloor structures, and the evolution of the seafloor. It can be used for planning ship navigation routes, submarine navigation, deep-sea resource development, marine engineering construction, and marine environmental monitoring. It has important applications in marine science research, military oceanographic support, national economic development, and the protection of marine rights and interests.

The main method for rapidly measuring global seafloor topography is to use the marine gravity field to invert the seafloor topography. The theoretical basis for this method is the strong correlation between gravity anomalies and seafloor topography in a certain wave band. Based on this theory, many scholars have developed methods to invert seafloor topography using ocean gravity anomalies. So far, the commonly used methods for inverting seafloor topography from marine gravity anomalies include the admittance function method, least squares adjustment method, Smith and Sandwell (S&S) method, and gravity-geologic method (GGM). The APM has reviewed the development of domestic and foreign seafloor exploration technologies and model construction, discussed the current research status and major challenges of global seafloor topography fine modeling, and summarized the development trend of global seafloor topography fine modeling in the future. It is believed that the inversion of ocean gravity field based on satellite altimetry technology will still be the main technical means for fine modeling of global seafloor topography in the future. Moreover, new-generation altimetry satellites such as the tandem altimetry and the SWOT two-dimensional sea surface height measurement mission will provide data sources for further improving the accuracy of marine gravity field and seafloor topography models. Combining terrain complexity and optimizing seafloor topography inversion theory methods is expected to bring theoretical innovation, and exploring the use of artificial intelligence technology for fine modeling of seafloor topography deserves attention (Sun et al., 2022). With the development of artificial intelligence technology, scholars have continuously explored the combination of machine learning for seafloor topography inversion and have achieved good results (Annan and Wan, 2022; Wan et al., 2022). Annan and Wan (2022) used convolutional neural networks to invert the seafloor topography of the Guinea Gulf area by fusing vertical deflection data, gravity anomaly data, and vertical gravity gradient data and evaluated the accuracy. The results showed that the seafloor topography inverted by convolutional neural networks has higher accuracy.

Research on underwater gravity-assisted navigation

Underwater gravity-assisted navigation has the characteristics of passive autonomy, stability, and strong anti-interference, and does not require the submarine to approach or float to the surface to receive or transmit signals. It can realize the underwater concealed calibration of the navigation system, providing better protection for the safe and concealed navigation of submarines during long voyages. In the current international situation, China's marine strategy faces severe challenges. Developing underwater gravity-matching assisted navigation is of great strategic and practical significance for China to establish an underwater long-term passive autonomous navigation system, ensure underwater navigation safety, consolidate national defense security, break through island chain blockades, and maintain deterrence capability.

The underwater gravity-assisted navigation system mainly consists of the navigation reference map, gravity measurement sensor, dynamic measurement and data processing, matching positioning, and navigation information output. The gravity navigation reference map is the basic data source necessary for underwater gravity-assisted navigation positioning. It provides basic reference coordinates and foundational data support for matching navigation positioning. The accuracy and resolution of the reference map determine the overall effectiveness of matching navigation. The ocean gravity field can provide a high-precision, high-resolution navigation reference map for underwater gravity-assisted navigation. In recent years, domestic scholars have conducted a lot of research related to underwater matching navigation based on the ocean gravity field. Harbin Engineering University has conducted relevant research in gravity pattern matching positioning technology, contour matching algorithms, inertial navigation initial alignment based on gravity information, and simulation of gravity matching navigation systems. The Naval University of Engineering and the Naval Oceanographic and Hydrographic Research Institute have cooperated to conduct a series of studies on the generation technology of simulated gravity maps, the influence of gravity fields on inertial navigation, and the related algorithms/ICCP algorithms of gravity matching. The Information Engineering University has explored and researched the disturbance correction of gravity information in gravity-assisted inertial navigation, the UKF algorithm for inertial/gravity combined navigation, the reconstruction method for ocean gravity anomaly maps for navigation, and the improved method for the ICCP algorithm of gravity matching. The APM proposed inertial/gravity combined navigation positioning algorithms such as multi-mode adaptive estimation, minimum variance sum, and relative position constraints. They have also jointly conducted several sea trials of gravity matching assisted navigation with the Naval University of Engineering, the Oceanographic and Hydrographic Research Institute, and others. The positioning accuracy reached 1.9 nautical miles (as shown in Figure 15) (Liu et al., 2021). The above research provides a solid theoretical basis and technical support for the use of the ocean gravity field for underwater gravity-assisted navigation.

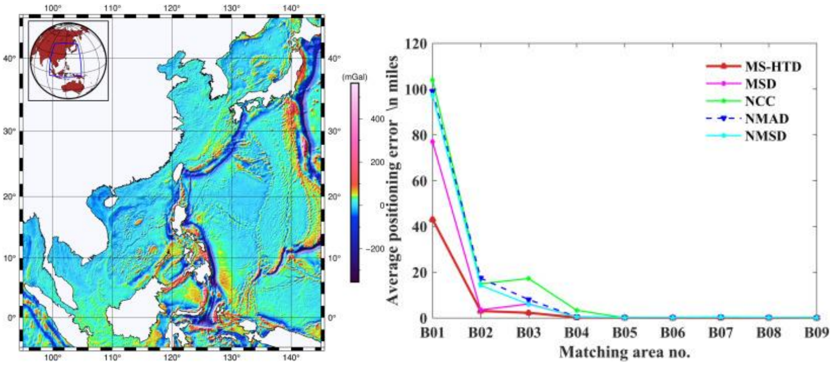

Figure 15. Average positioning error of matching navigation algorithm under different matching regions.

Research on seafloor tectonic movement

Seafloor spreading is a geodynamic phenomenon closely related to the mass transfer of Earth's interior materials. It is also an important aspect of geodynamics and global change research, and has a significant impact on the interactions between Earth's layers. Investigating and analyzing seafloor spreading, revealing the evolution laws of the Earth as a whole or in specific regions, and predicting its trends, are hot topics in modern Earth science research. Essentially, the mass transfer caused by tectonic movements will inevitably lead to slight changes in the Earth's external gravity field. The Earth's gravity field is one of its inherent physical characteristics, reflecting the distribution, movement, and changing states of materials within the Earth's interior. Through differential observations of gravity fields at different times (including gravity anomalies, gravity gradients, vertical deflection, and geoid), information on the temporal and spatial distribution of the global gravity field can be obtained, and combined with plate tectonic theory, will provide accurate data for explaining and analyzing geodynamic phenomena and geophysical features of the Earth.

The APM utilizes the technical advantages of precise and quantitative geodetic measurements to detect rapid mass transfer phenomena in typical regions of the Earth's surface, such as the magma activity during submarine volcanic eruptions, through repeated observations of the ocean gravity field over multiple periods. Taking the submarine volcanic activity of Nishinoshima, Japan as an example, DEXP three-dimensional imaging technology was used to quickly image the magma distribution within the volcano, and the magma movement was analyzed by comparing the imaging results corresponding to the three periods before, during, and after the volcanic eruption. The research reveals the complex characteristics of magma movement during volcanic eruptions, including both lateral and vertical magma transport, and the magma chamber in the northeast is the main source of volcanic eruption materials (as shown in Figure 16). The research involves many disciplines, such as geodesy, geophysics, and geodynamics. The results provide a new research approach for a profound understanding of the characteristics and current activity status of oceanic plate tectonics, the formation process of oceanic islands, the explanation of geodynamic mechanisms, and the exploration of the mysteries within the Earth (Li et al., 2021).

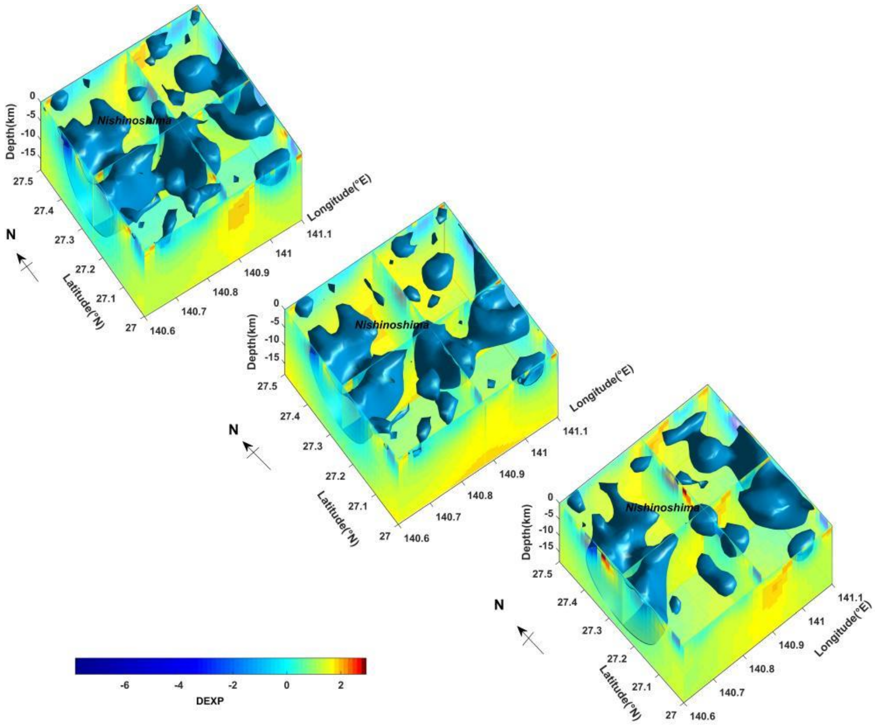

Figure 16. 3D DEXP image of the anomalous sources of the Nishinoshima from the detrend Bouguer gravity anomalies in 2013, 2014 and 2019 (Top: Before the eruption, 2013; Middle: During the eruption, 2014; Bottom: After the eruption, 2019).

Bibliography

Andersen, OB., Knudsen, P. (2019). The DTU17 global marine gravity field: first validation results. In: International association of geodesy symposia, Berlin, Heidelberg.

Annan, R.F., Wan, X. (2022). Recovering Bathymetry of the Gulf of Guinea Using Altimetry-Derived Gravity Field Products Combined via Convolutional Neural Network. Surv Geophys, 43, 1541–1561.

Bao, L., Xu, H. (2014). Twin-satellites Altimetry Mode and Its Orbit Design. Acta Geodaetica et Cartographica Sinica, 43(07):661-667.

Chang, L., Qin, F., Wu, M. (2018). Gravity disturbance compensation for inertial navigation system. IEEE Transactions on Instrumentation and Measurement, 68(10), 3751-3765.

Che, H., Li, A., Fang, J., Ge, G., Gao, W., Zhang, Y., Liu, C., Xu, J., Chang, L., Huang, C., Gong, W., Li, D., Chen, X., Qin, F. (2022). Ship-Borne Dynamic Absolute Gravity Measurement Experiment Based on Cold Atomic Gravimeter. Acta Physica Sinica, 71(11): 113701.

Chen, S., Zhuang, J., Li, X., Lu, H., Xu, W. (2019). Bayesian approach for network adjustment for gravity survey campaign: methodology and model test. Journal of Geodesy, 93, 681-700.

Chen, X., Li, H., Deng, M., Jiang, L., Sun, H., Li, D., Bai, L. (2020). Experimental study of the surface subsidence in the city using gravity observing techniques. Chinese Journal of Geophysics, 63(8), 2882-2892.

Chen, Z., Chen, S., Zhang, B., Wang, L., Shi, L., Lu, H., Xu, W. (2022). Uncertainty quantification and field source inversion for the continental-scale time-varying gravity dataset: a case study in SE Tibet, China. Pure and Applied Geophysics 180, 683–702.

Cheng, B., Zhou, Y., Chen, P., Zhang, K., Zhu, D., Wang, K., Weng, K., Wang, H., Peng, S., Wang, X., Wu, B., Lin, Q. (2021).

Absolute Gravity Measurement Based on Atomic Gravimeter Under Ship-Borne Mooring State. Acta Physica Sinica, 70(4):7.

Cui, X., Sun, H., Xu, J., Zhou, J., Chen, X. (2020). Relationship between free core nutation and geomagnetic jerks. Journal of Geodesy, 94, 1-13.

Han, J., Chen, S., Chen, Z., Lu, H., Xu, W. (2021a). Determination of the degree 120 time-variable gravity field in the Sichuan-Yunnan region using Slepian functions and terrestrial measurements. Earthquake Science 34(3):211-221.

Han, J., Chen, S., Lu, H., Xu, W. (2021b). Time-variable gravity field determination using Slepian functions and terrestrial measurements: A case study in North China with data from 2011 to 2013. Chinese Journal of Geophysics 64:1542-1557 (in Chinese).

Han, Y., Wang, J., Xu, R. (2020). Fractal characteristics and earthquake monitoring capability of the CMONOC gravity network. Earthquake Research in China 36 (4): 879–887 (in Chinese).

He, Q., Chen, X., Sun, H., Xu, J., Liu, Z., Zhou, S., Chen, Z. (2022). Quantitative separation of the local vadose zone water storage changes using the superconductive gravity technique. Journal of Hydrology, 609, 127734.

Jia, L., Chen, S., Wang, L., Xiang, L., Lu, H., Shi, W. (2023). Gravity yearly transient change around the epicenter of 2022 Ms 6.9 Menyuan earthquake, China and seismotectonic implications. Tectonophysics 846: 229676.

Jin, T., Zhou, M., Zhang, H., Li, J., Jiang, W., Zhang, S., Hu, M. (2022). Analysis of vertical deflections determined from one cycle of simulated SWOT wide-swath altimeter data. Journal of Geodesy, 96(4), 30.

Li, H., Chen, S., Zhuang, J., Zhang, B., Shi, L. (2021). Gravity inversion method base on Bayesian-assimilation and its application in constructing crust density model of the Longmenshan region. Chinese Journal of Geophysics 64(4): 1236-1252.

Li, H., Xu, J., Chen, X., Sun, H., Zhang, M., Zhang, L. (2020). Extracting long-period surface waves and free oscillations using ambient noise recorded by global distributed superconducting gravimeters. Seismological research letters, (4), 91.

Li, H., Chen, X. D., Xu, J. Q. (2020). Comparison of noise levels between gravimeters and co-located seismometers at the seismic frequency band. Geodesy and Geodynamics, 40(8), 843-848.

Li, Q., Bao, L., Shum, CK. (2020). Analysis of seafloor plate motion using ocean gravity field variations. Chinese Journal of Geophysics, 63(7): 2506-2515.

Li, Q., Bao, L., Shum, C.K. (2021). Altimeter-derived marine gravity variations reveal the magma mass motions within the subaqueous Nishinoshima volcano, Izu–Bonin Arc, Japan. Journal of Geodesy, 95, 46.

Li, Q., Bao, L., Wang, Y. (2021). Accuracy Evaluation of Altimeter-Derived Gravity Field Models in Offshore and Coastal Regions of China. Frontiers in Earth Science, 9(649).

Li, Y., Chen, S., Li, H., Zhang, B. (2022). Contrastive analysis of the three-dimensional density structure characteristics of the focal area of moderate-strong earthquakes in southern Sichuan. Chinese Journal of Geophysics 65(11): 4326-4340.

Liang, Y., Chen, X. D., Sun, H., Cui, X., Zhang, M., Niu, X. (2020). Gravity Tide Observation with OSG-066 and Their Applications at Lijiang Station, Yunnan Province, China. Geodesy and Geodynamics, 40(7): 713-719.

Liu, H., Wu, L., Bao, L., Li, Q., Zhang, P., Wang, Y. (2022). Gravity matching navigation algorithm based on multiscale search and Hadamard transformed difference. ISA transactions, 128, 409-422.

Liu, X., Chen, S., Xing, H. (2022). Gravity changes caused by crustal fluids invasion: A perspective from finite element modeling. Tectonophysics 833: 229335.

Sandwell, D. T., Harper, H., Tozer, B., Smith, W. H. F. (2021). Gravity Field Recovery from Geodetic Altimeter Missions. Adv.

Space Res. 68, 1059–1072.

Sun, H., Cui, X., Xu, J., Ding, H., Zhang, M., Li, H., Wang, Z., Zhou, J., Chen, X. (2022). Progress of Research on the Earth's Gravity Tides and its Application in Geodynamics in China. Pure and Applied Geophysics, 1-17.

Sun, H., Li, Q., Bao, L., Wu, Z., Wu, L. (2022). Advancements and trends in high-resolution modeling of global seafloor topography. Journal of Wuhan University: Information Science Edition, 47(10): 1555-1567.

Sun, H., Zhang, M., Xu, J., Chen, X. (2019a). Reanalysis of background free oscillations using recent SG data. TAO: Terrestrial, Atmospheric and Oceanic Sciences, Vol. 30, No. 6, 1-7.

Sun, H., Zhang, H., Xu, J., Chen, X., Zhou, J., Zhang, M. (2019b). Influences of the Tibetan plateau on tidal gravity detected by using SGs at Lhasa, Lijiang and Wuhan Stations in China. TAO: Terrestrial, Atmospheric and Oceanic Sciences, Vol. 30, No. 1, 139-149.

Sun, Z., Guan, B., Zhai, Z., Ouyang, M. (2022). Research progress of ocean satellite altimetry and its recovery of global marine gravity field and seafloor topography model. Acta Geodaetica et Cartographica Sinica, 51(6): 923-934.

Wan, X., Liu, B., Sui, X., Annan, R. F., Hao, R., Min, Y. (2022). Bathymetry inversion using the deflection of the vertical: A case study in South China Sea. Geodesy and Geodynamics, 13(5), 492-502.

Wang, B., Zhu, J., Deng, Z., Fu, M. (2018). A characteristic parameter matching algorithm for gravity-aided navigation of underwater vehicles. IEEE Transactions on Industrial Electronics, 66(2), 1203-1212.

Wang, L., Chen, S., Zhuang, J., Xu, W. (2022). Simultaneous calibration of instrument scale factor and drift rate in network adjustment for continental-scale gravity survey campaign. Geophysical Journal International, 228(3), 1541-1555.

Yang, J., Chen, S., Zhang, B., Zhuang, J., Wang, L., Lu, H. (2021). Gravity observations and apparent density changes before the 2017 Jiuzhaigou Ms7. 0 earthquake and their precursory significance. Entropy, 23(12), 1687.

Wang, Y., Yang, Y., Sun, H., Xie, C., Zhang, Q., Cui, X., Chen, C., He, Y., Miao, Q., Mu, C., Guo, L., Teng, J. (2023). Observation and research of deep underground multi-physical fields—huainan 848 m deep experiment. Science China Earth Sciences, 66(1), 54-70.

Yu, D., Hwang, C., Andersen, O.B., Chang, E.T., Gaultier, L. (2021). Gravity recovery from SWOT altimetry using geoid height and geoid gradient. Remote Sensing of Environment, 265, 112650.

Yuan, Y., Gao, J., Wu, Z. Shen, Z., Wu, G. (2020). Performance estimate of some prototypes of inertial platform and strapdown marine gravimeters. Earth Planets Space 72, 89.

Zhai, Z., Sun, Z., Xiao, Y., Li, F. (2018). Two-Satellites Tandem Mode Design and Accuracy Analysis of Gravity Field Inversion for Independent Marine Altimetry Satellite. Geomatics and Information Science of Wuhan University, 43(07):1030-1035.

Zhang, M., Chen, X., Xu, J., Cui, X., Liu, M., Xing, L., Mu, C., Sun, H. (2021). A Preliminary Analysis of Gravity Noise Levels at the Deep Geophysical Experimental Field in Huainan. Advances in Earth Science, 36(5): 500-509.

Zhang, S., Abulaitijiang, A., Andersen, O. B., Sandwell, D. T., Beale, J. R. (2021). Comparison and evaluation of high-resolution marine gravity recovery via sea surface heights or sea surface slopes. Journal of Geodesy, 95(6), 66.

Zhang, Y., Chen, S., Xing, L., Liu, M., He, Z. (2020). Gravity changes before and after the 2008 Mw 7.9 Wenchuan earthquake at Pixian absolute gravity station in more than a decade. Pure and Applied Geophysics 177(1): 121-133.

Zheng, Q., Yao, X., Chen, S., Yang, J., Liu, D., Chen, Z. (2022). Data quality assessment of time-variable surface microgravity surveys in the southeastern Tibetan Plateau. Applied Sciences 12(7), 3310.

Zhu, C., Guo, J., Gao, J., Liu, X., Hwang, C., Yu, S., Yuan, J., Ji, B., Guan, B. (2020). Marine gravity determined from multi-satellite GM/ERM altimeter data over the South China Sea: SCSGA V1.0. Journal of Geodesy, 94, 1-16.

Development Status of Chinese Gravimetry Satellite

Yun Xiao[1,2], Yuanxi Yang[1,2] , Zhicai Luo[3], Yunlong Wu[4], Zongpeng Pan[1,2] , Hao Zhou[3], Xiaogang Liu[1,2] , Zhongmiao Sun[1,2], Zehua Guo[5], Guodong Xu[4], Sulan Liu[4]

[1] *Xi'an research Institute of Surveying and Mapping, Shanxi, Xi'an 710054, China*

[2] *State Key Laboratory of Geo-Information Engineering, Shanxi, Xi'an 710054, China*

[3] *Institute of Geophysics and National Precise Gravity Measurement Facility (PGMF), Huazhong University of Science and Technology (HUST)*

[4] *School of Geography and Information Engineering, China University of Geosciences, Wuhan*

[5] *School of Geodesy and Geomatics, Wuhan University*

1 Chinese First Satellite-to-Satellite Tracking Gravimetric Misson

The first pair of satellite to satellite tracking gravimetric satellites from China (Chinese Gravimetric mission) was successfully launched at the end of 2021. It adopts a hybrid measurement system of High-Low Satellite-to-Satellite Tracking (HL-SST) and Low-Low Satellite-to-Satellite Tracking (LL-SST) to obtain measurements of the global gravity field and its time-varying information, which can be used to study groundwater changes, glacier ablation, space micro-gravity fluctuations, ocean tides, earthquakes, etc. The data can be used for scientific research and engineering construction in the fields of natural resources, ocean, aerospace, and water conservancy, et al. The Chinese gravimetric satellite platform is designed to be ultra-silent, ultra-stable and ultra-accurate. In-orbit test results show that the working state of the platform is normal and all indicators meet the design requirements. This significantly improves the development level of the satellite platform and the level of space micro-gravity measurement, and will expand the prospect for scientific applications in various fields.

Chinese gravimetric satellite platform is designed and produced firstly, can provide an environment with low vibrations, stable temperature, precise space pointing and tiny deformation of the structure for the whole satellite, and ensures that the payloads of the inter-satellite ranging system and electrostatic suspension accelerometer work in suitable conditions.

The inter-satellite ranging system, electrostatic suspension accelerometer, BDS/GPS common mode receiver, star sensors, et al. are mounted. The inter-satellite ranging system is working in the dual-one way ranging configuration, and ranging noise level being better than 3μm/√Hz in the frequency band of 0.025-0.1Hz. The accelerometer works with electrostatic suspension mode, which is highly sensitive to the residual thrust of the attitude control thruster, switching of the magnetic torque and other small vibrations. The spectrum analysis shows its high-sensitive axis noise level is being 3×10^{-10}m/s2/√Hz near the frequency 0.1Hz, and being 1×10^{-9}m/s2/√Hz for the less-sensitive axis. The three star sensors are designed integrally with the tiny deformation structure. The angles between star sensor boresights were calculated, then the average of the angles was removed, the standard deviation (STD) of residuals was better than 3". The center of mass detection and adjustment system reaches the accuracy level of 100 microns. The BDS/GPS common mode receiver observers BDS-3 signals and GPS signals simultaneously. The data from the BDS/GPS receiver is used for satellite Precise Orbit

Determination (POD) and time synchronization. The achieved accuracy of the satellite orbits is better than 2 cm determined from a comparison of the kinematic and reduced-dynamic orbits. Comparing the baseline of the KBR system with the POD yields RMS residuals of less than 1 mm.

The time-varying Earth gravity model with a maximum degree of 60 was recovered using satellite data from April 1, 2022 to August 30, 2022, being named Chinese Earth Gravity Field Model 22-01 (CEGM22S-01) (Figure 1). The model can well characterize global hydrological changes, such as the mass loss of Greenland and the terrestrial water storage changes of the Amazon River, and correlates strongly with the results of GRACE Follow-On with the root mean square (RMS) difference of 2 cm in global equivalent water height (Figure. 2.3.2). The model is converted into an equivalent water height which can be applied to Amazon terrestrial water storage monitoring.

With the accumulation of further satellite data, the continuous time-varying gravity field, space atmospheric density, space horizontal ionosphere, space magnetic field and other products can be produced, which will provide abundant information services for the fields of geophysics, geodesy, earthquake, water resources environment, ocean, national defense, etc.

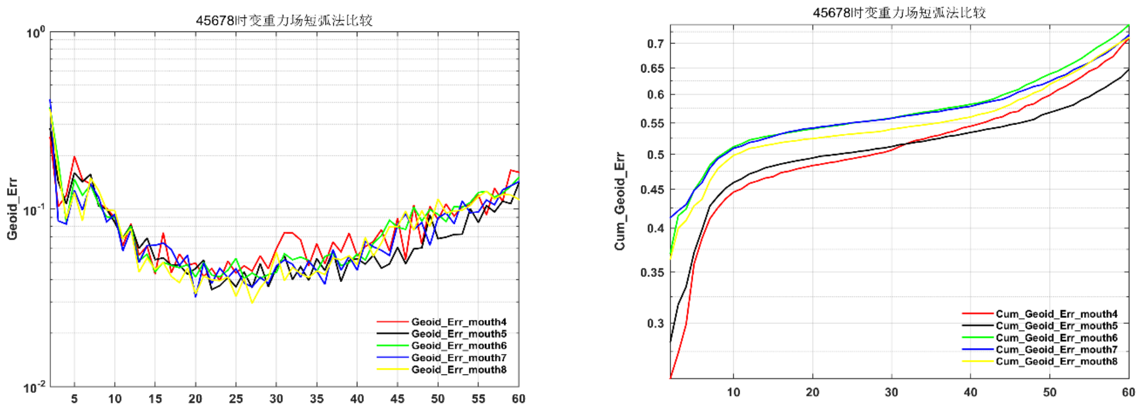

Figure 1. The degree error spectrum and accumulated error of the Chinese Earth Gravity Model CEGM22S-01 (Xiao et al.， 2023).

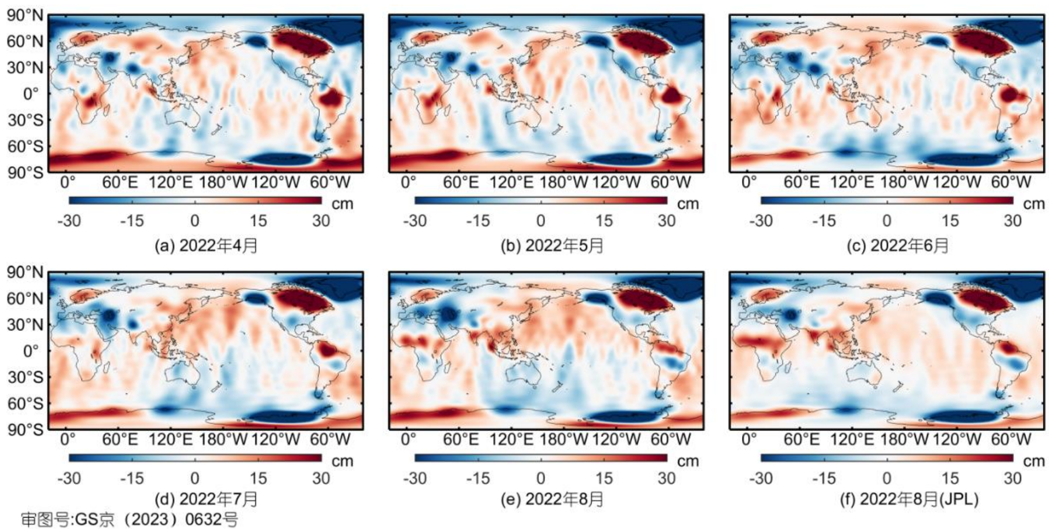

Figure 2. The power spectrum of the Chinese Earth Gravity Model CEGM22S-01 (Xiao et al., 2023)

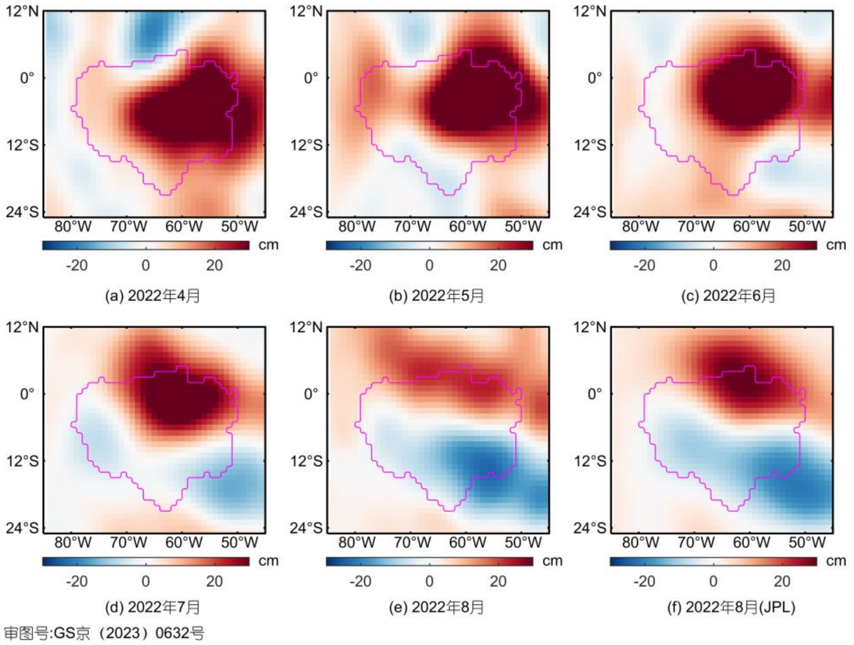

Figure 3. The inversion results of Amazon groundwater (Xiao et al., 2023)

2 Chinese Next Generation Gravimtric Mission

Tianqin (TQ) mission is a Chinese proposed project for space-based gravitational wave detection. The concept of TQ envisions an equilateral triangle constellation of three drag-free satellites orbiting the Earth with an orbital radius of about 10^5km (Gong et a., 2021; Mei et al., 2021). To achieve the final goal of TQ mission, the TQ mission set a roadmap from TQ-1, TQ-2 to TQ-3.

The TQ-1 satellite, which is the first technology demonstration satellite for the TQ project, was launched on 20 December 2019. The first round of experiment had been carried out from 21 December 2019 until 1 April 2020. The residual acceleration of the satellite is found to be about 1×10^{-10} m/s^2/Hz$^{1/2}$at 0.1 Hz and about 5×10^{-11} m/s^2/Hz$^{1/2}$at 0.05 Hz, measured by an inertial sensor with a sensitivity of 5×10^{-12} m/s^2/Hz$^{1/2}$at 0.1 Hz. The micro-Newton thrusters has demonstrated a thrust resolution of 0.1 μN and a thrust noise of 0.3 μN/Hz$^{1/2}$ at 0.1 Hz. The residual noise of the satellite with drag-free control is 3×10^{-9} m/s^2/Hz$^{1/2}$at 0.1 Hz. The noise level of the optical readout system is about 30 pm/Hz$^{1/2}$at 0.1 Hz. The temperature stability at temperature monitoring position is controlled to be about ±3 mK per orbit, and the mismatch between the center-of-mass of the satellite and that of the test mass is measured with a precision of better than 0.1 mm. This successful mission has marked a new milestone in the development of the TQ project.

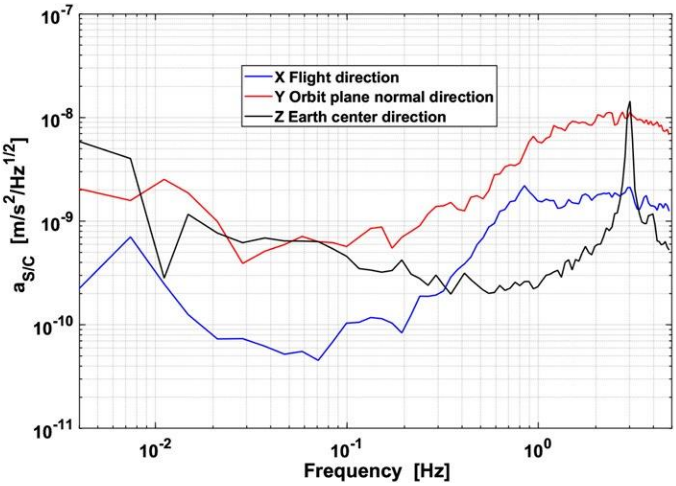

Figure 4. The actual acceleration level of the satellite measured by the inertial sensor onboard TQ-1. Note X is along the flight direction and Z points to the center of Earth.

Based on the successful TQ-1 mission, the TQ group has also focus on propose the TQ-2 mission. TQ-2 mission is designed as a totally experimental satellite for gravitational wave detection at low Earth orbit, which can detect the Earth's gravity field simultaneously. Therefore, it can be also regarded as the Chinse NGGM. For NGGM, the most promising NGGM is the Bender-type mission, which consists of a polar satellite pair and an inclined satellite pair. Due to the extra observations at the east-west direction derived from the inclined satellite pair, there are significant improvements in detecting temporal signals with higher accuracy and spatial-temporal resolution.

Based on the Bender-type NGGM concept, researchers have systematically analyzed the key mission design parameters and foreseen the extended application scopes in geosciences.In the context of Bender-type NGGM, the payload requirement is limited to approximately 20 nm/Hz$^{1/2}$ at the measurement bandwidth (MBW) of 0.01 ~ 1 Hz for laser ranging instrument (LRI), and 10^{-11} m/s^2 at 0.001 ~ 0.1 Hz for accelerometer (ACC). Low frequency noise is also respectively limited to $1/f$ and $1/f^{\,2}$ for LRI and ACCs due to unavoidable electronic noise. However, due to the complex payload manufacture procedures and volatile space observation environment, in reality LRI or ACCs noise may not be rigorously consistent with the designed noise models in frequency domain. Frequency dependent noise in *in-situ* observations always results in different MBW boundaries or different low frequency features. Therefore, Zhou et al. (2023) assesses the impacts of frequency dependent instrument noise for NGGM on determining temporal gravity field model. The results indicates that in the instrument noise only scenarios, a similar behavior is shown between the frequency spectrum of instrument's frequency dependent noise in terms of amplitude spectral density and the corresponding gravity solution in terms of geoid height error, while the frequency dependent instrument noise plays less role when the background force model errors are included. In the full noise contaminated scenarios, to achieve the scientific goal of Bender-type NGGM, it is feasible to shift the low MBW boundary from 0.001 Hz to 0.004 Hz for ACC, and from 0.01 Hz to 0.1 Hz for LRI (Figure 5 and Figure 6). The results are helpful to specify the requirement of manufacturing key payloads for the Bender-type NGGM.

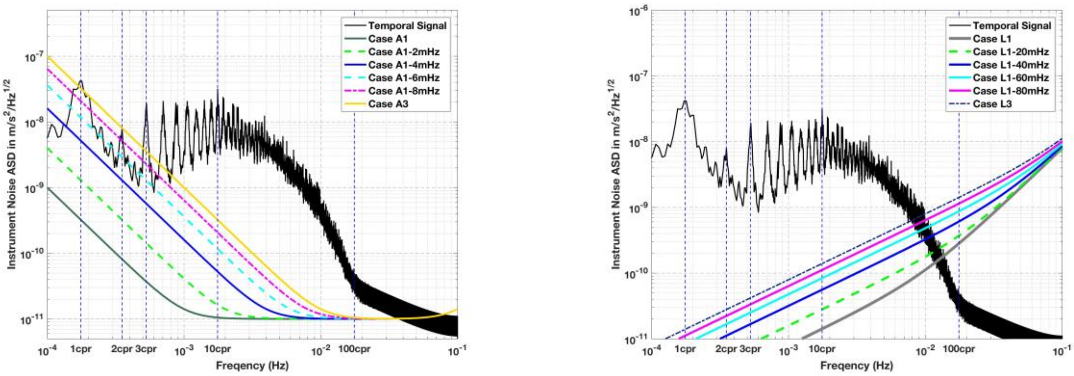

Figure 5. Ampliltude speatral densties of accelerometer (left) and laser ranging interformeter (right) noise model considering different measurement bandwidths in terms of accelerations.

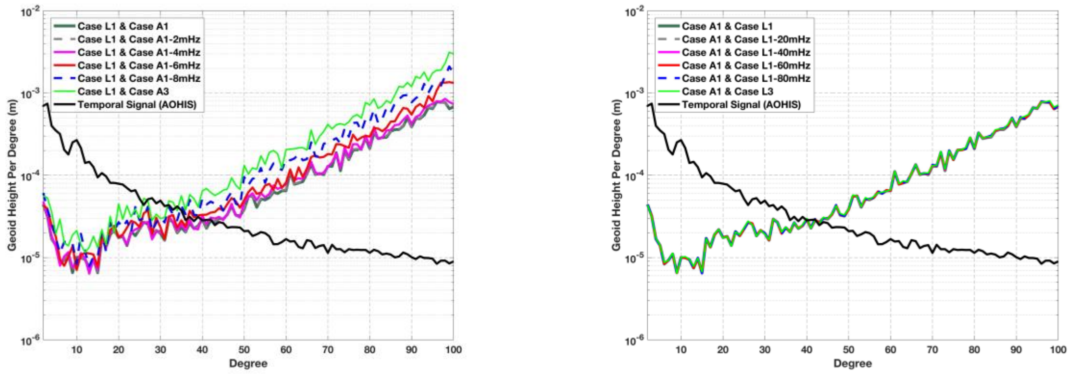

Figure 6. Geoid height errors per degree of gravity field solutions derived from the instrument noise model combinations considering different accelerometer (left) and laser ranging interformeter measurement bandwidths (right). Here non-tidal atmosphere and ocean aliasing error is fully considered, and the wiese-apporach is applied to reduce the temporal aliasing error.

The prerequisite of implementing the Bender-type mission is to ensure the combination as well as the independency of the missions in the polar satellite formation (PSF) scenario as well as in the inclined satellite formation (ISF) scenario. To promote NGGM, Zhou et al. (2023a) implement a close-loop simulation study to evaluate the performance of the stand-alone ISF mission. In spectral domain, the ISF estimations show extremely poor quality for zonal and near-zonal coefficients due to the absence of observations over the polar regions, while the sectorial and near-sectorial coefficient estimations show approximately 71~77% noise reductions when compared with the PSF estimations. In spatial domain, the ISF mission presents its superior capability in detecting the Earth's mass variations within its observational areas than the PSF mission. The improvements of ISF are also obtained over the transition zones (50°N ~ 70°N and 50°S ~ 70°S) with 41% noise reductions. The simulation results demonstrate the feasibility of implementing a stand-alone mission in the inclined orbits, and the further possibility of promoting a Bender-type mission via a profound cooperation by two institutions.

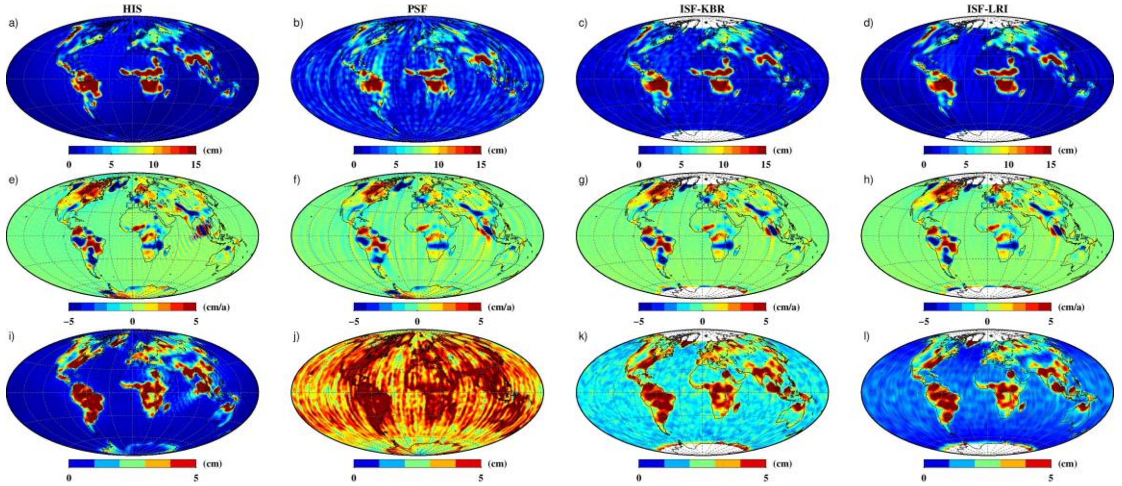

Figure 7. Annual amplitude (top), yearly trend (middle) and RMS residuals (bottom) derived from ESM HIS model (column 1), polar satellite formation(PSF, column 2), inclined satellite formation with K-band ranging system (ISF-KBR, column 3) and inclined satellite formation with laser ranging interferometer (ISF-LRI, column 4).

To proposal Chinese Bender-type NGGM, we also need to figure out the possibility of improve gravity field estimations via polar satellite formation. For the polar satellite formation, the errors in atmospheric and oceanic de-aliasing (AOD) model are still the key limitation especially taking advantages of improved laser ranging interferometer (LRI). Zhou et al. (2023b) explores the realistic assumption of continuously reducing AOD model error in global scale and regional scale (e.g., ocean, Greenland, Qinghai-Tibet plateau and South America) in the anticipated future. For this, using a realistic orbit scenario and error assumptions both for instrument and background model errors, the 5-year full-scale simulations are implemented in the context of 26 scenarios with different AOD model errors. The results demonstrate that when the AOD model errors are reduced in the global scale, the corresponding gain in temporal gravity field determination is significant, with 26.3-65.2% noise reduction in terms of mean RMS residuals over ocean in spatial domain (Figure 8). However, when the AOD model errors are reduced in the regional scale, the most notable noise reduction, with 22.9-43.9% noise reduction in spatial domain, is observed when the AOD model error decreases in ocean. The limited noise reductions (0.1% and 1.3% respectively in spectral and spatial domain) are observed in the temporal gravity field estimations if the AOD model is refined in other typical regions such as the Qinghai-Tibet plateau, the Greenland and the South America. Meanwhile, when the satellites passing over the AOD model refined regions, the along-orbit range rate analysis indicates that, there are visible differences by about 50.0 nm/s in terms of range rate residuals as well as 11.0-48.5 nm/s in terms of the mean RMS of range rate residuals. These results reflect the beneficial of reducing AOD model error in both global and regional scale for improving GRACE-type temporal gravity estimation, especially considering the development of LRI technology.

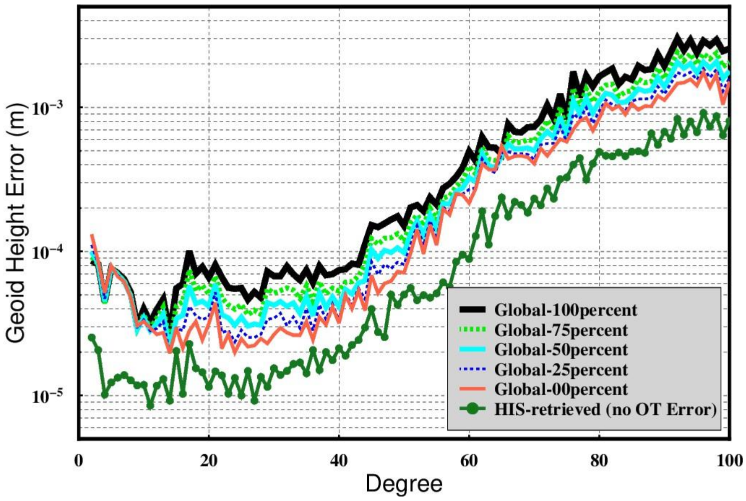

Figure 8. Geoid height error per degree of temporal gravity field models derived from different simulation scenarios where the different noise levels of global AOD models are considered.

In addition, to ensure the global observability of next generation gravimetric mission (NGGM), different agencies have to repeatedly launch satellites to about 89.0° orbit inclination. However, due to the poor isotropy of observation system, only minor improvement in terms of temporal gravity field estimation can be obtained via these repeatedly launched polar pair missions. To ensure the global observability as well as the isotropy of observation system, a near-polar pair mission rather than a polar mission is likely an optimal selection, especially considering that the Gravity Recovery and Climate Experiment (GRACE) Follow-On mission has been already in operation. Therefore, for the Chinese NGGM, Zhou et al. (2023c) design a closed-loop simulation to assess the performance of a near-polar mission at a near-circular orbit with about 500 km altitude for detecting the Earth's temporal gravity field. Based on the statistic results, 85.0° is selected as the optimal orbit inclination for the near-polar mission, which provides 37% noise reduction in terms of cumulative geoid height error in spectral domain, but also 31% noise reduction in terms of mean oceanic root-mean-square (RMS) error in spatial domain when compared to the 89.0° polar mission (89-PM). Although there are inevitable 5.0° polar gaps in the 85-NPM, the analysis result still demonstrates a comparable performance of the 85-NPM in tracking mass variations over the Antarctic, and even an outperformance with 12% noise reduction over the Greenland when compared to the 89-PM. The result confirms the feasibility of implementing a near-polar mission as a stand-alone mission or a complementary observation system for the repeatedly launched polar missions, which offers an alternative option of launching the Chinese NGGM satellites to an 85.0° inclination orbit instead of 89.0°.

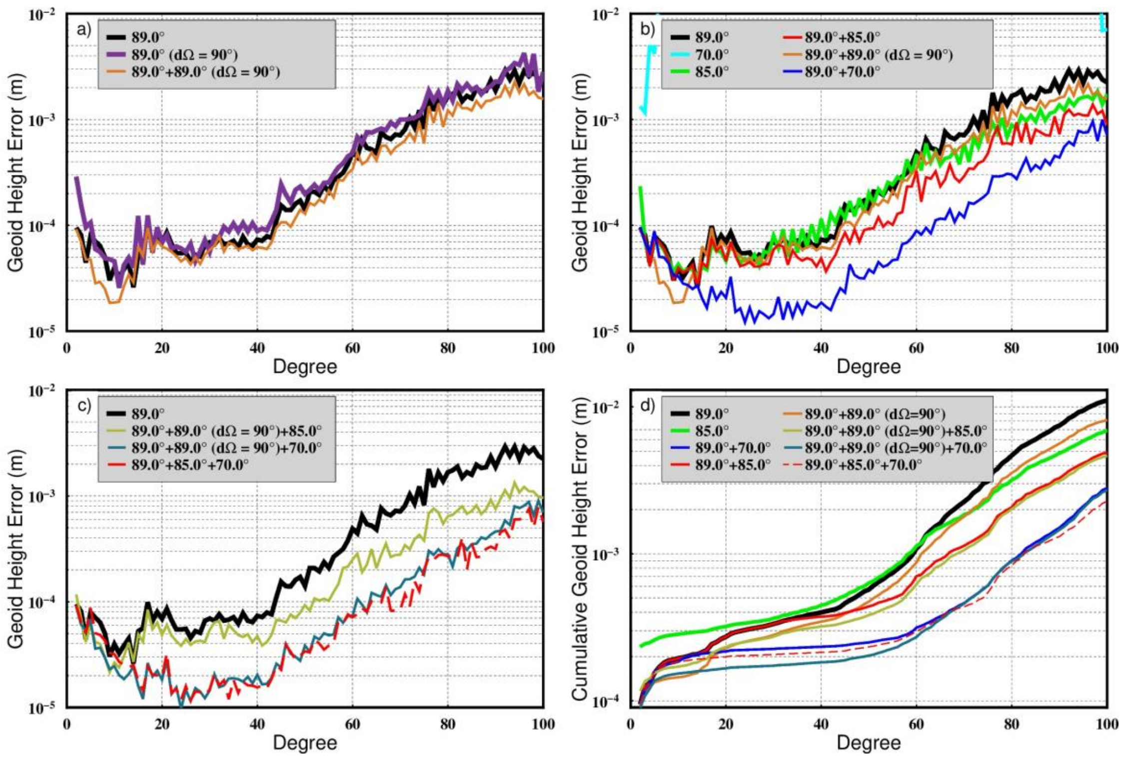

Figure 9. Geoid height error per degree (left) and cumulative geoid height error (right) from the simulation scenarios with different inclination combinations.

Based on the developed satellites and key payloads, the TQ group can provide an ultra-clean and stable environment for gravitational wave detection as well as Earth's gravity field determination. The new research results for satellite formations, key payloads and background foce models also confirm the promising improvements of detecting high accuracy and high resolution Earth's gravity field via Chinese NGGM.

3 L1 level Construction of Satellite Gravity Gradiometry Observations

The L1 level construction method of high-precision satellite gravity gradiometry observations is an important basic data processing technology for promoting the national gravity satellite mission. Base on the GOCE satellite pre-processing technology and raw data, the L1 level construction method of satellite gravity gradiometry observation is studied and initially implemented in this work, which aim for the needs of the national gravity gradiometry satellite mission. The main steps include the conversion of the accelerometer voltage data, the reconstruction of the angular rate based on the combination of the star sensors, and the construction of the gravity gradient of the satellite. The results indicate that the accuracy of the accelerometer ultra-sensitive axis is 10^{-10}-10^{-11} m/s^2/Hz$^{1/2}$, which achieve the designed accuracy requirements of the gradiometer. The optimal determination of the angular rate w_y、 w_z is improved by about 1 order of magnitude in the range of 10-100mHz at about 10^{-6} rad/s/Hz$^{1/2}$, which is effective in suppressing noise propagation caused by low precision angular velocity components in coordinate systems conversions. The square root power spectrum of the angular rate reconstruction based on the Wiener filtering method in the 5-100 mHz band is enhanced by 5.21-6.56×10^{-11} rad/s/$Hz^{1/2}$, which indicates the necessity of solving the gravity gradient based on high accuracy angular rate. Lastly, the calculated values for each component of the gravity gradient are of comparable accuracy to the official GOCE gravity gradient components. The trace of the gradient tensor is about 10 mE/$Hz^{1/2}$ in the frequency range of 20-100 mHz, which validates our method. This work provides the technical support and reserve of independent raw data processing for promoting the national civil gravity gradiometry satellite mission.

频率/Hz

Figure 10. The difference of x axis common mode acceleration PSD1/2

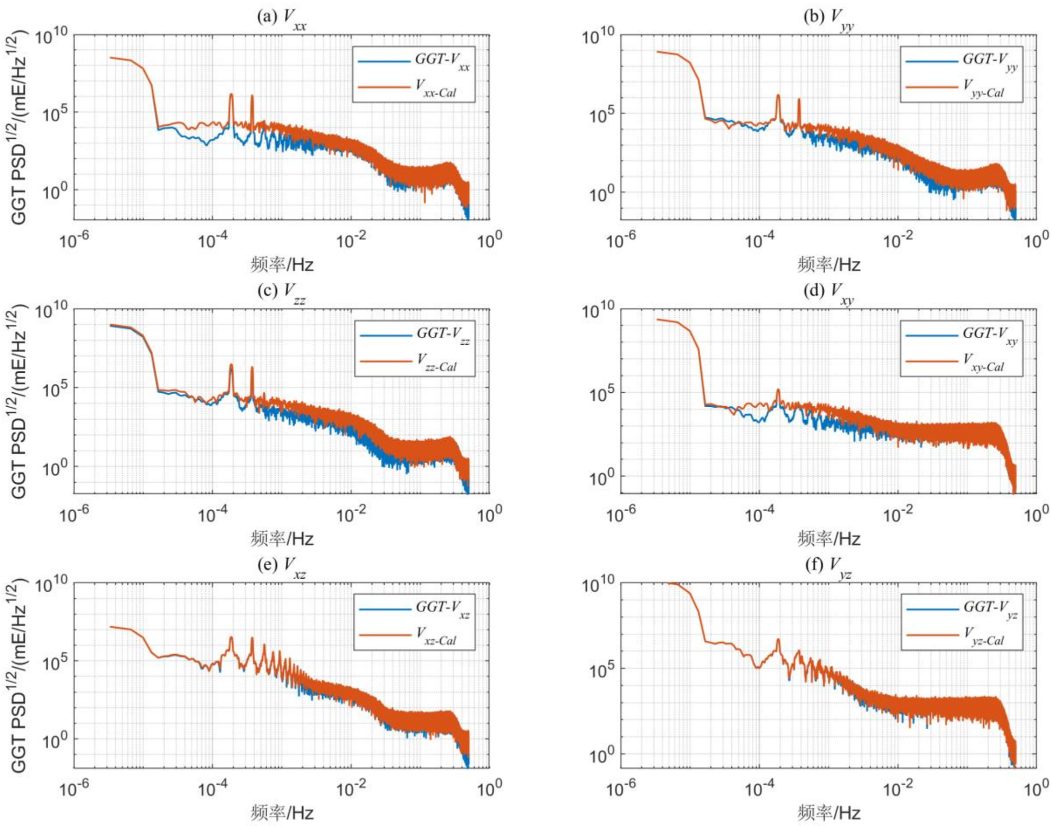

Figure 11. PSD1/2 of calculated gradient trace and L1b_GGT trace

4 The Data Processing Results of Chinese Gravimetry Satellite

Chinese first pair of gravimetry satellite has been in-orbit calibrated and verified completely. In-orbit test results show that the working state of the platform and payloads are normal and all indicators meet the design requirements. The achieved accuracy of the satellite orbits is better than 2 cm determined by combined BeiDou and GPS data. The stellar sensor accuracy 3'' is tested by analysis residuals of angle between star sensor boresights.

The inter-satellite ranging system works in the dual-one way ranging configuration. Its performance is stable. The spectrum of range, range rate and range acceleration are showed in figure 12. noise The Range and range rate noise being lessen than 3μm/√Hz and 1μm/s√Hz respectively in the frequency band of 0.025-0.1Hz. The electrostatic suspension accelerometer is working well. The accelerometer is highly sensitive to the residual thrust of the attitude control thruster, switching of the magnetic torque and other small vibrations. The spectrum analysis shows its high-sensitive axis noise level is being 3×10^{-10}m/s2/√Hz near the frequency 0.1Hz, and being 1×10^{-9}m/s2/√Hz for the less-sensitive axis (Figure 13).

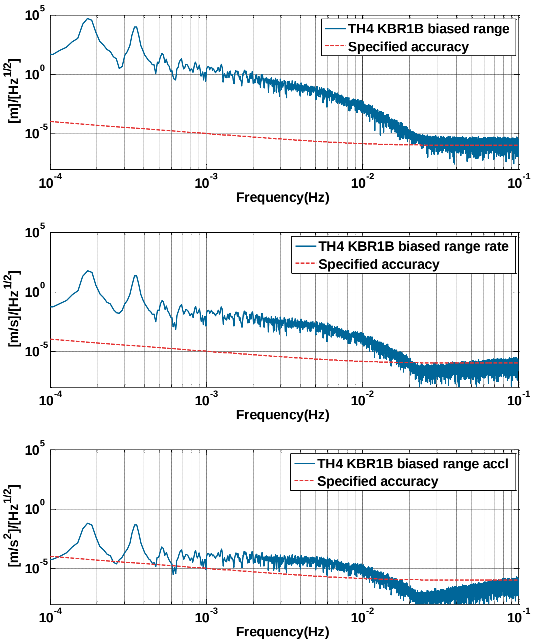

Figure 12. The spectrum of KBR biased range, range rate and range acceleration in the dual-one way ranging

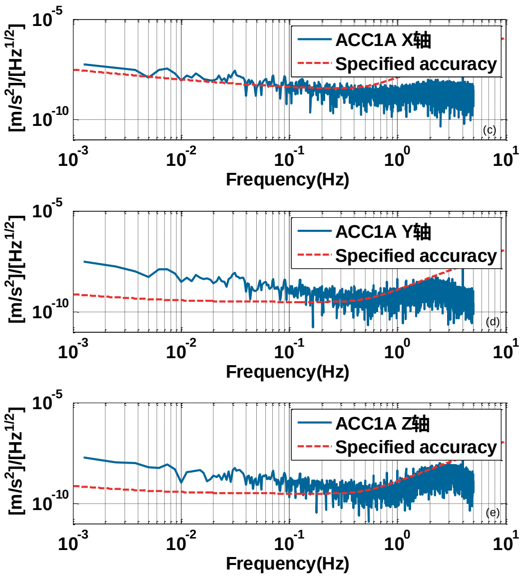

Figure 13. The accelerometer high-sensitive axis noise level being 3×10^{-10}m/s2/√Hz near the frequency 0.1Hz, and being 1×10^{-9}m/s2/√Hz for the less-sensitive axis

Bibliography

Chen Q J, Shen Y Z, Francis O, et al. Tongji-Grace02s and Tongji-Grace02k: High-Precision Static GRACE-Only Global Earth's Gravity Field Models Derived by Refined Data Processing Strategies. J Geophys Res Solid Earth, 2018, 123(7):6111-6137

Chen Q J, Shen Y Z, Zhang X F, et al. (2016).GRACE Data-based High Accuracy Global Static Earth’s Gravity Field (in

Chinese). Acta Geodaetica et Cartographica Sinica, 45（4）: 396-403

Ditmar P, Teixeira D E, Farahani H H. (2012). Understanding data noise in gravity field recovery on the basis of inter-satellite ranging measurements acquired by the satellite gravimetry mission GRACE. J Geod. 86(6): 441-465

Feng W. (2013).Satellite gravity monitoring of regional land water and sea level changes (In Chinese). Doctor Dissertation. Beijing：University of Chinese Academy of Sciences

Förste C, Bruinsma S L, Abrikosov O, et al. (2014).EIGEN-6C4-The latest combined global gravity field model including GOCE data up to degree and order 2190 of GFZ Potsdam and GRGS Toulouse. EGU General Assembly, held 27 April - 2 May, 2014 in Vienna, Austria, id.3707

Gong, Y., Luo, J., Wang, B. (2021). Concepts and status of Chinese space gravitational wave detection projects. Nature Astronomy, 5, 881.

Guo X, Ditmar P, Zhao Q L, Xiao Y. (2020).Improved recovery of temporal variations of the Earth's gravity field from satellite kenematic orbits using an epoch-difference scheme. Journal of Geodesy,94(8):94-69

GUO Zehua, WU Yunlong, XIAO Yun, HU Minzhang(2021) Reconstruction Method of Satellite Gravity Gradient Measurement Angular Velocity by Combining Star Tracker Quaternion. Geomatics and Information Science of Wuhan University, 46(9): 1336-1344

Hsu H Z, Lu Y, Zhong M, et al.(2012). Satellite gravity and its application to monitoring geophysical environmental change (in Chinese). Sci Sin Terrae, 42: 843-853

Kang Z, Bettadpur S, Nagel P, et al. (2020). GRACE-FL precise orbit determination and gravity recovery. Journal of Geodesy, 2020, 94(9): 1-17

Kvas A, Brockmann J M, Krauss S, et al. GOCO06s–a satellite-only global gravity field model. Earth System Science Data, 2021, 13(1): 99-118

Li J C, Fan C B, Chu Y X, et al. (2008).Using ICESAT Altimeter Data to Determine the Antarctic Ice Sheet Elevation Model (in Chinese). Geomatics and Information Science of Wuhan University,2008(03):226-228,248

Liang W, Xu X Y, Li J C, et al. (2018).The Determination of an Ultra-high Gravity Field Model SGG-UGM-1 by Combining EGM2008 Gravity Anomaly and GOCE observation Data (in Chinese). Acta Geodaetica et Cartographica Sinica, 47（4）: 425-434

Luo Z C, Li Q，Zhong B. (2012). Water Storage Variations in Heihe River Basin Recovered from GRACE Temporal Gravity Field (in Chinese). Acta Geodaetica et Cartographica Sinica, 41（5）: 676-681

Luo, J., Bai, Y., Cai, L., Cao, B., Chen, W., Chen, Y., et al. (2020). The first round result from the TianQin-1 satellite. Classical and Quantum Gravity, 37, 185013.

Mei, J., Bai, Y., Bao, J., Barausse, E., Cai, L., Canuto, E., Cao, B., et al. (2021). The TianQin project: Current progress on science and technology. Prog. Theor. Exp. Phys., 5, 05A107.

Nie Y F, Shen Y Z, Chen Q J, et al. (2022).Hybrid-precision arithmetic for numerical orbit integration towards future satellite gravimetry missions. Advance in Space Research，66(2020):671-688

Nie Y F, Shen Y Z, Roland P, et al. (2022).Revisiting Force Model Error Modeling in GRACE Gravity Field Recovery. Surveys in Geophysics，doi.org/10.1007/s10712-022-09701-8.

Ning J S, Wang Z T, Chao N F. (2016).Research status and progress of international new generation satellite gravity exploration program (in Chinese)，Geomatics and Information Science of Wuhan University,41(1):1-8

Ning J S. (2001).Following the Developments of the World, Devoting to the Study on the Earth Gravity Field (in Chinese).

Geomatics and Information Science of Wuhan University, 26(6): 471-474,486

Pang Z X, Ji J F, Xiao Y, et al. (2012).Estimation of the Resolution of Earth’s Gravity Field for GRACE Follow-On Using the Spectrum Method (in Chinese). Acta Geodaetica et Cartographica Sinica, 41（3）: 333-338

QU QingLiang, CHANG XiaoTao, ZHU GuangBin, YU ShengWen, ZHOU Miao, LIU Wei (2021) Calibration of satellite gravity gradients based on ground gravity data. Chinese Journal of Geophysics (in Chinese), 64(8): 2590-2598

Ran J J, Xu H Z, Shen Y Z, et al. (2012). Expected Accuracy of the Global Gravity Field for Next GRACE Satellite Gravity Mission (in Chinese). Chinese Journal of Geophysics，55（9）:2898-2908

Shen Y Z. (2017). Algorithm Characteristics of Dynamic Approach-based Satellite Gravimetry and its Improvement Proposals (in Chinese). Acta Geodaetica et Cartographica Sinica, 46（10）: 1308-1315

Siemes C. 2018. GOCE Level 1b gravity gradient processing algorithms. Technical Report ESA-EOPSM-GOCE-TN-3397, Paris, France: European Space Agency.

Stummer C, Siemes C, Pail R, et al. 2012. Upgrade of the GOCE Level 1b gradiometer processor. Advances in Space Research, 49(4): 739-752

Sun, H., Cui, X., Xu, J., Ding, H., Zhang, M., Li, H., Wang, Z., Zhou, J., Chen, X. (2022). Progress of Research on the Earth’s Gravity Tides and its Application in Geodynamics in China. Pure and Applied Geophysics, 1-17.

Sun, H., Li, Q., Bao, L., Wu, Z., Wu, L. (2022). Advancements and trends in high-resolution modeling of global seafloor topography. Journal of Wuhan University: Information Science Edition, 47(10): 1555-1567.

Tapley B D, Bettadpur S, Ries J C, et al. (2004).GRACE measurements of mass variability in the Earth system. science, 305(5683): 503-505

Wang C Q, Xu H Z, Zhong M, et al. (2015).An Investigation On GRACE Temporal Gravity Field Recovery Using the Dynamic Approach (in Chinese). Chinese Journal of Geophysics, 58（3）:756-766

WU YunLong, GUO ZeHua, XIAO Yun, MA Lin (2021) L1 level construction method of satellite gravity gradiometry observations. Chinese Journal of Geophysics (in Chinese), 64(12): 4437-4448

Xiao Y, Xia Z R, Wang X T. (2006).Error Analyses for Recovery of the Earth’s Gravity Field by HL-SST Technique (in Chinese). Acta Geodaetica et Cartographica Sinica, 35（2）:106-111

Xiao Y, Yang Y X, Pan Z P, Liu X G, Sun Z M. (2023). Performance and Application of the Chinese Satellite-to-Satellite Tracking Gravimetry System. Chinsese Scinece Bulletin. Doi/10.1360/TB-2022-1057

Xu H Z, Shen Y Z. (2001). Simulation of recovering the gravitational potential model from ephemerides of CHAMP (in Chinese). Geomatics and Information Science of Wuhan University, 26(6):483-486

Xu T H, Yang Y X. Recovering the Gravity Potential Model from the Ephemerides and Accelerometer of CHAMP (in Chinese). (2004). Acta Geodaetica et Cartographica Sinica, 33（2）:95-99

Yang Y, Wang J, Lou L, et al. (2022). Development status and prospect of satellite-based surveying (in Chinese). Space: Science and Technology, 2022, dio:10.16708/j.cnki.1000-758X.2022.0031

Zhou, H., Luo, Z., Zhou, Z., Yang, F., Pail, R., Tu, L., Yeh, H-C., Yang, S. (2021). What Can We Expect from the Inclined Satellite Formation for Temporal Gravity Field Determination? Surveys in Geophysics, 42, 699-726.

Zhou, H., Tang, L., Tan, D., Duan, H., Pail, R., Luo, Z., Zhou, Z. (2023a). Impacts of frequency-dependent instrument noise for next-generation gravimetric mission on determining temporal gravity field model. Journal of Geodesy, 97(23), 1-25.

Zhou, H., Wang, P., Pail, R., Guo, X., Wu, Y., Luo, Z. (2023c). Assessment of a near-polar pair mission for detecting the Earth’s temporal gravity field. Geophysical Journal International, 234, 852-869.

Zhou, H., Zheng, L., Pail, R., Liu, S., Qing T., Yang, F., Guo, X., & Luo, Z. (2023b). The impacts of reducing atmospheric and oceanic de-aliasing model error on temporal gravity field model determination. Geophysical Journal International, 234, 210-227.

Progress in Earth Gravity Model and Vertical Datum

Tao Jiang[1], Yonghai Chu[2], Xinyu Xu[2], Taoyong Jin[2,15], Zhongmiao Sun[3], Qiujie Chen[4], Jinyun Guo[5], Xiaoyun Wan[6], Yihao Wu[7], Yanguang Fu[8], Lin He[9], Xinwei Guo[10], Yong Su[11], Wei Liang[2], Yongjun Jia[12], Fukai Peng[13], Lianjun Yang[2]

[1] *Chinese Academy of Surveying and Mapping, Beijing, China*

[2] *School of Geodesy and Geomatics, Wuhan University, Wuhan, China*

[3] *Xi'an Research Institute of Surveying and Mapping, Xi'an, China*

[4] *Tongji University, Shanghai, China*

[5] *College of Geodesy and Geomatics, Shandong University of Science and Technology, Qingdao, China*

[6] *School of Land Science and Technology, China University of Geosciences, Beijing, China*

[7] *School of Earth Sciences and Engineering, Hohai University, Nanjing, China*

[8] *First Institute of Oceanography, Ministry of Natural Resources, Qingdao, China*

[9] *School of Resource Environmental Science and Engineering, Hubei University of Science and Technology, Xianning, China.*

[10] *Geodetic Data Processing Center of Ministry of Natural Resources, Xi'an, China*

[11] *Southwest Petroleum University, Chengdu, China*

[12] *National Satellite Ocean Application Service, Beijing, China*

[13] *College of Surveying and Geo-informatics, Tongji University, Shanghai, China*

[14] *School of Geodesy and Geomatics, Hubei Luojia Laboratory, Wuhan University, Wuhan, China*

1 Realization of the International Height Reference System in the region of Mount Qomolangma

For the first time, the orthometric height of Mount Qomolangma based on the International Height Reference System (IHRS) is determined and released in the 2020 height measurement campaign of Mount Qomolangma. In order to realize the IHRS in the region of Mount Qomolangma, the scheme of establishing high precision gravimetric geoid model in this area is adopted. Based on the spectral combination approach and data-driven spectral determination method, the gravimetric quasigeoid model in the area of Mount Qomolangma is computed from the combination of airborne and terrestrial gravity data. Optimal reference gravity model, its truncation degree and spherical cap integration radius are chosen through comprehensive test. The validation against highly accurate GNSS leveling measured height anomalies at 61 benchmarks indicates that the accuracy of the gravimetric quasigeoid model reaches 3.8 cm and the addition of airborne gravity data improves the model accuracy by 51.3 %. The interpolation method considering height difference correction is proposed for interpolating the height anomaly at the summit from the quasigeoid model. The rigorous formula for geoid–quasigeoid separation considering topographic masses is used for converting the height anomaly to the geoid undulation at the summit. Based on the IHRS defined gravity potential value W_0 and the GRS80 reference ellipsoid, and using the newly observed ground gravity at the summit, the high precision geoid undulation of Mount Qomolangma in the IHRS is determined.

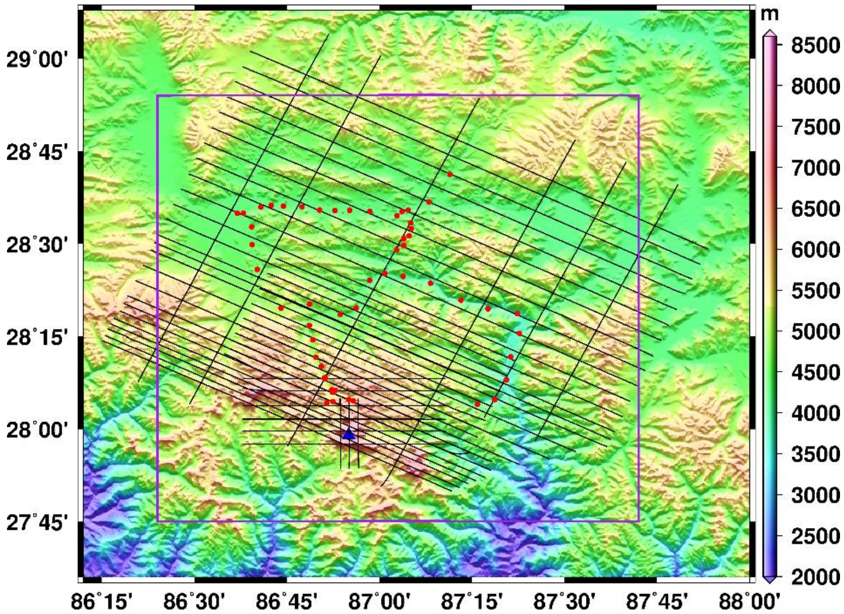

Figure 1. Airborne gravity survey lines and GNSS leveling points in the region of Mount Qomolangma (Blue triangle: Mount Qomolangma; Black Line: airborne gravity survey lines; Red point: GNSS leveling points; Purple rectangle: domain of quasigeoid model)

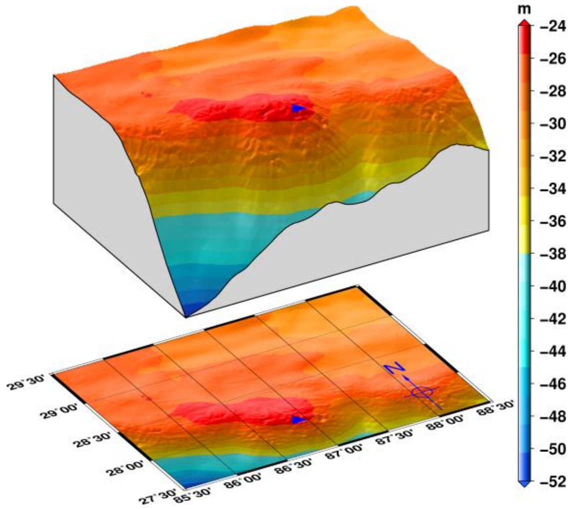

Figure 2. Gravimetric quasigeoid model computed from the combination of airborne and terrestrial gravity data (Blue triangle: Mount Qomolangma)

Table 1. Statistics of the differences between gravimetric geoid and GNSS leveling measured height anomalies (m)

Computation scheme	Min	Max	Mean	Std
Scheme 1 (Airborne + Ground)	0.148	0.333	0.270	0.038
Scheme 2 (Ground)	-0.129	0.270	0.169	0.078
Scheme 3 (Airborne + Ground)	0.166	0.371	0.314	0.048

2 The datum offset between the China's 1985 national vertical datum and global vertical datum

China's national height datum 1985, also known as China's national vertical datum 1985(Abbreviated as CNVD1985) was determined in 1985 based on the tidal observation data of Qingdao gauge recording from 1952 to 1979. In order to eliminate the impact of the 18.6-year tidal long period, the data are divided into 10 groups, each with a data duration of 19 years. The moving average method with a sliding step of 1 year, is used to derive 10 groups of mean sea level (MSL), and then the average is taken as the mean sea level in the Yellow Sea, which is the zero-height level surface of CNVD1985. Although the MSL at the Qingdao tide gauge shows a sea level rising at the rate of 1.07 mm/yr from 1952 to 1980 and increased to 1.62 mm/yr from 1980 to 2011(Wu et al.,2020), the height datum is usually regarded as a stable and constant reference for measuring height. From the point of view of gravity field and height datum, local MSL is a local tidal datum that is not consistent with global geoid.

As one of the equipotential surfaces of the Earth's gravity field, the geoid is an equipotential surface defined by a potential (W_0) that fits best the undisturbed mean sea level in a least squares sense (Amin et al.,2019). It is the classical Gauss–Listing definition of geoid and is usually selected as the global vertical datum (GVD). In the past few decades, satellite technology has opened a new era of earth exploration from the space. The satellite altimetry and satellite gravimetry provide a new space technology that can directly measure the internal structure and the surface of the Earth. Several global mean sea surface(MSS) height models with a resolution of $1'\times1'$ or $2'\times2'$, such as DTU15MSS, DTU18MSS, have been released due to the development of satellite altimetry technology and the accumulation of data. Satellite gravity has greatly improved the medium and long wavelength accuracy of the Earth's gravity field information(Jiang et al.,2020). High-resolution global gravity model (GGM), such as SGG-UGM-2(Liang et al.,2020), can be combined with MSS to quantify the potential (W_0).

The vertical datum offset can be defined as a geometric quantity (distance difference ΔH) or as a physical parameter (gravity potential difference ΔW), their relationship is expressed as $\Delta H = -\Delta W/\gamma$. Where, the gravity potential difference ΔW is the potential (W_0^L) of local vertical datum (CNVD1985) minus the potential (W_0) of GVD, i.e. $\Delta W = W_0^L - W_0$, γ is the normal gravity of Qingdao gauge station. So, the key problem of derive datum offset comes down to computing the W_0^L and W_0.

For the computation and analysis of the vertical datum offset, the following general parameters and model were adopted:

1.The geodetic reference system: GRS80, WGS84 and CGCS2000(Table 2).

2.Mean sea surface: DTU15MSS. During the computation, the geodetic height of DTU15MSS must be transformed from T/P ellipsoid to GRS80, WGS84 and CGCS2000 ellipsoid. Only 33951 grid points with a bathymetry greater than 2000m are kept considering to reduce the impact of tide offshore.

3.Global gravity model: EGM2008(Pavlis et al.,2012), EIGEN-6C4(Förste et al.,2014) and SGG-UGM-1(Liang et al.,2018).

Table 2. Basic parameters of the geodetic reference system

Geodetic reference system	Equatorial radius a (m)	Reciprocal flattening 1/f	geocentric gravitational constant GM (m^3s^{-2})	Angular velocity ω(rad/s)	Normal gravity potential U_0 (m^2s^{-2})
GRS80	6378137	298.257222101	3.986005000×10^{14}	7.292115×10^{-5}	62636860.8500
WGS84	6378137	298.257223563	3.986004418×10^{14}	7.292115×10^{-5}	62636851.7146
CGCS2000	6378137	298.257222101	3.986004418×10^{14}	7.292115×10^{-5}	62636851.7149

Firstly, if the GPS/Leveling data of point P is available, the gravity potential W_0^L is computed by(Li et al.,2017): $W_0^L = W^P + H^*\bar{\gamma}$. Where, H^* is normal height of point P reference to CNVD1985 zero-height point, $\bar{\gamma}$ is mean normal gravity along the normal gravity line passing point P. And the W^P is gravity potential of point P, which can be computed by spherical harmonic synthesis. The gravity potential (W_0^L) of CNVD1985 zero-height point is computed based on 152 GPS/leveling measurements around Qingdao (Figure 3). We did not use nationwide GPS/leveling data for calculation as we did in other study(He & Chu & Xu & Zhang,2019), which was mainly due to the fact that the error would be larger if the distance between leveling points was too far away, while the error of leveling data around Qingdao would be small. Therefore, the precision of the local vertical datum potential calculated by using the level data around the reference point will be better.

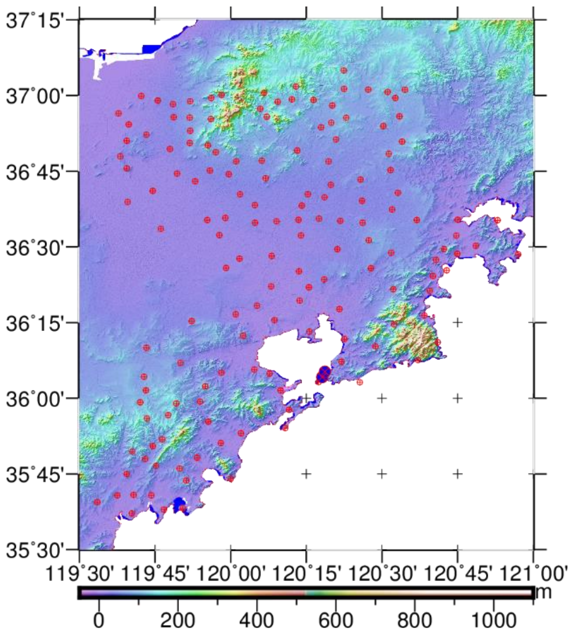

Figure 3. The distribution of GPS/leveling measurements around Qingdao

Then, a potential (W_0) must be chose or computed for GVD. In the general formula of physical geodesy, it is usually specified that $W_0 = U_0$. This could make the formula or function simple and easy. A good method for the potential (W_0) is computed it using MSS and GGM according to the definition of Gauss-Listing geoid, i.e. $W_0 = W_{MSS}$. For every grid point of DTU15MSS, the gravity potential W_{MSS}^i is computed by spherical harmonic synthesis and the final average is $W_{MSS} = \frac{1}{N}\sum_{i=1}^{N} W_{MSS}^{i}$. If the same GGM is used to compute the average of W_{MSS} for different geodetic reference system, the value from CGCS2000 and WGS84 are almost equal(Table 3) due to the parameters of these two reference systems are almost the same (Table 2). If keeping the same geodetic reference system, the value from EGM2008 and EIGEN-6C4 are almost equal, but the value from SGG-UGM-1 shows a slightly different. In any case, the numerical results calculated by the three GGMs are of comparable accuracy.

Two equipotential surfaces defined by U_0 or W_{MSS} are selected as the GVD, the gravity potential difference between CNVD1985 and GVD can be expressed as $\Delta W_1 = U_0 - W_0^L$ and $\Delta W_2 = W_{MSS} - W_0^L$. The corresponding geometric distance difference is obtained as $\Delta H_1 = \Delta W_1/\gamma$ and $\Delta H_2 = \Delta W_2/\gamma$. We calculated the gravitational potential difference and datum offset, which are all listed in Table 3.

From the numerical results, we can find that the CNVD1985 is about 24.2cm (SGG-UGM-1, CGCS2000) below the GVD defined by U_0, but about 19.6cm above the GVD defined by Gauss-Listing geoid. There is a difference of about 1~3cm between the numerical results when using EGM2008, EIGEN-6C4, and SGG-UGM-1 models to calculate. The choice of geodetic reference system has almost no impact on the calculation results, which is obvious. Because the actual vertical datum definition is independent of the geodetic reference system. Although the equipotential surfaces defined by U_0 has important theoretical significance, but it is inconsistent with the global mean sea level. So, Gauss-Listing geoid is the best choice for GVD.

Table 3. The gravity potential difference and vertical datum offset between Qingdao tide gauge and global datum defined by U_0 or W_{MSS}

GGM	**Geodetic reference system**	W_0^L **(m²s⁻²)**	U_0 **(m²s⁻²)**	W_{MSS} **(m²s⁻²)**	ΔW_1 **(m²s⁻²)**	ΔH_1 **(m)**	ΔW_2 **(m²s⁻²)**	ΔH_2 **(m)**
EGM2008	GRS80	62636862.9503	62636860.8500	62636865.1762	2.1003	-0.2144	-2.2259	0.2272
	WGS84	62636853.8143	62636851.7146	62636856.0389	2.0997	-0.2143	-2.2246	0.2270
	CGCS2000	62636853.8147	62636851.7149	62636856.0389	2.0998	-0.2143	-2.2242	0.2270
EIGEN-6C4	GRS80	62636863.1150	62636860.8500	62636865.1768	2.2650	-0.2312	-2.0618	0.2104
	WGS84	62636853.9790	62636851.7146	62636856.0396	2.2644	-0.2311	-2.0606	0.2103
	CGCS2000	62636853.9793	62636851.7149	62636856.0396	2.2647	-0.2311	-2.0603	0.2103
SGG-UGM-1	GRS80	62636863.2201	62636860.8500	62636865.1393	2.3701	-0.2419	-1.9192	0.1959
	WGS84	62636854.0841	62636851.7146	62636856.0021	2.3695	-0.2418	-1.9180	0.1957
	CGCS2000	62636854.0845	62636851.7149	62636856.0021	2.3696	-0.2418	-1.9176	0.1957

3 Geoid modeling from the combination of satellite gravity model, terrestrial and airborne gravity data

In 2017, The Joint Working Group (JWG) 0.1.2 (Strategy for the Realization of the International Height Reference System (IHRS)) and JWG 2.2.2 (the 1 cm geoid experiment) of the International Association of Geodesy (IAG) jointly launched the Colorado geoid experiment. The goal of this experiment is to assess the repeatability of gravity potential values as IHRS coordinates using different geoid modeling methods, and to compare and evaluate the corresponding gravimetric geoid models. In this frame, the National Geodetic Survey (NGS) of the United States of America (USA) provided the geodesy community with terrestrial, airborne gravity and GPS (global positioning system) leveling data as well as digital elevation model (DEM) for a mountainous area of about 400 thousand km^2 in Colorado, which allowed the comparison of different methods and softwares for geoid computation using the same input dataset in this challenging area.

We used the spectral combination method for geoid determination in Colorado as our contribution to the geoid experiment. The gravimetric geoid model obtained from the combination of satellite gravity model GOCO06S and terrestrial gravity data agrees with the GPS leveling measured geoid heights at 194 benchmarks in 5.8 cm in terms of the standard deviation of discrepancies, and the standard deviation reduces to 5.3 cm after including the GRAV-D airborne gravity data collected at ~6.2 km altitude into the data combination. The contributions of airborne gravity data to the signal and accuracy improvements of the geoid models were quantified for different spatial distribution and density of terrestrial gravity data. The results demonstrate that, although the airborne gravity survey was flown at a high altitude, the additions of airborne gravity data improved the accuracies of geoid models by 13.4% - 19.8% in the mountainous area (elevations > 2000 m) and 12.7% - 21% (elevations < 2000 m) in the moderate area in the cases of terrestrial gravity data spacings are larger than 15 km.

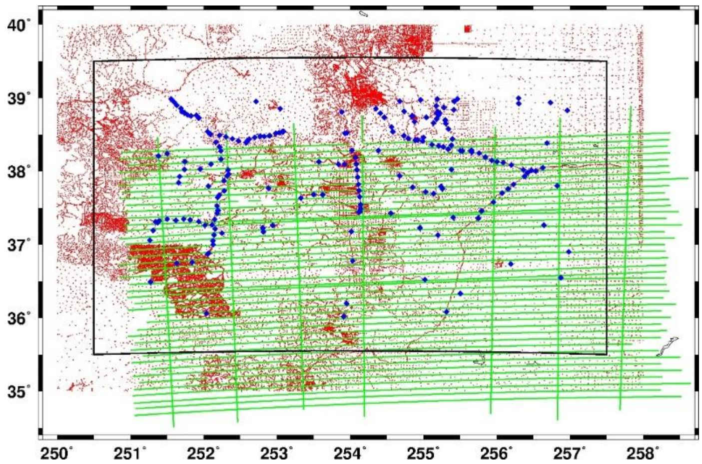

Figure 4. Distribution of terrestrial, airborne gravity and historic GPS leveling data in Colorado. Red points represent terrestrial gravity observations. Green lines represent GRAV-D airborne gravity data. Blue diamonds represent historic GPS leveling benchmarks. The computation area is bounded by the black rectangular.

Table 4. Statistics of the differences between the gravimetric geoid models based on different data combination modes and the GPS leveling measured geoid heights (unit: m)

Gravimetric geoid model	Min	Max	Mean	SD
EGM2008	0.625	1.008	0.847	0.061
EIGEN-6C4	0.575	0.999	0.851	0.067
XGM2019	0.563	1.034	0.836	0.075
GOCO06S + Terrestrial	0.703	1.029	0.864	0.058
GOCO06S + Terrestrial + Airborne	0.710	1.048	0.863	0.053

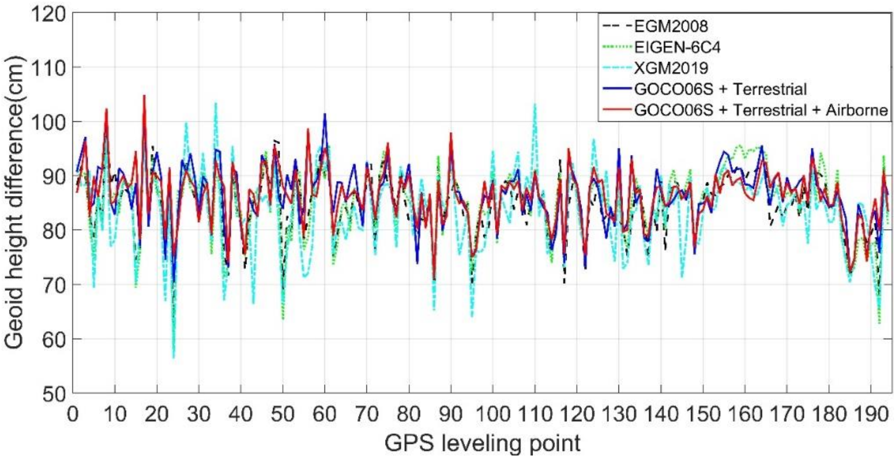

Figure 5. Differences between the gravimetric geoid models based on different data combination modes and the GPS leveling measured geoid heights. Results for EGM2008, EIGEN-6C4 and XGM2019 are included.

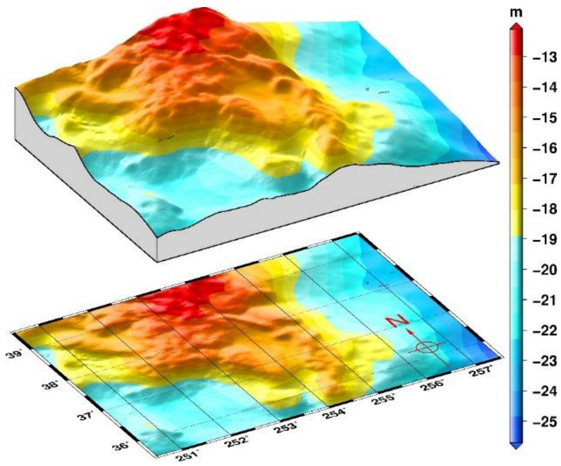

Figure 6. Gravimetric geoid model derived from the combination of satellite gravity model GOCO06S, terrestrial and GRAV-D airborne gravity data

Accurate knowledge of coastal gravity field is of importance for geodetic mean dynamic topography modelling, which is useful for studying coastal ecosystem processes and sea level change, as well as facilitating other offshore activities. However, coastal zones often present multiple challenges for quasi-geoid/geoid recovery. First, the satellite altimeter-derived data contain larger errors in coastal zones than in open seas, due to the land and calm water contamination on the return waveforms and degradation of the applied corrections. The poor data coverage in coastal boundary exacerbates this problem, which remains a barrier on coastal quasi-geoid/geoid determination. Airborne gravimetry provides seamless measurement both onshore and offshore with uniform accuracies, which can alleviate the mentioned problem of gravity field recovery in coastal areas.

We study the role of airborne data for gravity field recovery in a coastal region and the possibility to validate coastal gravity field model against recent altimetry data (CryoSat-2, Jason-1, and SARAL/Altika). Moreover, we combine airborne and ground-based gravity data for regional refinement and quantify and validate the contribution introduced by airborne data. Numerical experiments in the Gippsland Basin over the south-eastern coast of Australia show that the effects introduced by airborne gravity data appear as small-scale patterns on the centimetre scale in terms of quasi-geoid heights. Numerical results demonstrate that the combination of airborne data improves the coastal gravity field, and the recent altimetry data can be potentially used to validate the high-frequency signals introduced by airborne data. The validations of different models against the recent altimeter-derived quasi-geoid heights demonstrate that the incorporation of airborne data improves the local quasi-geoid in coastal areas. The validation results are shown in Figure 4 and Table 4, the comparisons with other existing models show that QGland_TSA (gravimetric quasi-geoid over the Gippsland Basin modelled with terrestrial (T), satellite altimetry (S), and airborne (A) gravity data) is of highest quality. QGland_TS, AGQG2017, and EGM2008 have comparable accuracies, and all these three models are worse than QGland_TSA, by the magnitudes of approximately 5–8 mm. The standard deviation (SD) of the misfit between altimeter-derived quasi-geoid heights and gravimetric quasi-geoid decreases from 0.028 to 0.023 m, when validating QGland_TS and QGland_TSA, respectively. The accuracies of EIGEN-6C4, GECO, and SGG-UGM-1 are between 3.4 and 3.7 cm, all of which are worse than the four models mentioned above. GOCO05c is of worst quality, and its accuracy decreases to 4.8 cm.

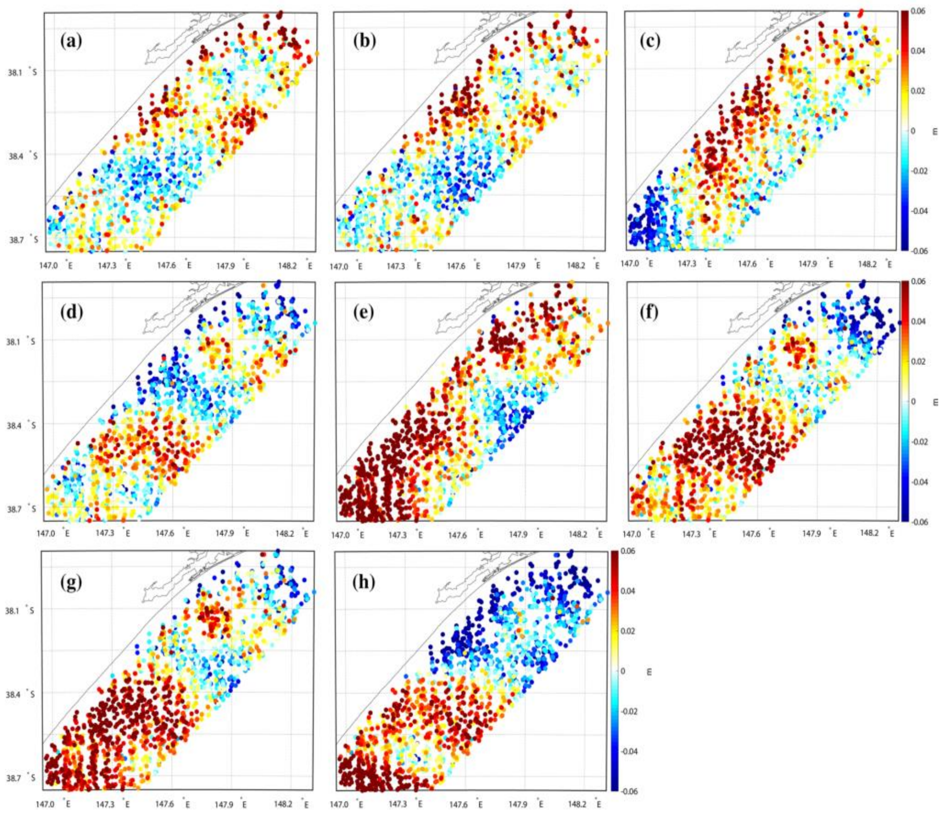

Figure 7. Evaluations of different gravimetric quasi-geoid models with the altimeter-derived quasi-geoid heights only located within the boundary of airborne survey. a QGland_TSA, b QGland_TS, c AGQG2017, d EGM2008, e EIGEN-6C4, f GECO, g SGG-UGM-1 and h GOCO05c.Note that the mean values of the misfit between gravimetric quasi-geoid models and altimeter-derived data are removed.

Table 5. Statistics of validations of different gravimetric quasi-geoids with the altimeter-derived quasi-geoid heights (units: m)

Quasi-geoid	Max	Min	SD
QGland_TSA	0.136	-0.169	0.023
QGland_TS	0.163	-0.189	0.028
AGQG2017	0.148	-0.179	0.031
EGM2008	0.171	-0.165	0.029
EIGEN-6C4	0.214	-0.127	0.037
GECO	0.150	-0.157	0.037
SGG-UGM-1	0.178	-0.138	0.034
GOCO05c	0.155	-0.194	0.048

4 Global Static Gravity Field Modeling

Global static gravity field recovering from satellite observations

The satellite gravity models SWPU-GRACE2021S, GOSG02S, Tongji-GMMG2021S and WHU-SWPU-GOGR2022S are constructed based on GRACE and GOCE satellite observations by different organizations, such as Wuhan University, Tongji University, Southwest Petroleum University and Guangdong University of Technology.

SWPU-GRACE2021S model up to degrees and order (d/o) 180 is determined based on the dynamic approach with the GRACE data throughout the entire mission cycle of 15 years. GOSG02S up to d/o 300 is an improved GOCE-only model of GOSG01S derived from reprocessed GOCE data by combining the 300 d/o SGG (Satellite Gravity Gradient) normal equation via the direct least squares approach, 130 d/o SST-hl (Satellite-to-Satellite in high-low mode) normal equation via the point-wise acceleration approach. WHU-SWPU-GOGR2022S is determined by combining the normal equation of GOSG02S and that of SWPU-GRACE2021S via the VCE technique. Tongji-GMMG2021S is a combined model up to d/o 300 by combining 300 d/o GOCE gravity gradient normal equation via the direct method, the 180 d/o Tongji-Grace02s normal equation via the modified short-arc approach and the Kaula’s regularization constraints.

The XGM2019 model and GPS/leveling data are used for precision analysis of, SWPU-GRACE2021S, GOSG02S, WHU-SWPU-GOGR2022S and Tongji-GMMG2021S in frequency domain and space domain respectively. The results show that the accuracy of GOSG02S and WHU-SWPU-GOGR2022S is comparable to GO_CONS_GCF_2_DIR_R6, GO_CONS_GCF_2_TIM_R6, GO_CONS_GCF_2_SPW_R5, GOCO06s and Tongji-GMMG2021S that use the entire mission data of GOCE satellite and the accuracy differences are in the order of millimeters. The SWPU-GRACE2021S model has the same accuracy below degree/order 160 as the international mainstream of GRACE satellite gravity field models, i.e., ITSG-Grace2018s and Tongji-Grace02s.

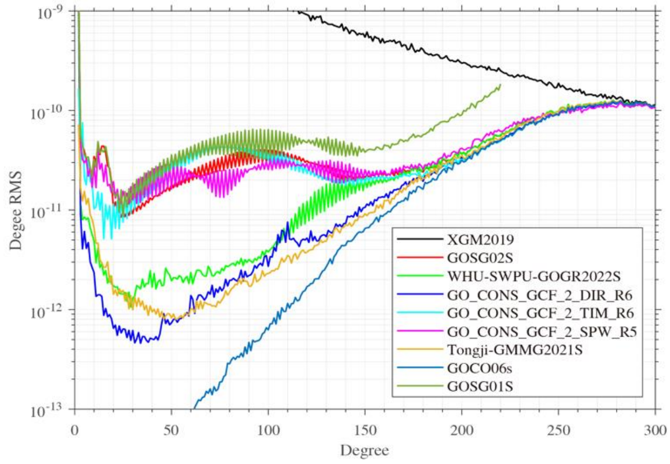

Figure 8. Degree Error RMS of models with respect to XGM2019.

Table 6. Statistical results of comparison with GPS/Leveling data in the USA (6169 points) and mainland China (649 points) (unit: m)

	Model	Max	Min	Mean	STD
USA	GOSG02S	1.046	-2.184	-0.562	0.441
	WHU-SWPU-GOGR2022S	1.050	-2.179	-0.561	0.440
	GO_CONS_GCF_2_DIR_R6	1.080	-2.196	-0.565	0.438
	GO_CONS_GCF_2_TIM_R6	1.038	-2.221	-0.554	0.432
	Tongji-GMMG2021S	1.068	-2.193	-0.561	0.437
	GOCO06s	1.001	-2.234	-0.557	0.435
China	GOSG02S	1.023	-1.690	0.073	0.388
	WHU-SWPU-GOGR2022S	1.024	-1.689	0.070	0.389
	GO_CONS_GCF_2_DIR_R6	0.969	-1.640	0.070	0.391
	GO_CONS_GCF_2_TIM_R6	0.963	-1.584	0.075	0.385
	Tongji-GMMG2021S	1.070	-1.665	0.072	0.389
	GOCO06s	0.953	-1.578	0.072	0.384

Determination of high-resolution Earth's gravity field model

Based on the EHA-CT (the theory of the Ellipsoidal Harmonic Analysis and Coefficient Transformation) method, we develop a new $5' \times 5'$ spatial resolution gravity field model SGG-UGM-2 up to degree 2190 and order 2160 by combining SGG (Satellite Gravity Gradient) and SST-hl (Satellite-to-Satellite in high-low mode) observations of GOCE (Gravity field and steady-state Ocean Circulation Explorer) mission, the ITSG-Grace2018 normal equation system, marine gravity anomalies recovered from satellite altimetry data and EGM2008-derived continental gravity data. The ellipsoidal harmonic coefficients of degrees 251—2159 are estimated by solving the block-diagonal form normal equations of the ground gravity anomalies (including the marine gravity data). The coefficients of degrees 2-250 are determined by combining the normal equations of satellite observations and ground gravity anomalies. The variance component estimation technique is used to estimate the relative weights of different observations.

The new SGG-UGM-2 model has a promising performance in the GPS/Leveling validation and error analysis compared to EGM2008 in the frequency and spatial domains. The GPS/Leveling data in China and the USA are used to validate the model SGG-UGM-2, together with EIGEN-6C4, SGG-UGM-1, GECO and EGM2008. SGG-UGM-2 shows the best performance in the USA, as indicated by the statistics of the differences between model-derived quasi-geoidal/geoidal heights and GPS/Leveling data, and their histograms and empirical variograms. Due to the contribution of the new GRACE normal equation and the new marine gravity anomalies, SGG-UGM-2 has a slightly better performance than that of its predecessor SGG-UGM-1 in both mainland China, the USA and the coastal city Qingdao of China. This indicates that the methods used for developing SGG-UGM-2 are valid and can be used for developing future SGG-UGM series by individually processing available terrestrial gravity datasets (e.g. mainland China). In addition, the accuracy of the new model SGG-UGM-2 indicates that this model will provide an alternative for users.

Table 7. Statistical results of comparison with GPS/Leveling data in the USA (6169 points) and mainland China (649 points) (unit: m)

	Model	**Max**	**Min**	**Mean**	**STD**	**RMS**
	EGM2008	0.360	-1.396	-0.511	0.284	0.584
	SGG-UGM-1	0.317	-1.407	-0.511	0.280	0.583
USA	SGG-UGM-2	0.386	-1.394	-0.511	0.277	0.578
	GECO	0.313	-1.391	-0.513	0.281	0.585
	EIGEN-6C4	0.397	-1.392	-0.512	0.282	0.585
	EGM2008	1.729	-1.535	0.239	0.240	0.339
	SGG-UGM-1	0.744	-0.618	0.246	0.162	0.294
China	SGG-UGM-2	0.744	-0.603	0.246	0.161	0.292
	GECO	1.165	-0.847	0.244	0.180	0.303
	EIGEN-6C4	0.729	-0.698	0.243	0.157	0.289

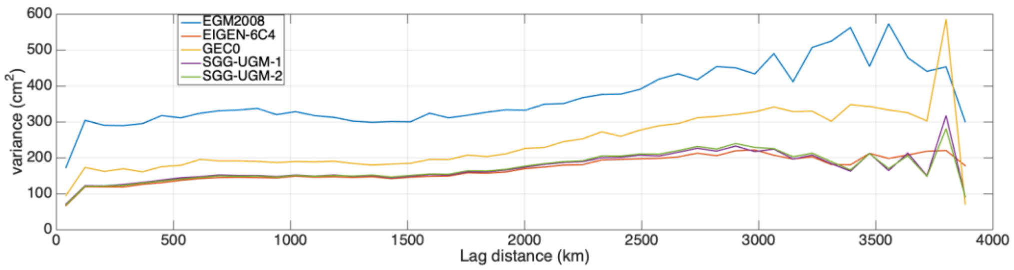

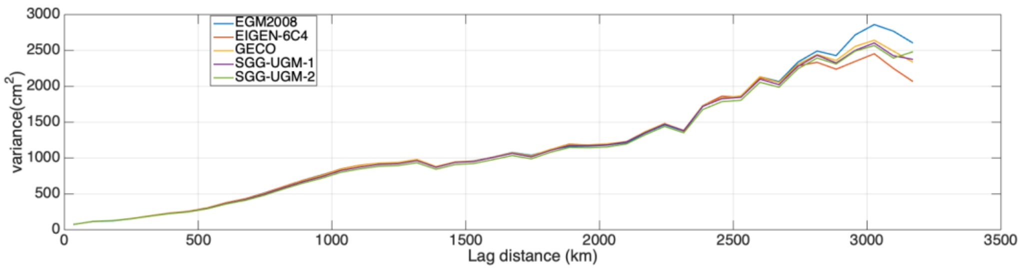

Figure 9. The empirical variograms of the differences with respect to the GPS/leveling data sets in China (top one) and USA (bottom one) for EGM2008, SGG-UGM-1, SGG-UGM-2, GECO and EIGEN-6C4.

5 Satellite Altimetry

Altimetry Data Processing

Satellite altimetry is a key technology for obtaining global sea surface height. In 2021, China built the first ocean dynamic environment satellite constellation, which included the HY-2B, HY-2C, and HY-2D ocean dynamic environment satellites. The HY-2B satellite is a sun-synchronous orbit satellite. HY-2C and HY-2D satellites are non-sun-synchronous orbital satellites with inclinations of 66° (Figure 1).

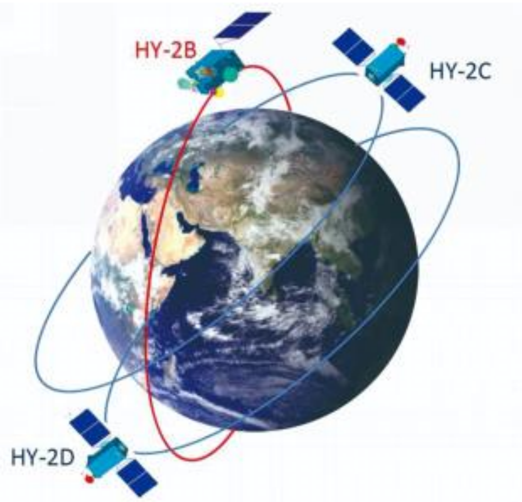

Figure 10. The orbits of HY-2B/2C/2D (http://www.nsoas.org.cn/news/content/2021-05/25/23_8462.html)

The radar altimeters are one of the main payloads of China's ocean dynamic environment satellite constellation. In 2023, two synthetic aperture radar (SAR) altimeter satellites were launched. The second constellation of the ocean dynamic environment satellite under development is also equipped with SAR altimeter (Lin and Jia, 2022). In recent years, relying on the HY-2 series of altimetry satellites, China has carried out a lot of relevant exploration. The orbit determination and other geophysical and environmental corrections, such as atmospheric correction, sea state bias, tropospheric correction, etc., are crucial for the precision of altimetry data. In addition, satellite altimetry is easily affected by sea-land changes in offshore areas (or by the environment around lakes), which may introduce much noise into the waveform and hence increase the uncertainties of determining the distance between the satellite and the water body surface. Chinese researchers proposed several re-tracking methods based on waveform decontamination, realignment, denoising, and derivation to obtain high-precision altimetry observations in nearshore areas and lakes. They also evaluated the impact of different re-tracking algorithms on the SAR altimeter.

Several studies were implemented to improve the precise orbit determination (Guo et al., 2022b, 2023) and sea state bias correction of altimetry satellites (Peng and Deng, 2020a; Peng et al., 2022). Guan et al. (2020) discussed the necessity of ionospheric delay filtering for satellite altimetry. For waveform retracking, Wang and Huang (2021) presented an upgraded strategy for decontaminating waveforms to improve altimeter-derived coastal SSHs. Compared with the old decontamination strategy, one important improvement of the update method is the realignment of waveforms prior to decontamination. Another is that they adopted gate-based outlier judging criteria, which enable outlier detectors to treat different parts of the waveform with different criteria. To reduce the smoothness of the effective signal and suppress background noise as much as possible, Li et al.(2020) proposed a piecewise adaptive-norm trend filtering method to take advantage of different norms in the regularized framework. The results verified that the method was superior to the other three commonly used waveform filtering methods, i.e., Gaussian filtering, wavelet transform, EMD and trend filtering methods. Li et al. (2020) proposed a new waveform retracking method that combines waveform denoising and waveform derivatives by analyzing the limitations of existing retracking methods. Yuan et al. (2020) proposed a processing strategy using SSA for waveform retracking, which can improve the accuracy of the mean sea surface model. Peng and Deng (2020b) proposed a modified Brown-peaky retracker to handle land-contaminated waveforms with land returns observed in the waveform trailing edge and developed a seamless combination of multiple retrackers to retrieve improved along-track sea surface height (Peng et al., 2021).

Moreover, for the SAR altimeter, Gao et al. (2021) selected four waveform retrackers, including ICE1, multi-threshold, SAMOSA, and IceSheet, to analyze their re-tracking accuracy within 20km near the coast using the in-situ sea level data from global tide gauge stations. The results show that the SAR multi-threshold retracker can retain the most valid data and obtain the highest correlation as well as the smallest root mean square error of the difference between the derived sea surface heights and the tide gauge sea levels within 6 km offshore.

Marine Gravity and Bathymetry Inversion

Earth's gravity field can provide important basic geospatial information support for research and development in earth science. Satellite altimetry is the main technical means for ocean gravity field recovery. China has mainly carried out several aspects of work, including analyzing the impact of different inversion methods on the accuracy, fusing multi-satellite data with HY-2 series, inversing the near-shore gravity field, discussing the possible accuracy improvement brought by SWOT, researching multi-source gravity observation data fusion, and introducing deep learning into the inversion of the gravity field.

Ouyang (2022) and Sun et al. (2022) discussed the research progress of satellite altimetry and its recovery of global marine gravity field and of seabed topography model. Based on the marine vertical deflection and gravity anomaly obtained through satellite altimetry data, Wang and Huang (2021) assessed the marine geoid determined using different methods, including the Molodensky method, least square collocation, Stokes formula, two-dimensional spherical FFT, and the satellite altimetry leveling method. The results indicate that the marine geoid directly obtained through the Molodensky method is the best with the lowest standard deviation. After evaluating the performance of HY-2A/GM data in marine gravity field recovery (Wan et al., 2020a) and assessing the HY-2A/GM data by deriving the gravity field and bathymetry over the Gulf of Guinea (Wan et al., 2020b), Wan et al. (2022) developed a global marine gravity anomalies dataset, named Global Marine Gravity Anomaly Version 1 (GMGA1), from multi-satellite altimeter data. Compared to worldwide products such as DTU17, S&S V31.1, as well as values from EGM2008, EIGEN-6C4, and XGM2019e_2159, GMGA1 has an accuracy of around 3.3 mGal. Hao et al. (2023) enhanced short-wavelength marine gravity anomaly using depth data and generated the Global Marine Gravity Anomaly Version 2 (GMGA2) dataset, whose accuracy is 0.7 mGal higher than GMGA1.

Zhang et al. (2020) calculated the 1′×1′ marine gravity field model over the South China Sea area and the verifications with published models and shipborne gravimetric data showed that HY-2A GM data is capable of improving marine gravity field modeling. In a global context, Zhang(2022) constructed global marine gravity results and validating results showed that the HY-2 dataset is capable of improving marine gravity anomaly recoveries and the accuracy of NSOAS22 with incorporated HY-2 data is comparable to DTU21 and SS V31.1. Meanwhile, another global 1′×1′ marine gravity field model is inversed based on the vertical deflection approach and the remove-restore procedure by introducing the EGM2008 as the reference model. The root-mean-square of differences at grids are respectively 3.4 mGal and 1.8 mGal with DTU and SIO SS series models (Zhang et al., 2020b). They also found that the SSH-based method (depending on geoid undulations) performs better in estimating marine gravity anomalies near the coast, while the SSS-based method (depending on vertical deflections) is more advantageous in regions with intermediate ocean depths and seamounts (Figure 2). However, the SSS-based method shows limitations in areas with north-south directional ocean currents and topography features. In the deep ocean, both methods have similar accuracy (Zhang et al., 2021). Several other studies on altimeter-derived gravity models were carried out on the regional scale (Zhu et al., 2020; Guo et al., 2022a; Ji et al., 2021; Zhu et al., 2019), and the global scale (Zhu et al., 2022).

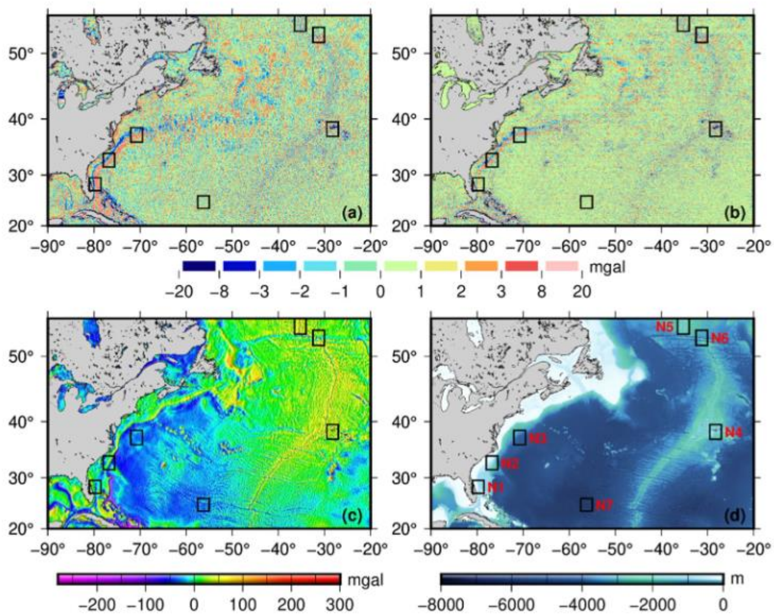

Figure 11. Residual marine gravity anomalies derived from SSS-based method and SSS-based method (Zhang et al. Journal of Geodesy, 2021)

Zhang et al. (2022) investigated the effect of the interpolation methods on accuracy when inverting the high spatial resolution marine gravity fields, especially in coastal areas where altimetry data is sparse. They presented an approach based on the ordinary kriging interpolation method, which uses the mean sea surface height as the constraint component in the vertical direction to improve the weight information of the ordinary kriging method and then improve the accuracy of the un-measured values. Compared to the ordinary kriging method, the experimental results show that this method can better assist in constructing marine gravity fields at high spatial resolution in coastal regions. Li et al. (2021) compared several typical gravity models with shipboard gravity measurements in offshore and coastal regions of China. The root mean squares of deviations between gravity models and shipboard gravity are all more than 7 mGal in offshore regions and within the range of 9.5-10.2 mGal in coastal regions. Further analysis in coastal regions indicates that the new gravity models with new satellite missions including Jason-2, SARAL/Altika, and Envisat data have relatively higher accuracy, especially SARAL/Altika data, significantly improving the coastal gravity field. Yu and Hwang (2022) found that the altimeter-derived gravity anomalies showed an average gravity accuracy improvement of 9.5% by calibrated and scaled covariances of geoid gradients compared with that of the altimeter-derived gravity when using the initial variances. Through simulating SWOT SSH, they also found that multiple-cycle SWOT observations can deliver high-quality marine gravity anomalies (Yu et al., 2021). Taking the Surface Water and Ocean Topography (SWOT) wide-swath altimeter mission as an example, Jin et al. (2022) simulated one cycle of SWOT sea surface height measurements and compared it with the EGM2008 gravity field model. The vertical deflections determined by one cycle of SWOT data are better than those determined by the combined dataset of Jason-1/GM, Cryosat-2/LRM, and SARAL/GM data and can significantly improve the accuracy of east vertical deflection (Figure 3).

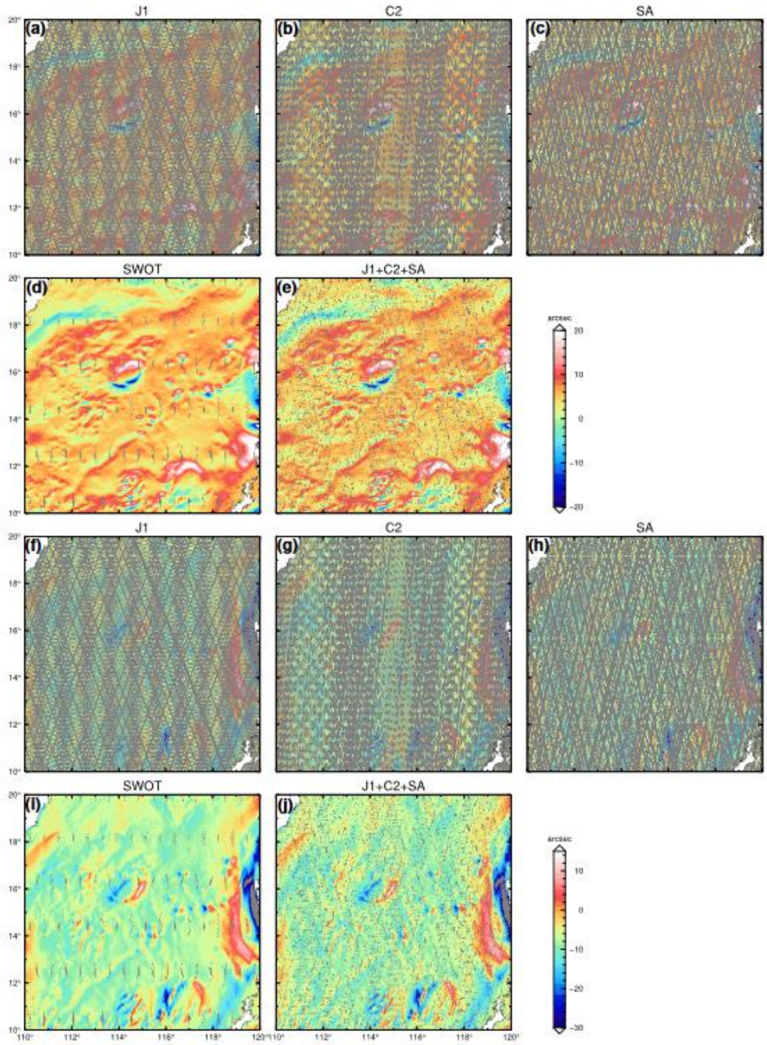

Figure 12. Vertical deflections from different SSH datasets in the South China Sea (Jin et al. Journal of Geodesy, 2022)

Regarding multi-source gravity data fusion, Zhao et al. (2022) improved the multi-surface function by introducing residual constraint factors to fuse the shipborne gravity data and satellite altimetry-derived gravity field model. Compared to the shipborne gravity data for verification, the improved method with residual constraint has the best accuracy, as well as the smallest extreme values and standard deviations. Furthermore, the improved method reduces the discrepancy between two kinds of data near the control shipborne measuring points and can extrapolate to the other areas to improve the accuracy of the satellite altimetry-derived gravity model with reasonably distributed residuals. Sun et al. (2021) developed a point-mass model with non-uniform point-mass density distribution based on iterative removal and recovery process. With the same shipborne gravity constraint, the fusion accuracy of the non-uniform density point-mass model can be improved by 12% compared with that of the uniform density point-mass model.

Annan and Wan (2022) recovered the bathymetry of the Gulf of Guinea using altimetry-derived gravity field products combined via a convolutional neural network. The spectral coherency analysis showed that the ship-borne depths correlated with the CNN-derived model better than with the other models. Wei et al. (2021) inverted bathymetry using HY-2A altimetry gravity data. An et al. (2022) proposed a GGM-based method using weighted averaging and distance factor to improve the accuracy of bathymetry modeling, by calculating short-wave gravity anomalies based on local seabed topography. Wan et al. (2023) computed altimetry-derived gravity gradients using the spectral method and verified their performance in bathymetry inversion using a back-propagation neural network, and the resultant bathymetries compare well with reference models from ship-borne depths, SRTM15+V2 and GEBCO_2021. The effects of environmental correction errors and interferometric radar altimeter errors on marine gravity field inversion were discussed as well (Wan et al., 2020c, 2022b).

Sea Surface Height and its Change

Global sea level change dataset is an important basis for understanding ocean dynamics, and satellite altimetry technology is currently the key technology for efficiently observing high-precision global sea surface. Domestic scholars have used deep learning to fuse altimetry and tide gauge data to improve the precision of coastal sea level changes. They also compared the accuracy of different mean dynamic topography (MDT) inversion methods. Furthermore, several products were generated, including a global mean sea surface height model, an Arctic mean sea surface height model and a global steric sea level change model.

Yang et al. (2021) proposed a fusion approach of altimetry and tide gauge data based on a deep belief network (DBN) method. They compared the fused sea level anomalies from the DBN method with those from the inverse distance weighted method, the kriging method, and the curvature continuous splines in tension method for different cases. The results show that the precision of the DBN method is better than that of the other three methods and is reduced by approximately 20% when the limited altimetry along-track data and in-situ tide gauge data are used. In addition, the sea level anomalies generated by the DBN model contain more spatial distribution information than others. Wu et al. (2022) compared the performances of the multivariate objective analysis (MOA) method with the rigorous least squares (LS) method. The results showed that the mean dynamic topography (MDT) derived from the LS method outperformed the MOA method, especially over coastal regions and ocean current areas. The root mean square (RMS) of the discrepancies between the LS-derived MDT and the ocean reanalysis data was lower than the RMS of the discrepancies computed from the MOA method by a magnitude of 1–2 cm. Moreover, the geostrophic velocities calculated by the LS-derived MDT were more consistent with buoy data than those calculated by the MOA-derived solution by a magnitude of approximately 1 cm/s. After several regional sea surface case studies(Yuan et al., 2020b, 2021), Yuan et al. (2023) constructed a high-precision and high-resolution global MSS model SDUST2020 (Figure 4) from multi-source altimetry data of the past 30 years.

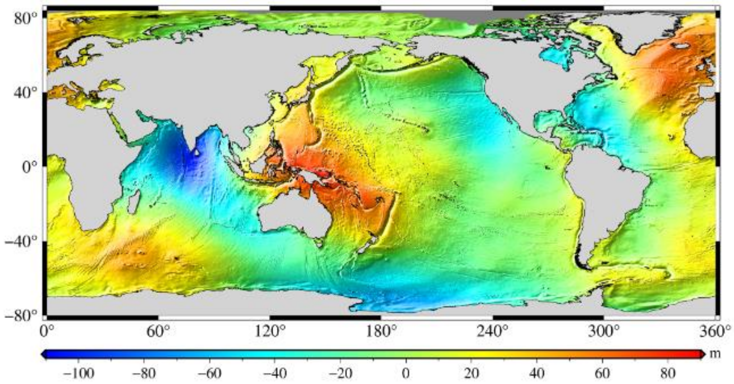

Figure 13. Global mean sea surface model SDUST 2020 (Yuan et al. Earth System Science Data, 2023)

By combining the measurements from ICESat and Cryosat-2 missions, Chen et al. (2022) published a new Arctic mean sea surface model named SUST22 (Figure 5), which has competitive precision and accuracy compared with other Arctic mean sea surface models.

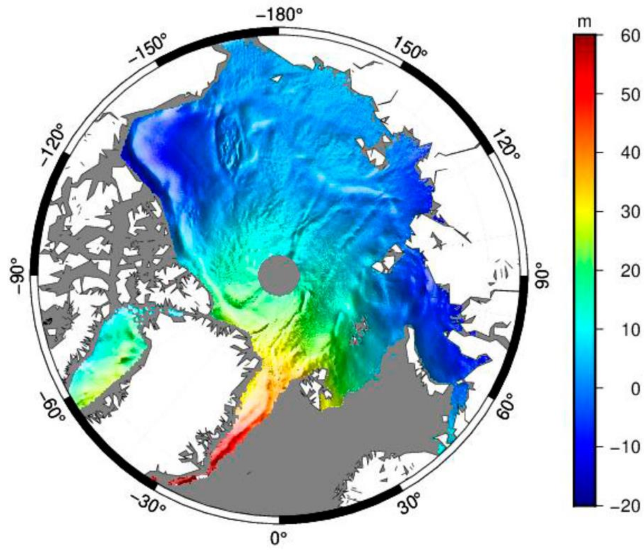

Figure 14. The Arctic mean sea surface model SUST22 (Chen et al. International Journal of Digital Earth, 2022)

In addition, Li et al. (2022) combined time-varying gravity data and satellite altimetry data to effectively determine the global steric sea level changes using sea level fingerprints and empirical orthogonal functions of the steric effect. Niu et al. (2020) used jointly the singular spectrum analysis and autoregressive moving average methods to predict sea level changes and crustal vertical changes in the near Japan seas, providing a new approach for predicting sea level changes in the near sea.

Ice Sheet and Water Level Changes

Satellite altimetry can also be applied in glaciology and hydrology. Several missions, such as Cryosat, Envisat, ICESat, SARAL, etc. were used to study the elevation and volume changes of ice sheets, and the water level changes of lakes, reservoirs, and other water bodies.

Sea ice is an important indicator of global climate change, and satellite altimetry can be used to obtain long-term and large-scale changes in sea ice. In recent years, several studies were using Cryosat, IceBridge, and Envisat to retrieve the ice thickness and ice freeboard variations in the Antarctic (Chen et al., 2019; Zhang et al., 2020; Gao et al., 2021), the Arctic (Zhang et al., 2019; Xiao et al., 2021; Zhang et al., 2021, 2022), and the Beaufort sea (Liu et al., 2019).

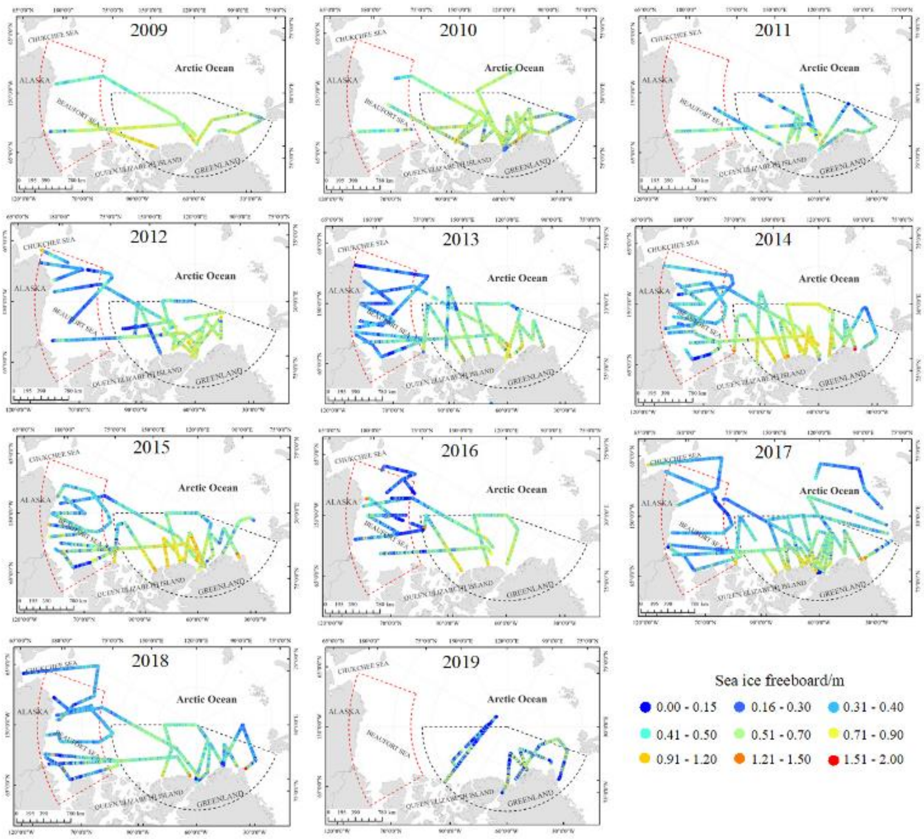

Figure 15. Arctic sea ice freeboard along the OIB flight lines from 2009 to 2019 (Zhang et al. IEEE Transactions on Geoscience and Remote Sensing, 2022)

In addition, Wang et al. (2022) used the laser altimetry ICESat-2 data to investigate the elevation and mass change of Svalbard from 2019 to 2021 by a hypsometric approach. The assessment shows that the Svalbard-wide elevation change rate is -0.775 ± 0.225 m/yr in 2019-2021, corresponding to the mass change of -14.843 ± 4.024 Gt/yr. Fan et al. (2022) obtained the time series of the ice surface elevation changes for 17 active lakes of the Antarctic using CryoSat-2 Baseline-D and ICESat-2 data from 2010 to 2020. Chen et al. (2020) combined the lCESat and CryoSat-2 altimeter datasets to monitor the activity of 17 glacial lakes in the Byrd glacier basin for 16 years. Then the water potential equation was used to obtain the drainage pathways map in the Byrd glacier basin, and subglacial lake activities were combined to analyze the hydrological relationship among them. The results show that the subglacial lakes have a periodic pattern of water storage and drainage activities for about 2~3 years. With an improved slope correction and adjustment model, Chen and Zhang (2019) studied the elevation and volume change rate of the Greenland Ice Sheet between 2003 and 2009 using ICESat observations, and analyzed the melting status of each glacier drainage in detail. Chen et al. (2021) proposed a new elevation difference method for ice sheet elevation change determination with combined Cryosat-2 and ATM observations, and studied the volume change rate of the Greenland Ice Sheet, which showed obvious volume loss of -200.22 km^3/a from 2010 to 2019.

Chao et al. (2019) used altimetry data from ENVISAT, ICESat, and SARAL to detect the water-level change in the Danjiangkou reservoir. The results show that the periodic signals between water levels from the altimetry mission, in situ observations and GRACE agree well with each other. For the lake areas, a modified retracker is used to determine heights from the first altimetric sub-waveform and applied to several lakes. Compared to the standard Ice retracker (0.11m), the new methodology can obtain lake levels with lower standard deviations (0.06m) (Yang, et al., 2021). Xu et al. (2022) employed ICESat and ICESat-2 altimetry data to obtain global water level changes for 22 008 lakes/reservoirs greater than 1 km^2 (Figure 7). They found that across the globe, 78.84% of lakes exhibit a rising water level and the figure for reservoirs is 56.01%.

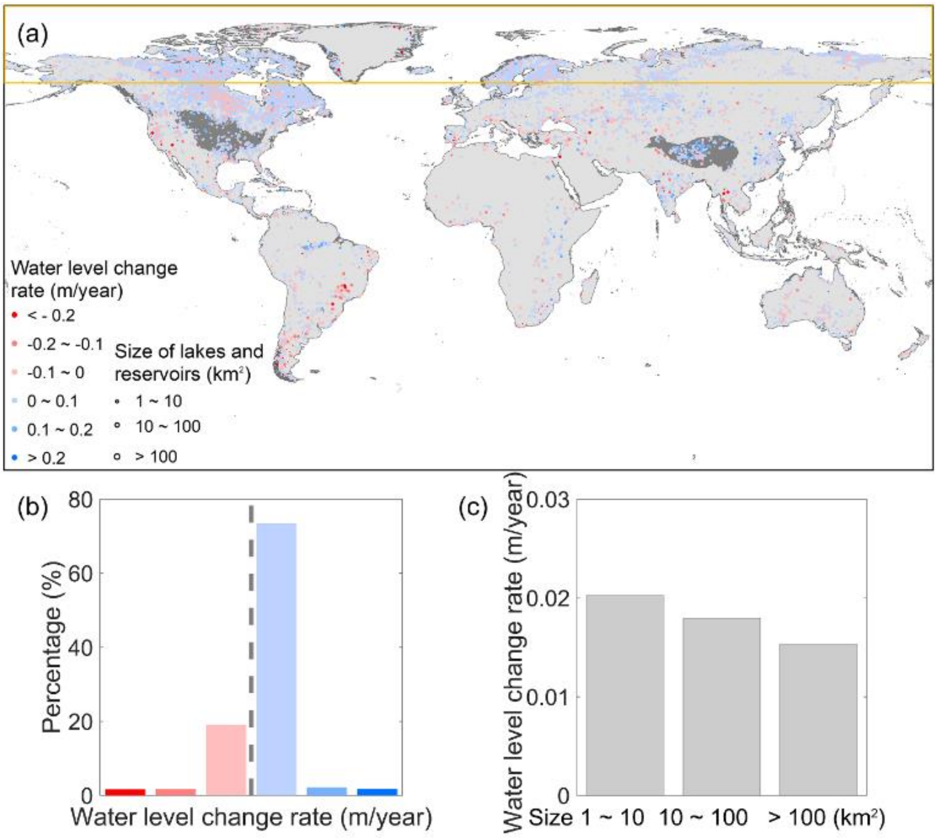

Figure 16. Global water level changes of 20776 lakes and 1232 reservoirs over 2003-2021 tracked by ICESat/ICESat-2 data (Xu et al. Environmental Research Letters, 2022)

To generate long-term and accurate lake level time series for the Tibetan lakes, Xu et al. (2022) presented a robust data processing strategy and constructed a 25-year-long lake level time series of Ngangzi Co using the TOPEX/Poseidon-family altimeter data from October 1992 to December 2017. They found that the lake level increased by ~8 m from 1998–2017 and changed at different rates in the past 25 years. Based on ICESat/ICESat-2 altimetry and Landsat imagery, Xu et al. (2021) estimated trends in surface water levels of 52 water bodies (lakes and reservoirs) with areas larger than 1 km^2 in Australia. From 2003 to 2019, the area-weighted mean of water level change rates of them is -0.046 m/year, with 17 lakes (32.7%) with increasing water levels and 35 lakes (67.3%) decreasing with water levels.

6 Vertical datum transformation

As sea level changes globally, accurate determination of the various vertical datums transformation plays an increasingly important role in analysis of sea level variation and ocean depth determination. Vertical datum transformation is the basic upon which to realize coastline definition and maritime features identification, and is of great importance for geospatial data expression under the same vertical datum.

From 2019 to 2023, We has made continuous breakthroughs and new progress in the vertical datum transformation between land and sea, mainly including three aspects as follows.

Construction and optimization of seamless chart datum model

As the accuracy of the global ocean tide models in determining short-period tidal constituents has improved gradually, i.e., the EOT20 model shows an improvement of ~ 0.2 cm in the root-square sum value compared to FES2014 model in the global ocean. A series of researches on the construction of chart datum (CD) model were performed based on the previous studies.

The accuracy of the performance of seven global ocean tide models, i.e., DTU10, EOT11a, FES2014, GOT4.8, HAMTIDE12, OSU12 and TPXO8, were analyzed in the South China Sea. The accuracy was investigated using tidal results from 37 tide gauge stations. Results showed that the FES2014 model exhibiting slightly superior performance, with the root sum square value of the short-period tidal constituents was 9.35 cm. To figure out the accuracy of tide models in China seas, comparisons between the observations from the 33 tide gauge stations with continuous 3-year records and the three latest models, i.e., FES2014, EOT20, and TPXO9, were performed, which also indicated that the FES2014 model exhibiting slightly superior performance with the root sum square value of 7.91 cm. Meanwhile, these studies imply that the accuracy performance of the long-period tidal constituents has not received sufficient attention, which is vital to the establishment of the LNLW.

To construct LNLW model in China seas, the FES2014 tide model was adopted firstly. Statistical analysis on the distribution of the datum values of LNLW in the study area (15 °N–42 °N, 105°E–128 °E), showed that the LNLW values ranged from -22.72 to -446.74 cm. Comparison with results calculated from 16 tide gauge stations showed that the standard deviation was 13.02 cm. Owing to the Sa and Ssa tidal constituents provided by most global tide models are the simulation results of pure fluid dynamics (amplitude <1 cm), the TOPEX/Poseidon and Jason series satellite altimetry data have been adopted to construct the empirical model of Sa and Ssa tidal constituent, and then analyze the long-period tidal correction to the LNLW. It is indicated that the long-period tidal contribution should not be neglected in LNLW construction. Furthermore, the latest CD datum has been constructed based on the combination of the empirical model and tide models. The spatial distribution of the LNLW value was shown in Figure 8.

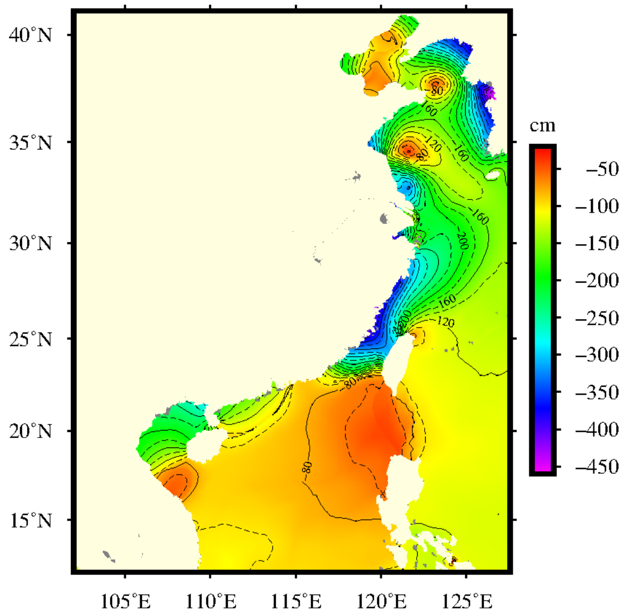

Figure 17. Spatial distribution of the lowest normal low water values in the China seas.

Vertical datum transformation in regional and special sea area

In recent years, with the implementation of "land-sea overall planning" of China, some coastal cities in China, such as Qingdao, Shenzhen, and Tianjin have constructed the vertical datum transformation between land and sea, have constructed the regional separation model with 1 '×1' resolution and conversion accuracy better than 15 cm. The Maritime Administration of the Ministry of Communications has also constructed the height and depth separation model in the Yellow Sea and Bohai Sea area.

The proposed technical route is as follows. A regional tide model is constructed, and then a LVLW model is constructed according to the definition. In addition, a sea surface topographic model like the geoid or CGCS2000 ellipsoid is also constructed. By superimposing LNLW model and sea surface topography model, and the construction of height and depth separation model is completed. Based on the above scheme, a high-resolution and high-precision separation model between the CGCS2000 ellipsoid, depth datum and quasi-geoid of Shandong Province was constructed, realizing the unification of the vertical datum of Shandong Province and its coastal regions.

We have also performed the vertical datum transformation in special sea areas. In the Yangtze estuarine waters, through the establishment of seamless CD and its transformant relationship with other vertical datums, combining with geoid, sea surface topography and three-dimensional numerical simulation of tidal wave motion. The standard error of the vertical datum transformation model was 12.4 cm. Although the Yangtze estuarine waters have complicated tidal wave characteristics and they are nearshore waters, which leads to poor accuracy of the mean sea surface topography model in this region, when the accuracy of satellite altimetry is further improved in the nearshore areas, the proposed method can be extended to nearshore and inland waters.

The transformation model of the geodetic height of the mean sea surface utilizes the gridded MSS model and chart datum model based on the DTU15 model and the Atlantic Ocean 2008 tide model was obtained in the Great Wall Bay, and mean sea surface model, geoid model and CD model were combined to realized the vertical datum transformation in the Ross Sea and surrounding waters.

Developed and revised the technical specification

The Technical specification for marine vertical datum transformation (CH/T 2021-2023), which is led by the First Institute of Oceanography, Ministry of Natural Resources, has been approved and issued of the National Technical Committee for Standardization of Geographic Information. It will come into effect on June 1, 2023. The specification stipulates the basic requirements of vertical datum transformation, data preprocessing, basic model construction, procedure of transformation, quality control and precision evaluation, the exchange of results and other contents. The specification provides technical guidance for the vertical datum transformation. Its implementation provides technical standard support for solving the transformation of land and sea datum and obtaining the achievements of land and sea seamless geographic information in our country.

7 Establishment of Vertical Movement Model of Chinese Mainland by Fusion Result of Leveling and GNSS

Geodetic survey is one of the important methods to quantitatively study the vertical movement of the crust, among which leveling and GNSS are the most classic means of monitoring the vertical movement of the crust. By taking full advantage of the high precision of leveling data and the high spatial and temporal resolution of GNSS, a robust and reliable vertical movement model of the curst can be established. Single data source is analyzed. The method of analyzing, compensating and suppressing systematic errors in multi-phase leveling network data is analyzed, and a complete function model and stochastic model are established to improve the reliability of the calculation results. Heterogeneous data fusion is analyzed. It is proposed to use the functional model and random model to weaken the influence of systematic errors of heterogeneous data, including functional model compensation method and heterogeneous data weight ratio adjustment method. A process-based heterogeneous data fusion method is proposed, such as the joint adjustment method with the restriction that the geodetic height velocity is equal to the normal height velocity at the GNSS-leveling points. A result-based heterogeneous data fusion method is proposed. By analyzing the distance between the discrete control point and the grid point of GNSS and leveling vertical movement model, the grid point weight of different model is determined, and the grid value weighted fusion is realized. The establishment of the vertical movement model is analyzed. Based on the stable bedrock point, the effective stripping of the vertical movement of the surface and the crust is realized. The methods of establishing the vertical movement model of the ground are studied, including Inverse Distance Weighting Method, Kriging Method, Minimum Curvature Method, etc. The vertical movement model in Chinese mainland is established based on the Kriging method. Meanwhile, the spatial distribution characteristic of the vertical movement in the Chinese mainland is analyzed. According to fused vertical movement model, the characteristic of vertical movement is analyzed: North China Plain and Jiangsu-shanghai area are severe subsiding, where the velocity of individual areas is up to 100 mm/a, the North-east of China and Tibet areas are uplifting, and the maximum velocity exceeds 5 mm/a in some local area, the vertical movement in other areas is relatively stable.

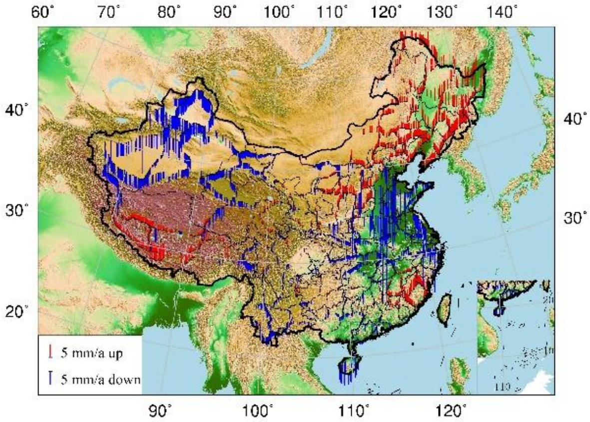

Figure 18. Vertical Velocity of Leveling Points

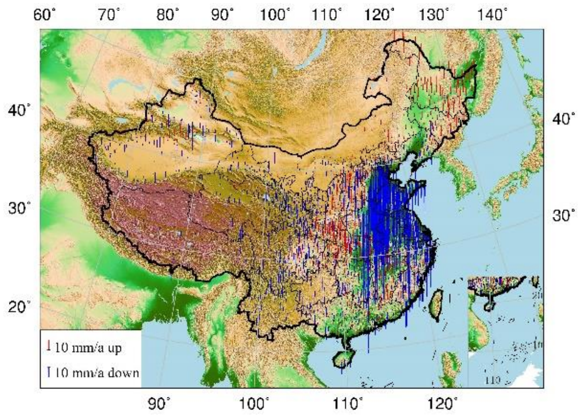

Figure 19. Vertical Velocity of GNSS Points

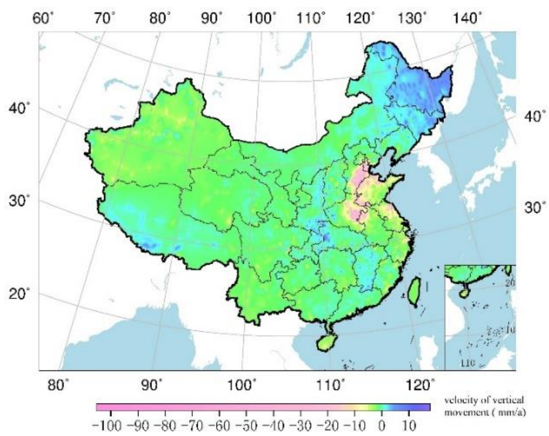

Figure 20. The vertical movement model of Chinese mainland by GNSS and Leveling data

Bibliography

Amin, H. , Sjöberg, L. E. , & Bagherbandi, M. A global vertical datum defined by the conventional geoid potential and the Earth ellipsoid parameters. Journal of Geodesy, 2019, 93: 1943-1961.

An, D., J. Guo, Z. Li, B. Ji, X. Liu, and X. Chang. Improved Gravity-Geologic Method Reliably Removing the Long-

Wavelength Gravity Effect of Regional Seafloor Topography: A Case of Bathymetric Prediction in the South China Sea. IEEE Transactions on Geoscience and Remote Sensing, 2022, 60:1-12.

Annan, R. F., and X. Wan. Recovering Bathymetry of the Gulf of Guinea Using Altimetry-Derived Gravity Field Products Combined via Convolutional Neural Network. Surveys in Geophysics, 2022, 43(5):1541-1561.

Chao, N., G. Chen, Z. Luo, X. Su, Z. Wang, and F. Li. Detecting Water Diversion Fingerprints in the Danjiangkou Reservoir from Satellite Gravimetry and Altimetry Data. Sensors, 2019, 19(16):3510.

Chen, G., and S. Zhang. Elevation and Volume Change Determination of Greenland Ice Sheet Based on ICESat Observations. Chinese Journal of Geophysics, 2019, 62(7):2417-2428.

Chen, G., S. Zhang, S. Liang, and J. Zhu. Elevation and Volume Changes in Greenland Ice Sheet From 2010 to 2019 Derived From Altimetry Data. Frontiers in Earth Science, 2021, 9:674983.

Chen, G., Z. Zhang, S. K. Rose, O. B. Andersen, S. Zhang, and T. Jin. A New Arctic MSS Model Derived from Combined Cryosat-2 and ICESat Observations. International Journal of Digital Earth, 2022, 15(1):2202-2222.

Chen, J., C. Zhou, and Q. Zhao. Subglacial lake activity and hydrological connection in the Byrd glacier basinduring 2003-2018: analysis of multimission satellite altimetry monitoringresults. Acta Geodaetica et Cartographica Sinica, 2020, 49(5):547-556.

Chen J., Zhang X., Chen Q., Shen Y., Nie Y. (2022). Static Gravity Field Recovery and Accuracy Analysis Based on Reprocessed GOCE Level 1b Gravity Gradient Observations. EGU General Assembly 2022, Vienna, Austria, 23–27 May 2022, EGU22-6771, 10.5194/egusphere-egu22-6771.

Chen Q., Shen Y., Francis O., Chen W., Zhang X., Hsu H. (2018). Tongji-grace02s and Tongji-grace02k: High-Precision Static GRACE-only Global Earth's Gravity Field Models Derived by Refined Data Processing Strategies. Journal of Geophysical Research: Solid Earth, 123(7), 6111-6137, 10.1029/2018JB015641.

Chen, Y., Q. Ji, and X. Pang. Spatio-Temporal Variation of Antarctic Sea Ice Thickness Using Cryosat-2 Satellite Altimeter Data. Journal of Glaciology and Geocryology, 2019, 41(5):1214-1220.

Dang, Y., Jiang, T., Guo, C., Chen, B., Zhang, C., Yang, Q., Wang, Z. (2023). Determining the new height of Mount Qomolangma based on the International Height Reference System. Geo-spatial Information Science, DOI: 10.1080/10095020.2022.2128901 (SCI).

Dang, Y., Guo, C., Jiang, T., Zhang, Q., Chen, B., Jiang, G. (2020). Height measurement and determination of Mount Qomolangma. Acta Geodaetica et Cartographica Sinica, 50(4): 556-561.

Dang, Y., Jiang, T., Chen, J. (2022). Review on Research Progress of the Global Height Datum. Geomatics and Information Science of Wuhan University, 47(10): 1576-1586.

Ding S, Chen J. Preliminary building and application of seamless vertical datum of land and sea in Shandong province. Bulletin of Surveying and Mapping, 2019(S2): 293-297． DOI: 10.13474/j.cnki.11-2246.2019.0647.

Hao, R., X. Wan, and R. F. Annan. Enhanced Short-Wavelength Marine Gravity Anomaly Using Depth Data. IEEE Transactions on Geoscience and Remote Sensing, 2023, 61:1-9.

He, L., Chu, Y. , Xu, X. , & Zhang, T. Evaluation of the GRACE/GOCE Global Geopotential Model on estimation of the geopotential value for the China vertical datum of 1985(in Chinese). Chinese J.Geophys, 2019, 62(6): 2016-2026.

Fan, Y., W. Hao, B. Zhang, C. Ma, S. Gao, X. Shen, and F. Li. Monitoring the Hydrological Activities of Antarctic Subglacial Lakes Using CryoSat-2 and ICESat-2 Altimetry Data. Remote Sensing, 2022, 14(4):898.

Förste, C. , Bruinsma, S. L. , Abrikosov, O. , Lemoine, J. , Marty, J. C. , Flechtner, F. , Balmino, G. , Barthelmes, F. , & Biancale,

R. EIGEN-6C4 The latest combined global gravity field model including GOCE data up to degree and order 2190 of GFZ Potsdam and GRGS Toulouse, 2014.

Fu Y, Feng Y, Zhou D, et al. 2020. Accuracy assessment of global ocean tide models in the South China Sea using satellite altimeter and tide gauge data. Acta Oceanologica Sinica, 39(12): 1–10. DOI: 10.1007/s13131- 020-1685-y;

Fu Y, Zhou D, Feng Y, et al. Long-period solar annual and semiannual tidal contributions to the lowest normal low water in seas surrounding China. 2021, Ocean Science, Discuss. DOI: 10.5194/os-2021-3, 2021.

Gao, Xianwen, T. Jin, and H. Huang. Analysis on the Accuracy of Waveform Retracking for the Coastal Synthetic Aperture Radar Altimeter Data. Journal of Geodesy and Geodynamics, 2021, 41(1):56-61.

Gao, Xiang, X. Pang, and Q. Ji. Spatiotemporal Variation of Sea Ice Freeboard in the Antarctic Weddell Sea Based on CryoSat-2 Altimeter Data. Geomatics and Information Science of Wuhan University, 2021, 46(1):125-132.

Guan, B., Z. Sun, X. Liu, and Z. Zhai. Necessity for Filtering for Ionospheric Delay in the Applications of Satellitealtimetry. Progress in Geophysics, 2020, 35(6):2064-2067.

Guo, C., Nie, J., Tian J., Wang, B., Jin, X., Zhao, D. (2020). Analysis of Vertical Deformation with the Adaptive Fusion of GNSS and Leveling Elevation Variation. Geomatics and Information Science of Wuhan University, 45(1):7-12

Guo, C., Guo, X., Nie, J., Wang, B., Liu, X., Wang, H. (2021). Establishment of Vertical Movement Model of Chinese Mainland by Fusion Result of Leveling and GNSS. Geomatics and Information Science of Wuhan University, DOI: 10.13203/j.whugis20200167.

Guo, J., H. Luo, C. Zhu, H. Ji, G. Li, and X. Liu. Accuracy Comparison of Marine Gravity Derived from HY-2A/GM and CryoSat-2 Altimetry Data: A Case Study in the Gulf of Mexico. Geophysical Journal International, 2022a, 230(2):1267-1279.

Guo, J., L. Qi, X. Liu, X. Chang, B. Ji, and F. Zhang. High-Order Ionospheric Delay Correction of GNSS Data for Precise Reduced-Dynamic Determination of LEO Satellite Orbits: Cases of GOCE, GRACE, and SWARM. GPS Solutions, 2023, 27(1):13.

Guo, J., G. Wang, H. Guo, M. Lin, H. Peng, X. Chang, and Y. Jiang. Validating Precise Orbit Determination from Satellite-Borne GPS Data of Haiyang-2D. Remote Sensing, 2022b, 14(10):2477.

Guo, X., Guo, C., Nie, J., Wang, H., Tian J. (2021). Vertical Movement Model in Chinese Mainland Based on First Order Leveling Results. Geomatics and Information Science of Wuhan University, 47(3):361-368

Jekeli, C., Hyo Jin, Y. , & Jay Hyoun, K. The Offset of the South Korean Vertical Datum from a Global Geoid. Journal of Civil Engineering, 2012, 5(16): 816-821.

Jiang, T., Dang, Y., Zhang, C. (2020). Gravimetric geoid modeling from the combination of satellite gravity model, terrestrial and airborne gravity data: a case study in the mountainous area, Colorado. Earth Planets Space 72, 189.

Jiang, T., Dang, Y., Guo, C., Chen, B., Zhang, C. (2022). Realization of the international height reference system in the region of Mount Qomolangma. Acta Geodaetica et Cartographica Sinica, 51(8): 1757-1767.

Ji, H., X. Liu, C. Zhu, J. Yuan, B. Ji, and J. Guo. On Performance of CryoSat-2 Altimeter Data in Deriving Marine Gravity over the Bay of Bengal. Marine Geophysical Research, 2021, 42(4):39.

Jin, T., M. Zhou, H. Zhang, J. Li, W. Jiang, S. Zhang, and M. Hu. Analysis of Vertical Deflections Determined from One Cycle of Simulated SWOT Wide-Swath Altimeter Data. Journal of Geodesy, 2022, 96(4):30.

Ke H, Zhao J, Zhou F, et al. Establishment of Sea - Land Vertical Datum Transformation for Hydrography Combining with Geoid, Sea Surface Topography and Numerical Simulation of Tidal Wave Motion in the Yangtze Estuarine Waters.

Geo- matics and Information Science of Wuhan University, 2022, 47(5): 731-737. DOI: 10.13203/j.whugis20200601.

Ke H, Li F, Ai S, et al. Establishment of Chart Datum and Vertical Datum Transformation for Hydrography in the Chinese Great Wall Bay, Antarctic Peninsula. Journal of Surveying Engineering, 2020, 146(2): 05020003.

Liang, W. , Li, J. , Xu, X. , Zhang, S. , & Zhao, Y. A High-Resolution Earth's Gravity Field Model SGG-UGM-2 from GOCE, GRACE, Satellite Altimetry, and EGM2008. Engineering, 2020, 6(8): 860-878.

Liang, W. , Xu, X. , Li, J. , & Zhu, G. The determination of an ultra high gravity field model SGG-UGM-1 by combining EGM2008 gravity anomaly and GOCE observation data(In Chinese). Acta Geodaeticaet Cartographica Sinica, 2018, 47(4): 425-434.

Li, J. , Chu, Y. , & Xu, X. Determination of Vertical Datum Offset between the Regional and the Global Height Datum(in Chinese). Acta Geodaetica et Cartographica Sinica, 2017, 46(10): 1262-1273.

Li, J, Fu, Y, Tang, Q, et al. Accuracy assessment of a seamless depth datum model established on the basis of the global ocean tide model. Journal of Coastal Research, Special Issue No. 99, pp. 74-78. 2020. Coconut Creek (Florida), ISSN 0749-0208.

Li, L., M. Cai, X. Guan, and D. Chu. Piecewise Adaptive-Norm Trend Filtering Method for ICESat/GLAS Waveform Data Denoising. IEEE Access, 2020, 8:168965-168979.

Li, Q., L. Bao, and Y. Wang. Accuracy Evaluation of Altimeter-Derived Gravity Field Models in Offshore and Coastal Regions of China. Frontiers in Earth Science, 2021, 9:722019.

Li, Y., J. Guo, Y. Sun, J. Yuan, X. Chang, and H. Zhang. Inversion of Global Sea Level Change and Its Component Contributions by Combining Timevarying Gravity Data and Altimetry Data. Acta Geodaetica et Cartographica Sinica, 2022, 51(8):1768-1778.

Li, Z., X. Liu, G. Jinyun, J. Yuan, Y. Niu, and J. Bing. A New Method of Satellite Radar Altimeter Waveform Retracking Based on Waveform Derivative. Revista Internacional de Métodos Numéricos Para Cálculo y Diseño En Ingeniería, 2020, 36.

Lin, M., and Y. Jia. Past, Present and Future Marine Microwave Satellite Missions in China. Remote Sensing, 2022, 14(6):1330.

Liu, S., F. Li, and Y. Yang. Inversion of Sea Ice Thickness Variation in Beaufort Sea from 2011 to 2017Based on CryoSat-2 Data. Journal of Geodesy and Geodynamics, 2019, 39(12):1310-1316.

Michael G H D, Gaia P, Denise D, et al. EOT20: a global ocean tide model from multi-mission satellite altimetry. Earth System Science Data, 2021, 13(8): 3869-3884.

Niu, Y., J. Guo, J. Yuan, C. Zhu, M. Zhou, X. Liu, and B. Ji. Prediction of Sea Level Change in Japanese Coast Using Singular Spectrum Analysis Andauto Regression Moving Average. Chinese Journal of Geophysics, 2020, 63(9):3263-3274.

Ouyang, M. Research Progress and Prospects of Seabed Topography Inversion Fromaltimetry Data. Progress in Geophysics, 2022, 37(6):2291-2300.

Pavlis, N. K. , Holmes, S. A. , Kenyon, S. C. , & Factor, J. K. The development and evaluation of the Earth Gravitational Model 2008 (EGM2008). Journal of Geophysical Research, 2012, 117(B04): 1-38.

Peng, F., and X. Deng. Improving Precision of High-Rate Altimeter Sea Level Anomalies by Removing the Sea State Bias and Intra-1-Hz Covariant Error. Remote Sensing of Environment, 2020a, 251:112081.

Peng, F., and X. Deng. Validation of Sentinel-3A SAR Mode Sea Level Anomalies around the Australian Coastal Region. Remote Sensing of Environment, 2020b, 237:111548.

Peng, F., X. Deng, and X. Cheng. Quantifying the Precision of Retracked Jason-2 Sea Level Data in the 0–5 Km Australian

Coastal Zone. Remote Sensing of Environment, 2021, 263:112539.

Peng, F., X. Deng, and X. Cheng. Australian Coastal Sea Level Trends Over 16 Yr of Reprocessed Jason Altimeter 20-Hz Data Sets. Journal of Geophysical Research: Oceans, 2022, 127(3):e2021JC018145.

Sun, H., T. Jin, and C. Zhao. A Non-Uniform Density Distributed Point-Mass Method for the Fusion of Altimetric and Shipborne Gravity. Journal of Geomatics, 2021, 46(4):17-22.

Sun W. Research on the vertical datum model construction in the Ross Sea and surrounding waters. 2022, Shandong University of Science and Technology.

Sun, Z., B. Guan, Z. Zhai, and M. Ouyang. Research Progress of Ocean Satellite Altimetry and Its Recovery of Globalmarine Gravity Field and Seafloor Topography Model. Acta Geodaetica et Cartographica Sinica, 2022, 51(6):923-934.

Wang, W., Guo, C., Ding, L., Zhao, H. (2019). Elevation Change Analysis of the National First Order Leveling Points in Recent 20 Years. Acta Geodaetica et Cartographica Sinica, 48(1):1-8

Wu, F. , Zeng, A. , & Ming, F. Analyzing the long-term changes in China's National Height Datum. Advances in Space Research, 2020, 66: 1342-1350.

Wu, Y., Abulaitijiang, A., Featherstone, W.E., McCubbine, J.C., Andersen, O.B. (2019). Coastal gravity field refinement by combining airborne and ground-based data. Journal of Geodesy, 93(12):2569-2584.

Wan, X., R. F. Annan, S. Jin, and X. Gong. Vertical Deflections and Gravity Disturbances Derived from HY-2A Data. Remote Sensing, 2020a, 12(14):2287.

Wan, X., R. F. Annan, and W. Wang. Assessment of HY-2A GM Data by Deriving the Gravity Field and Bathymetry over the Gulf of Guinea. Earth, Planets and Space, 2020b, 72(1):151.

Wan, X., R. F. Annan, and Y. Y. Ziggah. Altimetry-Derived Gravity Gradients Using Spectral Method and Their Performance in Bathymetry Inversion Using Back-Propagation Neural Network. Journal of Geophysical Research: Solid Earth, 2023, 128(2):e2022JB025785.

Wan, X., R. Hao, Y. Jia, X. Wu, Y. Wang, and L. Feng. Global Marine Gravity Anomalies from Multi-Satellite Altimeter Data. Earth, Planets and Space, 2022a, 74(1):165.

Wan, X., S. Jin, B. Liu, S. Tian, W. Kong, and R. F. Annan. Effects of Interferometric Radar Altimeter Errors on Marine Gravity Field Inversion. Sensors, 2020c, 20(9):2465.

Wan, X., F. Wang, H. Guo, and B. Liu. Impact of Errors in Environmental Correction on Gravity Field Recovery Using Interferometric Radar Altimeter Observations. Remote Sensing, 2022b, 14(24):6299.

Wang, H., and Z. Huang. Waveform Decontamination for Improving Satellite Radar Altimeter Data Over Nearshore Area: Upgraded Algorithm and Validation. Frontiers in Earth Science, 2021, 9:748401.

Wang, J., Y. Yang, C. Wang, and L. Li. Accelerated Glacier Mass Loss over Svalbard Derived from ICESat-2 in 2019–2021. Atmosphere, 2022, 13(8):1255.

Wei, Z., J. Guo, C. Zhu, J. Yuan, X. Chang, and B. Ji. Evaluating Accuracy of HY-2A/GM-Derived Gravity Data With the Gravity-Geologic Method to Predict Bathymetry. Frontiers in Earth Science, 2021, 9:636246.

Wu, Yihao, X. He, J. Huang, H. Shi, H. Wang, Yunlong Wu, and Y. Ding. Comparison of Mean Dynamic Topography Modeling from Multivariate Objective Analysis and Rigorous Least Squares Method. Remote Sensing, 2022, 14(21):5330.

Xiao, F., S. Zhang, J. Li, T. Geng, Y. Xuan, and F. Li. Arctic Sea Ice Thickness Variations from CryoSat-2 Satellite Altimetry Data. Science China Earth Sciences, 2021, 64(7):1080-1089.

Xu, N., Y. Ma, Z. Wei, C. Huang, G. Li, H. Zheng, and X. H. Wang. Satellite Observed Recent Rising Water Levels of Global

Lakes and Reservoirs. Environmental Research Letters, 2022, 17(7):074013.

Xu, N., Y. Ma, W. Zhang, and X. H. Wang. Surface-Water-Level Changes During 2003–2019 in Australia Revealed by ICESat/ICESat-2 Altimetry and Landsat Imagery. IEEE Geoscience and Remote Sensing Letters, 2021, 18(7):1129-1133.

Yang, L., T. Jin, X. Gao, H. Wen, T. Schöne, M. Xiao, and H. Huang. Sea Level Fusion of Satellite Altimetry and Tide Gauge Data by Deep Learning in the Mediterranean Sea. Remote Sensing, 2021, 13(5):908.

Yang, Y., P. Moore, Z. Li, and F. Li. Lake Level Change From Satellite Altimetry Over Seasonally Ice-Covered Lakes in the Mackenzie River Basin. IEEE Transactions on Geoscience and Remote Sensing, 2021, 59(10):8143-8152.

Yu, D., and C. Hwang. Calibrating Error Variance and Scaling Global Covariance Function of Geoid Gradients for Optimal Determinations of Gravity Anomaly and Gravity Gradient from Altimetry. Journal of Geodesy, 2022, 96(9):61.

Yu, D., C. Hwang, O. B. Andersen, E. T. Y. Chang, and L. Gaultier. Gravity Recovery from SWOT Altimetry Using Geoid Height and Geoid Gradient. Remote Sensing of Environment, 2021, 265:112650.

Yuan, J., J. Guo, X. Liu, C. Zhu, Y. Niu, Z. Li, B. Ji, and Y. Ouyang. Mean Sea Surface Model over China Seas and Its Adjacent Ocean Established with the 19-Year Moving Average Method from Multi-Satellite Altimeter Data. Continental Shelf Research, 2020a, 192:104009.

Yuan, J., J. Guo, Y. Niu, C. Zhu, and Z. Li. Mean Sea Surface Model over the Sea of Japan Determined from Multi-Satellite Altimeter Data and Tide Gauge Records. Remote Sensing, 2020b, 12(24):4168.

Yuan, J., J. Guo, C. Zhu, C. Hwang, D. Yu, M. Sun, and D. Mu. High-Resolution Sea Level Change around China Seas Revealed through Multi-Satellite Altimeter Data. International Journal of Applied Earth Observation and Geoinformation, 2021, 102:102433.

Yuan, J., J. Guo, C. Zhu, Z. Li, X. Liu, and J. Gao. SDUST2020 MSS: A Global 1′ × 1′ Mean Sea Surface Model Determined from Multi-Satellite Altimetry Data. Earth System Science Data, 2023, 15(1):155-169.

Zhang, B., J. Liu, Z. Wang, T. Liu, and Q. Yang. Antarctic Ice-Shelf Thickness Changes from CryoSat-2 SARIn Mode Measurements: Assessment and Comparison with IceBridge and ICESat. Journal of Earth System Science, 2020, 129(1):127.

Zhang, Shengjun, A. Abulaitijiang, O. B. Andersen, D. T. Sandwell, and J. R. Beale. Comparison and Evaluation of High-Resolution Marine Gravity Recovery via Sea Surface Heights or Sea Surface Slopes. Journal of Geodesy, 2021, 95(6):66.

Zhang, S., O. B. Andersen, X. Kong, and H. Li. Inversion and Validation of Improved Marine Gravity Field Recovery in South China Sea by Incorporating HY-2A Altimeter Waveform Data. Remote Sensing, 2020a, 12(5):802.

Zhang, Shengkai, T. Geng, C. Zhu, J. Li, X. Li, B. Zhu, L. Liu, and F. Xiao. Arctic Sea Ice Freeboard Estimation and Variations From Operation IceBridge. IEEE Transactions on Geoscience and Remote Sensing, 2022, 60:1-10.

Zhang, S., J. Li, and X. Kong. Inversion of Global Marine Gravity Anomalies with Vertical Deflection Method Deduced from Laplace Equation. Acta Geodaetica et Cartographica Sinica, 2020b, 49(4):452-460.

Zhang, Shengkai, Y. Xuan, J. Li, T. Geng, X. Li, and F. Xiao. Arctic Sea Ice Freeboard Retrieval from Envisat Altimetry Data. Remote Sensing, 2021, 13(8):1414.

Zhang, Shengjun, R. Zhou, Y. Jia, T. Jin, and X. Kong. Performance of HaiYang-2 Altimetric Data in Marine Gravity Research and a New Global Marine Gravity Model NSOAS22. Remote Sensing, 2022, 14(17):4322.

Zhang, S., C. Zhu, F. Xiao, L. Yuan, and J. Li. An Approach of Sea Ice Freeboard Retrieval with Operation IceBridge Airborne

Topographic Mapper Data. Journal of Geomatics, 2019, 44(3):21-27.

Zhang, W., J. Yan, and F. Li. An Improved Coastal Marine Gravity Field Based on the Mean Sea Surface Height Constraint Factor Method. Remote Sensing, 2022, 14(16):4125.

Zhao, C., T. Jin, P. Qin, and L. Yang. An Improved Multi-Surface Function Method with Residual Constraint for the Fusion of Shipborne and Satellite Altimetry Derived Gravity Data. Acta Geodaetica et Cartographica Sinica, 2022:1-11.

Zhu, C., J. Guo, J. Gao, X. Liu, C. Hwang, S. Yu, J. Yuan, B. Ji, and B. Guan. Marine Gravity Determined from Multi-Satellite GM/ERM Altimeter Data over the South China Sea: SCSGA V1.0. Journal of Geodesy, 2020, 94(5):50.

Zhu, C., J. Guo, C. Hwang, J. Gao, J. Yuan, and X. Liu. How HY-2A/GM Altimeter Performs in Marine Gravity Derivation: Assessment in the South China Sea. Geophysical Journal International, 2019, 219(2):1056-1064.

Zhu, C., J. Guo, J. Yuan, Z. Li, X. Liu, and J. Gao. SDUST2021GRA: Global Marine Gravity Anomaly Model Recovered from Ka-Band and Ku-Band Satellite Altimeter Data. Earth System Science Data, 2022, 14(10):4589-4606.

Zhou D, Sun W, Fu H, et al. Accuracy assessment of three latest global ocean tide models in coastal areas of China. Advances in Marine Science, 2023, 41(1): 54-63.

Temporal Gravity Field Modelling by Satellite Gravimetry

Zhicai Luo[1], Qiujie Chen[2], Bo Zhong[3], Wei You[4], Yong Su[3,5], Hao Zhou[1], Fan Yang[1], Xiang Guo[1], Qiong Li[5], Xiancai Zou[3], Yunzhong Shen[2]

[1] *Institute of Geophysics and National Precise Gravity Measurement Facility (PGMF), Huazhong University of Science and Technology, Wuhan, China*

[2] *College of Surveying and Geo-informatics, Tongji University, Shanghai, China*

[3] *MOE Key Laboratory of Geospace Environment and Geodesy, School of Geodesy and Geomatics, Wuhan University, Wuhan, China*

[4] *Faculty of Geosciences and Environmental Engineering, Southwest Jiaotong University, Chengdu, China*

[5] *School of Civil Engineering and Geomatics, Southwest Petroleum University, Chengdu, China*

The main activities and recent achievements on the data processing, theoretical and methodological development of temporal gravity field recovery have been summarized shortly in the report since 2019, which provided respectively by Huazhong University of Science and Technology (HUST team), Tongji University (TJU team), Wuhan University (WHU team), Southwest Jiaotong University (SWJTU team), and Southwest Petroleum University (SWPU team).

1 Research outcomes of the HUST team

The first representative work of the HUST team is the temporal gravity field model series. To reach the prelaunch baseline for GRACE mission, Zhou et al. (2019) developed two new hybrid processing strategies. One is for kinematic empirical parameters of range-rate observations, the other is for arc-specific parameters. For the kinematic empirical parameters, the proposed filter predetermined strategy is used to ensure the temporal signals while the pure predetermined strategy is applied to reduce the temporal noise. Based on the GRACE L1B V02 data and AOD RL05 model, the monthly gravity field models **HUST-Grace2019** shows the notable noise reduction of 19% in terms of cumulative geoid differences when compared to Center for Space Research (CSR) RL05 model (Figure 1). Furthermore, based on the new released dataset including GRACE L1B V03 and AOD RL06 model, the new **HUST-Grace2020** model is developed and it is included in the International Centre for Global Earth Models (ICGEM).

Meanwhile, the HUST team proposes a new concept for determining temporal gravity field models via a couple of high-low satellite-to-satellit trakcing (HLSST) missions. As for the current HLSST mission consisting of a GNSS receiver and an accelerometer, it is expected to observe monthly (or weekly) gravity solution at the spatial resolution of about 1300 km (or 2000 km). As for satellite constellations, a significant improvement is expected by adding the second satellite or the third satellite with various inclinations. Moreover, the accuracy of weekly solution is expected to improve for three (or two) HLSST missions when compared to one HLSST mission. Due to the low financial costs, it is worthy to build a satellite constellation of HLSST missions to fill the possible gaps between the dedicated temporal gravity field detecting missions (Zhou et al., 2020).

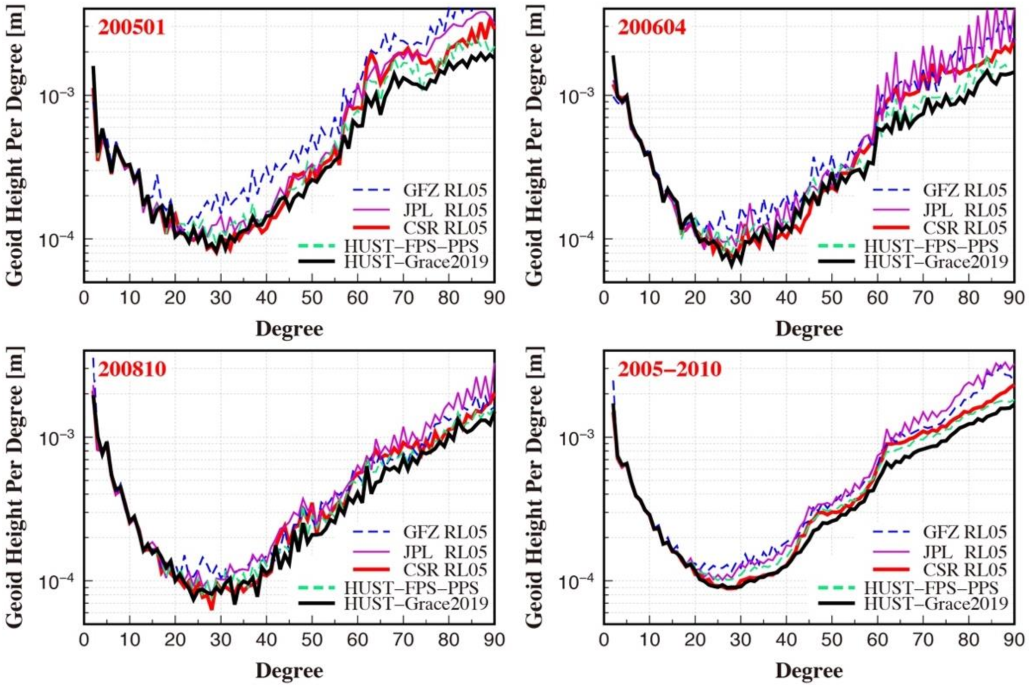

Figure 1. The geoid height per degree of GFZ RL05, JPL RL05, CSR RL05, HUST-FPS-PPS and HUST-Grace2019. The results in January 2005, April 2006 and October 2008 are presented, and that for the period January 2005 to December 2010 is also shown.

Another focus of the HUST team has been placed on the imperfect data processing from Level-1a to Level-1b. Typically, AOD (high-frequency non-tidal Atmosphere and Ocean De-aliasing) modelling, as one of the key prior model for temporal gravity recovery, has been seen as one major error source of the-state-of-the-art gravity mission, and likewise being a potential threaten to future gravity mission. On-going effort has been therefore made by HUST team in the past three years to refine the AOD modelling through densifying the vertical and time resolution of atmosphere mass with ERA-5 reanalysis data, and in this manner we have established a publicly available **HUST-ERA5** atmosphere de-aliasing product completely independent from the official RL06 but reaching better quality than RL06 (Yang et al., 2021), see Figure as below. Other efforts made by HUST team in terms of Level1a-to-Level1b include the refinement on attitude data processing, as which still remains non-negligible uncertainty so far. By fusing the star-cameras and gyroscope on-board, we has published a new attitude product **HUGG-01** (Yang et al., 2022). Evaluation of HUGG-01 against the official JPL-V04 has demonstrated an equivalent performance in the low-to-middle spectrum, with even a slightly lower noise level (in the high spectrum) than JPL-V04. Further analysis on KBR range-rate residuals and gravity recovery also indicates a minor discrepancy that is far below the sensitivity of the state-of-the-art satellite gravity mission, demonstrating a good agreement between HUGG-01 and JPL-V04.

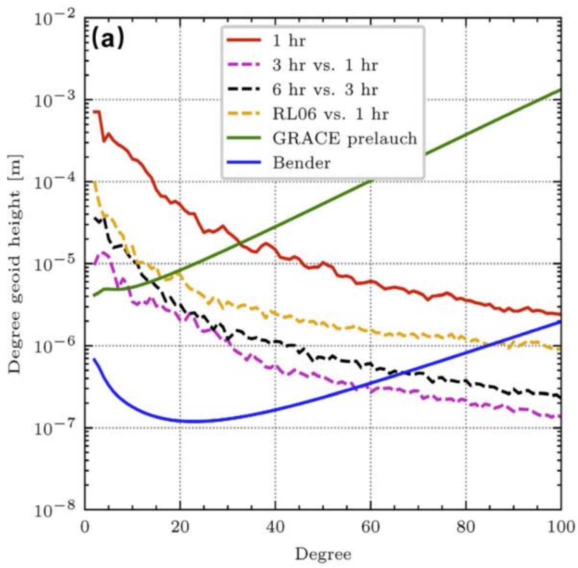

Figure 2. Evaluating 1-hourly HUST-ERA5 against RL06 in spectrum, with GRACE-prelaunch and Bender accuracy being as the reference.

2 Research outcomes of the TJU team

One of the most representative research outcomes is the development of an optimized short-arc approach (Figure 3), where the orbit integration length is successfully extended to 6 hours for a better signal-to-noise ratio and the colored noise of observation data is sufficiently taken into account by the filtering method. Based on the optimized short-arc approach, a refined GRACE monthly gravity field model series named **Tongji-Grace2018** has been produced, the quality of which is highly competitive to other state-of-art GRACE models (Chen et al., 2019). Moreover, considering the unconstrained time-variable GRACE spherical harmonic (SH) models are generally of low spatial resolution, especially after the indispensable filtering process, we developed a high-resolution SH model up to 180 degrees by incorporating spatial constraints determined from the filtered GRACE mass change estimates into the SH spectral domain. With this innovative regularization scheme, a time series of SH models named **Tongji-RegGrace2019** has been produced (Chen et al., 2021), which can be directly used without the need of any post-processing filtering. Comprehensive evaluations show that **Tongji-RegGrace2019** is of comparable quality in terms of both signal power and spatial resolution as the official Mascon solutions (Figure).

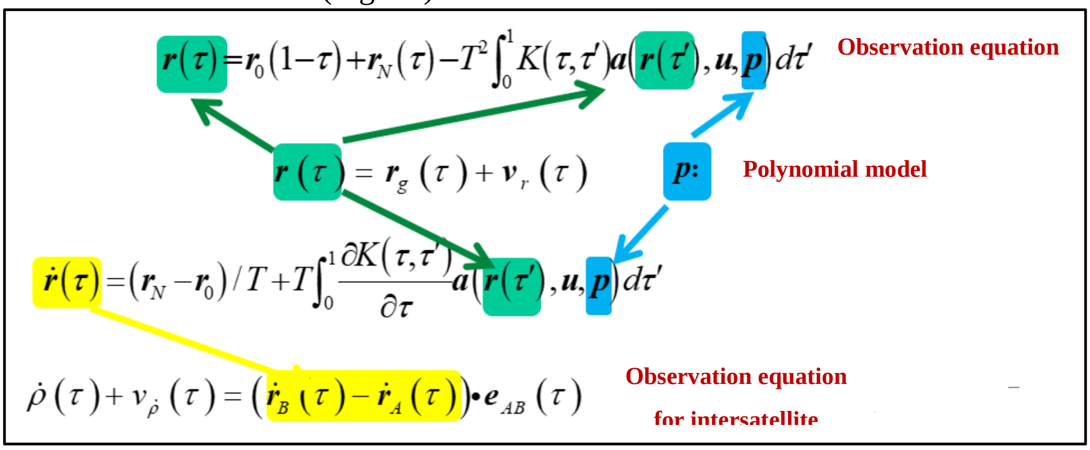

Figure 3. Optimized short-arc approach

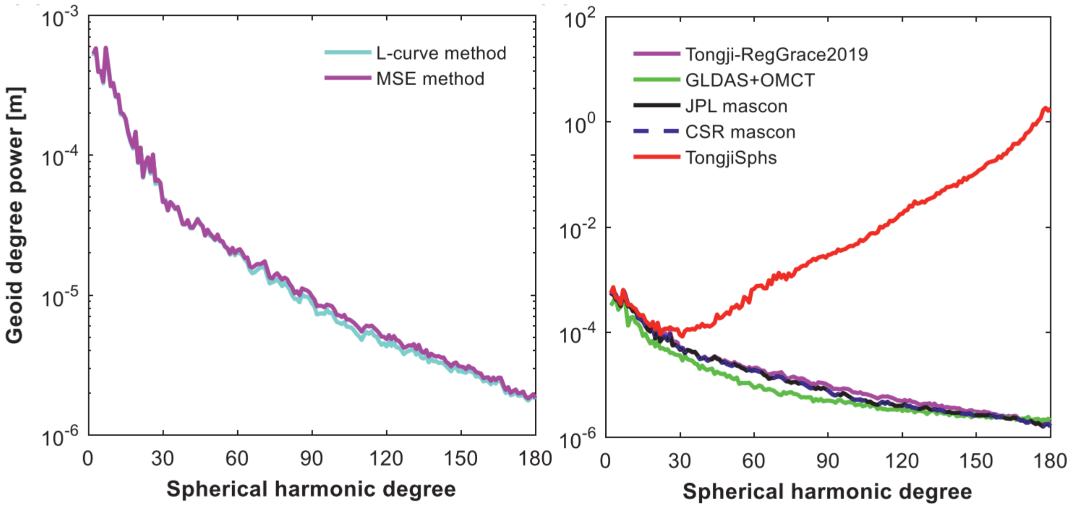

Figure 4. Geoid degree power of various models.

In addition, the team has focused on developing efficient methods for satellite geodetic data processing. On the one hand, an efficient variance component estimation (VCE) algorithm with rigorous trace calculation is proposed for large-scale least-squares problems, which is based on the local-global parameters partition scheme in satellite geodesy and is directly applicable to both the simplified yet common case where local parameters are unique to a single observation group and the generalized case where local parameters are shared by different groups of observations (Nie et al., 2022a). On the other hand, the team has systematically analyzed the connections and differences of four widely used noise-reduction approaches in GRACE gravity field recovery from both theoretical perspectives and numerical simulations, including the estimation of empirical accelerations (ACC method), the estimation of range-rate empirical parameters (KBR method), the use of fully populated covariance matrix (COV method) and the time series model-based filtering (FILT method). A unified theoretical framework is developed by the least-squares collocation model, which contributes to a deeper understanding of noise treatment in GRACE gravity field recovery (Nie et al., 2022b).

Combining the aforementioned theories and methods in processing observation data of low earth orbit (LEO) satellites prior to GRACE, a new time series of monthly gravity field models named **Tongji-LEO2021** has been developed and applied to directly quantify global mean ocean mass (GMOM) changes over the period January 1993 to December 2004 (Chen et al., 2022), since it is well-known that there are few time-variable gravity field models can be used before the GRACE era. In comparison to other measurements, Tongji-LEO2021-estimated GMOM change rates are nearly closed to the estimates from both Altimetry minus Steric observations and IGG-SLR-HYBRID solutions (Figure), indicating that the new model is able to provide an independent and accurate measure for studying the earlier global sea-level change.

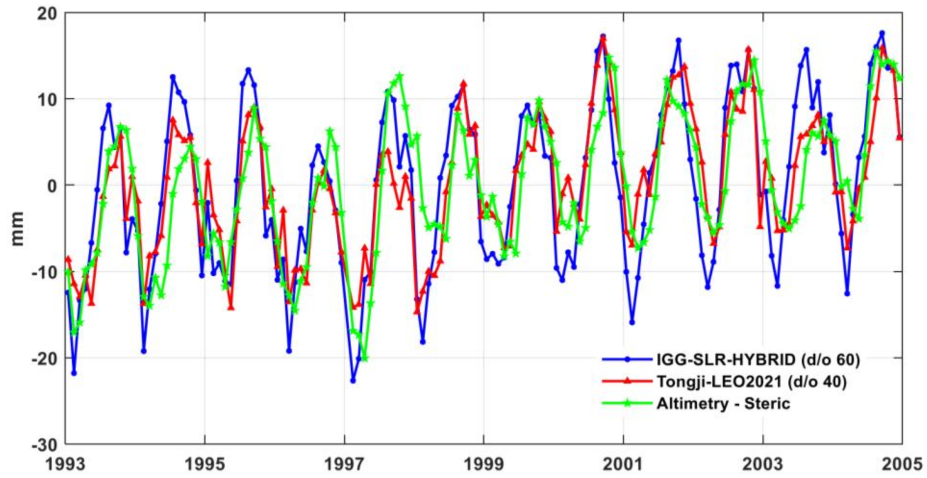

Figure 5. GMOM change estimates from Tongji-LEO2021, IGG-SLR-HYBRID solutions and Altimetry minus Steric observations covering the period January 1993 to December 2004.

3 Research outcomes of the WHU team

One of the WHU GRACE monthly gravity field solutions were produced using the classical dynamic approach. The first WHU time-series of monthly solutions (WHU RL01) were generated in 2017 based on the second release of GRACE Level-1B data. With the availability of the third release of the K-Band Ranging data and satellite attitude data (KBR1B RL03 and SCA1B RL03), the **WHU RL02** monthly solutions were produced. The background force models were also updated, mainly involving the static gravity fields (switch from EIGEN_6C4 to GOCO06s) and the atmosphere and ocean de-aliasing products (from AOD1B RL05 to AOD1B RL06). Additionally, the GRACE kinematic orbits, which were taken as pseudo observations when compiling WHU RL02, were generated in-house with integrated single- and double-differenced carrier phase integer ambiguity resolution (Guo et al. 2020b). For parameter setups, the accelerometer biases were modeled with three-order polynomials and the scales were modeled with a fully populated matrix on daily basis to account for thermal variations. Finally, WHU RL02 adopted the frequency-dependent data weighting method for both KBRR and kinematic orbits, and it is also included in the ICGEM. Compared to WHU RL01, the signal-to-noise ratios (SNRs) of RL02 over 180 major river basins are improved by 16% on average (Figure).

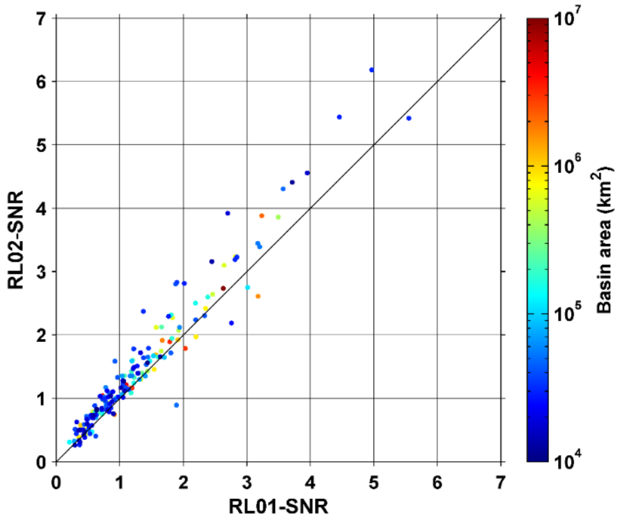

Figure 6. Signal-to-noise ratios over 180 major river basins

Another WHU GRACE monthly gravity field solutions are produced using the improved energy integral method. Based on the remove-compute-restore technique and improved energy balance equation, the precise geopotential difference (GPD) observations were estimated from GRACE Level-1B RL03 products according to the latest RL06 data processing standard (Zhong et al., 2022). To suppress the correlated noise of GRACE spherical harmonic (SH) solutions, we developed a series of constrained monthly gravity field solutions named **WHU-GRACE-GPD01s** from August 2002 to July 2016 using GRACE GPD observations (Zhong et al., 2023b). The constrained solutions were estimated using Kaula regularization, and the optimal regularization parameters were adaptively determined from GRACE data itself through variance component estimation. Extensive validations demonstrate that our constrained solutions are comparable to official sphereical harmonic (SH) solutions (GFZ, JPL, and CSR RL06) (Figure), and can be used without post-processing. The WHU-GRACE-GPD01s is also included in the ICGEM.

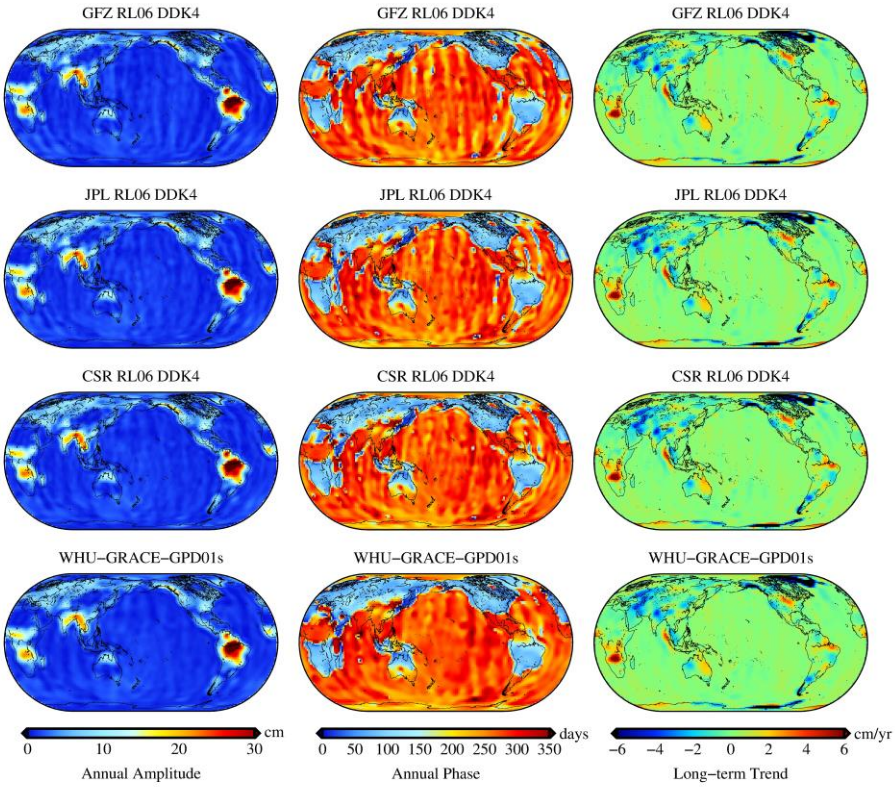

Figure 7. Annual amplitudes, annual phases, and long-term trends of global mass changes from the official unconstrained SH solutions (GFZ, JPL, and CSR RL06 with DDK4 filtering) and the constrained WHU-GRACE-GPD01s solutions over the period of January 2005 to December 2010.

To fill in the data gap between GRACE and GRACE Follow-On (GFO), other satellites' kinematic orbits derived from GPS-based high-low satellite-to-satellite tracking (hl-SST) data may be considered. We proposed an epoch-difference (ED) scheme in the context of the classical dynamic approach (CDA) to gravity field recovery. Compared to the traditional undifferenced (UD) scheme, the ED scheme can mitigate constant or slowly-varying systematic errors. To demonstrate the added value of the ED scheme, three sets of monthly gravity field solutions produced from six years of GRACE kinematic orbits are compared: two sets produced in-house (with the ED and UD scheme), and a set produced with the undifferenced scheme in the frame of the short-arc approach (SAA) (Zehentner and Mayer-Gürr 2015). As a reference, we use state-of-the-art ITSG-Grace2018 monthly gravity field solutions. A comparison in the spectral domain shows that the gravity field solutions suffer from a lower noise level when the ED scheme is applied, particularly at low-degree terms, with cumulative errors up to degree 20 being reduced by at least 20% (Figure). In the spatial domain, the ED scheme notably reduces noise levels in the mass anomalies recovered (Figure). In addition, the signals in terms of mean mass anomalies in selected regions become closer to those inferred from ITSG-Grace2018 solutions, while showing no evidence of any damping, when the ED scheme is used (Guo et al. 2020a).

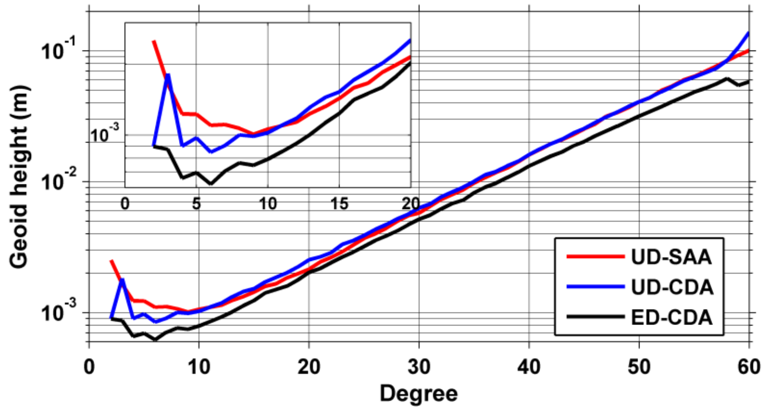

Figure 8. Geoid height errors per degree for different gravity field solutions (RMS values)

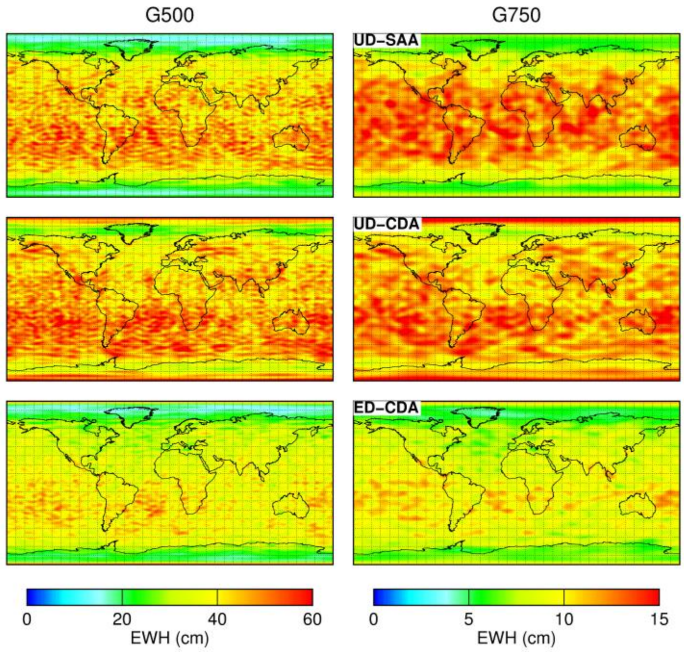

Figure 9. Geographical distribution of the gridded RMS differences with respect to ITSG2018 for different GPS-based solutions. The top, middle, and bottom rows show the results for the UD-SAA, UD-CDA, and ED-CDA solutions, respectively. G500/750: Gaussian smoothing filter with a 500/750 km radius.

In addition, the combination of high-low satellite-to-satellite tracking (HLSST) and satellite laser ranging (SLR) data is also investigated to determine the monthly gravity field solutions HLSST+SLR. The performance of the monthly HLSST+SLR solutions were evaluated in the spectral and spatial domains. Figure 10 shows that the accuracies of HLSST+SLR solutions are comparable to those from GRACE for SH coefficients below degree 10, and significantly improved compared to those of SLR-only and HLSST-only solutions (Zhong et al., 2021). It demonstrated that HLSST+SLR can be an alternative option to estimate temporal changes in the Earth gravity field, and can be used to monitor the large-scale mass transport during the data gaps between the GRACE and the GRACE follow-on missions.

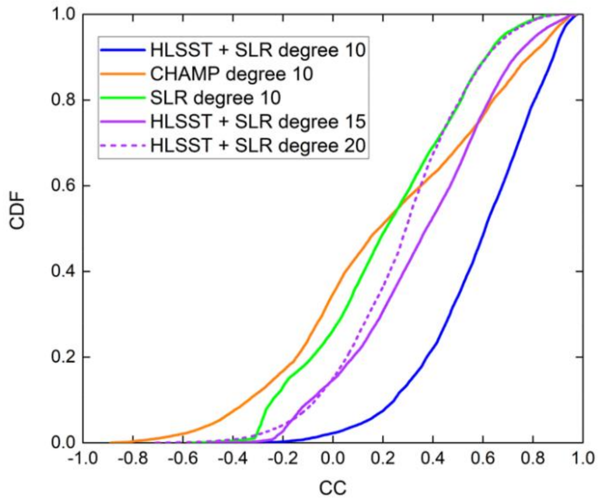

Figure 10. Cumulative distribution function (CDF) of spatial correlations from HLSST+SLR, CHAMP, SLR solutions with GRACE CSR. Note that the CC stands for coefficient correlation.

4 Research outcomes of the SWJTU team

Precise orbits provide the necessary position information for gravity satellite missions with the support of the on-board Global Navigation Satellite System (GNSS) receiver. The generated purely kinematic orbits are subsequently used as pseudo-observations in gravity field recovery. In the past three years, the SWJTU team has been dedicated to processing and producing precise kinematic orbits as an important part of our gravity field recovery routine. As shown in Figure , the GRACE-FO kinematic orbits can achieve centimeter-level precision with respect to the JPL precise science orbit (PSO).

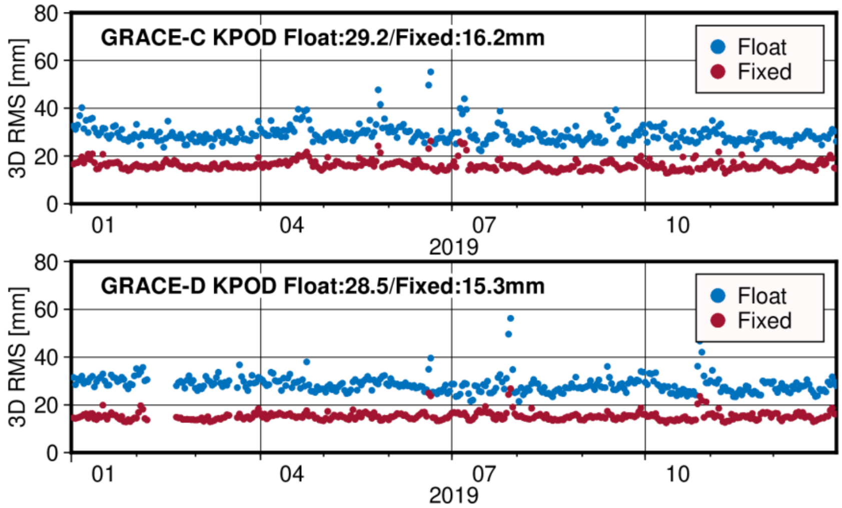

Figure 11. Daily RMS of orbit differences between GRACE-FO PSO products and orbits based on ambiguity float and fixed solutions.

Atmospheric and oceanic non-tidal high-frequency mass variations constitute a primary source of error that must be accurately modelled and removed before gravity field recovery. The SWJTU team utilized a first-generation atmospheric reanalysis dataset of China, CRA-40

(China Meteorological Administration's Global Atmospheric Reanalysis), to establish an atmospheric de-aliasing model called **CRA-40-AD**. For validation, CRA-40-AD displays comparable results with RL06 in geoid heights, as shown in Figure .

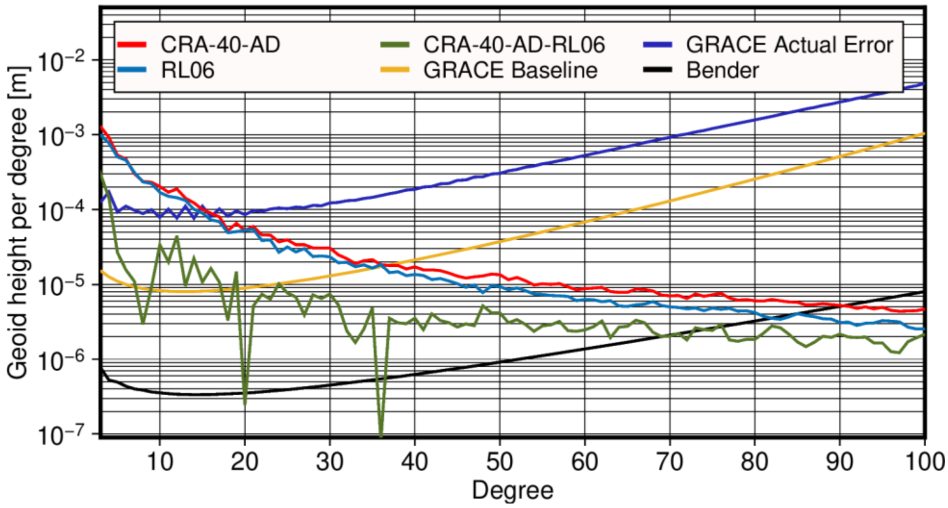

Figure 12. A comparison of geoid height per degree between CRA-40-AD and RL06, GRACE Baseline, Actual Error, and Bender Type curves are plotted as a reference.

Since 2019, the SWJTU team has been working on recovering a higher-precision temporal gravity field models with step-by-step improvements. In 2020, the **SWJTU-GRACE-RL02p** was derived based on original SWJTU-GRACE-RL01 with GRACE Level-1B RL03 data and a improved parametric strategy (Yu et al. 2021). Furthermore, we analyzed the residuals of SWJTU-GRACE-RL02p and considered the noises in calculated forces to decrease the correlations between residuals at different epochs to improve the quality of recoved models together with the determination of variance components of different observations. The new models present a better performance and the comparision of the two versions of models and official mdoels is shown in Figure .

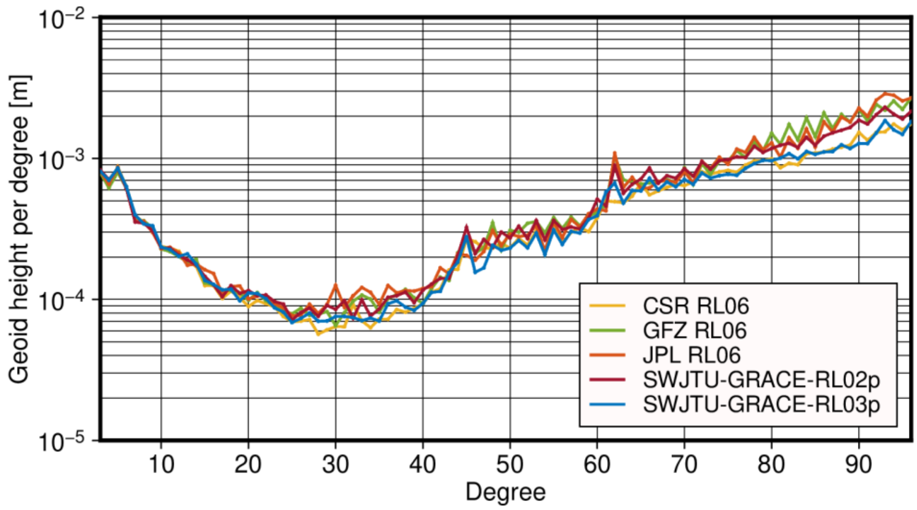

Figure 13. A comparison of geoid height per degree for 2009-03 with respect to EIGEN-6C4.

5 Research outcomes of the SWPU team

The SWPU team has extended the fundamental principle of the point mass model method and established a connection between satellite perturbation forces and surface mass changes in a rectangular coordinate system. By utilizing this improved method, we can directly compute surface mass changes using either gravity satellite observation data or a time-varying gravity field spherical harmonic coefficient model. The primary advantage of this method is its ability to enhance the theoretical model of the existing point mass model method. By including appropriate constraints in the computation of surface quality changes, the method can effectively reduce the impact of banded noise and signal leakage errors (Su et al., 2019). Furthermore, the team has meticulously processed the observation data over the entire lifecycle of GRACE and computed a 96 order monthly time-varying gravity field model **SWPU-GRACE2021** using dynamic methods. The model evaluation indicated that the overall accuracy of the model reached the sixth-generation official model's accuracy level, with the overall signal and noise levels conforming well with the CSR model (Su et al., 2022).

The team has also conducted investigations into the inversion of local surface mass changes using the Mascon method based on dynamic integration. This method is implemented by establishing a direct functional relationship between surface mass anomalies and satellite gravity observation data, thereby enabling the acquisition of high-precision and high-resolution inversion results of surface mass changes based on observation data and inversion region characteristics. To improve the ill-conditioned nature in the normal equation, spatiotemporal constraints (Mascon I) and prior information constraints (Mascon II) are introduced respectively. Taking the inversion of land surface mass changes in South America and Yangtze River Basin as examples, we utilized the GRACE Level-1B RL03 data and related mechanical models for 2005-2010 to calibrate orbit and accelerometer data, and obtained two sets of Mascon solution. By compared with the internationally released Mascon product (CSR/JPL Mascon RL06), Figure 14 shows that both constraint methods can yield relatively consistent inversion results, with the correlation coefficient of the Amazon basin reaching above 0.9. However, different Mascon solutions still exhibit certain differences in details. Without prior information, spatiotemporal correlation constraints can produce reliable Mascon inversion results. The Mascon solutions with different prior information models revealed that the inversion results do not rely on the prior model, but the detailed signals in the prior model have a certain impact on the inversion results. Hence, when abundant models or observation data exist in the study area, joint inversion of multi-source observation data can be conducted through prior information constraint methods (Li et al. 2020; Zhong et al., 2023a).

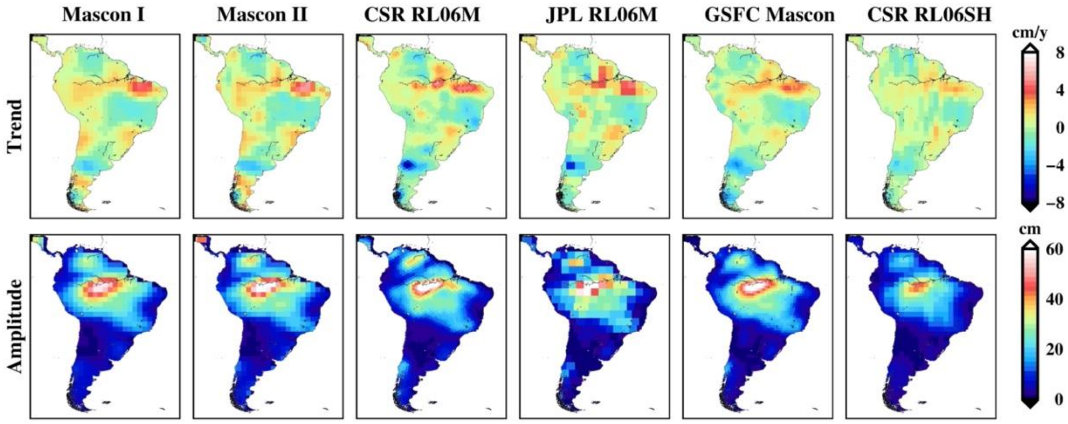

Figure 14. Spatial distribution of the amplitude and trend of land surface mass changes in South America from 2005 to 2010

Bibliography

Chen Q., Shen Y., Chen W., et al. (2019). An optimized short-arc approach: Methodology and application to develop refined time series of Tongji-Grace2018 GRACE monthly solutions. Journal of Geophysical Research: Solid Earth, 124(6), 6010-6038. https://doi.org/10.1029/2018JB016596.

Chen Q., Shen Y., Kusche J., et al. (2021). High-Resolution GRACE Monthly Spherical Harmonic Solutions. Journal of Geophysical Research: Solid Earth, 126(1), e2019JB018892. https://doi.org/10.1029/2019JB018892.

Chen Q., Wang F., Shen Y., et al. (2022). Monthly Gravity Field Solutions from Early LEO Satellites' Observations Contribute to Global Ocean Mass Change Estimates over 1993~2004. Geophysical Research Letters, e2022GL099917. https://doi.org/10.1029/2022GL099917.

Guo X, Ditmar P, Zhao Q, Xiao Y (2020a). Improved recovery of temporal variations of the Earth's gravity field from satellite kinematic orbits using an epoch-difference scheme. Journal of Geodesy, 94(8). doi: 10.1007/s00190-020-01392-6.

Guo X, Geng J, Chen X, Zhao Q (2020b). Enhanced orbit determination for formation-flying satellites through integrated single- and double-difference GPS ambiguity resolution. GPS Solutions, 24(1). doi: 10.1007/s10291-019-0932-1.

Li Q, Luo Z C, Zhong B, et al. Mascon method based on different constraints for inversion of regional surface mass changes, Annual Meeting of Chinese Geoscience Union (CGU), Oct, 2020, Chongqing, China (in Chinese).

Nie Y., Shen Y., Pail R., et al. (2022a). Revisiting Force Model Error Modeling in GRACE Gravity Field Recovery. Surveys in Geophysics, 43, 1169-1199. https://doi.org/10.1007/s10712-022-09701-8.

Nie Y., Shen Y., Pail R., Chen Q. (2022b). Efficient variance component estimation for large-scale least-squares problems in satellite geodesy. Journal of Geodesy, 96, 13. https://doi.org/10.1007/s00190-022-01599-9

Su Y, Zheng W L, Yu B. et al. (2019) Surface mass distribution derived from three-dimensional acceleration point-mass modeling approach with spatial constraint methods. Chinese Journal of Geophysics (in Chinese). 62(2): 508-519. doi: 10.6038/cjg2019L0770.

Su Y, Li, J C, Zou, X C, Xu X Y, Wang C Q, Yu B, Li Q. (2022). SWPU-GRACE2021: a new temporal gravity model from GRACE. GFZ Data Services. https://doi.org/10.5880/icgem.2022.001.

Yang F, Liang L, Wang C, Luo Z. (2022). Attitude Determination for GRACE-FO: Reprocessing the Level-1A SC and IMU Data. Remote Sensing. 14(1):126. https://doi.org/10.3390/rs14010126

Yang, F., E. Forootan, C. Wang, J. Kusche, and Z. Luo. (2021). A New 1-Hourly ERA5-Based Atmosphere De-Aliasing Product for GRACE, GRACE-FO, and Future Gravity Missions, Journal of Geophysical Research: Solid Earth, 126 (9), e2021JB021, doi:10.1029/2021JB021926.

Yu B, You W, Fan D-M, Su Y, Nigatu ZM (2021). A comparison of GRACE temporal gravity field models recovered with different processing details. Geophysical Journal International 227(2):1392-1417. https://doi.org/10.1093/gji/ggab279

Zehentner N, Mayer-Gürr T (2015). Precise orbit determination based on raw GPS measurements. Journal of Geodesy, 90(3): 275-286. doi: 10.1007/s00190-015-0872-7.

Zhong, B., Li, Q., Chen, J. & Luo, Z. (2022). A dataset of GRACE intersatellite geopotential differences from April 2002 to July 2016 (Version V2) [Dataset], Science Data Bank, doi: 10.11922/sciencedb.j00001.00365.

Zhong B, Li Q, Li X P, et al. (2023a). Basin-scale terrestrial water storage changes inferred from GRACE-based geopotential differences: a case study of the Yangtze River Basin, China. Geophysical Journal International, 233(2):1318-1338.

Zhong, B., Li, X., Chen, J. & Li, Q. (2023b). WHU-GRACE-GPD01s: A series of constrained monthly gravity field solutions derived from GRACE-based geopotential differences. Earth and Space Science, 10(4), e2022EA002699.

Zhong, L., Sośnica, K., Weigelt, M., Liu, B. & Zou, X. (2021). Time-variable gravity field from the combination of HLSST and SLR. Remote Sensing, 13(17): 3491.

Zhou, H., Zhou, Z. & Luo, Z. (2019). A new hybrid processing strategy to improve temporal gravity field solution. Journal of Geophysical Research: Solid Earth, 124(8), 9415-9432.

Zhou, H., Zhou, Z., Luo, Z., Wang, K. & Wei, M. (2020). What can be expected from GNSS tracking of satellite constellations for temporal gravity field model determination? Geophysical Journal International, 222, 661-677.

Progress and Achievements of Wide-area Real-time Precise Positioning

Xiaohong Zhang[1], *Yidong Lou*[1], *Xingxing Li*[1], *Shengfeng Gu*[1], *Xin Li*[1], *Pan Li*[1], *Xiaodong Ren*[1], *Xiaolei Dai*[1]

[1] *Wuhan University*

1 Overview

Nowadays, there is an increasing demand for wide-area, real-time, and high-precision positioning in support of mass-market applications such as smartphones, the Internet of Things (IoT), and the automotive industry. From 2019 to 2023, many Chinese scholars have conducted extensive research on wide-area real-time precise positioning models, methods, and system applications, leading to a series of innovative achievements. These achievements can be broadly categorized into several aspects:

(1) Real-time precise satellite orbit and clock

Real-time precise satellite orbit and clock corrections are prerequisites for wide-area real-time precise positioning. Numerous researchers have conducted research on orbit determination models, clock estimation models, ambiguity resolution, and efficiency improvement to provide precise and reliable orbit and clock products for real-time precise positioning.

(2) Real-time FCB and precise atmospheric products

Real-time FCB and precise atmospheric products play a crucial role in achieving rapid and precise positioning. In the past four years, along with the construction and modernization of GNSS, especially the completion of BeiDou-3, Chinese researchers have made continuous progress in refining the real-time GNSS FCB estimation, global/regional precise ionospheric and tropospheric modeling, and providing high-quality FCB and atmospheric products to users for high-precision positioning applications.

(3) Systems construction and commercial applications

Currently, China has established its wide-area real-time precision positioning system (such as SBAS and PPP-B2b) by providing precise satellite corrections via geostationary earth orbit (GEO) satellites. Besides, several Chinese companies are also devoted to constructing commercial high-precision systems (such as Qianxun XStar, Hi-Target Hi-RTP, UniStrong Atlas), to provide centimeter-level augmentation services in China and surrounding areas.

(4) Future development: LEO augmentation

Presently, the rapid development of the LEO constellation brings innovative opportunities for satellite navigation. The fusion of LEO and GNSS, which brings significant improvement in satellite visibility and spatial geometry, is expected to further enhance the performance of PPP and finally provide a wide-area real-time and accurate positioning service. Therefore, Chinese scholars started to pay attention to LEO-augmented GNSS with the focus on its advantages for PPP rapid convergence, ambiguity resolution, global ionosphere modeling, etc.

2 Real-time GNSS Satellite Orbit Determination

Ultra-rapid orbit determination

Due to the high accuracy of the satellite dynamical model, real-time GNSS satellite orbits are typically generated using predicted methods, such as the IGS ultra-rapid products. These orbits are extrapolated from batch least-squares (LSQ) POD solutions based on the latest available observations, and the accuracy and reliability depend on the stability of the satellite motion and force model, as well as the predicting duration. Various factors that impact the accuracy of precise orbit determination have been explored, such as the second- and third-order ionospheric corrections and different solar radiation pressure (SRP) models (Chen et al. 2019; Liu et al. 2019; Li et al. 2019, 2020; Yuan et al. 2020). Efficient processing strategies have also been developed to shorten the ultra-rapid updated time and improve orbit accuracy. Li et al. (2019) and Zhao et al. (2018) reduced the ultra-rapid updated time from 6h and 3h to 1h, resulting in an orbit improvement of about 20%~40%. The IGS analysis center of WHU has also released hourly-updated ultra-rapid orbit products, including GPS, GLONASS, Galileo, and BDS (ftp://igs.gnsswhu.cn/pub/gps/products/MGEX).

Filter-based real-time orbit determination

In addition to the traditional batch LSQ and orbit prediction method, the filter-based method has been adopted in recent years to produce high-quality real-time orbit products. Duan et al. (2019) found that real-time POD results are more accurate than 6-h predicted orbits when the same tracking stations are involved. The filter-based method allows dynamic noise and orbit states to be tuned at each epoch, making it suitable for real-time POD of orbital maneuver satellites for stable and continuous orbit products (Dai et al. 2019). The ambiguity resolution (AR) method has been used for real-time POD in both double-differenced (DD) (Li et al. 2019) and undifferenced (UD) (Kuang et al. 2021; Dai et al. 2022) methods. Generally, AR improves the 3D RMS of filter-based orbit solutions by 40%~45%, with the average 3D RMS of the filter orbits being smaller than that of the ultra-rapid products from WHU (Figure 1). In terms of the convergence time and accuracy of kinematic PPP AR, the better performance of the filter orbit products is validated compared to the ultra-rapid orbit products (Lou et al. 2022).

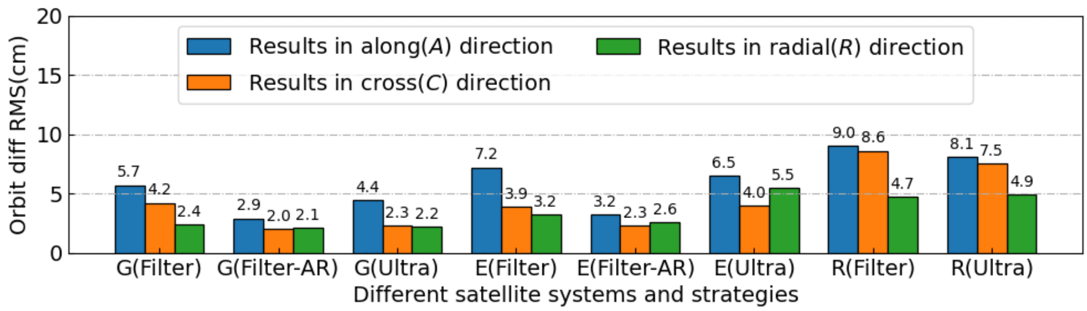

Figure 1. Average orbit accuracy of filtering solutions and ultra-rapid products from WHU for GPS, Galileo, and GLONASS satellites compared with the final products of CODE

3 Real-time GNSS Satellite Clock Estimation

Satellite clock estimation model

For the real-time clock estimation, three models are generally adopted, namely the undifferenced model (UD), epoch-differenced model (ED), and mixed model (MD). Two function models, namely the undifferenced model with all estimated parameters and the high-rate model introducing ambiguity estimates from the latest undifferenced model, were combined to improve the processing efficiency (Liu et al. 2019). A modified mixed-differenced approach for estimating multi-GNSS real-time clock offsets is presented, which further adds a satellite-differenced process and improves efficiency (Chen et al, 2018). Zhao et al. (2020) investigated the impacts of clock datum and initial clock of MD approach and proposed a flexible strategy for estimating real-time clock corrections, which consists of the clock prediction and the initial clock bias (ICB) bridging.

For traditional real time clock estimation, significant data discontinuity may arise an arbitrary clock jump between adjacent epochs. Shi et al. (2019) developed the oscillator noise model for the satellites of GPS, GLONASS, BDS, and Galileo accord ing to the oscillator type as well as the block type, then introduced this oscillator noise model in real time multi-GNSS satellite clock estimation to improve the stability and smoothness of clock estimates.

Efficient processing method

A huge number of carrier-phase ambiguities estimated in the UD method significantly degrades the efficiency, in particular for multi-constellation or high-rate satellite clock estimation. Gong et al. (2018) utilized the square root information filter based on the QR factorization and ambiguity resolution to significantly reduce the computational load. The sequential least square adjustment with an adapted online quality control procedure was proposed to decrease the calculation time (Fu et al. 2019). Cao et al. (2022) developed a high-rate clock estimation algorithm without an external complex matrix library, which can be easily implemented in cross-platforms. Li et al (2022) introduced OpenMP and OpenBLAS to accelerate the processing of multi-GNSS clock estimation. Compared to the traditional serial strategy, the computation efficiency is significantly improved by more than 70% (Figure 2).

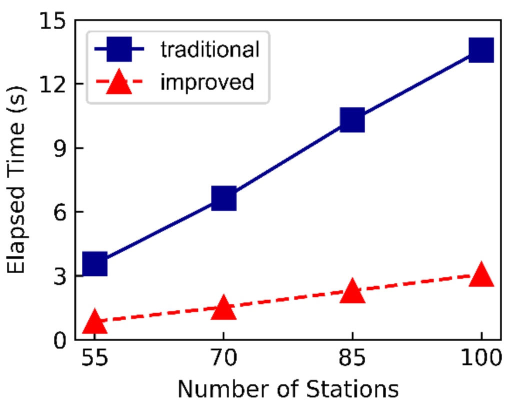

Figure 2. Elapsed time of quad-system clock estimation with 55-, 70-, 85-, and 100-station networks based on two computing strategies

Ambiguity fixed clock solution

With the constraint of fixed ambiguities, the traditional float-ambiguity clock solution is further refined, resulting in ambiguity-fixed clock solution. An undifferenced ambiguity fixing algorithm is proposed for the classical real-time GNSS clock estimation without requiring modifications to the current data processing strategy and product consistency (Dai et al. 2019). Yang et al. (2019) developed an undifferenced ambiguity-fixed BDS satellite clock estimation method with triple-frequency ambiguity resolution, which contributes to both the initialization time and accuracy. Xie et al. (2023) proposed a dual-thread integer ambiguity resolution method, which realizes rapid re-convergence and high accuracy in multi-GNSS real-time clock estimation in case of the interruption.

4 Real-time FCB estimation

Multi-GNSS FCB estimation

The multi-GNSS FCB and integer clock estimation method is promoted. Li et al. (2019) developed a multi-GNSS integer recovery clock (MIRC) model that improves real-time clock estimates. The average computation time per epoch for 150 stations is improved by 97.1% compared to standard float clock estimation. Fu et al. (2022) proposed a Kalman filter-based online FCB determination method for satellite clock estimation, achieving wide-lane (WL) and narrow-lane (NL) FCB estimation accuracy of 0.004 cycles and 0.080 cycles, respectively. Hu et al. (2022) assessed BDS FCB and demonstrated that the inter-system bias between BDS-2 and BDS-3 should be taken into consideration in BDS PPP. Moreover, BDS-3 outperforms BDS-2 in FCB stability, positioning accuracy, and convergence time.

Multi-frequency FCB estimation

The multi-frequency FCB is also investigated to fully exploit the multi-GNSS signal resource. Li et al. (2020) estimated phase and code biases of Galileo and BDS-3 binary offset carrier (BOC) signals, revealing Galileo E5a/E5b/E5ab signals and BDS-3 B2a/B2b signals exhibit the same phase biases with the resultant extra-wide-lane (EWL) FCBs very close to zero. Geng and Guo (2020) estimated the uncombined Galileo and BeiDou-3 multi-frequency phase biases and achieved single-epoch decimeter-level positioning using WL ambiguity resolution. Geng et al. (2020) estimated the triple-frequency GPS/BeiDou/Galileo/QZSS FCBs and found that EWL, WL, and NL FCBs were quite stable over time with standard deviations of less than 0.005, 0.025, and 0.030 cycles, respectively. The time-to-first-fix of triple-frequency PPP AR can be reduced from 9 min to 6 min compared with the legacy double-frequency solution. Jiang et al. (2022) estimated the multi-frequency phase OSB using the geometry-free and ionospheric-free (GF-IF) combination, achieving centimeter-level positioning accuracy with 3-h observation session. Furthermore, Geng et al. (2022) generated the GNSS OSB corrections for all-frequency PPP ambiguity resolution.

Real-time FCB estimation model refinement

Chinese researchers also focused on refining the GNSS error correction model to improve the FCB quality. Qu et al. (2021) demonstrated that the IGS ultra-rapid orbits errors significantly degrade the accuracy of real-time NL FCBs. Geng et al. (2021) identified the necessity of considering the differences in antenna phase center correction among frequencies in the Melbourne-Wübbena (MW) combination for WL FCB estimation. Cui et al. (2021) estimated receiver-type-dependent WL FCBs and discovered that deviations of up to 0.3 cycles can exist among different types of receivers. Shi et al. (2022) observed that signal distortion biases (SDBs) originating from receivers can significantly impact the FCB estimation of GPS and BDS, whereas the effect on Galileo is negligible (Figure 3). The application of SDBs led to an improvement of 46% and 13% in the accuracies of WL and NL FCBs, respectively. Furthermore, Zheng et al. (2023) reported that the correction of multipath errors resulted in a decrease in the mean RMS of NL FCB from 0.086 to 0.075 cycles.

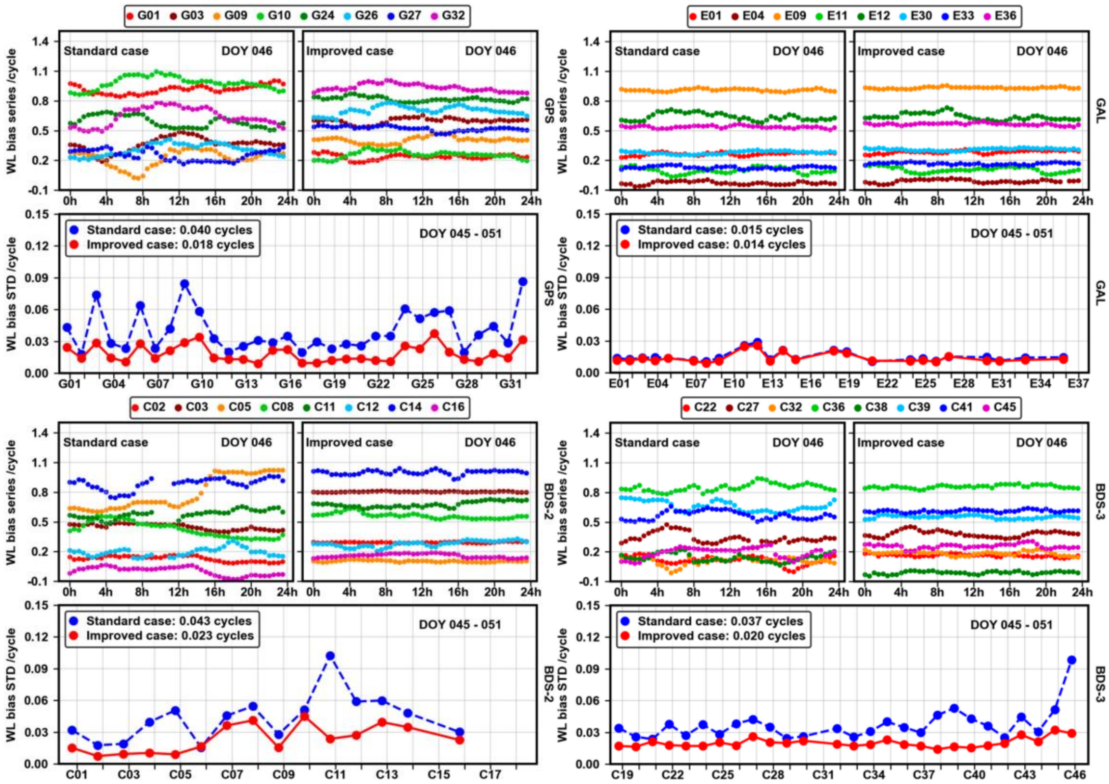

Figure 3. WL phase bias series on DOY 46, 2021 and the corresponding STDs across 7 days for GPS, Galileo, BDS-2, and BDS-3 before and after the calibration of signal distortion biases

5 Real-time ionospheric and tropospheric model

Ionosphere modeling

High-precision ionospheric models require precise extraction of ionospheric total electron content (TEC) measurements. The PPP AR method was employed to extract ionospheric observations from phase observations based on undifferenced integer ambiguity (Ren et al.

2020), which improves the precision of the TEC observations by 91.7% and 67.3% compared to the traditional PL-C and UD-PPP methods. Besides, Xu et al (2022) applied GNSS dual-frequency measurements derived from smartphone in the analysis of the performance of ionospheric TEC, which revealed that using consumer-level GNSS chipsets with optimal antennas in ionospheric studies is feasible.

In recent years, a series of novel ionosphere model such as two spherical harmonic regional real-time ionospheric model (Li et al 2019), Satellite-based Ionospheric Model (Li et al. 2022), Quasi-4-Dimension Ionospheric Modeling (Q4DIM, Gu et al 2022), Conventional Long Short-Term Memory (ConvLSTM)-based ionospheric model (Gao et al 2023), multi-layer VTEC model (Sui et al. 2023) was proposed. The results show that the proposed new models outperform the GIM and RIM products and significantly improve the convergence time of PPP. Currently, two institutions in China starts to provide real-time global ionospheric grid map, namely the Chinese Academy of Sciences (CAS, Li et al. 2020) and Wuhan University (WHU). Figure 4 gives an example of real-time global VTEC maps from CAS.

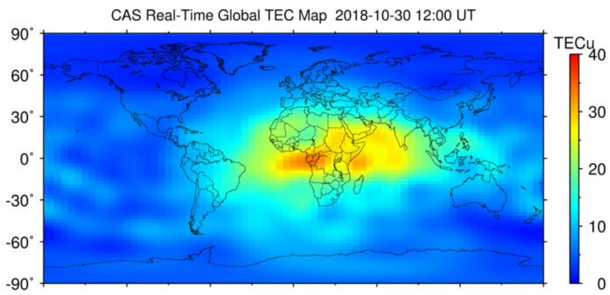

Figure 4. Real-time global VTEC maps from CAS on October 30, 2018, at 12:00 UT

Troposphere modeling

With the rapid development of satellite navigation systems around the globe, the demand for real-time and high-accuracy troposphere models has been growing dramatically. The traditional Hopfield and Saastamoinen ZTD models are refined by adding annual and semi-annual periodic terms and using the Back-Propagation Artificial Neutral Network (Yang et al. 2021). A new simplified zenith tropospheric delay model for GNSS real-time applications using numerical weather prediction data from the NCEP was established (Mao et al. 2021). Huang et al. (2023) derived an improved global grid ZTD model considering the height scale factor. To further improve the accuracy and spatial-temporal resolution of tropospheric products, a series of multi-source real-time tropospheric delay model that uses ground-based GNSS observations, meteorological data (such as ERA5), and empirical GPT2w models were developed (Yao et al. 2019; Xia et al. 2023; Lu et al. 2023).

6 Wide-area real-time precise positioning service

BDS high-precision positioning service

The BDSBAS service broadcasts various wide-area differential corrections, including satellite orbit/clock corrections, ionospheric grids, and satellite partition comprehensive corrections, through the B1C signal of GEO satellites (Yang et al. 2022). Users in the BDS GEO coverage areas can achieve decimeter-level positioning in real-time and the experiment results show that the RMS of the positioning errors for static/kinematic dual-frequency PPP is 12 cm/16 cm and 18 cm/20 cm in the horizontal and vertical components, respectively. With regard to the convergence performance, the horizontal and vertical positioning errors of kinematic PPP can converge to 0.5 m in less than 15 min and 20 min(Chen et al. 2021). PPP-B2b broadcasts precise orbit, clock offset, and DCB through BDS-3 GEO B2b_I navigation message for PPP users over China. The typical broadcast interval is 48 seconds and 6 seconds for orbit and clock, respectively (Yang et al. 2022). As evaluated by Lan et al. (2022), the precision of PPP-B2b orbits are 9.42 cm, 21.26 cm, and 28.65 cm in the radial, along-track, and cross-track components, while the accuracy of PPP-B2b clock is 0.18 ns, which meets the real-time kinematic decimeter-level positioning needs of PPP users.

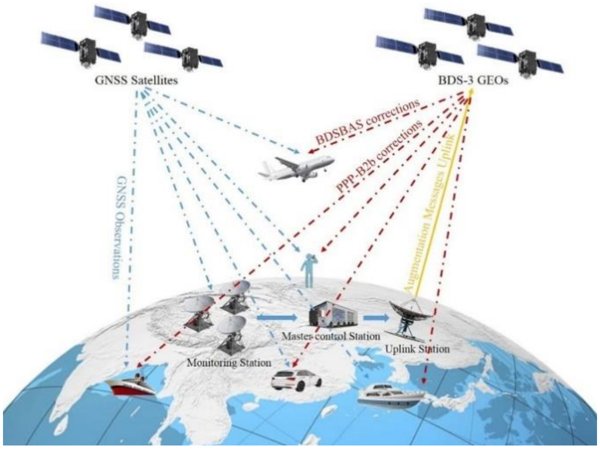

Figure 5. BDSBAS and PPP-B2b service of BDS-3

Commercial high-precision positioning service

Besides the built-in high-precision positioning service of BDS, several commercial companies, such as Qianxun, Sixents Technology, and China Mobile have successively established their high-precision service system. All these companies can provide high-precision positioning service through several thousands of stations in China, and the users within this region can get a positioning precision of centimeters to millimeters (Shi et al. 2022). More recently, Qianxun has declared that instantaneous centimeter-level positioning can be achieved all over the world through their PPP-AR technology.

Public high-precision positioning service

Attributed to the Real-Time Working Group (RTWG) of the International GNSS Service (IGS), Wuhan University has provided the real-time BDS/GNSS high precision orbit and clock for the worldwide PPP users. Li et al. (2022) compared SSR products from IGS RTS ACs (analysis centers), and the results indicated that Centre National D’Etudes Spatiales (CNES) and GNSS Research Center of Wuhan University (WHU) provide the most complete products with the best quality, with one-dimensional BDS orbit precision of MEO better than 10 cm and clock precision better than 0.35 ns. Concerning the potential applications of RTS for timing, Guo et al. (2022) further assessed the datum stability of WHU RT clock products, which is about 3.05E−13/120 s.

7 Performance of BDS-3 PPP-B2b Services

In addition to standard positioning, navigation, and timing (PNT) services, the BDS-3 also provides PPP service through B2b signals of GEO satellites (PPP-B2b). PPP-B2b service is a satellite-based service, which provides the precise orbits, clock offsets, and difference code bias (DCB) corrections of GPS and BDS-3 satellites to users in China and its surrounding areas (80°E~155°E，5°S~55°N). The central frequency of PPP-B2b signal is 1207.14 MHz and the bandwidth is 20.46 MHz (Yang et al. 2020, 2021, 2022).

Service coverage of PPP-B2b service

The PPP-B2b service coverage is relatively even across all of Asia, with the best coverage in eastern China (Tao et al. 2021). The number of GPS and BDS-3 satellites that can match and recover real-time products is about 5~7, and the number of BDS-3 satellites is about 6~8. Overall, there are fewer GPS satellites available for PPP-B2b than BDS-3 satellites. Liu et al. (2022) indicated that the availability of PPP-B2b is highest in eastern China and decreases gradually toward the edge of the service area. In Wuhan, the average availability of GPS is not less than 80%, and the average availability of BDS-3 is about 90%. In order to improve the availability of satellite-based augmentation diferential corrections, IGSO satellites can also be used to jointly broadcast the corrections of BDSBAS and PPP-B2b (Yang et al. 2022). The expected service coverage after the participation of the IGSO satellites is shown in Figure 6.

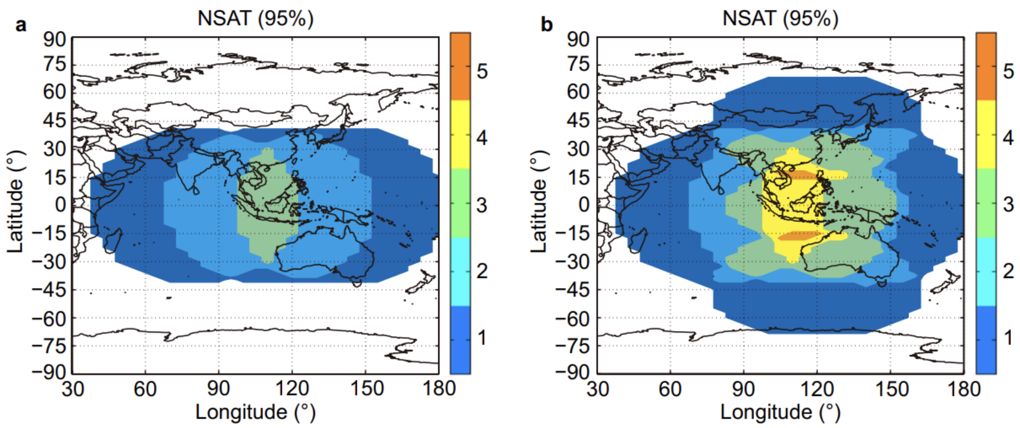

Figure 6. Visible satellites(a: 3GEO, b: 3 GEO+3 IGSO) with the elevation cut-of angle of 40°.

Accuracy of orbit, clock, and bias products of PPP-B2b

In terms of orbit accuracy, the BDS-3 satellites are 6.5 cm, 24.0 cm, and 21.0 cm in radial, along-track, and cross-track components, while the accuracy of the IGSO orbit is slightly lower than that of the MEO orbit. Compared with the satellite orbit generated from broadcast ephemeris, the PPP-B2b real-time orbit error sequence is more continuous and smoother. Xu et al. (2021) indicated that the broadcast ephemeris is updated at regular intervals, and the orbits generated before and after the ephemeris update have significant jumps. The PPP-B2b real-time orbits effectively weaken such jumps. The STD values of real-time clock offset errors are below 0.18 and 0.15 ns for BDS-3 and GPS satellites (Ren et al. 2021). Tang et al. (2022) analyzed the accuracy of different types of DCBs. The result shows that the DCB(B1I) errors are smaller than 2.0 ns, and the RMS of DCB for the remaining codes is 0.3 ns~0.7 ns.

PPP performance of PPP-B2b

The PPP performance based on PPP-B2b signals was comprehensively evaluated. The results show that after convergence, the RMS of BDS-3 PPP is better than 0.15 and 0.2 m in the horizontal and vertical directions, respectively. The average convergence time is about 18 min (Yang et al. 2022). The positioning accuracy of the B1C/B2a combination is basically comparable to that of the B1I/B3I combination, but its convergence time is longer (Song et al. 2021). Zhou et al. (2022) examined the positioning performance of PPP-B2b augmented single frequency PPP (SF-PPP) with 7 GNSS stations for 15 consecutive days. By applying the PPP-B2b corrections, SF-PPP achieves better than 0.3 m and 0.6 m accuracy for the horizontal and vertical directions, respectively. The mean convergence time is close to the final precise product-based PPP solution.

Table 1. Accuracy (RMS) and convergence time of BDS PPP-B2b kinematic positioning

Positioning performance		WUH2		BJF1		SHA1		KUN1	
		H	V	H	V	H	V	H	V
RMS (m)	DOY 248	0.077	0.125	0.080	0.124	0.061	0.075	0.087	0.118
	DOY 249	0.077	0.126	0.112	0.161	0.094	0.132	0.096	0.139
	DOY 250	0.077	0.136	0.116	0.132	0.093	0.122	0.107	0.111
	DOY 251	0.077	0.147	0.118	0.120	0.106	0.151	0.093	0.142
	DOY 252	0.056	0.138	0.079	0.114	0.068	0.116	0.090	0.129
	Average	0.073	0.134	0.101	0.130	0.085	0.119	0.094	0.128
Convergence time (min)		18.75		18.43		21.79		16.17	

8 LEO constellation augmented GNSS

An extended GNSS system with the LEO constellation transmitting navigation signals, which is called LEO enhanced Global Navigation Satellite Systems, consisting of high, medium, and low Earth orbit satellites, is proposed for the future precise positioning service (Li et al. 2019). To validate its advantages in accelerating the PPP convergence, the simulated LEO measurements are introduced to PPP processing in various challenging environments (Li et al. 2019; Li et al. 2022). As shown in Figure 7, with the augmentation of 60-, 96-, 192- and 288-satellite LEO constellation, the multi-GNSS PPP convergence time can be shortened from 9.6 to 7.0, 3.2, 2.1, and 1.3 min, respectively.

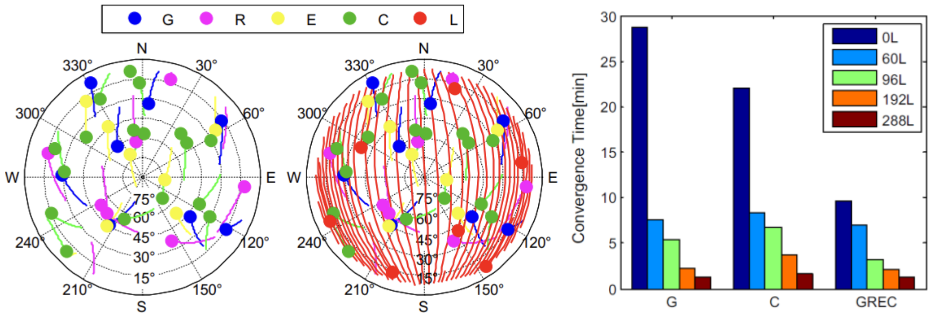

Figure 7. Sky plots of the multi-GNSS satellites without or with the augmentation of 192 LEO satellites (left panel); Average convergence time of LEO augmented PPP solutions(right panel)

The fusion of LEO constellation and GNSS can increase the number of visible satellites and optimize spatial geometry, which is expected to further improve the performance of PPP AR. Li et al. (2019) investigated the performance of LEO-augmented PPP AR with three types of LEO constellations. With observations of the 288-LEO constellation, the GREC fixed solutions can converge to 5 cm in all three directions within 1 min for all three stations.

Besides, the rapid development of LEO constellations provides a great opportunity to global ionospheric modeling, which is still not good over many regions (e.g., the oceans and the polar regions) due to the lack of ground-based GNSS stations. Ren et al. (2020) simulated observation data of three kinds of LEO constellations with 60, 96, and 192 satellites, and the results show that LEO observations can expand the coverage and increase the density of ionospheric pierce points (IPPs), thereby improving the precision of ionospheric modeling by 35.9%~50%.

Ge et al. (2022) comprehensively reviewed the current status of LEO-augmented GNSS, and analyzed the opportunities and challenges in terms of LEO constellation design, operation mode, and positioning performance, etc. Thanks to the fast geometric change brought by LEO satellites, LEO augmentation is expected to fundamentally solve the problem of the long convergence time of PPP without any augmentation. The convergence time can be shortened to within 1 min if appropriate LEO constellations are deployed. However, there are still some issues to overcome, such as the optimization of LEO constellation as well as the real-time LEO precise orbit and clock determination.

Bibliography

Andersen, OB., Knudsen, P. (2019). The DTU17 global marine gravity field: first validation results. In: International association of geodesy symposia, Berlin, Heidelberg.

Chen Xinghan, Ge Maorong, Haroldo Antonio Marques, Schuh Harald. Evaluating the impact of higher-order ionospheric corrections on multi-GNSS ultra-rapid orbit determination[J]. Journal of Geodesy, 2019, 93(9): 1347-1365.

Liu Yang, Liu Yanxiong, Tian Ziwen, Dai Xiaolei, Qing Yun, Li Menghao. Impact of ECOM Solar Radiation Pressure Models on Multi-GNSS Ultra-Rapid Orbit Determination[J]. Remote Sensing, 2019, 11(24).

Li Xingxing, Yuan Yongqiang, Huang Jiande, Zhu Yiting, Wu Jiaqi, Xiong Yun, Li Xin, Zhang Keke. Galileo and QZSS precise orbit and clock determination using new satellite metadata[J]. Journal of Geodesy, 2019, 93(8): 1123-1136.

Li Xingxing, Yuan Yongqiang, Zhu Yiting, Jiao Wenhai, Bian Lang, Li Xin, Zhang Keke. Improving BDS-3 precise orbit determination for medium earth orbit satellites[J]. GPS Solutions, 2020, 24(2): 53.

Yuan Yongqiang, Li Xingxing, Zhu Yiting, Xiong Yun, Huang Jiande, Wu Jiaqi, Li Xin, Zhang Keke. Improving QZSS precise orbit determination by considering the solar radiation pressure of the L-band antenna[J]. GPS Solutions, 2020, 24(2): 50.

Li Xingxing, Chen Xinghan, Ge Maorong, Schuh Harald. Improving multi-GNSS ultra-rapid orbit determination for real-time precise point positioning[J]. Journal of Geodesy, 2019, 93(1): 45-64.

Zhao Qile, Xu Xiaolong, Ma Hongyang, Liu Jingnan. Real-time precise orbit determination of BDS/GNSS: method and service[J]. Geomatics and Information Science of Wuhan University, 2018, 43(12): 2157-2166.

Duan Bingbing, Hugentobler Urs, Chen Junping, Inga Selmke, Wang Jiexian. Prediction versus real-time orbit determination for GNSS satellites[J]. GPS Solutions, 2019, 23(2): 39.

Dai Xiaolei, Lou Yidong, Dai Zhiqiang, Qing Yun, Li Min, Shi Chuang. Real-time precise orbit determination for BDS satellites using the square root information filter[J]. GPS Solutions, 2019, 23(2): 45.

Li Zongnan, Li Min, Shi Chuang, Fan Lei, Liu Yang, Song Weiwei, Tang Weiming, Zou Xuan. Impact of ambiguity resolution with sequential constraints on real-time precise GPS satellite orbit determination[J]. GPS Solutions, 2019, 23(3): 85.

Kuang Kaifa, Li Jiancheng, Zhang Shoujian, Wei Hui, Cao Xinyun. Improve real-time GNSS orbit with epoch-independent undifferenced ambiguity resolution[J]. Advances in Space Research, 2021, 68(11): 4544-4555.

Dai Xiaolei, Gong Xiaopeng, Li Chenglong, Qing Yun, Gu Shengfeng, Lou Yidong. Real-time precise orbit and clock estimation of multi-GNSS satellites with undifferenced ambiguity resolution[J]. Journal of Geodesy, 2022, 96(10) : 73.

Lou Yidong, Dai Xiaolei, Gong Xiaopeng, Li Chenglong, Qing Yun, Liu Yang, Peng Yaquan, Gu Shengfeng. A review of real-time multi-GNSS precise orbit determination based on the filter method[J]. Satellite Navigation, 2022, 3(1): 15.

Liu Teng, Zhang Baocheng, Yuan Yunbin, Zha Jiuping, Zhao Chuanbao. An efficient undifferenced method for estimating multi-GNSS high-rate clock corrections with data streams in real time[J]. Journal of Geodesy, 2019, 93(9): 1435-1456.

Chen Liang, Zhao Qile, Hu Zhigang et al. GNSS global real-time augmentation positioning: Real-time precise satellite clock estimation, prototype system construction and performance analysis[J]. Advances in Space Research,2018, 61(1), 367-384.

Zhao Lewen, Dousa, Jan, Ye Shirong, Pavel Vaclavovic. A flexible strategy for handling the datum and initial bias in real-time GNSS satellite clock estimation[J]. Journal of Geodesy, 2020,94, 1-11.

Shi Chuang, Guo Shiwei, Gu Shengfeng, Yang Xinhao, Gong Xiaopeng, Deng Zhiguo, Ge Maorong, Harald Schuh. Multi-GNSS satellite clock estimation constrained with oscillator noise model in the existence of data discontinuity[J]. Journal of Geodesy, 2019, 93, 515-528.

Gong Xiaopeng, Gu Shengfeng, Lou Yidong, Zheng Fu, Ge Maorong, Liu Jingnan. An efficient solution of real-time data processing for multi-GNSS network[J]. Journal of Geodesy, 2018, 92, 797-809.

Fu Wenju, Huang Guanwen, Zhang Qin, Gu Shengfeng, Ge Maorong, Schuh Harad. Multi-GNSS real-time clock estimation using sequential least square adjustment with online quality control[J]. Journal of Geodesy, 2019, 93, 963-976.

Cao Xinyun, Kuang Kaifa, Ge Yulong, Shen Fei, Zhang Soujian, Li Jiancheng. An efficient method for undifferenced BDS-2/BDS-3 high-rate clock estimation[J]. GPS Solutions, 2022, 26(3), 66.

Li Xingxing, Li Yuhao, Xiong Yun, Wu Jiaqi, Zheng Hongjie, Li Linyang. An efficient strategy for multi-GNSS real-time clock estimation based on the undifferenced method[J]. GPS Solutions, 2023, 27(1), 23.

Dai Zhiqiang, Dai Xiaolei, Zhao Qile, Liu Jingnan. Improving real-time clock estimation with undifferenced ambiguity fixing[J]. GPS Solutions, 2019, 23, 1-12.

Yang Xinhao, Gu Shengfeng, Gong Xiaopeng, Song Weiwei, Lou Yidong, Liu Jingnan. Regional BDS satellite clock estimation with triple-frequency ambiguity resolution based on undifferenced observation[J]. GPS Solutions, 2019, 23, 1-11.

Xie Wei, Huang Guanwen, Fu Wenju, Li Mengyuan, Du Shi, Tan Yue. Realizing rapid re-convergence in multi-GNSS real-time satellite clock offset estimation with dual-thread integer ambiguity resolution[J]. GPS Solutions, 2023, 27(1), 54.

Li Xingxing, Xiong Yun, Yuan Yongqiang, Wu Jiaqi, Li Xin, Zhang Keke, Huang Jiaxin. Real-time estimation of multi-GNSS integer recovery clock with undifferenced ambiguity resolution[J]. Journal of Geodesy, 2019, 93(12): 2515-2528.

Fu Wenju, Wang Jin, Wang Lei, Chen Ruizhi. A Kalman filter-based online fractional cycle bias determination method for real-time ambiguity-fixing GPS satellite clock estimation[J]. Measurement, 2022, 205: 112207.

Hu Jiahuan, Li Pan, Zhang Xiaohong, Bisnath Sunil, Pan Lin. Precise point positioning with BDS-2 and BDS-3 constellations: ambiguity resolution and positioning comparison[J]. Advances in Space Research, 2022, 70(7) : 1830-1846.

Li Xingxing, Li Xin, Liu Gege, Xie Weiliang, Guo Fei, Yuan Yongqiang, Zhang Keke, Feng Guolong. The phase and code biases of Galileo and BDS-3 BOC signals: effect on ambiguity resolution and precise positioning[J]. Journal of Geodesy, 2020, 94(1) : 9.

Geng Jianghui, Guo Jiang. Beyond three frequencies: an extendable model for single-epoch decimeter-level point positioning by exploiting Galileo and BeiDou-3 signals[J]. Journal of Geodesy, 2020, 94(1) : 14.

Geng Jianghui, Guo Jiang, Meng Xiaolin, Gao Kefu. Speeding up PPP ambiguity resolution using triple-frequency GPS/BeiDou/Galileo/QZSS data[J]. Journal of Geodesy, 2020, 94(1) : 6.

Jiang Weiping, Liu Tianjun, Chen Hua, Song Chuanfeng, Chen Qusen, Geng Tao. Multi-frequency phase observable-specific signal bias estimation and its application in the precise point positioning with ambiguity resolution[J]. GPS Solutions, 2022, 27(1) : 4.

Geng Jianghui, Wen Qiang, Zhang Qiyuan, Li Guangcai, Zhang Kunlun. GNSS observable-specific phase biases for all-frequency PPP ambiguity resolution[J]. Journal of Geodesy, 2022, 96(2) : 11.

Qu Lizhong, Zhang Pu, Jing Changfeng, Du Mingyi, Wang Jian, Zhao Qile, Li Juanjuan. Estimating the Fractional Cycle Biases for GPS Triple-Frequency Precise Point Positioning with Ambiguity Resolution Based on IGS Ultra-Rapid Predicted Orbits[J]. Remote Sensing, 2021, 13(16).

Geng Jianghui, Yang Songfeng, Guo Jiang. Assessing IGS GPS/Galileo/BDS-2/BDS-3 phase bias products with PRIDE PPP-AR[J]. Satellite Navigation, 2021, 2(1) : 17.

Cui Bobin, Li Pan, Wang Jungang, Ge Maorong, Harald Schuh. Calibrating receiver-type-dependent wide-lane uncalibrated phase delay biases for PPP integer ambiguity resolution[J]. Journal of Geodesy, 2021, 95(7) : 82.

Shi Chuang, Tian Yuan, Zheng Fu, Hu Yong. Accounting for Signal Distortion Biases for Wide-Lane and Narrow-Lane Phase Bias Estimation with Inhomogeneous Networks[J]. Remote Sensing, 2022, 14(1).

Zheng Kai, Tan Lingmin, Liu Kezhong, Li Pan, Chen Mozi, Zeng Xuming. Multipath mitigation for improving GPS narrow-lane uncalibrated phase delay estimation and speeding up PPP ambiguity resolution[J]. Measurement, 2023, 206: 112243.

Ren Xiaodong, Chen Jun, Li Xingxing, et al. Multi-GNSS contributions to differential code biases determination and regional ionospheric modeling in China[J]. Advances in Space Research, 2020, 65(1): 221-234.

Li Wen, Li Zishen, Wang Ningbo, et al. A satellite-based method for modeling ionospheric slant TEC from GNSS observations: algorithm and validation[J]. GPS Solutions, 2022, 26(1): 14.

Xu Li, Zhang Jiuping, Li Min, et al. Estimation of ionospheric total electron content using GNSS observations derived from a smartphone[J]. GPS Solutions, 2022, 26(4): 138.

Li Zishen, Wang Ningbo, Wang Liang, Liu Ang, Yuan Hong, Zhang Kefei. Regional ionospheric TEC modeling based on a two-layer spherical harmonic approximation for real-time single-frequency PPP[J]. Journal of Geodesy, 2019, 93(9) : 1659-1671.

Gu Shengfeng, Gan Chengkun, He Chengpeng, et al. Quasi-4-dimension ionospheric modeling and its application in PPP[J]. Satellite Navigation, 2022, 3(1): 24

Gao Xin, Yao Yibin. A storm-time ionospheric TEC model with multichannel features by the spatiotemporal ConvLSTM network[J]. Journal of Geodesy, 2023, 97(1): 9.

Sui Yun, Fu Haiyang, Wang Denghui, et al. Multi-layer Ionospheric Model Constrained by Physical Prior Based on GNSS Stations[J]. IEEE Journal of Selected Topics in Applied Earth Observations and Remote Sensing, 2023, 16: 1842-1857.

Li Zishen, Wang Ningbo, Hernández-Pajares Manuel, Yuan Yunbin, Krankowski Andrzej, Liu Ang, Zha Jiuping, Alberto García-Rigo, David Roma-Dollase, Yang Heng, Denis Laurichesse, Alexis Blot. IGS real-time service for global ionospheric total electron content modeling[J]. Journal of Geodesy, 2020, 94(3): 32.

Yang Fei, Meng Xiaolin, Guo Jiming, Yuan Debao, Chen Ming. Development and evaluation of the refined zenith tropospheric delay (ZTD) models[J]. Satellite Navigation, 2021, 2(1):21.

Mao Jian, Wang Qiang, Liang Yubin, Cui Tiejun. A new simplified zenith tropospheric delay model for real-time GNSS applications[J]. GPS Solutions, 2021, 25(2): 43.

Huang Liangke, Zhu Ge, Peng Hua, Liu Lilong, Ren Chao. An improved global grid model for calibrating zenith tropospheric delay for GNSS applications[J]. GPS Solutions, 2023, 27(1): 17.

Yao Yibin, Xu Xingyu, Xu Chaoqian, Peng Wenjie, Wan Yangyang. Establishment of a Real-Time Local Tropospheric Fusion Model[J]. Remote Sensing, 2019, 11(11): 1321.

Xia Pengfei, Tong Mengxiang, Ye Shirong, Qian Jingye, Hu Fangxin. Establishing a high-precision real-time ZTD model of China with GPS and ERA5 historical data and its application in PPP[J]. GPS Solutions, 2022, 27(1) : 2.

Lu Cuixian, Zhong Yaxin, Wu Zhilu, Zheng Yuxin, Wang Qiuyi. A tropospheric delay model to integrate ERA5 and GNSS reference network for mountainous areas: application to precise point positioning[J]. GPS Solutions, 2023, 27(2):81.

Yang Yuanxi, Ding Qun, Gao Weiguang, Li Jinlong, Xu Yangyin, Sun Bijiao. Principle and performance of BDSBAS and PPP-B2b of BDS-3[J]. Satellite Navigation, 2022, 3(1) : 5.

Chen Junping, Yu Chao, Zhou Jianhua, Wang Ahao, Zhang Yize, Song Ziyuan. Decimeter-level algorithm for satellite-based augmentation systems and performance analysis of BDS-2/BDS-3[J]. 2021, 51(1): 019507.

Lan Ruohua, Yang Cheng, Zheng Yanli, Xu Qiaozhuang, Lv Jie, Gao Zhouzheng. Evaluation of BDS-3 B1C/B2b Single/Dual-Frequency PPP Using PPP-B2b and RTS SSR Products in Both Static and Dynamic Applications[J]. Remote Sensing, 2022, 14(22).

Shi Junbo, Ouyang Chenhao, Yue Jinguang, Chen Ming, Guo Jiming. High-Precision Positioning Service Performance

Analysis of Three BDS Ground-Based Augmentation Systems[J]. Journal of Geodesy and Geodynamics, 2022, 42(7) : 712-715,770.

Li Bofeng, Ge Haibo, Bu Yuhang, Zheng Yanning, Yuan Leitong. Comprehensive assessment of real-time precise products from IGS analysis centers[J]. Satellite Navigation, 2022, 3(1) : 12.

Guo Wenfei, Zuo Hongming, Mao Feiyu, Chen Jiaqi, Gong Xiaopeng, Gu Shengfeng, Liu Jingnan. On the satellite clock datum stability of RT-PPP product and its application in one-way timing and time synchronization[J]. Journal of Geodesy, 2022, 96(8) : 52.

Yang Yuanxi, Gao Weiguang, Guo Shuren, Mao Yue, Yang Yufei. Introduction to BeiDou-3 navigation satellite system[J]. Navigation, 2019, 66(1) : 7-18.

Yang Yuanxi, Liu Li, Li Jinlong, Yang Yufei, Zhang Tianqiao, Mao Yue, Sun Bijiao, Ren Xia. Featured services and performance of BDS-3[J]. Science Bulletin, 2021, 66(20): 2135-2143.

Tao Jun, Liu Jingnan, Hu Zhigang, Zhao Qile, Chen Guo, Ju Boxiao. Initial Assessment of the BDS-3 PPP-B2b RTS compared with the CNES RTS[J]. GPS Solutions, 2021, 25(4) : 131.

Liu Jinhuo, Tang Chengpan, Zhou Shanshi, et al. The Bias in PPP-B2b real-time clock offset and the strategy to reduce it [J]. Remote Sensing, 2022, 14(18).

Xu Yangyin, Yang Yuanxi, Li Jinlong. Performance evaluation of BDS-3 PPP-B2b precise point positioning service[J]. GPS Solutions, 2021, 25(4) : 142.

Ren Zhiling, Gong Hang, Peng Jing, Tang Chengpan, Huang Xinming, Sun Guangfu. Performance assessment of real-time precise point positioning using BDS PPP-B2b service signal[J]. Advances in Space Research, 2021, 68(8) : 3242-3254.

Tang Chengpan, Hu Xiaogong, Chen Jinping, Liu Li, Zhou Shanshi, Guo Rui, Li Xiaojie, He Feng, Liu Jinhuo, Yang Jianhua. Orbit determination, clock estimation and performance evaluation of BDS-3 PPP-B2b service[J]. Journal of Geodesy, 2022, 96(9) : 60.

Song Weiwei, Zhao Xinke, Lou Yidong, Sun Weibin, Zhao Zhengyu. Performance Evaluation of BDS-3 PPP-B2b Service[J]. Geomatics and Information Science of Wuhan University, 2021: 1-11.

Zhou Haitao, Wang Lei, Fu Wenju, Han Yi, Li Tao, Li Wei, Chen Ruizhi. Real-time single-frequency precise point positioning using BDS-3 PPP-B2b corrections[J]. Measurement, 2022, 205: 112178.

Li Bofeng, Ge Haibo, Ge Maorong, Nie Liangwei, Shen Yunzhong, Harald Schuh. LEO enhanced Global Navigation Satellite System (LeGNSS) for real-time precise positioning services[J]. Advances in Space Research, 2019, 63(1) : 73-93.

Li Xingxing, Ma Fujian, Li Xin, Lv Hongbo, Bian Lang, Jiang Zihao, Zhang Xiaohong. LEO constellation-augmented multi-GNSS for rapid PPP convergence[J]. Journal of Geodesy, 2019, 93(5) : 749-764.

Li Xin, Li Xingxing, Ma Fujian, Yuan Yongqiang, Zhang Keke, Zhou Feng, Zhang Xiaohong. Improved PPP Ambiguity Resolution with the Assistance of Multiple LEO Constellations and Signals[J]. Remote sensing, 2019, 11(4): 408.

Li Min, Xu Tianhe, Guan Meiqian, Gao Fan, Jiang Nan. LEO-constellation-augmented multi-GNSS real-time PPP for rapid re-convergence in harsh environments[J]. GPS Solutions, 2022, 26: 1-12.

Ren Xiaodong, Zhang Xiaohong, Schmidt M et al. (2020) Performance of GNSS global ionospheric modeling augmented by LEO constellation[J]. Earth and Space Science 7(1): e2019EA000898.

Ge Haibo, Li Bofeng, Jia Song, Nie Liangwei, Wu Tianhao, Yang Zhe, Shang Jingzhe, Zheng Yanning, Ge Maorong. LEO enhanced global navigation satellite system (LeGNSS): Progress, opportunities, and challenges[J]. Geo-spatial

Information Science, 2022, 25(1): 1-13.

Development Status and Trend of Indoor Positioning and Navigation Technology

Baoguo Yu[1,2], Lu Huang[1,2], Yachuan Bao[1,2], Haonan Jia[1,2], Shuang Li[1,2], Ruizhi Chen[3], Xiaoji Niu[3], Zhongliang Deng[4], Jinzhong Bei[5], Dehai Li[5], Yunjia Wang[6], Feng Lu[7], Chun Liu[8], Ling Pei[9], Jian Wang[10]

[1] China Electronics Technology Group Network Communication Research Institute, Shijiazhuang City, Hebei Province

[2] State Key Laboratory of Satellite Navigation System and Equipment Technology, Shijiazhuang, Hebei

[3] Wuhan University Satellite Navigation and Positioning Technology Research Center,Wuhan,

[4] Beijing university of Posts and Telecommunications, Beijing

[5] China Academy of Surveying and Mapping Sciences, Beijing

[6] China University of Mining and Technology, Xuzhou, China

[7] Institute of Geographic Sciences and Resources, Chinese Academy of Sciences,Beijing

[8] School of Surveying, Mapping and Geographic Information, Tongji University, Shanghai, China

[9] Shanghai Jiao Tong University, Shanghai, China

[10] School of Geomatics and Urban Spatial Informatics, Beijing University of Civil Engineering and Architecture(BUCEA), Beijing, China

1 Introduction

The global satellite navigation system can provide all-weather, all-time, high-precision PNT (Positioning, Navigation, and Timing) services for various users on the surface and in near-Earth space, and has played an important role in many fields such as national security, national economy, and public life. However, it is still difficult for satellite navigation to provide accurate and reliable location services under signal shadowing environments. Therefore, extending navigation and positioning services from outdoors to indoors, developing high-precision indoor navigation and positioning technology, and labeling everything indoors with time and space are urgent needs of a modern smart society.

Compared with outdoor open space, the relationship between indoor channel environment and spatial topology is more complex, and GNSS spatial signals are attenuated due to building occlusion, resulting in the inability to effectively cover a large area in indoor environment. So academia and industry have explored a variety of indoor PNT theoretical methods and technical means. Although there are many types of indoor positioning and navigation information sources, they all have certain limitations. The fusion of different positioning information still faces the challenge of performance improvement brought about by environmental changes. The problems of wireless signal coverage, precise measurement, environmental perception, and map update brought about by the complex and changeable indoor environment are all difficulties faced by indoor and outdoor seamless positioning and navigation. These factors limit the large-scale application of related technologies in various indoor sheltered spaces and semi-sheltered spaces.

In general, the basic problems faced in the field of indoor and outdoor seamless positioning and navigation are mainly reflected in the following three aspects:

1) Architecture perspective. From the perspective of universal and unified space-time reference expression and Internet of Everything PNT service, no indoor and outdoor seamless navigation and positioning system and open standards for all applications and services have yet been established. Large-scale cross-domain promotion and ubiquitous unified applications are limited. So it is urgent to build a standardized architecture that is universal and applicable to most application scenarios.

2) System perspective. The current indoor positioning system side solutions are more oriented to local indoor environment applications, and a wide-area and large-scale network coverage capability has not been formed. Facing indoor spaces of different scales and environmental characteristics, it is an important development direction in the future to solve the system construction and deployment problems such as unified standards, low cost, easy implementation, wide coverage, and high concurrency. It is urgent to realize the breakthrough of a series of key technologies such as elastic and scalable networking of multi-mode base stations, integrated communication and navigation, and independent positioning by single base stations.

3) Application perspective. Different application scenarios have different user needs, and multiple factors such as cost, ease of use, reliability, real-time performance, and technology maturity must be considered comprehensively. Efforts should be made to solve problems such as chipification of user terminals, integration with outdoor positioning terminals, and application software ecology, and realize indoor positioning based on user multi-scenario roaming under unified system network deployment conditions.

Focusing on the above issues, this report summarizes the research status of indoor positioning and navigation technology in China, and focuses on the representative innovation achievements and applications of major scientific research institutions of indoor positioning technology in China in recent years. Finally, based on the challenges faced by the application and promotion of current indoor and outdoor seamless navigation and positioning systems, a trend analysis and prospect of future indoor integrated PNT systems are provided.

2 Development Status of Indoor Positioning Technology in China

The international research and industrial application of indoor positioning technology are currently in a rising trend, and the research and application of positioning technologies such as WiFi, Bluetooth, ultra wideband, 5G/6G, pseudo-satellite, audio, visual, inertial, and geomagnetic technologies are continuously developing globally.

In terms of WiFi indoor positioning technology, Google has built a mobile terminal network positioning service platform based on WiFi technology, which can achieve rough indoor positioning. In terms of Bluetooth indoor positioning technology, in 2019, SIG (Special Interest Group) added the "direction finding" function in Bluetooth standard specification 5.1, which greatly improves the positioning accuracy and realizes an accuracy of sub meter level in line of sight environment. In terms of UWB indoor positioning technology, thanks to the anti-multipath and high-precision signal system advantages, a ranging accuracy of 10 centimeters and a positioning accuracy of 30 centimeters can be achieved in ideal indoor environments. Currently, the international standard for UWB signal system continues to iterate, and the latest IEEE 802.15.4ab is under development. In terms of 5G/6G high-precision indoor positioning, 3GPP has proposed clear requirements for 5G high-precision positioning in TS 22.261 standard, and some globally well-known companies such as Qualcomm and Huawei have proposed 5G meter level positioning solutions.

The rapid development of indoor positioning technology in China led to the early proposal of the "Xihe Plan" by the Ministry of Science and Technology of China, aiming to solve the problem of seamless indoor and outdoor navigation and positioning. Recently, with the joint efforts of the technology and industry sectors, especially with the support of the 13th Five Year National Key R&D Plan, China has made significant breakthroughs in multiple indoor positioning technologies. Representative achievements include: the team from the State Key Laboratory of Satellite Navigation System and Equipment Technology of China Electronics Technology Group proposed the Beidou pseudosatellite high-precision positioning system and algorithm for indoor environment. Based on the "Beidou commercial chip+IP soft core" and the Beidou pseudosatellite micro base station network, Beidou sub meter level indoor and outdoor continuous positioning has been achieved.

Figure 1. Beidou pseudosatellite indoor positioning micro base station and positioning terminal "spatiotemporal box"

The Beidou pseudosatellite indoor positioning technology adopts multi-channel broadcasting of navigation signals compatible with Beidou/GPS with different spread spectrum codes using the same clock source, combined with a pseudosatellite carrier phase and Doppler frequency shift fusion positioning algorithm based on nonlinear filtering, to solve the problems commonly faced by pseudosatellite micro base stations in indoor positioning environments, such as time synchronization, ambiguity resolution, clock drift estimation, near-far effect, and multipath. It features wide indoor coverage, sub meter level positioning and compatibility with Beidou system. High-precision indoor and outdoor continuous positioning is achieved, with static positioning accuracy better than 0.1m and dynamic positioning accuracy better than 0.5m (3-sigma).

The technological achievement has been successfully applied to large indoor environments such as airports and shopping malls. Especially during the Beijing 2022 Winter Olympics, in response to the needs of emergency command and scheduling, epidemic prevention and control, unmanned distribution, and security control, a Beidou pseudosatellite micro base station indoor and outdoor integrated positioning service network was constructed. The system was deployed at the National Ski Jumping Center in Zhangjiakou District (Snow Ruyi Stadium, as shown in

Figure 2), providing fast positioning of personnel, vehicles, iron horses, robots, and other targets without dead corners within the accessible area of the entire venue, enabling adaptive seamless reception and switching between indoor Beidou micro base station signals and outdoor Beidou signals. The indoor and outdoor continuous positioning accuracy is better than 1 meter, solving the international problem of high-precision seamless positioning technology for large-scale indoor and outdoor areas.

Figure 2. Application of Beidou pseudosatellite indoor and outdoor positioning system in Beijing 2022 Winter Olympics

Based on the 14th Five Year Plan National Key R&D Program project, the team led by Baoguo Yu has expanded indoor navigation and positioning technology to underground spaces. They have proposed a continuous positioning technology for both inside and outside tunnels based on Beidou micro base stations and multi-sensor fusion, solving the problems of large-scale long-distance networking, continuous and stable tracking of positioning signals in tunnels. They have achieved a positioning capability with accuracy better than 2m for high-speed moving targets (speed>80km/h) and an ultimate accuracy better than 0.5m in long tunnel environments. A technological leap for Beidou micro base stations from low-speed moving target positioning to high-speed moving target positioning is achieved, and the application scenarios of Beidou pseudosatellites are expanded.

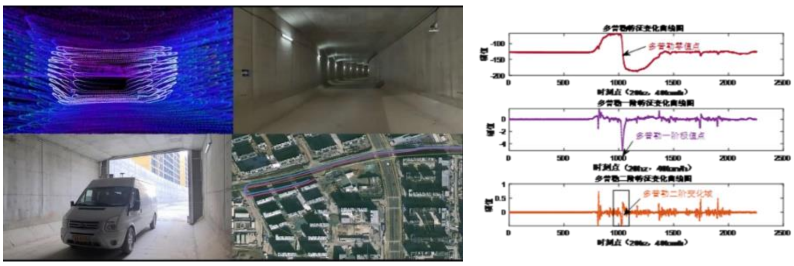

Figure 3. Test environment and results for continuous positioning of high-speed moving targets in underground space

To address the performance disadvantages of UWB indoor positioning technology in terms of service capacity, operating distance, and positioning networking, the Baoguo Yu team lead by Baoguo Yu has proposed a new HNav-UWB signal system, aiming to improve the measurement and positioning capabilities by signal layer design. The simulation shows that using ultra-low pulse repetition frequency and ultra-short frame structure design, the pulse repetition frequency can be as low as 915KHz, which greatly improves the ranging coverage and concurrent service capacity under low-power conditions. At the same time, the ULRP has concentrated energy and is more suitable for complex environments. The designed array-based single station positioning method adaptive to underground narrow and long spaces will significantly reduce the system deployment and application costs. The test results are shown in Figure 4.

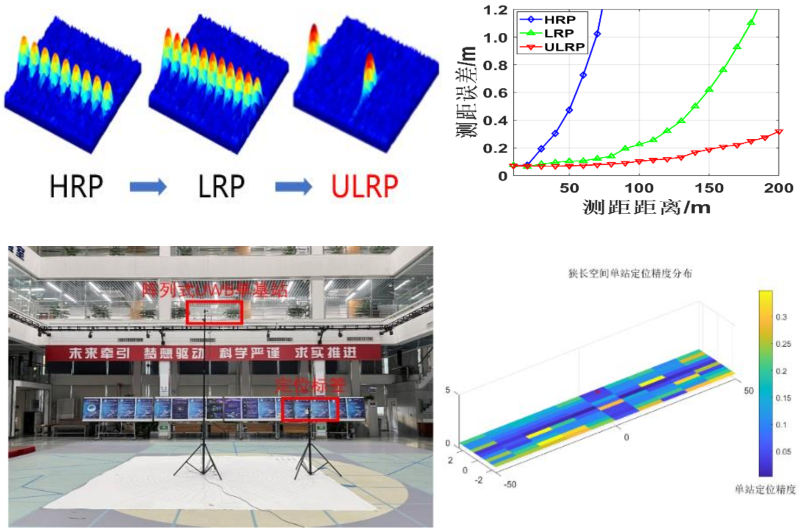

Figure 4. The proposed novel UWB signal system suitable for underground space and experimental results

Jinzhong Bei and Dehai Li of China Academy of Surveying and Mapping Sciences developed an indoor location cloud smart service platform and terminal application software, built an indoor location service system, broke through the adaptive interaction mechanism supported by user behavior pattern perception and platform knowledge model, developed a location cloud service system interconnection interface and operation overlay protocol, developed application systems for security monitoring and warning, emergency rescue and command, and public location service, and realized the transition expansion and practical application of the system in typical indoor scenarios.

The team of Ruizhi Chen at Wuhan University, China, has designed a weak audio signal detection method based on "coarse detection - signal normalization - fine detection - coarse difference rejection" mechanism, proposed and implemented a highly available audio signal robust detection algorithm based on time-frequency energy density matrix feature analysis and adaptive generalized correlation. With a breakthrough in the core technology of 50m long-distance high-precision ranging, the team have successfully developed and mass-produced the world's first audio positioning chip based on RISC-V architecture. On the basis of this chip, they built an integrated human-vehicle-object audio indoor positioning system across hardware and software platforms without changing any hardware or firmware of smartphones, realizing a high-precision, high-availability and wide-coverage indoor intelligence hybrid positioning system with positioning accuracy of 0.38 meters, location update rate of 20Hz and single base station signal coverage of 50 meters. The system has been deployed in indoor environments such as Nanjing South Station and Ezhou Airport in China, supporting applications such as smart security, smart logistics and smart communities, as shown in Figure 5.

Figure 5. Cross-system and Cross-platform audio positioning software and hardware ecology

Zhongliang Deng's team at Beijing University of Posts and Telecommunications (BUPT), China, proposed the theory of embedded signal-to-noise positioning, designed the 5G common-band and in-band localization reference signal system, and broke through the bottleneck of high-precision time reference and multi-source heterogeneous feature fusion high-precision positioning for wireless network positioning. They developed the first 5G high-precision positioning international standard 3GPP TS 38.211 proposal, proposed a series of methods for heterogeneous multi-source cooperative positioning, broke through the bottleneck of high-precision time reference for wireless network positioning and multi-source heterogeneous feature fusion positioning, The 5G positioning capability in 5G R16 standard published in 2020 was improved to sub-meter level. Industrialized applications are implemented in the fields of smart senior care, safe production, and smart transportation, etc., which provides important technical support for the application of 5G positioning in the field of industrial Internet, as shown in Figure 6.

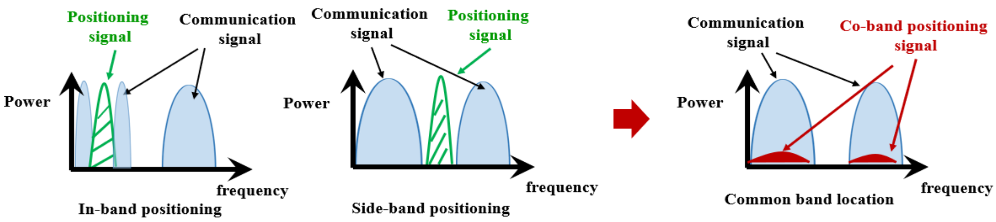

Figure 6. The principle of embedded signal-to-noise positioning

Indoor positioning technologies based on autonomous sensing typesensors have significant advantages in solving navigation and positioning problems in indoor non-cooperative environments. Usually, they can be broadly classified into two categories according to the source of information, one is to sense changes in carrier state information, such as inertial navigation, and the other is to sense changes in external environmental information, such as vision and LIDAR technologies. They have significant advantages in non-cooperative environments because they do not require early installation and deployment of infrastructure.

Baoguo Yu and Haonan Jia from the State Key Laboratory of Satellite Navigation System and Equipment Technology of CETC have developed a foot-worn positioning terminal (Figure 7) based on gyroscope, accelerometer, and barometer chips, with a weight of 50 g, dimensions of 47×33×26 mm, and power consumption of 200 mW. By embedding pedestrian motion pattern recognition, extended Kalman filter fusion algorithm based on zero velocity correction, and under purely autonomous navigation conditions, the positioning accuracy is 0.3%D, which is equivalent to walking of 1km with an error of less than 3m, and the speed measurement accuracy is better than 0.5m/s, realizing the autonomous, continuous and accurate positioning of personnel. Based on this technical achievement, the team won the championship in the 4th track competition of IPIN2022 International Indoor Positioning Competition.

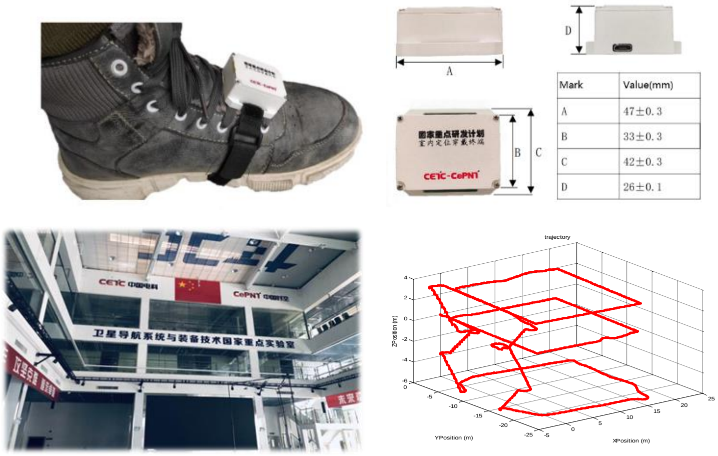

Figure 7. Pedestrian foot wearable positioning terminal and test results

Xiaoji Niu and Jian Kuang of Wuhan University designed a PDR scheme based on wearable inertial sensors, making full use of constrained information such as pedestrian motion patterns, human joint structures and environmental features to gradually reduce the dependence of PDR on gait assumptions from three aspects (e.g., Figure 8), such as single-foot inertial guidance, dual-foot inertial guidance and lower limb multiple inertial guidance. This method achieves the effect of improving the accuracy and robustness of autonomous pedestrian positioning in a length of about 1000m under a severe test scenario of no folding and no closure, and the positioning error is less than 1.5% of the walking distance.

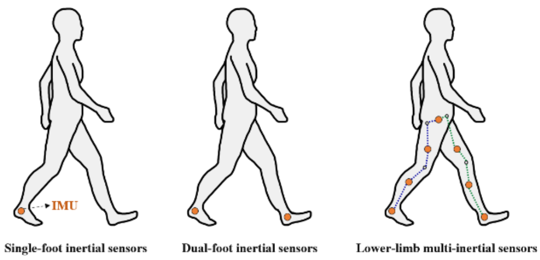

Figure 8. Single foot, daul-foot and lower limb multi-inertial guidance PDR solutions

To address the influence of complex dynamic scenes on visual positioning, Wang Yunjia et al. from China University of Mining and Technology established a robust indoor visual positioning algorithm that takes into account a wide range of indoor dynamic scenes. They used MEMS inertial sensor built in smart phones to build the geometric constraints and parameter optimization models in the inertial information assisted visual positioning algorithm, and solved the problem of visual feature matching failure. The number of internal points in the PnP solution process is increased to improve the stability of visual positioning. The technical framework is shown in Figure 9.

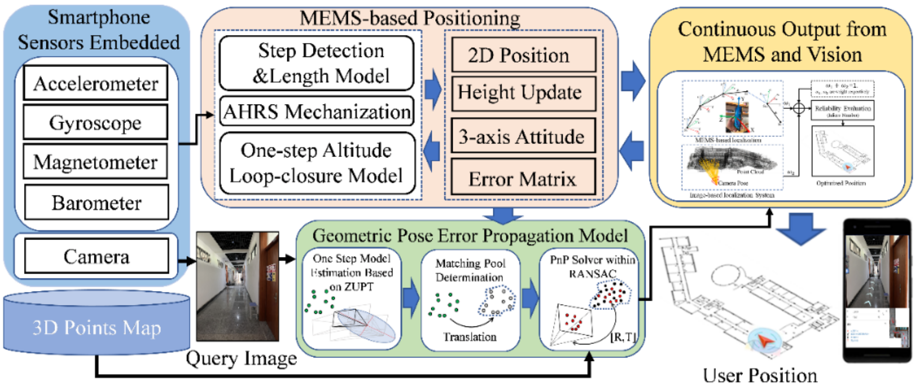

Figure 9. A robust positioning algorithm of indoor dynamic scene combining intelligent mobile MEMS and vision sensor

Ling Pei et al.of Shanghai Jiao Tong University have proposed a novel visual inertial odometer (VIO) method, which adopts structural regularity in an artificial environment and uses the Atlanta world model to describe the regularity. By fully exploring the structural lines consistent with each local world in Manhattan, the VIO method becomes more accurate and robust, and more flexible for different types of complex man-made environments. The proposed algorithm is compared with different existing advanced algorithms in multiple scenarios. The closed-loop error is 0.292% root mean square error, and the performance is more advanced. The test results are shown in Table 1.

Table 1. LOOP CLOSING ERROR OF DIFFERENT ALGORITHMS IN THREE INDOOR SCENES: RMSE ERROR (POS. [m]) MAX ERROR (DRIFT [m])

Seq. Name	Traveling Dist. [m]	OKVIS[5]		VINS[6](w/o loop)		Project Tango		Point-only		Point+Line		StructVIO	
		RMSE	Max.	RMSE	Max.	RMSE	Max.	RMSE	Max.	RMSE	Max.	RMSE	Max
Soft-01	315.167	6.702	9.619	4.861	6.688	5.715	8.181	**2.153**[2]	2.728	2.262	2.842	**1.931**[1]	2.437
Soft-02	438.198	4.623	6.713	2.713	4.086	4.238	6.226	3.905	5.243	**1.468**[2]	2.026	**1.429**[1]	1.984
Soft-03	347.966	**4.505**[2]	6.223	7.270	9.832	167.825	228.630	6.515	8.119	8.618	10.790	**0.325**[1]	1.020
Soft-04	400.356	3.993	5.784	28.667	75.479	2.453	3.544	**1.550**[1]	2.028	4.051	5.262	**1.722**[2]	2.241
Mech-01	340.578	3.627	4.745	2.452	3.260	**1.948**[2]	2.726	3.298	3.961	4.323	5.181	**0.909**[1]	1.165
Mech-02	388.548	3.079	4.195	3.570	4.754	**1.596**[2]	2.217	1.663	2.108	2.317	2.927	**0.779**[1]	1.022
Mech-03	317.974	3.875	5.324	4.682	9.113	4.220	5.781	**2.384**[2]	3.020	4.193	5.272	**1.161**[1]	1.532
Mech-04	650.430	-	-	3.002	8.592	1.915	5.808	1.785	4.663	**1.425**[2]	3.729	**0.742**[1]	1.940
MicroA-01	257.586	2.485	3.382	**0.654**[2]	1.148	45.599	61.058	2.849	3.505	2.189	2.721	**0.642**[1]	1.225
MicroA-02	190.203	3.428	5.186	14.222	57.172	**1.145**[1]	1.692	1.964	2.514	**1.723**[2]	2.207	2.089	2.661
MicroA-03	388.730	0.078	0.779	**1.800**[1]	2.578	4.400	6.253	3.824	5.169	3.072	4.232	**1.884**[2]	2.892
MicroA-04	237.856	6.136	8.532	**0.994**[2]	1.765	55.200	75.318	2.056	2.897	2.406	2.879	**0.350**[1]	0.448
MicroB-01	338.962	2.898	4.025	**1.856**[2]	2.944	38.197	50.572	7.084	8.576	7.337	8.913	**1.477**[1]	1.902
MicroB-02	306.316	2.240	3.490	**1.030**[2]	2.431	5.660	8.652	2.521	3.714	3.197	4.610	**0.470**[1]	0.799
MicroB-03	485.291	-	-	2.132	3.368	**2.009**[2]	2.960	6.490	8.978	4.507	6.301	**0.445**[1]	0.675
MicroB-04	357.251	4.064	6.481	**1.332**[2]	2.068	13.962	22.028	5.078	7.713	1.977	3.074	**0.473**[1]	0.777
Mean Drift Err.(%)		1.078%		1.410%		6.180%		0.957%		**0.956%**[2]		**0.292%**[1]	
Median Drift Err.(%)		0.781%		**0.538%**[2]		0.900%		0.559%		0.570%		**0.176%**[1]	

Indoor high-precision mapping and real-time GIS are the application basis of high-precision indoor positioning technology. In the past five years, Lu Feng et al. from the Institute of Geographic Sciences and Natural Resources Research of the Chinese Academy of Sciences proposed the indoor GIS framework under the support of the national key research and development project "Indoor Hybrid Intelligent Positioning and Indoor GIS Technology". It makes key technological breakthroughs such as high-precision indoor mapping and updating, automatic construction of indoor navigation network based on crowdsourcing trajectory, indoor mobile object management and location prediction, and indoor large-scale crowd pattern mining. It has developed high-precision indoor mapping technology and equipment, and formulated the crowdsourcing collaborative production technology and product standards for indoor navigation electronic maps. The application demonstration of location-based geographic information service in the indoor three-dimensional scene is carried out, as shown in Figure 10.

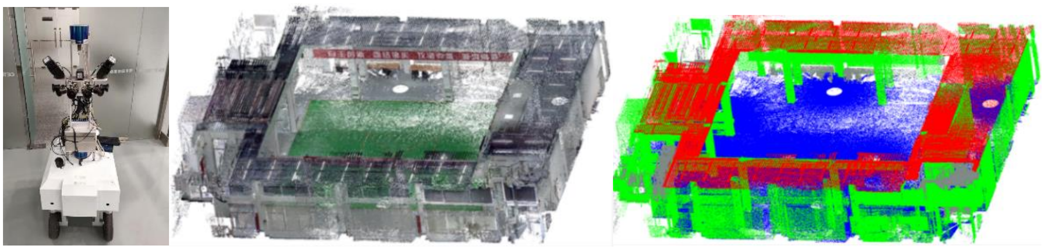

Figure 10. Results of semantic segmentation between light and small mobile indoor mapping platform and building interior

Liu Chun team of Tongji University is committed to the development of indoor mapping robot. They developed a high-precision time synchronization board, built an environment modeling and positioning navigation robot platform, integrated component recognition, semantic mapping, high-precision positioning, obstacle avoidance navigation and other functions on the platform. An average real-time positioning and orientation accuracy of 1km walking better than 15cm/0.1° is realized under the conditons of more than 30m long passage/corridor light texture in complex indoor scenes, and a standard visual map data set over

5000m^2 for typical scenes such as shopping malls, factories, communities and offices with accuracy better than 5cm is established. The coverage of 3D map construction is >90%, and the accuracy is better than 0.2m. The visual obstacle avoidance success rate is ≥95% (Figure 11), and the identification accuracy of more than 10 types of indoor and outdoor fixed facilities is ≥95%.

Figure 11. Laboratory mapping robot and test results

Wang Jian's team from Beijing University of Civil Engineering and Architecture proposed an indoor positioning method based on computer vision and coded graphics. Firstly, a series of coded graphics for indoor object positioning were designed, and a method for calculating the spatial coordinates of coded graphics was proposed. Then, two kinds of spatial excising models based on unit weight and Tukey weight were constructed. Finally, the object positioning in indoor environment was achieved. The experimental results show that both models can calculate the object position well.The spatial excising model based on Tukey weight can correctly identify the residual of observed values, and obtain robust positioning results with high positioning accuracy. Thirty-nine coded graphics were posted in the test environment. The coded images were automatically obtained from twelve different sites when the object was moving. Each coded image consisted of five to eight coded graphics. The test results show that the position accuracy calculated by Tukey weight method is improved more significantly than that by unit weight method. The accuracy of plane minimum value is increased by 16.96%, the maximum value by 66.34%; the elevation minimum value is increased by 9.40% and the maximum value by 71.05%. The test scene and results are shown in Figure 12.

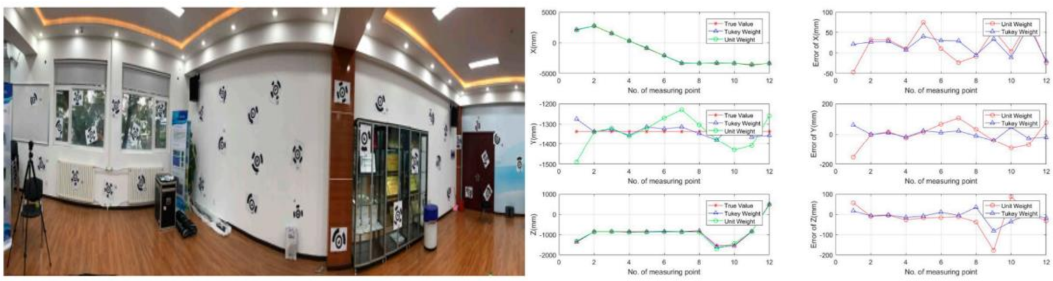

Figure 12. Test environment and results

3 Future development trends and suggestions

There are various existing indoor positioning technologies, while there are still problems in terms of positioning accuracy, scene generalization ability, indoor and outdoor continuity, and system capacity. So far, there is no single indoor positioning solution suitable for all indoor environments, so it is an important way to solve the problem of indoor positioning at present by designing an efficient multi-source information fusion solution, using a tight coupling of absolute positioning and relative positioning, autonomous positioning and wireless positioning, and integrating other heterogeneous information to obtain the optimal estimation of the position. At the same time, the current indoor positioning technology also faces problems such as different user needs, diverse application scenarios, complicated technical means, inconsistent standards and specifications, and no breakthrough in the general technical system. There is still a lack of a universal indoor positioning and navigation system that can be widely promoted.

In response to the above problems, the State Key Laboratory of Satellite Navigation System and Equipment Technology of China proposed an indoor and outdoor seamless PNT standardized architecture, which mainly includes the network layer, cloud processing layer and user layer. The network layer includes a public network for public users, a private network for professional users, and a mobile network for special users. The cloud processing layer includes a network map comprehensive management and control platform, a multi-information fusion intelligent control system, indoor and outdoor integrated GIS information, and a unified space-time reference. The user layer includes smart terminals for mass users, integrated indoor and outdoor positioning chips, large-capacity and high-concurrency positioning service application software, etc., as shown in Figure 13.

Indoor and outdoor seamless PNT system architecture

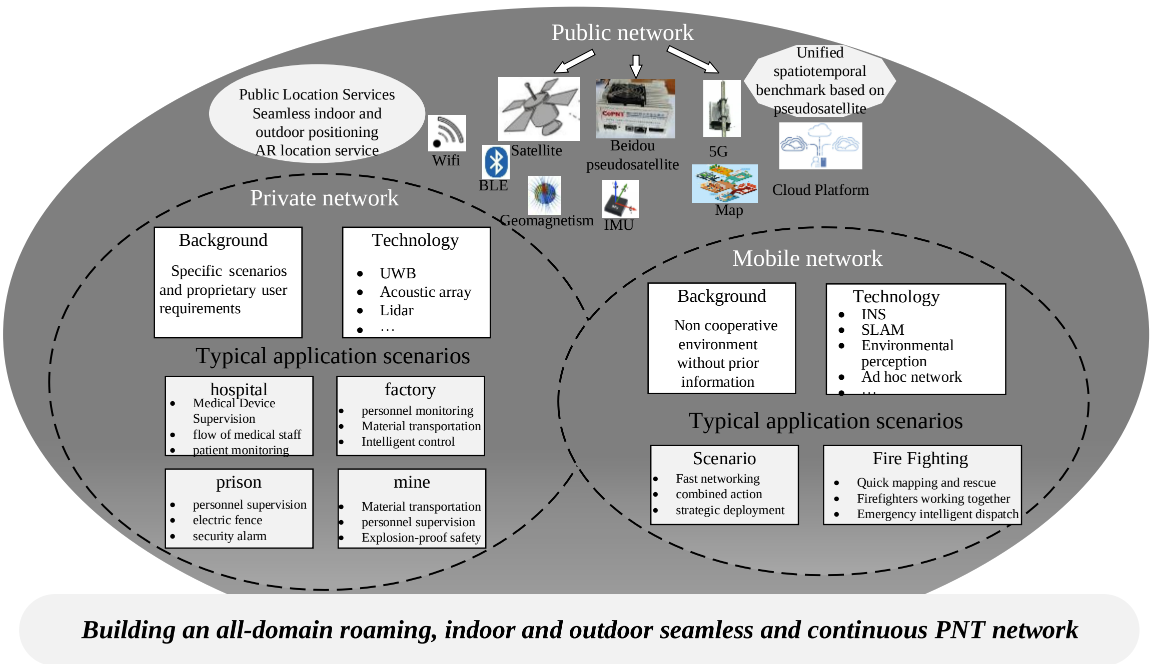

Figure 13. Architecture of seamless indoor and outdoor navigation and positioning system

Based on the seamless indoor and outdoor navigation positioning system architecture mentioned above, it is recommended to focus on the following three key tasks in the future:

1) Strengthen theoretical research on indoor positioning and navigation, and consolidate the foundation for the development of indoor high-precision positioning technology. With the improvement of indoor positioning service capabilities as the core, strengthen the theoretical foundation researchof indoor high-precision navigation and positioning, and promote the coordinated development of technologies and equipment of hybrid positioning networks, integrated terminals, location service platforms, and standards.

2) Develop multi-source positioning information fusion technology and equipment, and establish a unified indoor positioning standard technology architecture. The fused use of multiple indoor positioning technologies with complementary characteristics will become the future development direction. Therefore, it is necessary to address the challenge of multi-source fusion positioning technology, and build a scalable and extensible general-purpose hardware integration mechanism, which can flexibly respond to the application requirements of complex scenarios. At the same time, it is necessary to establish a complete and unified indoor positioning standard technology architecture, coordinate indoor positioning resources, study a series of fusion positioning technology suitable for man-machine, universal terminal and map standards, and promote the integrated development of indoor positioning technology through standards.

3) Accelerate the practical application of indoor navigation and positioning technology, and open up a new pattern for the development of integrated positioning, navigation and timing system. Facing the needs of large-scale indoor and outdoor seamless positioning public applications such as smart cities and emergency rescue in the future, through the development of standardized indoor geographic information and location service interface specifications, it is convenient for enterprises and individuals to customize personalized location services. A full-space intelligent location service ecosystem can be formed from the aspects of infrastructure and application modes, and large-scale, multi-scenario free roaming positioning among cities can be realized.

In summary, indoor positioning and navigation technology is an important cornerstone of the digitalization of the whole society in the future, and an important support for GNSS service expansion and capability improvement. In the future, a standardized indoor PNT infrastructure of "wide area + local area + triple play" will be formed, containing indoor high-precision positioning signals and information networks, a general technology engine for multi-user scenarios, and a standardized "cloud + terminal" service model. Facing the needs of most application scenarios, it is necessary to form relevant standard recommendations and provide ubiquitous, continuous, accurate, and intelligent indoor PNT services for public users, proprietary users, and special users on this basis. It will surely promote the rapid development of industrial manufacturing 2025, digital twins, and smart cities. At the same time, in terms of multi-system collaboration in the future, core interfaces with satellite Internet, 5G/6G mobile communication networks, and the Internet of Things will be formed to ensure that the indoor PNT system provides accurate spatio-temporal information services for various users. The continuous positioning, navigation and timing service performance of the global integrated PNT under the condition of GNSS shadowing will be greatly improved, and a more ubiquitous, fused and intelligent integrated space-time system and intelligent location service will be realized.

Bibliography

Chen Yang. Indoor positioning is an important cornerstone of digitalization of the whole society - interview with Wei Baoguo, chief scientist of China Electronics Technology Group, director of the State Key Laboratory of Satellite Navigation System and Equipment Technology [J]. China Surveying and Mapping, 2022,No.212(02):16-21.

Niu X, Liu T, Kuang J, et al (2022). Pedestrian trajectory estimation based on foot-mounted inertial navigation system for multistory buildings in postprocessing mode. IEEE Internet of Things Journal, 2021, 9(9): 6879-6892.

Zhang, Z., G. Chen, X. Wang & M. Shu (2021a) DDRNet: Fast point cloud registration network for large-scale scenes. Isprs Journal of Photogrammetry and Remote Sensing, 175, 184-198.

Li, Boying, Danping Zou, Daniele Sartori, Ling Pei, and Wenxian Yu. "Textslam: Visual slam with planar text features." In 2020 IEEE International Conference on Robotics and Automation (ICRA), pp. 2102-2108. IEEE, 2020.

Zheng X, Zhang H, Wang Z, et al. Nonlinear state estimation with multisensor stochastic scheduling[J]. IEEE Transactions on Systems, Man, and Cybernetics: Systems, 2021, 52(5): 3349-3359.

Danni. Audio Positioning, Curve Overtaking with Autonomous Indoor Positioning Technology——Interview with Chen Ruizhi, Director of State Key Laboratory of Surveying, Mapping and Remote Sensing Information Engineering, Wuhan University[J]. China Surveying and Mapping, 2022,No.212(02):12-15.

Wan W, Yu T, Di K, et al. (2021) Visual Localization of the Tianwen-1 Lander Using Orbital, Descent and Rover Images. Remote Sensing 13(17):3439-3450.

Pei, Ling, Kun Liu, Danping Zou, Tao Li, Qi Wu, Yifan Zhu, You Li, Zhe He, Yuwei Chen, and Daniele Sartori. "IVPR: An instant visual place recognition approach based on structural lines in Manhattan world." IEEE Transactions on Instrumentation and Measurement 69, no. 7 (2019): 4173-4187

Gan X, Yu B, Huang L, et al. Deep learning for weights training and indoor positioning using multi-sensor fingerprint[C]//2017 International Conference on Indoor Positioning and Indoor Navigation (IPIN). IEEE, 2017: 1-7.

Huang L, Yu B, Du S, et al. Multi-Level Fusion Indoor Positioning Technology Considering Credible Evaluation Analysis[J]. Remote Sensing, 2023, 15(2): 353.

Zhang Hengcai, et al. "Research Progress and Development Trend of Integrated PNT Scene Enhancement System." Journal of Wuhan University (Information Science Edition) 48.04(2023):491-505. doi:10.13203/j.whugis20220320.

Liu F, Zhang J, Wang J, et al. The indoor localization of a mobile platform based on monocular vision and coding images[J]. ISPRS International Journal of Geo-Information, 2020, 9(2): 122.

Undifferenced and Uncombined GNSS Data Processing Activities

Baocheng Zhang[1], Pengyu Hou[1], Teng Liu[1], Jiuping Zha[1], Yunbin Yuan[1]

[1] State Key Laboratory of Geodesy and Earth's Dynamics, Innovation Academy for Precision Measurement Science and Technology, Chinese Academy of Sciences

1 Introduction

Pseudo-range (code) and carrier-phase (phase) observations provide the basic data for global navigation satellite system (GNSS) positioning, navigation and timing applications. GNSS data processing aims to estimate the parameters of interest using the code and phase observations. In addition to the global positioning system (GPS) and GLONASS observations used for several decades, the emergence of the European Galileo and the Chinese BeiDou navigation satellite system (BDS) provides more observations on multiple frequencies. In this multi-GNSS and multi-frequency context, an attractive choice is to directly process the undifferenced and uncombined (UDUC) data since it enables the simplest stochastic model and a unified functional model formulated with an arbitrary number of systems and frequencies.

In this contribution, we introduce the latest status of UDUC data processing activities in China, including single-station and multi-station data processing. UDUC data processing starts with original rank-deficient observation equations, with which one cannot estimate all parameters unbiasedly. One can turn to the S-system theory to address this rank deficiency problem, which selects a minimum number of parameters as the S-basis and formulates a full-rank model estimating linear functions of original parameters (Teunissen 1985). In the single-station case, we focus on the precise point positioning (PPP) technique which determines single-receiver positions using precise orbits and clocks (Zumberge et al. 1997). Another positioning technique, known as integer ambiguity resolution-enabled PPP or PPP-RTK, extends the PPP by further correcting satellite phase biases and atmospheric delays estimated in a multi-station network. We also introduce multi-station data processing in GNSS PPP-RTK (Wübbena et al. 2005).

2 Single-station UDUC PPP data processing

The PPP technique enables one to obtain precise positions by processing single-station GNSS data with the use of precise satellite orbits and clocks externally provided. This section introduces the formulation of UDUC PPP models for single-station data processing in recent years.

Dual- and Multi-frequency PPP

Initial studies on UDUC PPP focused on processing of dual-frequency GPS data (Zhang et al. 2012). Researchers then combined multi-GNSS data to accelerate the convergence of UDUC PPP (Liu et al. 2017; Liu et al. 2018). To further improve the performances, one task of great importance is to process the emerging multi-frequency observations, e.g., BDS B1C, B2a, and B3I signals (Yang et al. 2019).

Liu et al. (2019) extended the dual-frequency UDUC PPP to a multi-frequency case. Compared with dual-frequency PPP, the addition of observations on more frequencies increases the size of rank deficiencies. These additional rank deficiencies stem from the ambiguities and phase biases on the third frequencies and beyond. Considering the same way adopted in the dual-frequency case, one can combine phase biases with ambiguities to eliminate the rank deficiency. The difference between dual-frequency and multi-frequency PPP lies in the estimability of code biases. There are no estimable code biases in the dual-frequency PPP model since code biases on the first two frequencies are selected as the S-basis, thereby entering into other estimable parameters. However, the multi-frequency PPP model needs to estimate the code biases on the third frequencies and beyond. We remark that multi-frequency UDUC PPP can obtain comparable results compared to ionospheric-free PPP (Li et al. 2015; Pan et al. 2019; Zhang et al. 2020).

UDUC PPP explicitly parameterizes ionospheric delays for estimation, implying its potentiality in ionospheric modeling. Liu et al. (2020) processed the GPS, BDS, GLONASS, and Galileo data on available triple frequencies and established an improved global vertical total electron content (VTEC) model with the spherical harmonic function. Moreover, they generated multi-GNSS differential code biases (DCBs) as by-products. Next to that, Liu and Zhang (2021) proposed a rigorous, flexible, and efficient approach to estimate code observable-specific biases (OSBs) using UDUC data. They processed one-month data and generated 32 types of code OSBs for GPS, GLONASS, BDS, Galileo and QZSS. Moreover, researches extended the concept of OSB from code to phase biases (Geng et al. 2022; Li et al. 2022).

Single-frequency PPP

Although current GNSSs transmit multi-frequency signals, many low-cost mass-market receivers can only track single-frequency observations, demanding a single-frequency PPP model for data processing. To deal with the ionospheric delays, one can rely on external ionospheric products (e.g., global ionospheric map, GIM) and describe the uncertainty of products with a proper stochastic model, thereby formulating the ionosphere-weighted single-frequency PPP model. When ionospheric products are inaccessible, one can parameterize the ionospheric delays without any constrain in the UDUC observations and formulate the ionosphere-float model (Li et al. 2019; Zhang et al. 2018; Zhao et al. 2018).

With the addition of ionosphere pseudo-observations, there are no rank deficiencies related to ionospheric delays in the single-frequency UDUC observations. However, one size of rank deficiency exists between the receiver clock and satellite differential code bias. The satellite differential code bias appears in the single-frequency PPP model because the external satellite clocks contain the ionosphere-free combination of satellite code bias. To eliminate the rank deficiency, one can select the receiver clock of the first epoch as the S-basis and thus formulate the full-rank model estimating between-epoch time-differenced receiver clocks.

Ionosphere-float single-frequency PPP needs to deal with additional rank deficiencies due to the exclusion of ionosphere pseudo-observations. These rank deficiencies originate from ionospheric delays and satellite code biases, for which one can lump the ionospheric delays with satellite differential code biases. This implies that one can only estimate biased ionospheric delays with the ionosphere-float single-frequency model. Moreover, the estimable ionospheric delays are also biased by the receiver clock of the first epoch since the rank deficiency described in the ionosphere-weighted model before still exists in the ionosphere-float model and involves ionosphere delays. With the establishment of the single-frequency ionosphere-float UDUC PPP, researchers have applied it to the ionosphere and troposphere retrieval using low-cost GNSS receivers (Li et al. 2019; Zhao et al. 2019). Moreover, Zhao et al. (2021) provided an open-source toolbox for processing multi-GNSS single-frequency data.

Modified PPP

Single and multi-frequency PPP models introduced above implicitly assume that the receiver code biases stay constant over time. However, studies in recent years have shown that this assumption is not always valid, as the receiver code biases may vary with temperature change (Zhang et al. 2021b). This motivates researchers to modify the PPP model by considering time-varying receiver code biases.

Instead of one identical receiver code bias parameterized for all epochs, Zhang et al. (2021b) proposed a modified PPP model that parameterizes one receiver code bias in each epoch. However, one cannot estimate all receiver biases uniquely due to the rank deficiency between receiver clocks, receiver code biases, ionospheric delays, and ambiguities. For this, the modified PPP selects the receiver code bias of the first epoch as the S-basis. As a result, the full-rank modified PPP model estimates the receiver clock, ionospheric delay, and ambiguities lumped with the receiver code biases of the first epoch. Moreover, the modified PPP estimates from the second epoch the differential receiver code biases with respect to the first epoch. This implies that the temporal variations of the receiver code biases become estimable, and their adverse effects on PPP parameters, such as receiver clocks and ionospheric delays, are mitigated. Numerical tests conducted by Zhang et al. (2021b) showed that the modified PPP obtained more accurate slant total electron content (STEC) compared to the original PPP model with regard to the reference values of those derived from the geometry-free (GF) carrier phase observations (Ke et al. 2022; Li et al. 2020; Zhang et al. 2019). Concerning time transfer, the modified PPP is expected to improve the medium- and long-term frequency stability of receiver clocks.

3 Multi-station UDUC PPP-RTK data processing

Although PPP can achieve high-accuracy positioning with a single-station receiver, it requires a long time (typically tens of minutes) to converge since it discards the integer nature of phase ambiguities and lacks atmosphere (troposphere and ionosphere) corrections. This motivates researchers to extend the PPP by correcting, in addition to satellite orbits and clocks, the satellite phase biases and atmospheric delays. Satellite phase biases play an important role in recovering the integer nature of ambiguities for single-receiver users, while correction of atmospheric delays makes fast integer ambiguity resolution achievable. This is the basic principle of PPP-RTK, which relies on a multi-station network to generate precise corrections (Wübbena et al. 2005). This section introduces multi-station data processing in PPP-RTK product generation.

Ionosphere-weighted PPP-RTK

Multi-station PPP-RTK data processing can also adopt the ionosphere-weighted strategy. Instead of parameterizing the ionospheric delays without any constraints, ionosphere-weighted PPP-RTK imposes a zero-mean constraint to between-receiver single-differenced ionospheric delays and considers the uncertainty of this constraint by a proper weighting scheme, as formerly done in relative positioning (Schaffrin and Bock 1988). This ionosphere-weighted strategy considers the spatial correction of ionospheric delays to formulate a stronger model than its ionosphere-float counterpart (Zha et al. 2021; Zhang et al. 2022b). In formulating the UDUC ionosphere-weighted PPP-RTK model, Zha et al. (2021) pointed out that adding ionospheric constraint reduces the rank deficiencies between ionospheric delays and receiver code biases from the number of receivers to only one. As a result, the estimable ionospheric delays of the ionosphere-weighted model are commonly affected by the differential code biases referring to a particular receiver assigned as the pivot, which eases the ionospheric interpolation on the user side. Experiments conducted on low and high solar activity days demonstrated that ionospheric-weighted PPP-RTK outperformed the ionosphere-float PPP-RTK regarding integer ambiguity resolution and positioning accuracy (Zha et al. 2021).

Phase-only PPP-RTK

PPP-RTK commonly formulates its data processing model with both GNSS phase and code observations. The inclusion of code observations eases the rank deficiency problem and contributes to positioning if one cannot fix the phase ambiguities with a high success rate. In the case where rapid integer ambiguity resolution is possible, the contribution of code observations is marginal. Moreover, the unmodeled code-related errors, typically the code multipath, may reach several meters and deteriorate the positioning.

To avoid the adverse effects of unmodelled code-related code errors, Hou et al. (2022) formulated a phase-only PPP-RTK model with multi-frequency UDUC observations. Due to the exclusion of code observations, more rank deficiencies arise in the phase observation equations. One type of rank deficiency originates from the receiver clocks and receiver phase biases, for which one can select the receiver phase biases at the first frequency as the S-basis, resulting in estimable differential receiver phase biases at the second frequency and above. Another type stems from the satellite clocks, ionospheric delays, and satellite phase biases. Selecting the satellite phase biases at the first two frequencies can eliminate the rank deficiency. This implies that phase-only PPP-RTK only provides users with the satellite phase biases on the third frequencies and beyond since the satellite phase biases at the first two frequencies are lumped with satellite clocks. By correcting, among others, the satellite clocks and satellite phase biases, users can recover the integer nature of ambiguities at each frequency.

FDMA PPP-RTK

PPP-RTK aims to recover the integer nature of ambiguities and fix them with a high success rate. Although we work with UDUC observations, only the double-differenced ambiguities are integer-estimable since we select part of ambiguities as the S-basis to address the rank deficiency problem. It is straightforward for code division multiple access (CDMA) systems to formulate double-differenced integer ambiguities. However, the GLONASS frequency division multiple access (FDMA) system defines different frequencies to identify satellites and thus cannot formulate double-differenced integer ambiguities, implying huge challenges in FDMA PPP-RTK. Fortunately, Teunissen (2019) proposed a new integer-estimable FDMA model which guarantees the integer nature of ambiguities and ensures a high success rate of partial ambiguity resolution.

Zhang et al. (2021a) presented a GLONASS PPP-RTK concept based on the integer-estimable FDMA model. They formulated a code-plus-phase GLONASS PPP-RTK model for homogeneous networks deployed with the same type of receivers, antennas, and firmware. In this case, the integer-frequency biases (IFBs) can be implicitly eliminated through re-parametrization, thereby preventing them from destroying the integer nature of ambiguities. For heterogeneous networks, they excluded the code observations and formulated a phase-only GLONASS PPP-RTK model that circumvents the unmodelled code IFBs. Although the phase-only GLONASS PPP-RTK model is too weak to achieve fast integer ambiguity resolution, one can combine GLONASS with other GNSSs to improve performances. Experiments conducted in both homogenous and heterogenous networks showed that the integration of GLONASS and GPS yielded an improvement of 8-34% in accuracy and led to a reduction of 25-50% in TTFF as compared with GPS-only PPP-RTK.

All-in-view PPP-RTK

Due to the rank deficiency in UDUC observation equations, one cannot estimate the original satellite phase bias but only the biased one lumped with ambiguities. The number of ambiguities absorbed in the estimable satellite phase biases depends on the S-basis choices. A preferable S-basis choice shall prevent a large number of ambiguities from entering into satellite phase biases since the discontinuities of ambiguities will lead to jumps in satellite phase biases and eventually result in the re-estimation of user ambiguities. Hence, one commonly selects the phase biases and ambiguities pertaining to one receiver as the S-basis and formulates the estimable satellite phase biases containing only one ambiguity, provided that all network receivers track the same satellites. However, this common-view assumption implies a default exclusion of non-common-view satellites, resulting in degraded user positioning.

Zhang et al. (2022a) extended the PPP-RTK from common-view to all-in-view networks where at least one satellite is visible to all receivers. This relieves the stringent requirement of satellite visibility and can be guaranteed in most regional networks. The formulation of the all-in-view PPP-RTK model selects as the S-basis the phase biases and the ambiguities pertaining to one satellite that is tracked by all receivers. As a result, the estimable satellite phase biases always contain two ambiguities in all-in-view networks, thereby reducing to the best extent the jumps of satellite phase biases and the re-estimation of user ambiguities. In a network where enough common-view satellites were tracked, the results showed that the all-in-view PPP-RTK performed as well as the common-view PPP-RTK. This confirmed that the all-in-view PPP-RTK model is identical to the common-view model if processing the same common-view satellites. However, results in a network where many non-common-view satellites were tracked showed that all-in-view PPP-RTK improved the positioning accuracy and reduced the TTFF compared to the common-view PPP-RTK. This was because the all-in-view PPP-RTK utilized more satellites to formulate a stronger model.

Bibliography

Geng J, Wen Q, Zhang Q, et al. (2022) GNSS observable-specific phase biases for all-frequency PPP ambiguity resolution. Journal of Geodesy 96(2):1-18

Hou P, Zhang B, Yasyukevich YV, et al. (2022) Multi-frequency phase-only PPP-RTK model applied to BeiDou data. GPS Solutions 26(3):1-14

Ke C, Sheng C, Wang S (2022) Determination of receiver code bias variations with a modified geometry-free GNSS model. Journal of Spatial Science 67(1):79-89

Li B, Ge H, Shen Y (2015) Comparison of ionosphere-free, UofC and uncombined PPP observation models. Acta geodaetica et cartographica sinica 44(7):734-740

Li M, Yuan Y, Zhang X, et al. (2020) A multi-frequency and multi-GNSS method for the retrieval of the ionospheric TEC and intraday variability of receiver DCBs. Journal of Geodesy 94(10):1-14

Li M, Zhang B, Yuan Y, et al. (2019) Single-frequency precise point positioning (PPP) for retrieving ionospheric TEC from BDS B1 data. GPS Solutions 23(1):1-11

Li X, Li X, Jiang Z, et al. (2022) A unified model of GNSS phase/code bias calibration for PPP ambiguity resolution with GPS, BDS, Galileo and GLONASS multi-frequency observations. GPS Solutions 26(3):1-16

Liu T, Yuan Y, Zhang B, et al. (2017) Multi-GNSS precise point positioning (MGPPP) using raw observations. Journal of geodesy 91(3):253-268

Liu T, Zhang B (2021) Estimation of code observation-specific biases (OSBs) for the modernized multi-frequency and multi-GNSS signals: an undifferenced and uncombined approach. Journal of Geodesy 95(8):1-20

Liu T, Zhang B, Yuan Y, et al. (2018) Real-Time Precise Point Positioning (RTPPP) with raw observations and its application in real-time regional ionospheric VTEC modeling. Journal of Geodesy 92(11):1267-1283

Liu T, Zhang B, Yuan Y, et al. (2019) Multi-GNSS triple-frequency differential code bias (DCB) determination with precise point positioning (PPP). Journal of Geodesy 93(5):765-784

Liu T, Zhang B, Yuan Y, et al. (2020) On the application of the raw-observation-based PPP to global ionosphere VTEC modeling: an advantage demonstration in the multi-frequency and multi-GNSS context. Journal of Geodesy 94(1):1-20

Pan L, Zhang X, Liu J (2019) A comparison of three widely used GPS triple-frequency precise point positioning models. GPS Solutions 23(4):1-13

Schaffrin B, Bock Y (1988) A unified scheme for processing GPS dual-band phase observations. Bulletin Geodesique 62(2):142-160

Teunissen PJG (1985) Generalized inverses, adjustment, the datum problem and S-transformations. In: Grafarend EW, Sanso F (eds) Optimization of Geodetic Networks, Springer, Berlin

Teunissen PJG (2019) A new GLONASS FDMA model GPS Solutions 23(4):1-19

Wübbena G, Schmitz M, Bagge A (2005) PPP-RTK: precise point positioning using state-space representation in RTK networks. Paper presented at the Proc. ION GNSS 2005, The Institute of Navigation, Long Beach, CA, September 13-16

Yang Y, Gao W, Guo S, et al. (2019) Introduction to BeiDou-3 navigation satellite system. NAVIGATION, Journal of the

Institute of Navigation 66(1):7-18

Zha J, Zhang B, Liu T, et al. (2021) Ionosphere-weighted undifferenced and uncombined PPP-RTK: theoretical models and experimental results. GPS Solutions 25(4):1-12

Zhang B, Hou P, Odolinski R (2022a) PPP-RTK: from common-view to all-in-view GNSS networks. Journal of Geodesy 96(12):1-20

Zhang B, Hou P, Zha J, et al. (2021a) Integer-estimable FDMA model as an enabler of GLONASS PPP-RTK. Journal of Geodesy 95(8):1-21

Zhang B, Hou P, Zha J, et al. (2022b) PPP–RTK functional models formulated with undifferenced and uncombined GNSS observations. Satellite Navigation 3(1):1-15

Zhang B, Ou J, Yuan Y, et al. (2012) Extraction of line-of-sight ionospheric observables from GPS data using precise point positioning. Science China Earth Sciences 55(11):1919-1928

Zhang B, Teunissen PJG, Yuan Y, et al. (2018) Joint estimation of vertical total electron content (VTEC) and satellite differential code biases (SDCBs) using low-cost receivers. Journal of Geodesy 92(4):401-413

Zhang B, Zhao C, Odolinski R, et al. (2021b) Functional model modification of precise point positioning considering the time-varying code biases of a receiver. Satellite Navigation 2(1):1-10

Zhang X, Hu J, Ren X (2020) New progress of PPP/PPP-RTK and positioning performance comparison of BDS/GNSS PPP. Acta Geodaetica et Cartographica Sinica 49(9):1084-1100

Zhang X, Zhang B, Yuan Y, et al. (2019) A refined carrier-to-code levelling method for retrieving ionospheric measurements from dual-frequency GPS data. Measurement Science and Technology 31(3)035010

Zhao C, Yuan Y, Zhang B, et al. (2018) Ionosphere sensing with a low-cost, single-frequency, multi-GNSS receiver. IEEE Transactions on Geoscience and Remote Sensing 57(2):881-892

Zhao C, Zhang B, Li W, et al. (2019) Simultaneous Retrieval of PWV and VTEC by Low-Cost Multi-GNSS Single-Frequency Receivers. Earth and Space Science 6(9):1694-1709

Zhao C, Zhang B, Zhang X (2021) SUPREME: an open-source single-frequency uncombined precise point positioning software. GPS Solutions 25(3):1-8

Zumberge J, Heflin M, Jefferson D, et al. (1997) Precise point positioning for the efficient and robust analysis of GPS data from large networks. Journal of geophysical research: solid earth 102(B3):5005-5017

Progress and Achievements of Multi-sensor Fusion Navigation

Xingxing Li[1], Xiaohong Zhang[1], Xiaoji Niu[2], Bijun Li[3,4], Jian Wang[5], Ling Pei[6], Fangwen Yu[7], Hongjuan Zhang[3,4], Zhouzheng Gao[8], Feng Zhu[1], Weisong Wen[9], Quan Zhang[2], Tuan Li[10,11], Tao Li[6], Tong Hua[6], Wenxian Yu[6], Jianchi Liao[1], Xin Li[1], Houzeng Han[5], Qiaozhuang Xu[8], Jie Lv[8], Cheng Yang[8], Haitao Jiang[10], Chuang Shi[10]

[1] *School of Geodesy and Geomatics, Wuhan University, Wuhan, China*

[2] *Integrated & Intelligent Navigation Group, GNSS Research Center, Wuhan University, Wuhan, China*

[3] *State Key Laboratory of Information Engineering in Surveying, Mapping and Remote Sensing, Wuhan University, Wuhan, China*

[4] *Engineering Research Center for Spatio-Temporal Data Smart Acquisition and Application, Ministry of Education of China, Wuhan University*

[5] *School of Geomatics and Urban Spatial Informatics, Beijing University of Civil Engineering and Architecture, Beijing, China*

[6] *Shanghai Jiao Tong University, Shanghai, China*

[7] *Center for Brain-inspired Computing Research, Tsinghua University, Beijing, China*

[8] *School of Land Science and Technology, China University of Geosciences (Beijing), Beijing, China*

[9] *Department of Aeronautical and Aviation Engineering, The Hong Kong Polytechnic University*

[10] *School of Electronic and Information Engineering, Beihang University*

[11] *Advanced Research Institute of Multidisciplinary Sciences, Beijing Institute of Technology*

1 Overview

Nowadays, the advent of a new technological era characterized by digitalization and intelligence has been permeating various industries. Numerous emerging domains, including mobile robotics, unmanned aerial vehicles (UAVs), and autonomous driving, are currently undergoing rapid developments. Real-time, high-precision, and all-scenario positioning services play a critical role in enabling a range of intelligent devices to execute tasks such as environmental perception, path planning, and behavior decision-making. Currently commonly used positioning technologies include dead reckoning (DR), inertial navigation system (INS), global navigation satellite system (GNSS), map matching (MM) positioning, visual/Lidar Simultaneous Localization and Mapping (SLAM) and so on. To address the inherent limitations of single positioning technology and achieve the desired performance of the positioning module, the utilization of a combination of heterogeneous and complementary sensors has become a common practice and the research of integrated navigation has become a hot topic. From 2019 to 2023, Chinese research institutes and related enterprises have been conducting extensive research on multi-sensor fusion navigation technology, resulting in a series of innovative achievements. These accomplishments can be broadly classified into multi-sensor fusion navigation models and methods, platforms and software, datasets, and applications, as described below.

2 Models and Methods

GNSS/INS integration navigation

Before the integration of GNSS and INS, initializing the heading angle was a challenging task due to the inadequate performance of MEMS gyroscopes. Static alignment including coarse alignment and fine alignment is unable to achieve an accurate initialization of the heading angle for MEMS IMU. An optimization-based alignment (OBA) approach based on the least square estimation has been proposed, in which the constant direction cosine matrix (DCM) at the initial time is separated by attitude decomposition technique to construct the least square constraint optimization problem, then Davenport's q-method is used to solve this problem (Ouyang, et al. 2022). Zhang et al. (2020) developed a velocity-based optimization-based alignment method for low dynamic scenarios with low speed and low acceleration, which relies on the multiple-epochs velocity rather than the acceleration of the vehicle. An in-motion coarse alignment for GNSS-aided strapdown SINS is introduced based on Kalman filter (KF), and the simulation, vehicle test and lake trial are carried out (Huang et al. 2022). Besides, Huang et al. (2020) and Liu et al. (2022) employed the OBA method as a foundation and utilized GNSS observations to facilitate the alignment process. Additionally, the trajectory consistency was applied in IMU heading estimation. The IMU heading is calculated as the angle between the INS- and GNSS RTK-indicated position increment vectors in the horizontal direction based on the fact that the INS- and GNSS RTK-indicated trajectories are similar in shape (Chen et al. 2020).

In field environments, interruptions of satellite signals are common due to obstructions from buildings, foliage, and tunnels. The reliability of GNSS ambiguity resolution (AR) is affected by both the precision of observations and environmental factors. The fixing carrier phase integer ambiguities is a critical factor in achieving centimeter-level high-precision positioning through GNSS/INS integrated algorithms. Zhang et al. (2019) proposed an INS-aided integer ambiguity resolution enhancement method for precise point positioning (PPP) solutions in complex environment, which reveals the INS adding effect on PPP-AR from both the theoretical analysis and performance assessment. Ma et al. (2022) proposed a baseline vector constrained ILS ambiguity resolution method for moving-baseline based positioning and attitude determination scenes, which transformed the prior baseline length to a 3D baseline vector through the INS attitude information, used to assist ambiguity search and fix. The results show significant improvement on ambiguity resolution success rate and positioning precision, especially in the weak GNSS models with severe occlusion. Yang et al. (2019) proposed a robust unscented Kalman filter (UKF) based on the generalized maximum likelihood estimation (M-estimation) to improve the robustness of the integrated navigation system of GNSS and IMU. The proposed robust M–M unscented Kalman filter (RMUKF) applies the M-estimation principle to both functional model errors and measurement errors. In addition, an equivalent weight matrix, composed of the bi-factor shrink elements, is proposed in order to keep the original correlation coefficients of the predicted state unchanged.

Land Vehicle Sensor and Dynamic Constraints Aided Positioning

The motion constraint is a kind of natural auxiliary information for land vehicle navigation, which does not require the addition of auxiliary sensors and has the advantage of simple algorithm. The non-holonomic constraint (NHC) is a common auxiliary information based on the motion characteristics of civilian vehicles to improve the navigation accuracy of GNSS/INS integration on interruption of GNSS signal. Zhang et al. (2021) evaluated the navigation performance of multi-information integration based on a low-end inertial measurement unit (IMU) in precision agriculture by utilizing different auxiliary information (ie, GNSS real-time kinematic (RTK), NHC, and dual antenna GNSS), and a series of experiments with different operation scenes (e.g., open sky in wet and dry soils) were carried out for quantitative analysis.

The correct utilization of NHC requires a compensation of lever arm between the IMU center and the valid point of this constraint on the vehicle. The lever arm impact to NHC is investigate by two integrated navigation systems with different grade of IMUs, and analysis results show the forward lever arm is the most important influence factor, and the lever arm error should be controlled within sub-decimeter to ensure the accuracy and reliability of the NHC assistance (Zhang et al. 2020). Zhang et al. (2021) proposed an optimal mounting parameter estimation scheme based on the velocity vector observations is proposed, the quaternion-based optimal attitude determination method is used to estimate the mounting angle, and the weighted recursive least squares are applied to estimate the lever arm. Chen et al. (2020) designed a DR scheme using the attitude, derived incremental distance measurements from GNSS/INS smoothing solutions, and integrated the derived with the GNSS/INS position to estimate the pitch and heading mounting angles of the IMU.

The odometer and non-holonomic constraint are disturbed to a greater extent by more serious vibrations and bumping, and the distance increment model was applied to not only the odometer measurement but also the NHC constraint for superior robustness in the cases of carrier vibration, emergency stops, and passing speed bumps (Wang et al. 2022). Ouyang et al (2020) analyzed odometer pulse increment and pulse speed measurement models based on a navigation-level IMU for land vehicles. Gao et al. (2020) provided a tightly coupled integration mode among BDS triple-frequency PPP, INS, odometer, attitude measurements, and NHC, in which significant improvements on the accuracies of positioning and attitude determination can be obtained after adding odometer, attitude measurements, and NHC. Wu et al. (2021). compared the velocity and displacement increment measurement models of a wheel-mounted MEMS IMU-based dead reckoning system. Xu et al. (2023) analyzed the enhancements of low-cost INS, odometer, NHC, and dual-antenna attitudes on upgrading ambiguity fixing rate and reliability of single-frequency RTK.

Multi-sensor fusion navigation

The rapid accumulation of inertial errors causes the positioning accuracy of GNSS/INS integration algorithms to inevitably diverge rapidly when the GNSS signal is obstructed for long periods of time or frequently. Visual-inertial navigation system (VINS) has become a practical solution for autonomous navigation due to its higher accuracy and lower cost. The integration of GNSS, INS and visual sensors provides significant benefits for navigation. On one hand, GNSS provides a spatial and temporal reference and helps in eliminating cumulative errors. On the other hand, in scenarios where GNSS signals are blocked, visual and inertial sensors can provide high-precision relative positioning information. Hu et al. (2023), Niu et al. (2022), Liao et al (2021) and Xu et al. (2022) fused stereo vision with GNSS/ SINS integration, where GNSS and stereo vision are loosely coupled and tightly coupled with SINS under the earth-centered earth-fixed (ECEF) frame, respectively. The results show that with the support of stereo vision and SINS, GNSS accuracy can be considerably improved by 60%~80% in complex environments, which also outperforms the GNSS/SINS integration. Compared with loosely coupled integration, tightly coupled integration can utilize more complete sensor information to achieve more accurate positioning results. Li et al. (2022) and Li et al. (2022) proposed a centralized Extended Kalman Filter (EKF) to directly fuse raw data from GNSS carrier phase and pseudorange measurements, IMU, and visual features at the observation level. The system is integrated with the widely used high-precision GNSS models including PPP, real-time kinematic (RTK) and PPP-RTK to increase usability and flexibility. Li et al. (2022) proposed a tightly-coupled PPP/INS/Visual SLAM system that models and optimizes all raw data using a factor graph framework. To eliminate ionospheric effects and leverage carrier phase measurements, the system utilizes the ionosphere-free (IF) model through dual-frequency observations and incorporates phase ambiguity into the estimated states. Apart from positioning accuracy of the integrated navigation system, the integrity is important to ensure the safety of integrated navigation system. Integrity monitoring algorithm consists of fault detection and calculation of the protection level (PL). It provides the ability to alarm users when faults occur. Jiang et al. (2022) proposed an effective integrity monitoring (IM) scheme for GNSS/INS/vision integration based on error state extended Kalman filter (EKF) model. The corresponding PL was derived and vehicular field test was conducted to validate the effectiveness and performance of the proposed IM algorithm for the GNSS/INS/Vision integration. Results show that the proposed integrity monitoring algorithm is effective and can assure the integrity of the GNSS/INS/Vison integration at different fault modes.

The visual sensor is highly dependent on texture features, leading to a greater requirement for illumination and texture characteristics. In contrast, the laser sensor, as a distance sensor, primarily depends on the spatial structural features. As a result, laser sensors can achieve good complementarity with visual sensors. Li et al. (2023) proposes a navigation system tightly coupling PPP/ INS/ LiDAR with the DRANSAC- RAIM and the doppler iterative closet point algorithm (DICP) as its initialization procedure is established for accurate and reliable positioning in urban environments. Li et al (2023) develop a LiDAR sliding-window plane-feature tracking method to further improve PPP/INS/LiDAR integrated system. The vehicular experiments demonstrate that the GNSS/INS/LiDAR integration can maintain submeter level horizontal positioning accuracy in GNSS-challenging environments. Li et al (2023) achieved a tightly-coupled fusion of PPP/INS/Vision/LiDAR through a centralized EKF. The vehicle experiments results indicate that the PPP/INS/Vision/LiDAR integration can maintain sub-meter level positioning in GNSS difficult environments (Figure 1).

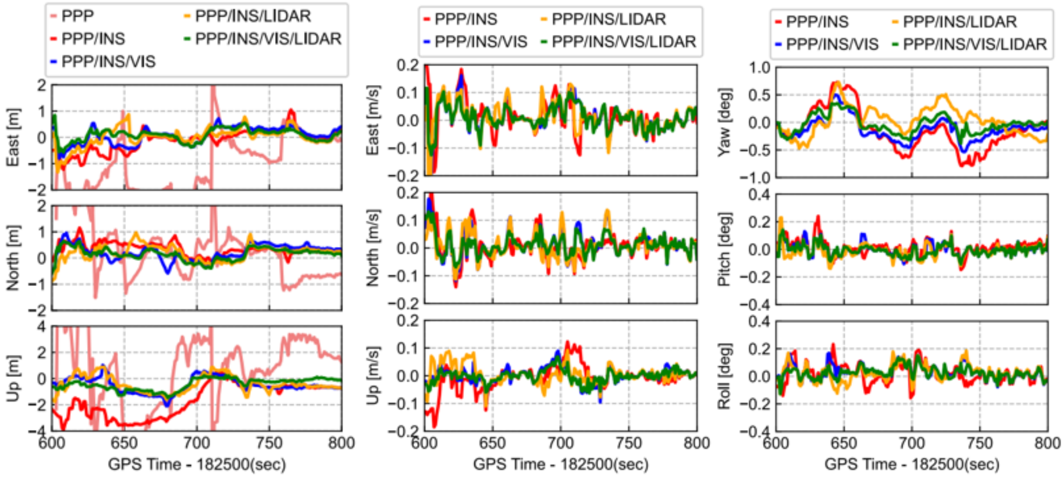

Figure 1. Position, velocity and attitude errors of PPP, PPP/INS, PPP/INS/Vision, PPP/INS/LiDAR and PPP/INS/Vision/LiDAR configurations

High-Definition Map-based Localization for Intelligent Vehicle

In addition to real-time sensor observations, High definition (HD) map is also a common option for intelligent vehicles to achieve high-precision localization. The HD map is different from LiDAR cloud point map or occupancy grid map, which is much more lightweight to save and process. Some map standards have been proposed to formalize the HD map for intelligent vehicles, such as NDS, Lanelets, and OpenDrive, and they are broadly used in automotive enterprises, like Daimler, Toyota, and VOLKSWAGEN. Zhou et al. (2022) firstly generate a HD map of areas of interest from crowdsourced data as in Figure 2. In the first step, the lane mask propagation network (LMPNet) based on the feature pyramid network (FPN) is applied to road image sequences for lane detection. The lane markings are projected from a perspective space into a three-dimensional (3D) space to calculate the world coordinate of the lanes. The lane information collected via multiple crowdsourcing vehicles is discrete and has low accuracy. Therefore, data clustering and fitting are necessary. In the second step, an improved version of the density-based spatial clustering of applications with noise (DBSCAN) clustering algorithm is used to cluster the lanes extracted in the first step. The lane markings are more accurately described by utilizing a gradual fitting algorithm and a B-spline to fit the clustered data.

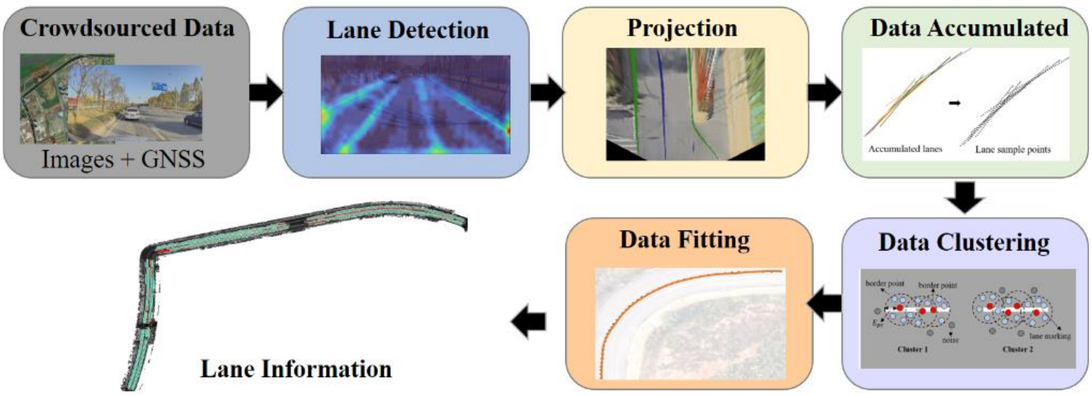

Figure 2. Extraction of lane information from multiple crowdsourcing vehicles

Lane markings can be used as topological and geometrical information in map-based localization methods, and the lateral vehicle-to-lane distance as can be used as the main measurement information in improving the positioning accuracy. Niu et al. (2023) proposed a multi-information integration method aided by lane distance to further eliminate lateral error. The lateral vehicle-to-lane distance measurements from camera-based systems, and the map-matching lane distance based on high-definition map were utilized to provide absolute lane distance measurement corrections in GNSS-denied environments. Xu et al. (2022) proposed a method to enhance GNSS/IMU integrated positioning by using a monocular camera and straight lane lines in HD maps. The positions are corrected by projecting lanes from OpenDRIVE maps onto the image, matching them with the visually detected ones, and minimizing the reprojected linear coefficients residuals. The tests demonstrate that positions in the lateral and up directions can be corrected to within 10 cm under current HD maps accuracy.

Brain-inspired Navigation

In recent years, brain-inspired navigation has emerged as a cutting-edge topic in the field of multi-source fusion intelligent navigation, garnering essential attention from scholars. This approach involves the use of artificial neural networks to model the function or structure of navigation cells by drawing upon various neural mechanisms of spatial perception, representation, and navigation. With the integration of new neuromorphic sensors and computing chips, brain-inspired navigation enables the development of a new type of biologically-inspired intelligent navigation technology with brain-like performance, or even surpassing the navigation ability of the brain. This technology provides a promising technical route to overcome the limitations of traditional navigation technology in terms of intelligence, robustness, adaptability, and energy efficiency. Based on recent discoveries in neuroscience regarding the function and mechanism of navigational neural circuits, researchers have made essential progress in the theoretical methods and key technologies of brain-inspired navigation. Studies have been conducted on neural mechanisms, computational models, and navigation systems related to brain-inspired navigation, with some scholars providing systematic reviews (Cong M, et al., 2019; Yang C, et al., 2020; Guo C, et al., 2021; Liu J, et al., 2022; Meng Z, et al., 2023). In China, researchers have focused on developing computational models of navigation cells and methods for path integration, spatial mapping, path planning and navigation. In this section, we will analyze and summarize the research carried out by Chinese researchers in these areas.

Several computational models have been proposed based on the functional characteristics of spatial navigation cells. Gong Z, et al. (2021) introduced a theoretical model of three-dimensional grid cells that can adaptively represent two-dimensional and three-dimensional space according to different navigation modes. Meanwhile, Wang Y, et al. (2021) used computational modeling methods to analyze the activity patterns of grid cells encoding three-dimensional space. By employing a gravity-modulated oscillation model combined with animal body plane information, the firing field of grid cells on a curved surface can be generated. Another model was proposed by Han K, et al. (2020) based on differential Hebbian learning.

This model spontaneously generates input associations of the Mexican hat model by modulating the firing rates of cells. By competitively and nonlinearly restricting the synaptic weights from place cells to grid cells, the hexagonal firing field distribution of grid cells is generated. Wang J, et al. (2020) proposed a dynamic multiscale grid cell model that can perform multiscale path integration based on self-motion information. These computational models are essential in understanding the working principles and functional properties of navigation cells, and they can guide the development of brain-inspired navigation methods.

Path integration is a critical component of brain-inspired navigation that involves estimating a robot's position based on environmental and self-motion data. Constructing a path integration algorithm that combines the functional characteristics of navigational cells is a significant area of research in brain-inspired navigation. Several researchers have developed brain-inspired path integration algorithms by merging the grid cell to place cell model and the visual place cell model through information fusion to represent space. For example, Yang et al. (2020) proposed a vector-based method using multiscale grid cell models for unmanned aerial vehicles in large-scale space. They achieved multiscale path integration by introducing an exponentially increasing velocity gain factor in multiple attractor neural networks. Yang et al. (2022) built a multiscale three-dimensional grid cell model that supports path integration during four-degree-of-freedom motion in three-dimensional space. Zeng et al. (2020) proposed a Bayesian attractor network model that models head direction cell networks and grid cell networks, updating the neural encoding of each subnetwork in a Bayesian manner to improve the robustness of multimodal information integration. Zhao et al. (2021) presented a path integration model based on a novel stacking algorithm that enhances the accuracy of path integration by introducing multiscale grid cells. These path integration methods serve as a foundation for robot localization.

Creating maps is also an important research topic in brain-inspired navigation as they serve as the basis for implementing path planning and navigation control. Efficient encoding and construction of these maps is key. Zhao C, et al. (2020) proposed a cognitive map construction method that uses radial basis function neural networks to learn the mapping relationship between grid cells and place cells. The improved Q-learning algorithm is used to learn the Q-value of target-oriented place cells, which are used to represent space. The target-oriented direction information is then calculated based on the principle of centroid estimation, resulting in an accurate and reliable cognitive map. Zou Q, et al. (2020) developed a cognitive map learning framework for robots that adapts grid cells and place cells based on self-motion speed, continuously constructing a cognitive map of the environment during exploration. Chen M, et al. (2021) proposed a method for converting information from multiscale grid cells to place cells, constructing a bio-inspired SLAM algorithm that covers the entire spatial environment with multiscale grid cells and establishes a conversion relationship between these and place cells. Finally, Zhao D, et al. (2022) proposed a perception-motion integration neural network model that learns cognitive map representation by integrating perception and motion information. This model includes a deep neural network that represents environmental visual features, a recurrent neural network that encodes spatial information, and a neural network that decodes position information from spatial representation, allowing for effective updates to cognitive maps based on self-motion and visual information.

The path integration and map construction have been used in several navigation models to provide real-time position and map for robot navigation. Yu N, et al. (2019) proposed a navigation algorithm based on the cognitive mechanism of the hippocampus, updating the state of grid cells and place cells according to stripe cells. Gu Y, et al. (2021) developed a vector navigation method for large-scale space based on the oscillation interference model, improving the robustness of vector navigation. Liao Y, et al. (2022) proposed a navigation method for two-dimensional space using spatial cells, correcting the error of path integration through a visual pathway computation model. Zhou Y, et al. (2022) constructed a bio-inspired target-oriented navigation model based on spatial exploration and cognitive map construction, generating a cognitive map and achieving target-oriented navigation. Chao L, et al. (2023) created an effective navigation path planning algorithm for unmanned aerial vehicles using spiking neural networks based on place cells.

Several systemic methods of brain-inspired SLAM and navigation for robots have been developed using navigation cell models. Yu et al. (2019) proposed a brain-inspired SLAM methods for 3D environments that uses 3D grid cells and multi-layer head direction cells to encode the robot's four degrees of freedom pose information, allowing for the construction of a 3D experience map that can be used for path planning and navigation control. Zeng T, et al. (2021) developed a compact brain-inspired cognitive mapping method that can generate the overall layout map of an environment while maintaining a small map size. Liu K, et al. (2022) developed a method based on neuromorphic chips that uses all-spiking neurons for path integration and map representation, enabling low-power and low-error spatial mapping. Tang H, et al. (2018) developed a brain-inspired cognitive navigation method for 2D indoor spaces that integrates cognitive mapping ability in the entorhinal cortex and episodic memory ability in the hippocampus to support robot execution of multiple tasks. In this model, a 3D continuous attractor network is used to model the functionality of the entorhinal cortex, and a recurrent spiking neural network is used to model the functionality of the hippocampus. Shen C, et al. (2019) proposed a brain-inspired navigation method that integrates inertial sensors to effectively reduce navigation errors, while Zou Q, et al. (2021) developed a self-learning system based on episodic memory that supports robot experience map learning, construction, and navigation, improving map construction and navigation efficiency and accuracy. Finally, Liu D, et al. (2022) proposed a robot navigation method based on experience and predictive maps that supports accurate construction of environment experience maps and path planning.

Indeed, the interdisciplinary collaboration between neuroscience, brain-inspired intelligence, robotics, and navigation is crucial for the development of brain-inspired navigation technology. The integration of knowledge from different fields can lead to the development of more advanced and efficient models and algorithms for robot navigation. By exploring the neural mechanisms of navigation, researchers can gain insights into how the human brain performs navigation tasks, and then apply these insights to develop new brain-inspired navigation technology that is highly robust, adaptive, and intelligent. Continued efforts in this direction can lead to the development of intelligent navigation systems that are capable of performing complex navigation tasks in various environments, such as search and rescue, logistics, and transportation.

3 Platform and Software

In addition to the notable advancements made by Chinese scholars in multi-sensor fusion navigation Models and Methods, there has also been significant progress in the development of multi-source fusion navigation platforms and software. The purpose of these platforms and software is to enhance the reliability, accuracy, and robustness of navigation systems in complex environments, thereby achieving high-precision navigation and positioning services tailored to different application scenarios. On the one hand, these platforms and software provides a foundational platform and toolset for scholars in related fields, including data input/output interfaces, visual interfaces, development interfaces and other features, that can effectively reduce the development difficulty and workload for researchers. On the other hand, they open up broader prospects for the development and application of multi-source fusion navigation algorithms.

The GREAT group in School of Geodesy and Geomatics at Wuhan University developed the Satellite Geodesy and Multi-source Navigation Software and Hardware Platform (GREAT software) as in Figure 3. The platform software not only supports common multi-sensor fusion navigation algorithms such as GNSS/INS integration, VINS, and GNSS/Visual/IMU/Lidar integration, but also provides a complete set of multi-frequency and multi-system GNSS post-processing and real-time products. The platform's hardware enables time synchronization of different sensors and support data collection of various sensors such as GNSS, IMU, Lidar, and Camera. A part of the platform's software, GREAT-UPD, has been open-sourced (Li et al. 2021).

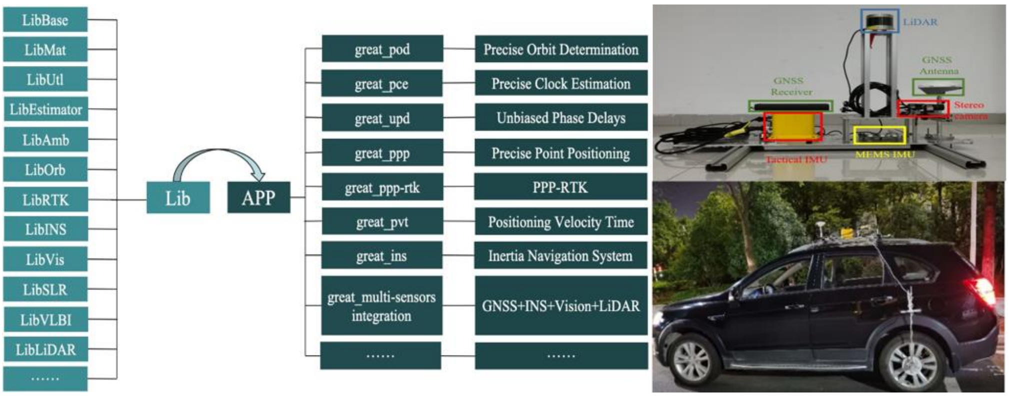

Figure 3. GREAT software: satellite geodesy and multi-source navigation software and hardware platform

The PLANET group in School of Geodesy and Geomatics at Wuhan University independently designed multi-sensor integration platforms SmartPNT-mate and SmartPNT-mini, which integrate GNSS, IMU, odometer, camera, LiDAR as well as high-precision time synchronization board and embedded AI edge computer. The group use hard synchronization to achieve microsecond-level time synchronization of various sensors and a millimeter-level spatial synchronization is achieved by precision design and machining, accurate calibration in laboratory and online dynamic estimation. Based on the SmartPNT-mate and SmartPNT-mini platforms, the group have collected multi-sensor data with a length of more than 1400 KM and a data volume of about 50TB in typical scenes, including open road sections, viaducts, urban canyons, avenues and tunnels.

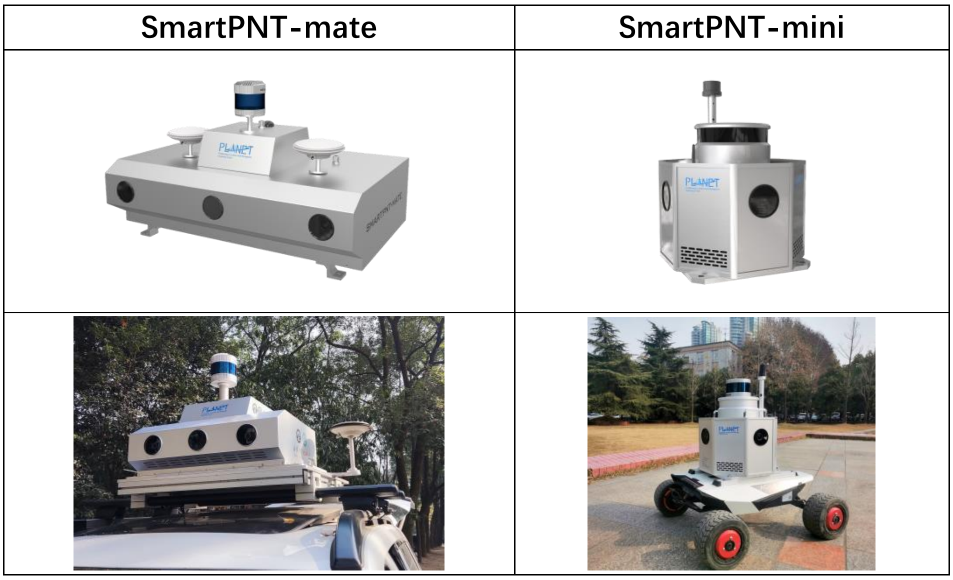

Figure 4. SmartPNT-mate and SmartPNT-mini hardware platform

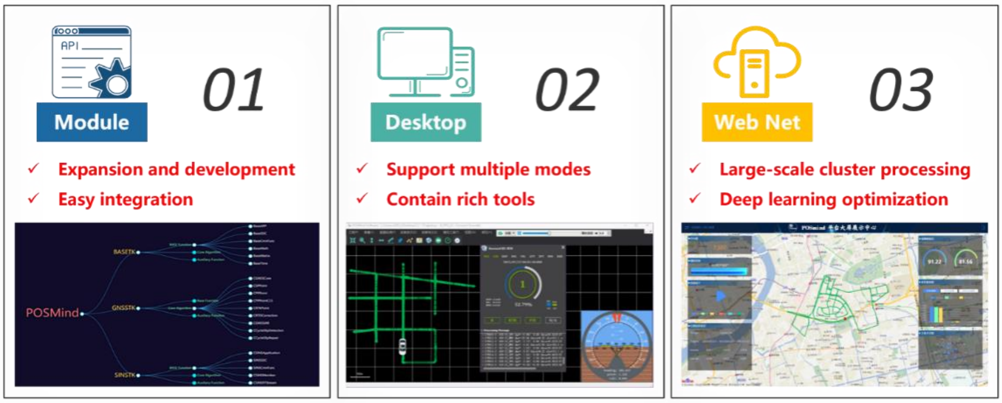

Figure 5. POSMind software system for PNT service

The Integrated & Intelligent Navigation Group (http://i2nav.cn/) at Wuhan University has made available an open-source platform for GNSS/INS integrated navigation systems based on both Extended Kalman Filter and graph optimization approaches. This platform aims to provide a general, modular, and easily extensible research environment for peers to develop and refine GNSS/INS integrated positioning algorithms. To mitigate the fragility of GNSS signals in complex environments, the research team has also proposed two novel algorithms, namely IC-GVINS (https://github.com/i2Nav-WHU/IC-GVINS) and Wheel-SLAM (https://github.com/i2Nav-WHU/Wheel-SLAM), which incorporate visual sensors and wheel encoders into the GNSS/INS integration system.

The team led by Prof. Ling Pei from Shanghai Jiao Tong University has developed an electronic system called S-Cube, which combines RTK capabilities, industrial cameras, high-precision inertial sensors, and multi-beam lidar as in Figure 6. The system is well suitable for academic research, particularly for the development and testing of SLAM algorithms. All sensors on the device are synchronized with a self-developed hardware platform, resulting in millisecond-level time differences between each sensor. Furthermore, the device can also plug in different other sensors, like panoramic camera. To benefiting the multi-sensors navigation community, the code and hardware design will be open-sourced at https://github.com/DreamWaterFound/S-Cube.git.

Figure 6. S-Cube: Plug-and-Play All-source Navigation Platform

4 Dataset

The assessment of precision is a critical aspect of the exploration of multi-sensor fusion navigation algorithms. As the number of required sensors and application scenarios increases in research, The acquisition of experimental data inevitably incurs substantial time and economic costs. Moreover, the use of disparate experimental data by various research institutions poses challenges in conducting impartial assessments of algorithmic performance. From 2019 to 2023, numerous public datasets were released by Chinese scholars. These datasets enabled many researchers worldwide to research without system and data limitations.

The integrated & intelligent navigation group at Wuhan university has opened source a vehicle GINS dataset for GNSS/INS integration applications (https://github.com/i2Nav-WHU/awesome-gins-datasets). The biggest feature of the dataset is that four different grades of MEMS IMUs are included, which provide an opportunity for the researchers to comprehensively evaluate their algorithms. The dataset was collected in an open-sky industrial area, where the GNSS RTK was well satisfied. The duration of the whole dataset is 1617 seconds, including the raw IMU data, GNSS RTK positioning results, and the ground-truth for each IMU.

Wen et al. (2020) provided the UrbanLoco: a mapping/localization dataset collected in highly-urbanized environments with a full sensor-suite.13 trajectories were collected in San Francisco and Hong Kong, covering a total length of over 40 kilometers. As shown in Figure 7, the dataset included a wide variety of urban terrains: urban canyons, bridges, tunnels, sharp turns, etc. Moreover, the dataset incorporated information from various sensors, including LIDAR, cameras, IMU, and GNSS receivers.

Figure 7. Urban terrains and sensor data of UrbanLoco

Yin et al. (2022) released M2DGR: a novel large-scale dataset collected by a ground robot with a full sensor-suite including six fish-eye and one sky-pointing RGB cameras, an infrared camera, an event camera, a Visual-Inertial Sensor, an inertial measurement unit, a LiDAR, a consumer-grade GNSS receiver and a GNSS-IMU navigation system with real-time kinematic signals (Figure 8). All those sensors were well-calibrated and synchronized, and their data were recorded simultaneously. The ground truth trajectories were obtained by the motion capture device, a laser 3D tracker, and an RTK receiver. The dataset comprises 36 sequences (about 1 TB) captured in diverse scenarios including both indoor and outdoor environments.

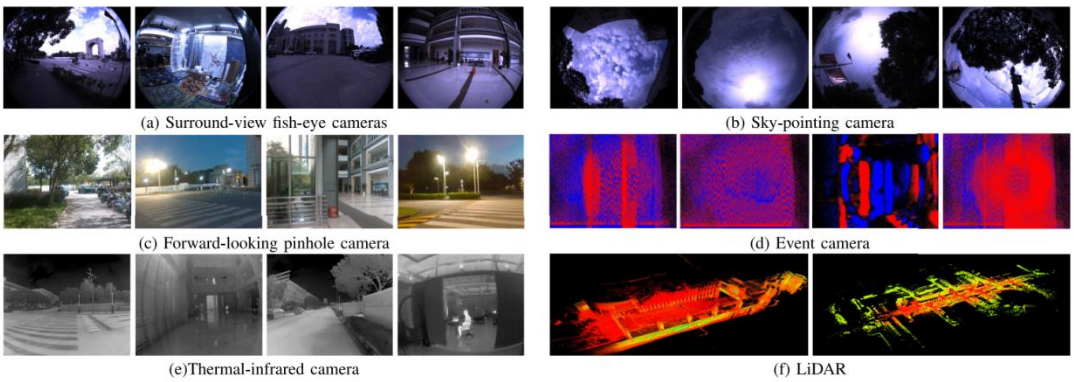

Figure 8. Typical scenarios and sensor data of M2DGR

5 Application

Multi-sensor fusion navigation can effectively overcome the limitations of single sensor navigation and provide high precision, reliability, and availability positioning services.The application prospects of multi-sensor fusion navigation are vast, encompassing traditional sectors such as transportation, agriculture, and urban construction, as well as emerging areas such as autonomous driving, UAVs, and intelligent robotics. From 2019 to 2023, Chinese scholars have made significant achievements in the application of multi-sensor fusion navigation.

The achievements of the the integrated & intelligent navigation group (http://i2nav.cn/) in the application of multi-sensor fusion navigation are remarkable (Figure 9). They are manifested in the following aspects:

1) land vehicle navigation: The license of low-cost and high-precision vehicle-mounted integrated navigation scheme has been transferred to the mainstream Beidou /GNSS chip supplier in China. The high-precision and multi-source integrated navigation scheme has served frontline autonomous driving schemes. Relevant mass production navigation chips and modules have achieved an annual sales of 100,000 sets, and are widely used in autonomous driving, intelligent transportation, precision agriculture and other hot fields.

2) low-cost integrated hardware: INS-Probe, with independent intellectual property rights, can output 50Hz real-time high-precision position, speed and attitude information, and support sensor original observation output and post-processing calculation. INS-Probe supports external IMUs, GNSS, odometer and other sensors, and provides high precision time synchronization for cameras, Lidar and other sensors, realizing multi-source data fusion and positioning, and further improving system adaptability and robustness. It can provide a complete set of hardware and software solutions for low cost and high precision navigation applications such as unmanned vehicles, robots and UAVs.

3) pipeline measuring instrument: The pipeline measuring instrument series products were developed in collaboration with Guangzhou Datie Ruiwei Technology Co., LTD. (http://dt-railway.com/), whose accuracy and overall performance are at an international leading level and won the previous engineering comparison with the same type of products at home and abroad. The products have been successfully promoted in the gas, electric power, petrochemical and other industries.

4) railway track geometry measuring trolley system: A railway track geometry measuring trolley system based on INS was completed, and applied to Wuhan MAP Space Time Navigation Technology Co., LTD. (http://www.whmpst.com/cn/) and Guangzhou Datie Ruiwei Technology Co., LTD. (http://dt-railway.com/) for three models of inertial Rail vehicle inspection hardware and software products.

5) deeply coupled GNSS/INS receiver: Proprietary intellectual property GNSS/INS deep combination receiver software and hardware prototype support achievement transformation, can provide a full set of solutions. Deep combination software has been transformed to famous mobile phone terminal manufacturers, and deep combination hardware prototype has been transformed to aerospace research institute. In complex urban scenes, the positioning

performance of deep combined receiver is better than that of Ublox integrated navigation product M8U.Under 100g/s ultra-high dynamic, the deep-depth combined receiver can output GNSS carrier phase stably.

Figure 9. The application of multi-source fusion navigation from integrated & intelligent navigation group

The team led by Prof. Jian Wang from Beijing University of Civil Engineering and Architecture have developed integrated navigation equipment for high precision automatic driving based GNSS/INS tightly coupled integration algorithm as in Figure 10. In urban environments, centimeter-level positioning results and high accuracy attitudes can be obtained. Combining with odometer information from the vehicle, the high precision positioning results can still be maintained in short GNSS outage duration. The GNSS/INS tightly coupled navigation equipment has been tested more than ten thousand times in urban environments, and it has been widely used in typical automatic driving application scenarios, such as automatic car, ports and fixed-route park area. At the same time, an automatic position and orientation system (POS) cloud processing platform has been developed for high-definition map production, the users can easily obtain the POS results by uploading the collected raw data combined with BDS ground-based augmentation system data.

Figure 10. GNSS/INS tightly coupled navigation equipment and automatic driving applications

Bibliography

Ouyang W, Wu Y. Optimization-based strapdown attitude alignment for high-accuracy systems: Covariance analysis with applications[J]. IEEE Transactions on Aerospace and Electronic systems, 2022, 58(5): 4053-4069.

Zhang Q, Li S, Xu Z, et al. Velocity-based optimization-based alignment (VBOBA) of low-end MEMS IMU/GNSS for low dynamic applications[J]. IEEE Sensors Journal, 2020, 20(10): 5527-5539.

Huang H, Wei J, Wang D, et al. In-Motion Initial Alignment Method Based on Vector Observation and Truncated Vectorized K-Matrix for SINS[J]. IEEE Transactions on Instrumentation and Measurement, 2022(71): 1-15.

Huang Y, Zhang Z, Du S, et al. A high-accuracy GPS-aided coarse alignment method for MEMS-based SINS[J]. IEEE Transactions on Instrumentation and Measurement, 2020, 69(10): 7914-7932.

Liu W, Cheng X, Ding P, et al. An optimal indirect in-motion coarse alignment method for GNSS-aided SINS[J]. IEEE Sensors Journal, 2022, 22(8): 7608-7618.

Chen Q, Lin H, Guo R, et al. Rapid and accurate initial alignment of the low-cost MEMS IMU chip dedicated for tilted RTK receiver[J]. GPS Solutions, 2020(24): 1-13.

Zhang X, Zhu F, Zhang Y, et al. The improvement in integer ambiguity resolution with INS aiding for kinematic precise point positioning[J]. Journal of Geodesy, 2019(93): 993–1010.

Ma L, Zhu F, Liu W, et al. VC-LAMBDA: a baseline vector constrained LAMBDA method for integer least-squares estimation[J]. Journal of Geodesy, 2022(96): 59.

Yang C, Shi W, Chen W. Robust M–M unscented Kalman filtering for GPS/IMU navigation [J]. Journal of Geodesy, 2019, 93:1093–1104.

Zhang Q, Chen Q, Xu Z, et al. Evaluating the navigation performance of multi-information integration based on low-end inertial sensors for precision agriculture[J]. Precision Agriculture, 2021, 22(3): 627-646.

Zhang Q, Hu Y, Niu X. Required lever arm accuracy of non-holonomic constraint for land vehicle navigation[J]. IEEE Transactions on Vehicular Technology, 2020, 69(8): 8305-8316.

Zhang Q, Hu Y, Li S, et al. Mounting parameter estimation from velocity vector observations for land vehicle navigation[J]. IEEE Transactions on Industrial Electronics, 2021, 69(4): 4234-4244.

Chen Q, Zhang Q, Niu X. Estimate the pitch and heading mounting angles of the IMU for land vehicular GNSS/INS integrated system[J]. IEEE transactions on intelligent transportation systems, 2020, 22(10): 6503-6515.

Wang L, Niu X, Zhang T, et al. Accuracy and robustness of ODO/NHC measurement models for wheeled robot positioning[J]. Measurement, 2022(201): 111720.

Ouyang W, Wu Y, Chen H. INS/odometer land navigation by accurate measurement modeling and multiple-model adaptive estimation[J]. IEEE Transactions on Aerospace and Electronic Systems, 2020, 57(1): 245-262.

Gao Z, Ge M, Li Y et al. Modeling of multi-sensor tightly aided BDS triple-frequency precise point positioning and initial assessments [J]. Information Fusion, 2020, 55:184-198

Wu Y, Niu X, Kuang J. A comparison of three measurement models for the wheel-mounted MEMS IMU-based dead reckoning system[J]. IEEE Transactions on Vehicular Technology, 2021, 70(11): 11193-11203.

Xu Q, Gao Z, Lv J et al. Tightly Coupled Integration of BDS-3 B2b RTK, IMU, Odometer, and Dual-Antenna Attitude [J]. IEEE Internet of Things Journal, 2023, 10(7): 6415-6427.

Hu J, Zhu F, Zhuo D, et al. Performance evaluation of Stereo Vision aided Loosely Coupled GNSS/SINS Integration for land vehicle navigation in Different Urban Environments[J]. IEEE Sensors Journal, 2023.

Niu X, Tang H, Zhang T, et al. IC-GVINS: A Robust, Real-Time, INS-Centric GNSS-Visual-Inertial Navigation System[J]. IEEE Robotics and Automation Letters, 2022, 8(1): 216-223.

Liao J, Li X, Wang X, et al. Enhancing navigation performance through visual-inertial odometry in GNSS-degraded environment[J]. Gps Solutions, 2021(25): 1-18.

Xu Q, Lv J, Gao Z. Evaluation on Low-cost GNSS/IMU/Vision Integration System in GNSS-denied Environments[C]. 2022 IEEE 12th International Conference on Indoor Positioning and Indoor Navigation (IPIN). IEEE, 2022: 1-6.

Li X, Li S, Zhou Y, et al. Continuous and Precise Positioning in Urban Environments by Tightly Coupled Integration of GNSS, INS and Vision[J]. IEEE Robotics and Automation Letters, 2022, 7(4): 11458-11465.

Li X, Li X, Huang J, et al. Improving PPP–RTK in urban environment by tightly coupled integration of GNSS and INS[J]. Journal of Geodesy, 2021(95): 1-18.

Li T, Pei L, Xiang Y, et al. P3-VINS: Tightly-Coupled PPP/INS/Visual SLAM Based on Optimization Approach[J]. IEEE Robotics and Automation Letters, 2022, 7(3): 7021-7027.

Jiang H, Li T, Song D, et al. An effective integrity monitoring scheme for GNSS/INS/vision integration based on error state EKF model[J]. IEEE Sensors Journal, 2022, 22(7): 7063-7073.

Li T, Pei L, Xiang Y, et al. P3-LINS: Tightly Coupled PPP-GNSS/INS/LiDAR Navigation System With Effective Initialization[J]. IEEE Transactions on Instrumentation and Measurement, 2023(72): 1-13.

Li S, Wang S, Zhou Y, et al. Tightly Coupled Integration of GNSS, INS, and LiDAR for Vehicle Navigation in Urban Environments[J]. IEEE Internet of Things Journal, 2022, 9(24): 24721-24735.

Li S, Li X, Wang H, et al. Multi-GNSS PPP/INS/Vision/LiDAR tightly integrated system for precise navigation in urban environments[J]. Information Fusion, 2023(90): 218-232.

Zhou J, Guo Y, Bian Y, et al. Lane Information Extraction for High Definition Maps Using Crowdsourced Data[J]. IEEE Transactions on Intelligent Transportation Systems, 2022.

Xu Q, Zhu F, Hu J, et al. An enhanced positioning algorithm module for low-cost GNSS/MEMS integration based on matching straight lane lines in HD maps[J]. GPS Solutions, 2023, 27(1): 22.

Niu X, Peng Y, Dai Y, et al. Camera-Based Lane-Aided Multi-Information Integration for Land Vehicle Navigation[J]. IEEE/ASME Transactions on Mechatronics, 2023, 28(1): 152-163.

Cong M, Zou Q, Liu D, et al. Review of robot navigation inspired by the localization cells' cognitive mechanism. Journal of Mechanical Engineering, 2019, 55(23): 1–12.

Yang C, Liu J Y, Xiong Z, et al. Brain-inspired navigation technology integrating perception and action decision: a review and outlook[J]. Acta Aeronautica et Astronautica Sinica, 2020, 41(1): 30-44..

Guo C, Luo B, Li F, et al. Review and verification for brain-like navigation algorithm. Geomatics and Information Science of Wuhan University, 2021, 46(12):1819-1831.

Liu J, Luo Y, Guo C, et al. PNT intelligence and intelligent PNT. Acta Geodaetica et Cartographica Sinica, 2022, 51(6):811-828.

Meng Z, Zhao D, Si B, Dai S. A survey on robot navigation based on mammalian spatial cognition. Robot, 2023, 1-17.

Gong Z, Yu F. A Plane-Dependent Model of 3D Grid Cells for Representing Both 2D and 3D Spaces Under Various Navigation Modes[J]. Frontiers in Computational Neuroscience, 2021, 15: 739515.

Wang Y, Xu X Y, Pan X C, et al. Grid cell activity and path integration on 2-D manifolds in 3-D space. Nonlinear Dynamics, 2021, 104(2): 1767-1780.

Han K, Wu D, Lai L. A model of generating grid cell based on difference Hebbian learning in brain-inspired navigation. Systems Engineering and Electronics, 2020, 42(3):674-679.

Wang J, Yan R, Tang H. Multi-Scale Extension in an entorhinal-hippocampal model for cognitive map building[J]. Frontiers in Neurorobotics, 2021, 14: 112.

Yang C, Liu J, Xiong Z, et al. Brain-inspired vector navigation method based on model of multi-scale grid cells. Journal of Chinese Inertial Technology, 2022, 28(2):179-185.

Yang C, Xiong Z, Liu J, et al. A 3D path integration approach based on multi-scale grid cells for large-scale navigation. IEEE Transactions on Cognitive and Developmental Systems, 2022, 14(03): 1009-1020.

Zeng T, Tang F, Ji D, Si B. NeuroBayesSLAM: Neurobiologically inspired Bayesian integration of multisensory information for robot navigation. Neural Network, 2020, 126:21-35.

Zhao C, Wu D, Han K, et al. Path integration model based on multi-scale grid cell. Systems Engineering and Electronics, 2020, 43(10): 2961-2967.

Zhao C, Wu D, He J, et al. Navigation cognitive map construction based on improved Q-learning algorithm. Journal of Air Force Engineering University: Natural Science Edition, 2020, 21(2): 53–60.

Zhao D, Zhang Z, Lu H, et al. Learning cognitive map representations for navigation by sensory–motor integration. IEEE transactions on cybernetics, 2022, 52(1):508-21.

Zou Q, Cong M, Liu D, et al. Robotic episodic cognitive learning inspired by hippocampal spatial cells. IEEE Robotics and Automation Letters, 2020, 5(4):5573-5580.

Yu N, Zhai Y, Yuan Y, et al. A bionic robot navigation algorithm based on cognitive mechanism of hippocampus. IEEE Transactions on Automation Science and Engineering, 2019, 16(4), 1640–1652.

Gu Y, Zhao X, Dai C. Brain-like large-scale spatial vector navigation method based on grid cell model. Control Theory & Applications, 2021, 32(12): 2094-2100.

Liao Y, Yu H, Yu N. A brain-like navigation method inspired by the spatial cells' cognitive mechanism. Computers and Electrical Engineering, 2022, 103:108305.

Chen M, Tian D. Bionic slam algorithm based on multi-scale grid cell to place cell [J]. Journal of Computer-Aided Design & Computer Graphics,2021, 33.

Zhou Y, Wu D, Song Y, et al. Biological inspired goal-oriented navigation model based on spatial exploration and construction of cognitive map. Journal of Electronics & Information Technology, 2022.

Chao L, Augenstein P, Roennau A, et al. Brain inspired path planning algorithms for drones. Frontiers in Neurorobotics, 2023, 17:29.

Li X, Han X, Li X, et al. GREAT-UPD: An open-source software for uncalibrated phase delay estimation based on multi-GNSS and multi-frequency observations[J]. GPS Solutions, 2021(25): 1-9.

Wen W, Zhou Y, Zhang G, et al. UrbanLoco: A full sensor suite dataset for mapping and localization in urban scenes[C].2020 IEEE international conference on robotics and automation (ICRA). IEEE, 2020: 2310-2316.

Yin J, Li A, Li T, et al. M2dgr: A multi-sensor and multi-scenario slam dataset for ground robots[J]. IEEE Robotics and

Automation Letters, 2021, 7(2): 2266-2273.

Yu F, Shang J, Hu Y, et al. (2019) NeuroSLAM: A arain inspired SLAM system for 3D environments. Biological Cybernetics, 113(5-6):515-545.

Zeng T, Si B. (2021) A brain-inspired compact cognitive mapping system. Cognitive Neurodynamics,15:91-101.

Liu K, Cui X, Kuang Y, et al. (2022) An all-neuron spiking 2-D path integration and map representation model implemented on neuromorphic chips. 2022 IEEE 16th International Conference on Solid-State & Integrated Circuit Technology (ICSICT), Nangjing, China, 1-3.

Tang H, Yan R, Tan KC. (2018) Cognitive navigation by neuro-inspired localization, mapping, and episodic memory. IEEE Transactions on Cognitive and Developmental Systems, 10(3):751–761.

Shen C, Liu X, Cao H, et al. (2019) Brain-like navigation scheme based on MEMS-INS and place recognition. Applied Sciences, 9(8):1708.

Zou Q, Cong M, Liu D, et al. (2021) A neurobiologically inspired mapping and navigating framework for mobile robots. Neurocomputing, 460: 181-194.

Liu D, Lyu Z, Zou Q, et al. (2022) Robotic navigation based on experiences and predictive map inspired by spatial cognition. IEEE/ASME Transactions on Mechatronics, 27(6):4316-26.

Progress of Geodesy related Ionosphere

Zishen Li[1,9], Ningbo Wang[1], Liang Wang[1], Xingliang Huo[2], Xiaodong Ren[3], Min Li[2], Qiang Zhang[3], Heng Yang[11], Qi Liu[13], Dongsheng Zhao[4], Cheng Wang[6], Ang Liu[1], Andong Hu[4], Ang Li[1], Chengpan Tang[5], Peng Chen[12], Lei Wang[3], Haiyang Fu[7], Jiahao Zhong[8], Ming Ou[10], Wang Li[14], Changyong He[15]

[1] *Aerospace Information Research Institute, Chinese Academy of Sciences*

[2] *Innovation Academy for Precision Measurement Science and Technology, Chinese Academy of Sciences*

[3] *Wuhan University, Wuhan,*

[4] *China University of Mining and Technology*

[5] *Shanghai Astronomy Observatory*

[6] *Beihang University*

[7] *Fudan University*

[8] *Sun Yat-sen University*

[9] *Qilu Aerospace Information Research Institute*

[10] *China Research Institute of Radiowave Propagation*

[11] *Yangtze Normal University*

[12] *Xi'an University of Science and Technology*

[13] *Henan University*

[14] *Kunming University of Science and Technology*

[15] *Hunan University of Science and Technology*

The ionosphere is the ionized part of the upper atmosphere of Earth, from about 40 km to 1000 km above sea level, and it plays an important role in atmospheric electricity and forms the inner edge of the magnetosphere. It has practical importance because, among other functions, it influences radio propagation, such as the Global Navigation Satellite System (GNSS), to distant places on Earth. Meanwhile, the GNSS, including BDS, GPS, Galileo and GLONASS, is also an essential technique for sensing the variation of ionosphere. During the years of 2019-2023, a large number of Chinese geodesy scientists, particularly more and more young researchers, devoted much efforts to the geodesy related ionosphere. Due to the very limited length, the achievements are carried out from the following six aspects, including

(1) the ionospheric correction models for BDS and BDSBAS,

(2) real-time global ionospheric monitoring and modeling,

(3) the ionospheric 2D and 3D modeling based on GNSS and LEO satellites,

(4) the ionospheric prediction based on artificial intelligence,

(5) the monitoring and mitigation of ionospheric disturbances for GNSS users,

(6) the ionospheric related data products and classical applications.

1 Ionospheric Correction Models for BDS-3 and BDSBAS

The application of space-based radio systems in L-band, like the Global Navigation Satellite System (GNSS), is severely affected by the signal propagation error induced by the earth's ionosphere. While the first order of ionospheric range error can be mitigated by forming the ionospheric-free linear combination of simultaneous GNSS measurements at two or more frequencies due to the dispersive nature of the ionosphere, a large number of single-frequency GNSS applications are reliant on the prior ionospheric information to correct the ionospheric path delay. Among them, ionospheric correction parameters transmitted in the navigation message of the Global Positioning System (GPS), Galileo and BeiDou are commonly used for the ionospheric error mitigation in single-frequency positioning (Yuan et al. 2019).

For BeiDou, different correction models are designed for single-frequency users of the regional BDS-2 and global BDS-3. BDS-2 adopts a Klobuchar-like model, which resembles GPS Ionospheric Correction Algorithm (ICA) but is formulated in a geographic coordinate system, to provide ionospheric correction service in the Asia-Pacific region (Wu et al. 2013). BDS-3 uses a newly designed broadcast ionospheric model BDGIM – BeiDou Global Ionospheric delay correction Model – to mitigate the ionospheric delay errors in single-frequency positioning (Yuan et al. 2019). In contrast to the Klobuchar-like model adopted in the regional BDS-2 system, the BDGIM describes global VTEC distributions with a simplified spherical harmonic expansion referring to a sun-fixed geomagnetic reference frame. The BDGIM is a two-dimensional ionospheric correction model, which relays on an elevation-dependent mapping function to convert ionospheric delays from vertical to slant directions. The nine broadcast parameters are designed to drive BDGIM, and they are transmitted in the BDS-3 navigation message with an update rate of 2 hours.

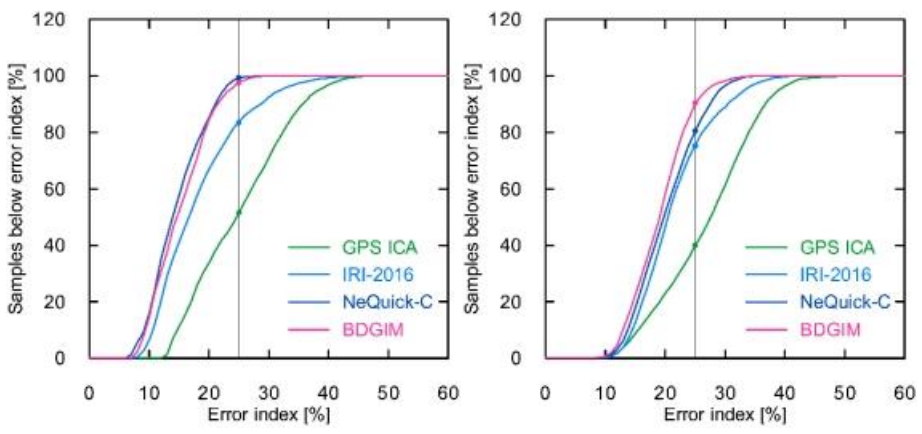

Figure 1. Cumulative distribution of different correction model errors compared to IGS-GIM (left) and Jason VTECs (right) covering solar maximum and minimum conditions. The vertical line denotes the targeted 25% error index (adapted from Wang et al. 2020).

The performance of the derived BDGIM had been assessed under different solar activities. BDGIM can achieve an overall correction capability of better than 75% for 98% of all observed samples compared to the IGS Global Ionospheric Maps (GIM) and 90% compared to Jason

VTECs. In comparison with GPS ICA, BDGIM enables a 10–20% reduction of residual ionospheric errors. Furthermore, BDGIM exhibits a comparable performance with NeQuick-C model and about 5% better than the empirical IRI-2016 model. In the analysis of BDGIM performance under disturbed and quiet geomagnetic conditions, the model RMS error increases by 60% in GIM and Jason VTEC assessments, and the 3D positioning error increases by 17% in the stand point positioning assessment (Wang et al. 2020). A notable degradation of model performance is found during the geomagnetic storm period. It can be an additional point to improve the model, especially considering the upcoming high solar conditions of the cycle 25.

For the BDS Satellite-based Augmentation System, i.e., BDSBAS, an adjusted Spherical Harmonics Adding KrigING method (SHAKING) approach was proposed for regional ionospheric VTEC modeling over China and its surrounding regions (Liu et al. 2021). In the SHAKING method, the VTEC information over the sparse observation data area is extrapolated by the Adjusted Spherical Harmonic (ASH) function, and the boundary distortion in regional VTEC modeling is corrected by the stochastic VTEC estimated using Kriging interpolation. Compared to the ASH-only solution, the quality of SHAKING generated regional ionospheric maps improves by 13-31% and 6-33% during high and low geomagnetic conditions, respectively. Compared to the inverse distance weighting (IDW) generated result, the significant quality improved of SHAKING-based VTEC maps is also observed, especially over the edge areas with an improvement of 60-80% (Liu et al. 2021). The GPS-L1 positioning augmented by BDSBAS corrections was also analyzed using the Huawei-P40 smartphone. Compared to the GPS-L1 stand positioning, the accuracy of BDSBAS augmented smartphone positioning increases by 27% in the horizontal component and 41% in a vertical component in the open-sky environment, and 50% improvement in both directions in the second experiment where the smartphone connects with an external geodetic GNSS antenna to reduce the negative effects of multipath errors (Liu et al. 2023).

2 Real-time Global Ionospheric Monitoring and Modelling

Real-time global ionospheric modeling

During the years of 2019-2023, the ionospheric associated analysis centers (IAAC) of China have continued to make significant contributions to the computation of real-time global ionospheric maps (RT-GIMs). Besides CAS, who had been working on the routine generation of RT-GIMs, Wuhan University (WHU) has also started RT-GIM computation and distribution. At CAS, an adjusted spherical harmonic expansion is used for its real-time regional ionospheric map computation (Li et al. 2019). The current implementation of the VTEC modelling approach of CAS relies on an approach that combines the periodical component and statistical part in the TEC modelling. At WHU, the global VTEC representation with a time resolution of 5 min uses the spherical harmonic expansion up to degree 12, and the real-time data streams of about 120 IGS Multi-GNSS stations (Zhang et al. 2018). WHU continues to encode its near-real-time TEC maps for real-time distribution in the RTCM format, which distributes the proposed RTCM SSR message type 1264 at 1 minute rate. As one of the analysis centers of the international GNSS Monitoring & Assessment System (iGMAS), Shanghai Astronomical Observatory

(SHAO) has been actively participating in the space weather monitoring activities initiated by IAG, contributing to the integration of the real-time ionospheric map products of IGS and iGMAS for the Asia-Pacific region.

Li et al. (2019) described a two-layer two-SH approximation is applied to GPS and BDS for regional RT-TEC modelling and a significant improvement in the convergence time of precise point positioning is highlighted with the use of regional RT-ionospheric corrections. A predicting-plus-modelling approach is employed for its RT-GIM computation using multi-GNSS streams of the IGS-RTS (Li et al. 2020). Wang et al. (2020) proposed an approach for NRT modeling of global ionospheric TEC by using the hourly IGS data based on a solar geomagnetic reference frame with spherical harmonic expansions up to a degree and order of 15. In the study of Han et al. (2022), the multi-GNSS multi-frequency observations from ground networks and space-borne ionospheric observations were assimilated to improve the real-time ionospheric modeling. Chen et al. (2022) provided an adaptive method for determining the Kalman filter process noise covariance matrix, which allows NRT modelling of the global VTEC from IGS hourly data. Yang et al. (2021) developed a new interpolation technique of RT-GIMs, i.e. Atomic Decomposition Interpolator of GIMs (ADIGIM), which minimizes the difference between observed VTEC measurement and weighted VTEC from historical GIMs in similar ionosphere conditions. Since January 2021, ADIGIM has been implemented in the RT-GIM modelling of UPC-IonSAT (one of classical IGS IAACs) by connecting the RT TOMographic IONosphere (RT-TOMION) model.

Real-time Global Ionospheric Map combination

The first experimental combination of IGS RT-GIM has been generated by applying the weights given by the real-time dSTEC assessment technique to RT-GIMs provided by CAS, CNES and UPC-IonSAT since October 2018 (Li et al. 2020). The IGS RT-GIM is now generated using four RT ionospheric streams, which includes two Chinese centers, i.e. CAS and WHU, broadcasted in IGS-SSR message type 1264 and available from the IGS caster (products.igs-ip.net). A new version of IGS combined RT-GIM was developed at CAS with additional data streams from NRCan since April 2021, compared to the legacy RT-GIM combination organized by UPC-IonSAT, supporting the IGS-SSR ionospheric message (Wang et al. 2022). An example of real-time global VTEC maps from CAS-combined and UPC-combined RT-GIMs are plotted in Figure 2, and similar global VTEC distributions can be found from both data sources. CAS combined RT-GIM streams are transmitted in both RTCM-SSR (IONO01IGS0) and IGS-SSR (IONO01IGS1) standards, which are freely accessible from the IGS data streaming server (products.igs-ip.net:2101) since January 2022.

Table 1. An overview of RT ionospheric streams used for RT-GIM combination and comparison

Analysis centers	Caster	Mountpoint	Interval / s	Format
CAS	products.igs-ip.net:2101	SSRC00CAS1	60	IGS-SSR
WHU	58.49.94.212:2101	IONO00WHU0	60	RTCM-SSR
CAS-combined	products.igs-ip.net:2101	IONO01IGS1	60	IGS-SSR

RT-GIM assessment by different approaches

Since the quality of CNES RT-GIMs are investigated by RT-SF-PPP and IGS final maps (Nie et al. 2019), the performance of RT-GIMs of CAS, WHU, and IGS RT-GIM combination, were able to be evaluated in detail over 2 years by taking difference references, for instance the IGS final GIMs, JASON3 VTEC, and slant total electron content (dSTEC), and by the SF-PPP solutions. The results showed that the accuracy of the CAS RT-GIM is slightly better than that of the other two RT-GIMs (Ren et al. 2019). In addition, DORIS dSTEC assessment provides an independent reference for the validation of RTGIM, which confirmed a better consistency with GNSS dSTEC assessments (Liu et al. 2023).

In summary, the performance of global VTEC representation in the available RT-GIMs has been assessed by IGS final product IGSG VTEC. During the testing period from 17/2/2022 to 13/03/2022 (see Figure 2), the results indicates that the RT-GIMs in particular the RT-GIM combination of CAS (marked by IONO01IGS1) turn out to be reliable sources of real-time global VTEC information.

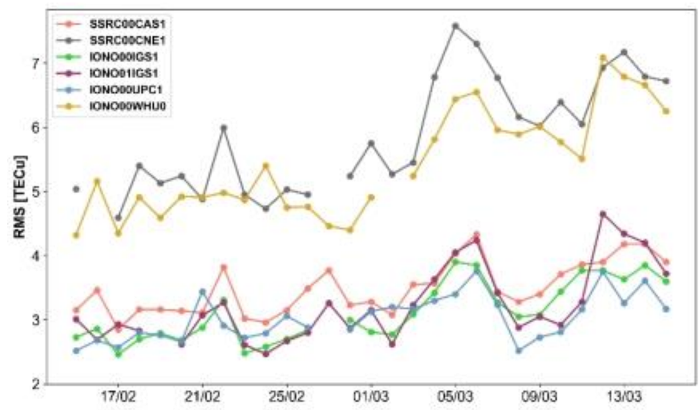

Figure 2. RMS series of different RT-GIMs (IONO01IGS1 for RT-GIM combination of CAS, IONO00IGS1 for RT-GIM combination of UPC-IonSAT, SSRC00CAS1 for CAS RT-GIM, SSRC00CNE1 for CNES RT-GIM, IONO00UPC1 for UPC-IonSAT RT-GIM, IONO00WHU0 for WHU RT-GIM) compared to IGS-GIM

3 Ionospheric 2D and 3D modeling based on GNSS and LEO satellites

A global ionosphere model with high accuracy and resolution is of great importance for ionospheric research and GNSS precise positioning applications. In the last 20 years, the accuracy and reliability of the global ionospheric model have benefited from the development of GNSS technology, but their performance is still not very good over many regions (e.g., the oceans and the polar regions) due to the lack of ground GNSS stations. Fortunately, the rapid development of low-Earth-orbit (LEO) satellite constellations provides a potential opportunity to address this issue. In 2019–2023, many Chinese researchers have been investigating global ionospheric 2D and 3D modeling by a combination of GNSS and LEO satellites through both simulated and real-data experiments.

Establishing high-precision and high-resolution ionospheric TEC models requires precise

GNSS TEC measurements as well as LEO-based TEC measurements over the ocean. Ren et al. (2020a) used the PPP-Fixed method to extract ionospheric observations from phase observations based on zero-difference integer ambiguity. This method greatly improves the precision of the TEC observations. In the space-borne TEC retrieval, one of the main error sources that should be deducted is satellite and receiver differential code bias (DCB). Zhong et al. (2016a) proposed an improved DCB estimation method based on zero TEC assumption and optimized the parameter in the least square method for space-borne TEC determination. Based on space-borne GNSS observations, Zhong et al. (2016b, 2020) indicated that the long-term variations of GPS DCBs are primarily attributed to the satellite replacement under the zero-mean constraint condition. With Chinese Fengyun satellite onboard observations, Li et al. (2017) estimated DCBs for both BDS and GPS, and Li et al. (2019) discussed the stability of DCBs for different solutions. Ren et al. (2020) estimated the LEO DCBs and generated the global topside ionospheric map using observations from multiple LEO satellites at different orbital altitudes. The mapping function is also fundamental in the space-borne TEC retrieval. Zhong et al. (2016c) evaluated different combinations of ionospheric effect height and mapping function for LEO satellites. Wu et al. (2021) proposed a new mapping Function based on the plasmaspheric scale height, and Wu et al. (2022) further analyzed the ionospheric horizontal gradients in the TEC mapping for space-borne TEC. Yuan et al. (2020, 2021) estimated LEO DCB and GPS DCB based on inequality constrained least square and multi-layer mapping function.

As an emerging remote sensing technique, GNSS reflectometry (GNSS-R) showed great potential in the ionospheric TEC monitoring and modeling over data-void or data-sparse regions. Wang and Morton (2021) investigated the feasibility of utilizing coherent GNSS-R measurements obtained by Spire CubeSats carrier phase data source to estimate slant TEC along the reflection signal path ionospheric and the results show that the slant TEC retrieved from GNSS-R measurements and from GIMs follow a similar trend. Furthermore, Liu et al. (2021) presented a simulation study of Arctic TEC mapping by integrating coherent GNSS-R measurements obtained from LEO CubeSat constellations with available ground-based GNSS observations. Ren et al. (2022) proposed an improved method which considers the influence of tropospheric delays and the topside ionospheric delays above the spaceborne GNSS-R receiver to estimate ionospheric TEC over oceans using the spaceborne GNSS-R technique.

Due to the emergence of LEO constellations, ionospheric research has gradually begun to differentiate between the top and bottom layers. LEO satellites typically orbit at altitudes ranging from 400 to 1400 km, which is around or above the ionospheric electron density maximum. The space-borne GNSS receivers bring great opportunities for the ionospheric sensing of the bottomside ionosphere (Li et al., 2022) and topside ionosphere (Ren et al., 2020b).

LEO satellites provide a great opportunity for global ionospheric modeling, however due to the limited number of LEO satellites available at present, Ren et al. (2020c) firstly simulated three kinds of designed LEO constellations with 60, 96, and 192 satellite data, the results show that LEO observations can expand the coverage and increase the density of ionospheric pierce points (IPPs), as shown in Figure 3.

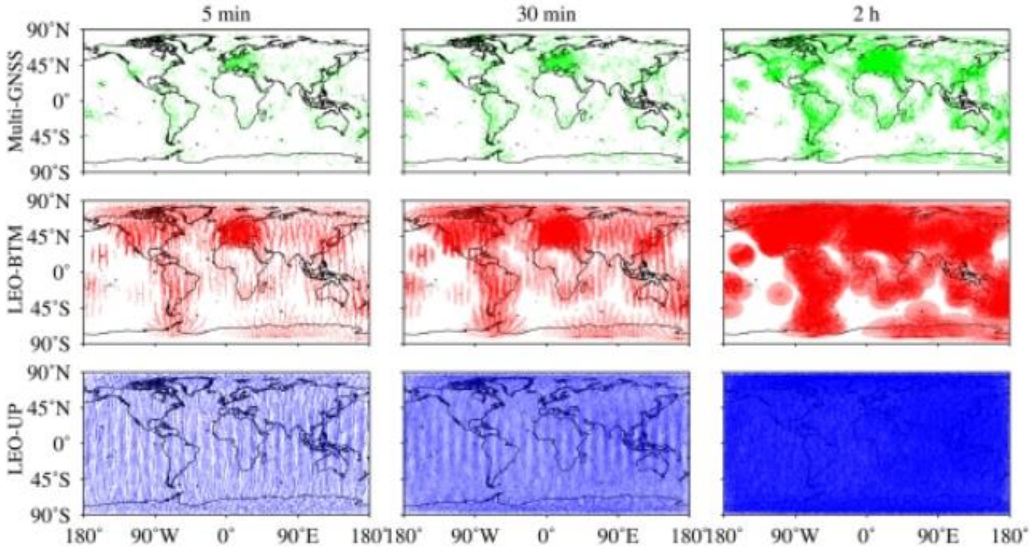

Figure 3. Distribution of ionospheric pierce points derived from Low-Earth-Orbiting (LEO) constellation with 192 satellites within different time spans, that is, 5 min, 30 min, and 2 hours, respectively.

Additionally, multi-source data such as GNSS data, satellite altimetry data, ionospheric occultation, and DORIS data can be used to generate a global ionospheric model with a significant improvement in accuracy (Hu et al., 2019; Han et al., 2022 ; Ren et al., 2021a ; Chen et al., 2021). To solve the problem that the satellite-based observation of ionospheric height cannot cover the whole ionospheric height range, Zhang et al. (2020) attributed the satellite altimetry and GNSS radio occultation products to a unified observation scale, and confirmed that the satellite-based ionospheric TEC products can be an effective supplement to the ground-based ionospheric TEC observation in ocean regions. An et al. (2019) attempted to fuse the ground GNSS with the IRI model and satellite altimetry. Shi et al. (2022) introduced the artificial neural network (ANN) to investigate the electron content at low latitudes. Using the ANN technique to combine the TEC from the IGS tracking station observations and the TEC measured by the COSMIC-2, the new model describes the ionospheric structure well.

In a global 3D ionospheric tomographic model, Zhou et al. (2020) used computer tomography to reconstruct three-dimensional electron density in the topside ionosphere using TEC observations from the Swarm-A/C satellites. Similarly, there are also limited space-borne measurements available for global ionospheric tomography. Thus, Ren et al. (2021b) investigated the potential improvements of GNSS-based ionospheric tomography at a global scale by combining the upcoming LEO constellations through simulation experiments. Wang et al. (2022) proposed using the ionospheric profile data of COSMIC-2 as the initial scale factor to constrain GNSS data. The work indicated that the fusion of GNSS and COSMIC-2 can improve the accuracy and spatial resolution of the 3-D tomographic modeling results. The combined GNSS-InSAR techniques will play an important role for imaging multiple scale ionospheric irregularities. Sui et al. (2020) verified the feasibility of three-dimensional tomography of the ionospheric electron density in the imaging area based on the Lutan-1 system and a possible combination of GNSS-InSAR technology for ionospheric parameter retrieval.

Ionospheric data assimilation is a now-casting technique to incorporate irregular ionospheric measurements into a certain background model, which is an effective and efficient way to overcome the limitation of the unbalanced data distribution and to improve the accuracy of the model, so that the model and the data can be optimally combined with each other to produce a more reliable and reasonable system specification. Data assimilation technology has also been widely applied in ionospheric specification and prediction. Ou et al. (2022) adopted observation system simulation experiments (OSSE) to analyze the impacts of multi-source observations on ionospheric assimilation, and verified that space-based observations can improve the accuracy of ionospheric TEC and electron density. In particular, GNSS occultation can significantly improve the accuracy of nowcast and forecast of ionospheric electron density. The results also show that the existing observation system layout improves the data assimilation accuracy in the middle and low latitudes better than in the high latitudes. Ou et al. (2021) developed a near-real-time global ionospheric data assimilation and forecasting system (RT-GIDAM) based on a cloud computing platform. RT-GIDAM can realize the global ionospheric TEC and electron density nowcast and forecast in near real-time with higher spatio-temporal resolution (2.5°×5°×15min). In order to improve the forecast accuracy of the ionosphere, He et al. (2019; 2020) constructed an EnKF ionosphere and thermosphere data assimilation algorithm through a sparse matrix method and found that the ionosphere forecast quality could be enhanced by optimizing the thermospheric neutral components via the EnKF method. The ionosphere electron density forecast accuracy can be improved by at least 10% for 24 hours.

4 Ionospheric Predictions based on Artificial Intelligence

Artificial Intelligence related approaches have been more widely used in ionospheric modeling by Chinese scholar since 2019 than ever, especially machine learning (ML) methods. ML approaches do not require a pre-defined base function in comparison with the traditional ionospheric modeling method, such as spherical harmonics. MLs can automatically construct a non-linear base function (using layers, unit, and activation functions) from a large amount of data. This can significantly reduce the model error during the model training.

Xia et al. (2021) developed a regional forecast model for TEC over China with a support vector machine. The variation of seasonal and local characteristics is also validated by the SVM model.

Li et al. (2021) developed an artificial neural network model for electron density is using the multi-observations, including COSMIC, FY-3C and Digisondes. Tang et al. (2020) investigated three machine learning models for TEC forecasting, including the long short-term memory (LSTM), autoregressive integrated moving average, and sequence-to-sequence models. Shi et al. (2022) adopted bidirectional long short-term memory (bi-LSTM) to forecast the ionospheric total electron content maps over China using long-term ground-based global positioning system observations from the Crustal Movement Observation Network of China. Yang et al. (2022) implemented pix2pixhd, one of the generative adversarial networks (GANs) to forecasting the one-day-ahead global TEC map.

LSTM has also been utilized in TEC map completion. Liu et al. (2020) uses LSTM to forecast the traditional coefficients to construct global ionospheric maps, and the typical ionospheric structures are sighted during geomagnetic events.

GAN, as developed for image completion initially, has proved to be effective tool in reconstructing global TEC maps. Pan et al. (2020, 2021) developed GANs named DCGAN-PB and SNP-GAN for global TEC completion. DCGAN-PB applies Poisson blending as a post-processing procedure and shows a superior TEC completion performance over the traditional single-image inpainting methods such as TELEA and NS using the realistic MIT-TEC masks. While SNP-GAN, as a more enhanced tool, equips with an end-to-end generator, and robustness in different masks is the main advantage of SNP-GAN over DCGAN-PB. Moreover, SNP-GAN has shown the potential in uncovering meso-scale structures such as cusp. An illustration of results is shown in Figure 5. Our work show that the deep learning methods can learn from thousands of TEC maps in different conditions and extract useful features to overcome the challenges of effectively recovering the missing data in a large area not covered by the observation network. Chen et al. (2019, 2022) and Chen et al. (2021) also investigated several possibilities to improve the performance of GANs in global TEC completion, including take extra physical parameters into consideration and develop a new multi-step auxiliary prediction named MSAP.

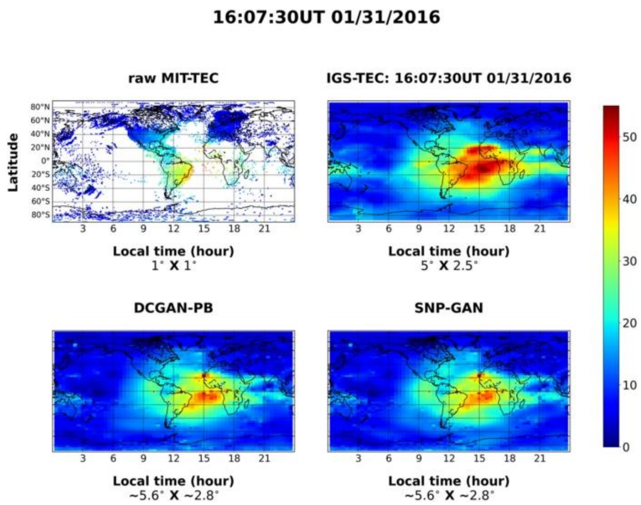

Figure 5. Global TEC maps at 16:07:30 UT on January 31, 2016. TEC peaks above the Atlantic ocean can be seen in all completed maps.

5 Monitoring and Modeling of Ionospheric Disturbances for GNSS users

Sudden changes in various space conditions, such as solar flare, geomagnetic storm and severe geological disasters, can cause evident ionospheric disturbances, resulting in plasma irregularities, which can disturb the trans ionospheric radio wave signals. For instance, the ground-based GNSS receivers can observe rapidly fluctuated carrier phase and amplitude signals if the radio wave strikes ionospheric irregularities. Monitoring and modeling ionospheric irregularities precisely is a key mean to correct its adverse impact on GNSS, making it become one of the heated research topics in the fields of both geodesy and space physics. This paper will initially summarize the recent research progress on monitoring and modeling of ionosphere by Chinese researchers, including monitoring network, monitoring methods, models and their applications in enhancing the accuracy of positioning and revealing the coupling relationship with space events.

China has established a three-dimensional monitoring network in recent years to monitor ionospheric disturbances. Since July 31, 2020, China has completed the construction of BeiDou navigation satellite system. Different from other existing navigation systems, BeiDou has Geostationary Orbit (GEO) satellites, which benefits the research of the ionospheric disturbances (Hu et al. 2021), as the stationary IPPs of GEO satellites are free from the Doppler effect of the relative motion between satellites and receivers. Besides GEO, China has also launched a number low earth orbit (LEO) satellites with Langmuir probes, such as China Seismo-Electromagnetic Satellite (CSES) (Yan et al. 2020), FY3C and FY3D. On the ground, China has established multiple ionospheric monitoring networks, e.g., Crustal Movement Observation Network of China (CMONC) with more than 2000 stations, Meridian Project Phase II with 31 stations, BDSMART Space Atmospheric Monitoring Network with 55 stations led by Aerospace Information Research Institute (AIR), Chinese Academy of Sciences, and Ionospheric Observation Network for Irregularity and Scintillation in East/Southeast Asia (IONOISE) with 74 stations (Sun et al. 2020).

Supported by the development of instruments and networks, significant progress has achieved in the methods of monitoring ionospheric disturbance, especially in the application of GNSS geodetic receivers to ionospheric scintillation monitoring. Currently, GNSS receivers used in ionospheric monitoring can be divided into two types, the ionospheric scintillation monitoring receiver (ISMR) and the geodetic receiver. Two scintillation indices are available from ISMR, i.e. amplitude scintillation index (S_4) and phase scintillation index (σ_ϕ). The distribution of ISMR is limited by its expensive price, while the accuracy of its scintillation indices is affected by the cut-off frequency of the Butterworth filter adopted in the detrending process. Although various studies have been carried out, it has not reached an agreement on the common cut-off frequency globally (Song et al. 2022), resulting in phase without amplitude scintillations in the Artic region. Recently, low-cost and widely distributed GNSS geodetic receivers have been widely used in ionospheric scintillation monitoring, mainly benefitted from the wide application of ROTI (Yang et al. 2020). Besides ROTI, a variety of scintillation indices for geodetic receivers are also proposed, e.g. $\sigma_{\phi f,\mathrm{wavelet}}$ (Zhao et al. 2021) and $\mathrm{SI}_{\mathrm{det}}$ (Luo et al. 2020), when ISMR is not available. The observations from geodetic receivers with 1s sampling interval is tried to provide nearly identical scintillation monitoring performance as ISMR, shown in Figure 6. For the data with 30s sampling interval, which is more generally available at all GNSS networks, existing scintillation indices still cannot provide accurate scintillation monitoring performance at the epoch level, where further research is needed.

Another important research direction of ionospheric disturbance is to model ionospheric scintillation, which is one of the key methods to eliminate the adverse effects of scintillation on positioning. Two types of approaches are usually adopted to model scintillation, i.e. the analytical model based on physical mechanisms and the data-driven model. The factors controlling the generation, evolution and changes between days are still unclear, limiting the accuracy of analytical model on the short-term variations (Li et al. 2021). With the accumulation of ionospheric monitoring data and the development of deep learning technology, existing research has established a number of data-driven ionospheric scintillation models (Liu et al. 2021). AIR has already provided the ROTI-based ionospheric scintillation model covering China as a free product with a time resolution of 5 minutes.

One application of ionospheric disturbance monitoring and modeling is to eliminate the adverse effects of scintillation on GNSS positioning. The following three approaches are usually adopted to improve the positioning accuracy under scintillation conditions. The first is to correct cycle slips. Frequent cycle slips caused by scintillation will lead to excessive ambiguity resets, affecting the parameter calculation of both PPP and RTK technology (Zhao et al. 2019). However, determining the optimal threshold for judging cycle slip correctly is still a problem affect the performance of this method. The second method is to adjust the stochastic model adaptively according to the magnitude of scintillation (Luo et al. 2020), while it is difficult to apply in real-time applications due to the dependence on the processing efficiency of scintillation index. The third method is to eliminate the modeling residual error during the ionospheric active period with the model value. Recently, several Chinese companies, e.g. Qianxun and CHC Navigation, have released their product on GNSS positioning under the condition of strong ionospheric activity, which can basically ensure a fixed solution of RTK equipment.

Another application of ionospheric disturbance monitoring and modeling is to understand the coupling relationship between ionospheric disturbances and space events. As solar irradiation is the main energy in driving the ionospheric dynamic convection, significant attention has been paid to the remarkable ionospheric disturbances triggered by the sudden solar event, e.g. the X9.3 solar flare and the following G4 geomagnetic storm in September 2017 (Li et al. 2022, Ren et al. 2022), showing the increase of global daytime currents and the reduction of the eastward electric fields during the daytime from the equator to middle latitudes. The coupling relationships are also studied between the ionospheric disturbance and severe natural disasters, such as Nepal (2015), Ridgecrest (M7.1, 2019), Xinjiang (M6.2, 2016), Kaikoura (M7.8, 2016) and Fukushima (M6.9, 2016) earthquakes (Kong et al. 2018), showing either pre-seismic or co-seismic ionospheric disturbances. The destructive Tonga volcanic eruption attracts significant attention (Li et al. 2023), leading to a significant local ionospheric hole and the equatorial plasma bubbles across the wide Asia-Oceania area. Studies were also focused on the ionospheric disturbances caused by human activities, such as nuclear explosion and rocket launching (Liu et al. 2020), revealing the total electron content perturbation and its propagation speed.

Overall, this paper briefly summarized the outstanding achievements of Chinese researchers in monitoring and modeling ionospheric disturbances. In the past few years, China has established a space-ground based ionospheric disturbance monitoring network, including the BeiDou system, the LEO satellites and the ground GNSS receivers, especially those geodetic receivers benefitted from the development of the ionospheric scintillation indices. Regional ionospheric scintillation models were established and broadcasted as a product based on the long-term observations. The monitoring results and the established models were adopted to improve the positioning accuracy during the period with strong ionospheric activities and study the coupling relationship between ionospheric disturbances and solar-terrestrial events, natural disasters and human activities.

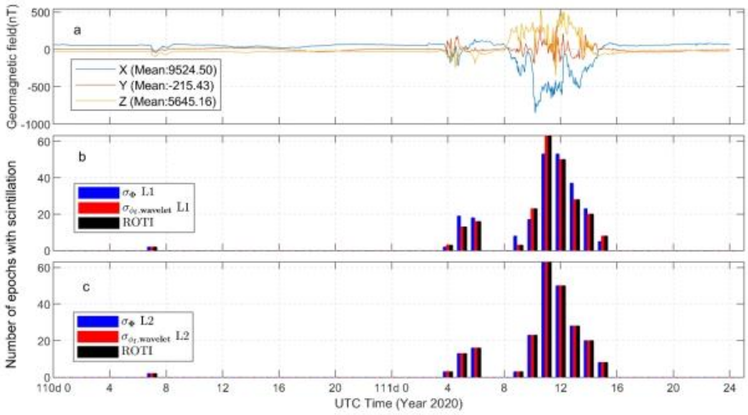

Figure 6. Scintillation monitoring performance with 1s sampling interval data from geodetic GNSS receiver

6 Ionospheric related Data Products and Classical Applications

Ionospheric services for satellite navigation

Dual- or triple-frequency GNSS users can mitigate the ionospheric delay errors by forming the ionospheric-free (IF) linear combinations, but which will cause noise amplification as well as the loss of ionospheric delay information. A priori ionospheric information with high accuracy is required to correct the ionospheric delay in single-frequency PPP and can be used as virtual observations to constrain the parameters (Liu et al., 2023). Aside from terrestrial geodetic GNSS receivers, the mass-market smartphones might also benefit from the ionospheric augmentation service, e.g., BDSBAS ionospheric GIVD, GIMs, regional ionospheric maps (RIMs). Wang et al. (2021) proposed an PPP approach named Smart-PPP to achieve the sub-meter-level positioning accuracy for smart phone, as shown in Figure 8, in which the priori ionospheric information is introduced to eliminate ionospheric effects. Based on the investigations of Yi et al. (2021), smartphone PPP enjoys more beneficial effects from ionospheric constraints (IC) than low-cost and geodetic hardware, with a significant 30% horizontal improvement in the first epoch. Wang et al. (2020) find horizontal positioning accuracies of the smartphones with PPP-IC model are better than 1 m, while those with the SPP and the traditional PPP models are about 2 m. The ambiguity fixing success rate of the uncombined PPP models, which is proceed with high-precise ionospheric delay corrections, is slightly higher than that of the combined model (Wang et al., 2019). In additional, Zhao et al. (2021) also analyzed the reliability of GIM RMS maps for high-precision positioning by comparing the actual error of the differential STEC (dSTEC) with the RMS of the dSTEC derived from the RMS maps.

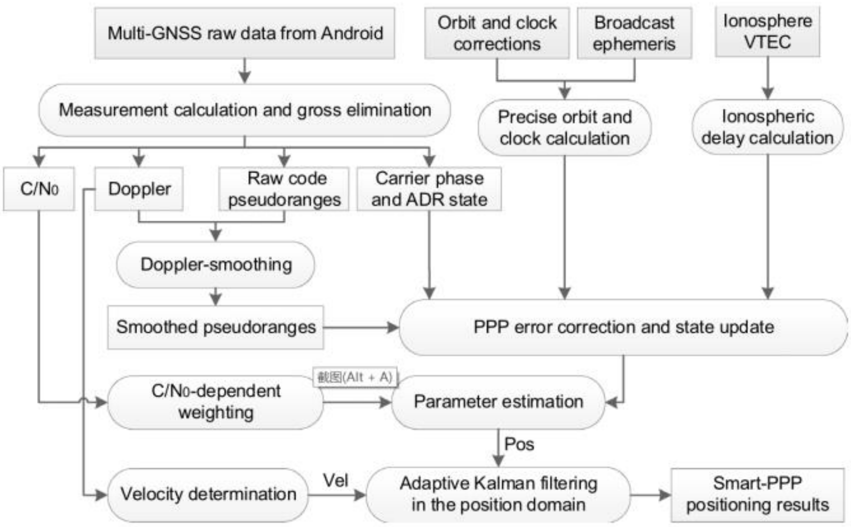

Figure 8. Flow diagram of PPP processing, in which the priori ionospheric information is introduced to eliminate ionospheric effects. After Wang et al. (2021).

Ionospheric applications for Civil Aviation

In particular, International Civil Aviation Organization (ICAO) has also put forward new requirements for state monitoring of the ionosphere, which is used to promotes migration to GNSS-based navigation from conventional (ground-based). The requirements defined by ICAO is that all the requirements (accuracy, integrity, continuity, and availability) with high safety (integrity) must be fulfilled together for operational systems. In the framework of ICAO, the ionospheric products are released for civil aviation, e.g., TEC Real Time Maps, global error of the NRT TEC map derived from errors of the GNSS measurement, TEC rate of the dynamic of the ionosphere, TEC-gradients, TEC-map prediction (1h - 24h), TEC-map Quality, 3D ionosphere reconstruction and model, scintillation measurement, ROTI (Rate of Change of TEC index), AATR (Along-Arc Tec Rate) or similar ionospheric index. In ICAO, the ionospheric TEC gradients research attracts more scholars' attention. Chang et al. (2021) gives the spatial decorrelation result on March 7, 2012, using the time-step method and the Brazilian GNSS network data, for the SLS-4000 GBAS. Jin et al. (2020) used the vertical ionospheric delay differences and residual differences at IPPs to perform the correlation analysis, and applied the annular data deprivation and three quadrants deprivation methods to create the undersampled threats over China region.

Scientific applications with ionospheric products

The multi-source ionospheric data service also provides convenient conditions for studying the spatiotemporal characteristics of the ionosphere and carrying out corresponding scientific applications, which covers the following topics: ionospheric space weather, ionospheric structures and climatology, ionospheric dynamics and couplings, and planetary ionospheres (Liu et al., 2022b). The ionosphere space weather has significant temporal and spatial changes, which is generally controlled by the Sun’s photoionization effect. Solar activity events can significantly affect the spatiotemporal variation of the ionosphere, e.g., solar eclipse, flare-enhanced ionospheric events, solar wind and so on (Zhang et al., 2020a , Jin et al., 2021 , Sun et al., 2021). A solar eclipse transiently shields the solar ionizing radiation falling into the atmosphere of the Earth, in which the rapid solar input reduction results in the ionospheric disturbances (Zhang et al., 2020a), as shown in Figure 9. The geomagnetic storms are mainly due to Coronal Mass Ejection (CME) or High-Speed Solar Winds (HSSWs), with the emission from sporadically rotating coronal holes during active geomagnetic days. These geomagnetic storms propagate significant energy inputs into the Earth's magnetosphere via solar winds, whose energy coupled with the Earth through many physical processes (e.g., field aligned currents, auroral electrojet, magnetospheric convection, etc.) in the auroral zone. The storm time ionospheric responses can easily be measured with the ground and space-based observations, e.g., GNSS, ionosondes, magnetometers and in situ multi-instrumental satellite systems.

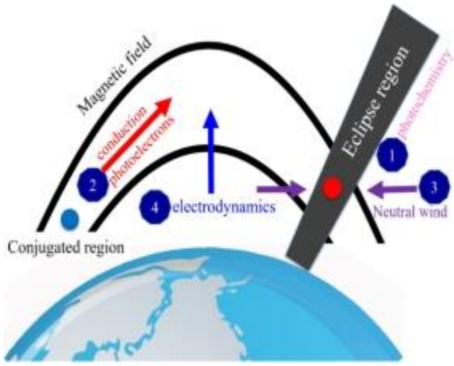

Figure 9. The related physical processes during the eclipse, including the photochemistry, interhemispheric photoelectron transport, thermal conduction, neutral wind, and electrodynamics. After Zhang et al.(2020a).

One application of ionospheric scientific exploration is to study ionospheric dynamics and couplings, including sudden stratosphere warming and lower atmospheric forcing, ionospheric dynamics, lithosphere-ionosphere coupling and solar wind-magnetosphere-polar ionosphere coupling (Huang et al., 2020 , Liu et al., 2022a). Based on the ROCSAT-1 satellite observations during 1999–2004, Zhang et al. (2020b) present the first analysis of the dependence of the afternoon downward plasma drifts on the season, longitude, solar activity, and lunar phase. Li et al. (2020a) investigated the responses of the ionosphere and the neutral winds in the mesospheric and lower thermospheric region to two SSWs, respectively. In the investigations of Li et al. (2022), effective ionospheric perturbations were reported immediately, respectively, two weeks and one week prior to these two earthquakes events, which reconfirms that ionospheric information can be utilized for short-term EQ prediction.

Another application covers ionospheric structures and climatology, which aims at ionospheric spatial structure and temporal variation (Chen et al., 2020 , Li et al., 2020b , Kuai et al., 2021 , Li et al., 2021 , Ma et al., 2021 , Liu et al., 2022a). The former mainly studies the uneven distribution of the ionosphere in the spatial dimension, which is represented by ionospheric climatology in equatorial ionization anomaly (EIA) and mid-latitude trough regions, topside ionosphere, night-time zonal ionospheric and polar region ionospheric. The latter takes the characteristics of the ionospheric morphology in the time dimension as the main research target, e.g., climatology of mid-latitude F2-layer bite-out, electron density enhancements, equatorial sunrise enhancement, ionospheric diurnal double-maxima (DDM) patterns and ionospheric sensitivity to the solar Extreme Ultraviolet (EUV).

In addition, the mechanism of some ionospheric anomalies is also a hotspot of ionospheric scientific research, for examples, Es Layer, traveling ionospheric disturbances (TID), ionosphere and equatorial plasma bubbles (EPB), polar cap patches (Sun et al., 2020 , Xie et al., 2020 , Xu et al., 2020).

Bibliography

An X, Meng X, Jiang W et al (2019) Global ionosphere estimation based on data fusion from multisource: Multi-GNSS, IRI model, and satellite altimetry. Journal of Geophysical Research: Space Physics, 124(7), 6012-6028.

Chang H, Yoon M, Pullen S, et al. 2021. Ionospheric spatial decorrelation assessment for GBAS daytime operations in Brazil[J]. Navigation, 68(2): 391-404.

Chen P, Liu L, Liu H et al (2021). Accuracy evaluation of XUST's global ionospheric products. Advances in Space Research, 68(1), 201-213.

Chen P., Liu H., Schmidt M., Yao Y.,Yao W. (2021) Near Real-Time Global Ionospheric Modeling Based on an Adaptive Kalman Filter State Error Covariance Matrix Determination Method, IEEE Transactions on Geoscience and Remote Sensing, 60, 1-12, 2022, 5800812.

Chen Y, Liu L, Le H, et al. 2020. Latitudinal Dependence of Daytime Electron Density Bite-Out in the Ionospheric F2-Layer[J]. Journal of Geophysical Research: Space Physics, 126(1).

Chen, J., H. Fang, and Z. Liu (2021), The Application of a Deep Convolutional Generative Adversarial Network on Completing Global TEC Maps, Journal of Geophysical Research: Space Physics,126.

Chen, Z., M. Jin, Y. Deng, J. S. Wang, H. Huang, X. Deng, and C. M. Huang (2019), Improvement of a Deep Learning Algorithm for Total Electron Content Maps: Image Completion, Journal of Geophysical Research: Space Physics, 124(1), 790-800.

Chen, Z., W. Liao, H. Li, J. Wang, X. Deng, and S. Hong (2022), Prediction of Global Ionospheric TEC Based on Deep Learning, Space Weather, 20(4), e2021SW002854.

Han Y, Wang L, Chen R et al (2022). Toward real-time construction of global ionosphere map from ground and space-borne observations. GPS Solutions, 26(4), 147.

He J, Yue X, Le, H et al (2020). Evaluation on the quasi-realistic ionospheric prediction using an ensemble Kalman filter data assimilation algorithm. Space weather, 18(3), e2019SW002410.

He J, Yue X, Wang W et al (2019). EnKF ionosphere and thermosphere data assimilation algorithm through a sparse matrix method. Journal of Geophysical Research: Space Physics, 124(8), 7356-7365.

Hu A, Li Z, Carter B et al (2019). Helmert-VCE-aided fast-WTLS approach for global ionospheric VTEC modelling using data from GNSS, satellite altimetry and radio occultation. Journal of Geodesy, 93, 877-888.

Hu L, Lei J, Sun W, et al. (2021) Latitudinal variations of daytime periodic ionospheric disturbances from Beidou GEO TEC observations over China. Journal of Geophysical Research: Space Physics 126(3): e2020JA028809.

Huang F, Lei J, Zhang R, et al. 2020. Prominent Daytime TEC Enhancements Under the Quiescent Condition of January

2017[J]. Geophysical Research Letters, 47(14).

Jin B, Chen S, Li D, et al. 2020. Ionospheric Correlation Analysis and Spatial Threat Model for SBAS in China Region[J]. Advances in Space Research, 66(12): 2873-2887.

Jin Y, Zhao B, Li G, et al. 2021. Inhibition of F3 Layer at Low Latitude Station Sanya During Recovery Phase of Geomagnetic Storms[J]. Journal of Geophysical Research: Space Physics, 126(12).

Kong J, Yao Y, Zhou C (2018) Tridimensional reconstruction of the Co-Seismic Ionospheric Disturbance around the time of 2015 Nepal earthquake. Journal of Geodesy 92(13):1255–1266.

Kuai J, Li Q, Zhong J, et al. 2021. The Ionosphere at Middle and Low Latitudes Under Geomagnetic Quiet Time of December 2019[J]. Journal of Geophysical Research: Space Physics, 126(6).

Li G, Ning B, Otsuka Y, et al. (2021) Challenges to Equatorial Plasma Bubble and Ionospheric Scintillation Short-Term Forecasting and Future Aspects in East and Southeast Asia. Surveys in Geophysics 42(9):201–238.

Li J, Chen Y, Liu L, et al. 2021. Occurrence of Ionospheric Equatorial Ionization Anomaly at 840 km Height Observed by the DMSP Satellites at Solar Maximum Dusk[J]. Space Weather, 19(5).

Li M, Wang H, Liu J, et al. 2022. Two Large Earthquakes Registered by the CSES Satellite during Its Earthquake Prediction Practice in China[J]. Atmosphere, 13(5).

Li N, Luan X, Lei J, et al. 2020a. Variations of Mesospheric Neutral Winds and Tides Observed by a Meteor Radar Chain Over China During the 2013 Sudden Stratospheric Warming[J]. Journal of Geophysical Research: Space Physics, 125(5).

Li Q, Huang F, Zhong J, et al. 2020b. Persistence of the Long-Duration Daytime TEC Enhancements at Different Longitudinal Sectors During the August 2018 Geomagnetic Storm[J]. Journal of Geophysical Research: Space Physics, 125(11).

Li R, Lei J, Kusche J, et al. (2023) Large-Scale Disturbances in the Upper Thermosphere Induced by the 2022 Tonga Volcanic Eruption. Geophysical Research Letters 50(3):e2022GL102265.

Li T, Wang L, Fu W et al (2022). Bottomside ionospheric snapshot modeling using the LEO navigation augmentation signal from the Luojia-1A satellite. GPS Solutions, 26, 1-13.

Li W, Li M, Shi C et al (2017). GPS and BeiDou differential code bias estimation using Fengyun-3C satellite onboard GNSS observations. Remote Sensing, 9(12), 1239.

Li W, Zhao D, He C, et al. (2022) Spatial-Temporal Behaviors of Large-Scale Ionospheric Perturbations During Severe Geomagnetic Storms on September 7–8 2017 Using the GNSS, SWARM and TIE-GCM Techniques. Journal of Geophysical Research: Space Physics 127(3):e2021JA029830.

Li X, Zhang W, Zhang K et al (2021). GPS satellite differential code bias estimation with current eleven low earth orbit satellites. Journal of Geodesy, 95(7), 76.

Li Z, Wang N, Hernández-Pajares M, Yuan Y, Krankowski A, Liu A, Zha J, García-Rigo A, Roma-Dollase D, Yang H, Laurichesse D, Blot A (2020). IGS real-time service for global ionospheric total electron content modeling. J. Geod. 94 (3).

Li Z, Wang N, Wang L, Liu A, Yuan H, Zhang K (2019). Regional ionospheric TEC modeling based on a two-layer spherical harmonic approximation for real-time single-frequency PPP. J. Geod. 93 (9): 1659–1671.

Li, W., Zhao, D., He, C., Shen, Y., Hu, A., & Zhang, K. (2021). Application of a multi-layer artificial neural network in a 3-D global electron density model using the long-term observations of COSMIC, Fengyun-3C and Digisonde.Space Weather, 19, e2020SW002605.

Liu A, Li Z, Wang N, et al. 2023. SHAKING: Adjusted spherical harmonics adding KrigING method for near real-time ionospheric modeling with multi-GNSS observations[J]. Advances in Space Research, 71(1): 67-79.

Liu J, Zhang D, Hao Y, et al. 2022a. The time delay between the equatorial ionization anomaly and the equatorial electrojet in the eastern Asian and American sectors[J]. Advances in Space Research, 69(1): 187-196.

Liu L, Lei J, Liu J. 2022b. Ionospheric Investigations Conducted by Chinese Mainland Scientists in 2020–2021[J]. Chinese Journal of Space Science, 42(4).

Liu L, Morton Y J, Wang Y et al (2021). Arctic TEC Mapping Using Integrated LEO-Based GNSS-R and Ground-Based GNSS Observations: A Simulation Study. IEEE Transactions on Geoscience and Remote Sensing, 60, 1-10.

Liu L, Morton YJ, Liu Y (2021) Machine learning prediction of storm-time high-latitude ionospheric irregularities from GNSS-derived ROTI maps. Geophysical Research Letters 48(20):e2021GL095561.

Liu Y, Zhou C, Zhang X, et al. (2020) GNSS observations of ionospheric disturbances in response to the underground nuclear explosion in North Korea. Chinese Journal of Geophysics 63(4):1308–1317.

Liu, A., Wang, N., Dettmering, D., Li, Z., Schmidt, M., Wang, L., & Yuan, H. (2023). Using DORIS Data for Validating Real-Time GNSS Ionosphere Maps. Advances in Space Research.

Liu, A., Li, Z., Wang, N., Zhang, Y., Krankowski, A., & Yuan, H. (2022). SHAKING: adjusted Spherical Harmonics Adding KrigING method for near real-time ionospheric modeling with multi-GNSS observations. Advances in Space Research.

Liu, B., Liu, A., Chen, L., Li, Z., Wang, N., Shao, B., & Wang, L. (2023). Smartphone-Based Positioning Augmented by BDSBAS Ionospheric Corrections. IEEE Geoscience and Remote Sensing Letters, 20, 1-5.

Liu, L., Zou, S., Yao, Y., & Wang, Z. (2020). Forecasting global ionospheric TEC using deep learning approach. Space Weather, 18, e2020SW002501.

Luo X, Gu S, Lou Y, et al. (2020) Amplitude scintillation index derived from C/N0 measurements released by common geodetic GNSS receivers operating at 1 Hz. Journal of Geodesy 94(2):27.

Luo X, Gu S, Lou Y, et al. (2020) Better thresholds and weights to improve GNSS PPP under ionospheric scintillation activity at low latitudes. GPS Solutions 24(1):17.

Ma H, Liu L, Chen Y, et al. 2021. Longitudinal Differences in Electron Temperature on Both Sides of Zero Declination Line in the Mid-latitude Topside Ionosphere[J]. Journal of Geophysical Research: Space Physics, 126(2).

Nie, Z., Yang, H., Zhou, P. (2019) Quality assessment of CNES real-time ionospheric products. GPS Solut 23, 11.

Ou M, Chen L, Wang Y et al (2022) Impact analysis of ground-based GNSS and space-based occultation observations on global ionospheric data assimilation. Chinese journal of radio science，2022, 37(4): 619-628.

Ou M, Chen L, Xu N et al (2021). A near real-time global ionospheric data assimilation and forecast system. In 2021 13th International Symposium on Antennas, Propagation and EM Theory (ISAPE), 1-3.

Pan, Y., M. Jin, S. Zhang, and Y. Deng (2020), TEC Map Completion Using DCGAN and Poisson Blending, Space Weather, 18(5), e2019SW002390.

Pan, Y., M. Jin, S. Zhang, and Y. Deng (2021), TEC Map Completion Through a Deep Learning Model: SNP-GAN, Space Weather, 19(11), e2021SW002810.

Ren X, Chen J, Li X et al (2020a). Ionospheric total electron content estimation using GNSS carrier phase observations based on zero-difference integer ambiguity: methodology and assessment. IEEE Transactions on Geoscience and Remote Sensing, 59(1), 817-830.

Ren X, Chen J, Zhang X (2021a). High-resolution and high-accuracy global ionosphere maps estimated by GNSS and LEO constellations: simulative and real data experimental results. In EGU General Assembly Conference Abstracts (pp. EGU21-10527).

Ren X, Chen J, Zhang X et al (2020b). Mapping topside ionospheric vertical electron content from multiple LEO satellites at different orbital altitudes. Journal of Geodesy, 94, 1-17.

Ren X, Liu H, Zhang J et al (2022). An Improved Method for Ionospheric TEC Estimation Using the Spaceborne GNSS-R Observations. IEEE Transactions on Geoscience and Remote Sensing, 60, 1-12.

Ren X, Mei D, Liu H, et al. (2022) Investigation on horizontal and vertical traveling ionospheric disturbances propagation in global-scale using GNSS and Multi-LEO satellites. Space Weather 20(5):e2022SW003041.

Ren X, Mei D, Zhang X et al (2021b). Electron density reconstruction by ionospheric tomography from the combination of GNSS and upcoming LEO constellations. Journal of Geophysical Research: Space Physics, 126(10), e2020JA029074.

Ren X, Zhang X, Schmidt M et al (2020c). Performance of GNSS global ionospheric modeling augmented by LEO constellation. Earth and Space Science, 7(1), e2019EA000898.

Ren, X., Chen, J., Li, X. (2019) Performance evaluation of real-time global ionospheric maps provided by different IGS analysis centers. GPS Solut 23, 113.

Shi S, Wu S, Zhang K et al (2022). An investigation of a new artificial neural network-based TEC model using ground-based GPS and COSMIC-2 measurements over low latitudes. Advances in Space Research, 70(8), 2522-2540.

Shi, S., Zhang, K., Wu, S., Shi, J., Hu, A., Wu, H., & Li, Y. (2022). An Investigation of Ionospheric TEC Prediction Maps Over China Using Bidirectional Long Short-Term Memory Method. Space Weather, 20(6), e2022SW003103.

Song K, Meziane K, Kashcheyev A, et al. (2022) Multifrequency observation of high latitude scintillation: A comparison with the phase screen model. IEEE Transactions on Geoscience and Remote Sensing 60:1-9.

Sui Y, Fu H, Wang K et al (2020). Tomography of Equatorial Ionization Anomaly based on GNSS-InSAR Techniques. In AGU Fall Meeting Abstracts, SA032-08.

Sun W, Ning B, Hu L, et al. 2020. The Evolution of Complex Es Observed by Multi Instruments Over Low-Latitude China[J]. Journal of Geophysical Research: Space Physics, 125(8).

Sun W, Wu B, Wu Z, et al. (2020) IONISE: An Ionospheric Observational Network for Irregularity and Scintillation in East and Southeast Asia. Journal of Geophysical Research: Space Physics 12(8): e2020JA028055.

Sun Y Y, Chen C H, Qing H, et al. 2021. Nighttime Ionosphere Perturbed by the Annular Solar Eclipse on June 21, 2020[J]. Journal of Geophysical Research: Space Physics, 126(9).

Tang, R., F. Zeng, Z. Chen, J. Wang, C. Huang, and Z. Wu (2020), The Comparison of Predicting Storm-Time Ionospheric TEC by Three Methods: ARIMA, LSTM, and Seq2Seq, Atmosphere, 11, 316.

Wang G, Bo Y, Yu Q, et al. 2020. Ionosphere-Constrained Single-Frequency PPP with an Android Smartphone and Assessment of GNSS Observations[J]. Sensors (Basel), 20(20).

Wang J, Huang G, Yang Y, et al. 2019. FCB estimation with three different PPP models: equivalence analysis and experiment tests[J]. Gps Solutions, 23(4).

Wang L, Li Z, Wang N, et al. 2021. Real-time GNSS precise point positioning for low-cost smart devices[J]. Gps Solutions, 25(2): 69.

Wang N., Zhang Y., Krankowski A., Li Z., Li A., Kotulak K., Fron A. (2022) The Combined Real-Time Global Ionospheric Map for Operational Ionospheric Space Weather Monitoring, 2022 3rd URSI Atlantic and Asia Pacific Radio Science Meeting (AT-AP-RASC), Gran Canaria, Spain, 2022, 1-3, Wang Y, Morton Y J (2021). Ionospheric total electron content and disturbance observations from space-borne coherent GNSS-R measurements. IEEE Transactions on Geoscience and Remote Sensing, 60, 1-13.

Wang Y, Yao Y B, Kong J, et al (2022) Analysis of the 3-D Evolution Characteristics of Ionospheric Anomalies During a Geomagnetic Storm Through Fusion of GNSS and COSMIC-2 Data [J]. IEEE Transactions on Geoscience and Remote Sensing, 60: 19.

Wang Z., Xue K., Wang C., Zhang T., Fan L., Hu Z., Shi C., Jing G. (2020). Near real-time modeling of global ionospheric vertical total electron content using hourly IGS data, Chinese J. Aeronaut.

Wang, N., Li, Z., Yuan, Y., & Huo, X. (2021). BeiDou Global Ionospheric delay correction Model (BDGIM): performance analysis during different levels of solar conditions. GPS Solutions, 25(3), 97.

Wu M, Guo P, Xue J et al (2022). Analysis and Empirical Modeling of Ionospheric Horizontal Gradients in the TEC Mapping Onboard LEO Satellites. IEEE Transactions on Geoscience and Remote Sensing, 60, 1-14.

Wu M, Guo P, Zhou W et al (2021). A new mapping function for spaceborne TEC conversion based on the plasmaspheric scale height. Remote Sensing, 13(23), 4758.

Wu, X., Hu, X., Wang, G., Zhong, H., & Tang, C. (2013). Evaluation of COMPASS ionospheric model in GNSS positioning. Advances In Space Research, 51(6), 959-968.

Xia, G., Liu, Y., Wei, T., Wang, Z., Zhou, C., Du, Z., et al. (2021). Ionospheric TEC forecast model based on support vector machine with GPU acceleration in the China region. Advances in Space Research, 68(3), 1377–1389.

Xie H, Yang S, Zhao X, et al. 2020. Unexpected High Occurrence of Daytime F-Region Backscatter Plume Structures Over Low Latitude Sanya and Their Possible Origin[J]. Geophysical Research Letters, 47(22).

Xu T, Hu Y, Deng Z, et al. 2020. Revisit to SporadicELayer Response to Presumably Seismogenic Electrostatic Fields at Middle Latitudes by Model Simulation[J]. Journal of Geophysical Research: Space Physics, 125(3).

Yan R, Zhima Z, Xiong C, et al. (2020) Comparison of electron density and temperature from the CSES satellite with other space-borne and ground-based observations. Journal of Geophysical Research: Space Physics 125(10): e2019JA027747.

Yang H., Monte-Moreno E., Hernández-Pajares M., David R.D. (2021) Real-time interpolation of global ionospheric maps by means of sparse representation. J Geod, 95, 71.

Yang Z, Morton YTJ, Zakharenkova I, et al. (2020) Global view of Ionospheric disturbance impacts on kinematic GPS positioning solutions during the 2015 St. Patrick's Day storm. Journal of Geophysical Research: Space Physics 125(7): e2019JA027681.

Yang, D., Q. Li, H. Fang, and Z. Liu (2022), One day ahead prediction of global TEC using Pix2pixhd, Advances in Space Research,70(2).

Yi D, Bisnath S, Naciri N, et al. 2021. Effects of ionospheric constraints in Precise Point Positioning processing of geodetic, low-cost and smartphone GNSS measurements[J]. Measurement, 183.

Yuan L, Hoque M, Jin S (2021). A new method to estimate GPS satellite and receiver differential code biases using a network of LEO satellites. GPS Solutions, 25, 1-12.

Yuan L, Jin S, Hoque M (2020). Estimation of LEO-GPS receiver differential code bias based on inequality constrained least square and multi-layer mapping function. GPS Solutions, 24(2), 57.

Yuan, Y., Wang, N., Li, Z., & Huo, X. (2019). The BeiDou global broadcast ionospheric delay correction model (BDGIM) and its preliminary performance evaluation results. Navigation, 66(1), 55-69.

Zhang R, Le H, Li W, et al. 2020a. Multiple Technique Observations of the Ionospheric Responses to the 21 June 2020 Solar Eclipse[J]. Journal of Geophysical Research: Space Physics, 125(12).

Zhang R, Liu L, Yu Y, et al. 2020b. Westward Electric Fields in the Afternoon Equatorial Ionosphere During Geomagnetically Quiet Times[J]. Journal of Geophysical Research: Space Physics, 125(12).

Zhang S, Huang L, Yin F et al (2020). Feasibility of the Data Fusion Between Space-Borne and Ground-Based TEC Products. Geomatics and Information Science of Wuhan University, 45(4), 557-564.

Zhang, Q. and Zhao, Q. (2018) Global ionosphere mapping and differ ential code bias estimation during low and high solar activity periods with GIMAS software, Remote Sens.-Basel, 10, 705.

Zhao D, Li W, Li C, et al. (2021) Extracting an ionospheric phase scintillation index based on 1 Hz GNSS observations and its verification in the Arctic region. Acta Geodaetica et Cartographica Sinica 50(3):368-383.

Zhao D, Roberts GW, Hancock CM et al. (2019) A triple-frequency cycle slip detection and correction method applied on GPS and BDS. GPS Solutions 23(1):22.

Zhao J, Hernández-Pajares M, Li Z, et al. 2021. Integrity investigation of global ionospheric TEC maps for high-precision positioning[J]. Journal of Geodesy, 95(3): 35.

Zhong J, Lei J, Yue X (2020). Comment on Choi et al. Correlation between Ionospheric TEC and the DCB Stability of GNSS Receivers from 2014 to 2016. Remote Sens. 2019, 11, 2657. Remote Sensing, 12(21), 3496.

Zhou K, Cai H, Song F et al (2020). Computerized ionospheric tomography study of three-dimensional electron density distribution in the top ionosphere based on Swarm satellites GPS/TEC observations. Chinese Journal of Geophysics, 63(9), 3219-3230.

2020 Qomolangma Height Survey

Yamin Dang[1], Tao Jiang[1], Chunxi Guo[2], Bin Chen[3], Chuanyin Zhang[1], Qiang Yang[1], Zhengtao Wang[4]

[1] *Chinese Academy of Surveying and Mapping, Beijing, China*

[2] *Geodetic Data Processing Centre of Ministry of Natural Resources, Xi'an, China*

[3] *China Aero Geophysical Survey and Remote Sensing Center for Natural Resources, Beijing, China*

[4] *School of Geodesy and Geomatics, Wuhan University, Wuhan, China*

Mount Qomolangma (MQ, known as Mount Everest in western countries) is located on the border between China and Nepal. It is not only the main peak of the Himalayas, but also the highest peak in the world, its height has attracted worldwide attention for a long time. In 2019, China and Nepal decided to jointly announce the new height of MQ. From 2019 to 2020, the height survey campaign of MQ was carried out and its latest height was precisely determined.

In previous campaigns of Qomolangma Height Survey (QHS) implemented by China in 1975 and 2005, the heights of MQ were referred to the mean sea level of Yellow Sea (Zhu 1976; Chen et al. 2001, 2006). The primary goal of 2020 QHS is to determine and announce the height of MQ through the cooperation between China and Nepal. However, the obstacle for determining the unique height of MQ is the inconsistency in height datum between the two countries, the 1985 National Height Datum of China is the mean sea level of the Yellow Sea and that of Nepal is the mean sea level of the Bay of Bengal in the Indian Ocean. Consequently, the key for 2020 QHS is to establish a high precision geoid model that realizing the common height datum recognized by both countries. We decided to establish a gravimetric geoid model in the area of MQ based on the IHRS, and use it as the datum of the height of MQ. However, high altitude and complex terrain in this region pose a great challenge for geoid modeling. Most places in this region are inaccessible for terrestrial gravity survey, yielding lots of gravity data gaps in areas with strong variations in topography and gravity field. The lack of gravity observations significantly limits the accuracy of geoid model, as well as the precision of the height of MQ. In the campaign of 2020 QHS, the science team carried out an airborne gravity survey over the area of MQ, performed terrestrial gravity measurements and BeiDou Navigation Satellite System (BDS) measurements at its peak, and combined a variety of geodetic technologies to precisely determine the new height of MQ.

1 Data collection of 2020 Qomolangma Height Survey

Gravity data

1 Airborne gravity data

During April-June 2020, 13 sorties of airborne gravity survey were implemented using the GT-2A airborne gravimeter. A King Air 350ER aircraft equipped with dual frequency GPS receivers is used to carry this gravimeter. The aircraft flied at a speed of 441.7 km/h relative to the ground and at the average altitude of 10 249 m (ellipsoidal height). Three ground GNSS stations were set up for the differential kinematic positioning of the aircraft coordinate. A total of 5635.2 km flight trajectory was completed over the area of 12 700 km^2, yielding 83 803 points of airborne gravity data with a sampling interval of 0.5 s. The airborne gravity data block is formed by 39 data lines in east-west direction and 9 inspection lines in north-south direction, resulting in 264 crossover points. The average spacing between data lines is 5 km, and is reduced to 2.5 km over the central area of MQ. An along track, time domain 100 s Kalman filtering was applied to smooth out the high frequency noises. The Root Mean Squares (RMS) of crossover differences is 1.1 mGal. The spatial distribution of airborne gravity survey lines are plotted in Figure (green lines).

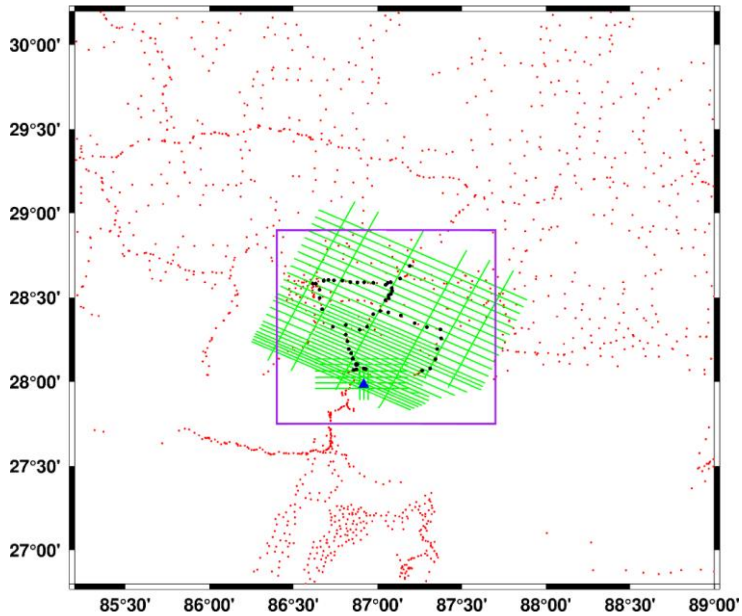

Figure 1. Distribution of airborne (green lines) and terrestrial (red points) gravity data, GNSS leveling data (black points), location of MQ (blue triangle), and the boundary of quasigeoid computation area (purple rectangle)

2 Terrestrial gravity data

Using the Z400 portable relative gravimeter specifically designed and developed for the 2020 campaign, the terrestrial gravity data at the peak of MQ was successfully collected for the first time. The Z400 relative gravimeter is designed and produced by Beijing Aodi Detection Instruments Co., Ltd, it only weights 4.5 kg, which makes it convenient to carry during mountaineering. Note that during the campaign of 2005 QHS, the highest altitude at which terrestrial gravity was observed is 7790 m above sea level (Guo et al. 2008).

Terrestrial gravity data at 210 points were newly collected in the 2020 campaign, which consist of 2 absolute gravity points, 6 control points and 202 data points. 2 points of absolute gravity values were determined using the FG5 absolute gravimeter with a precision better than 0.3 μGal, and gravity values at other points were acquired using round-trip relative gravity measurements by CG-6 gravimeters. Based on the relative gravity network adjustment, the standard error of gravity values at 6 control points and 202 data points is 5.2 μGal and 39.5 μGal, respectively. At all the gravity points, GNSS observations of 20~60 min are carried out to obtain the geodetic coordinates, and the average precision of the measured ellipsoidal heights is 5.7 cm.

GNSS data

At 11:00 am on May 27, 2020, the Chinese survey mountaineering team successfully climbed to the peak of MQ. The surveyors located the highest point of snow surface by visual inspection and set up the survey target at this point. A GNSS antenna and 6 reflection prisms were installed on the top of the survey target. The surveyors carried out GNSS measurements at the peak using CHCNAV P5 receiver and Trimble ALLOY receiver. Both GNSS receivers were connected to the common antenna on the top of the survey target, which enables simultaneous GNSS data collection. The duration of valid observations for CHCNAV P5 receiver is 40 min 53 s and that for Trimble ALLOY receiver is 41 min 39 s. Both GPS and BDS data were collected with a sampling interval of 0.05 s. In the meantime, GPS and BDS measurements were conducted at 6 ground GNSS stations for more than 8 h. The spatial distribution of the peak GNSS network consisting of the peak point and the 6 ground stations are plotted in Figure 17.

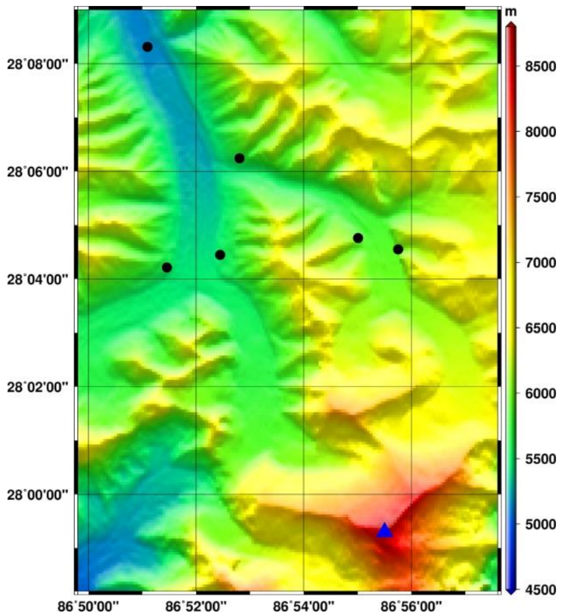

Figure 17. Distribution of the peak GNSS network. (Blue triangle: MQ; Black points: ground GNSS stations)

Geodetic leveling and trigonometric height measurements

From November 2019 to June 2020, the geodetic leveling campaign along leveling routes of 800.2 km were carried out to transfer the 1985 National Height Datum of China to the 6 ground stations (Base Camp, Zhong Rong, III7, Xi Rong, Dong Rong 2 and Dong Rong 3) at the foot of MQ. The 6 ground stations are to be used for measuring the height of the peak by means of trigonometric leveling. The leveling network consists of 520 km first order leveling route, 253.1 km second order route, 8.6 km third order route and 18.5 km trigonometric leveling traverse, yielding 238 leveling points. The above-mentioned 61 GNSS stations are co-located with geodetic leveling measurements, see Figure 2 (black points) for the spatial distribution of these stations.

In addition, the intersection and trigonometric height measurements were carried out by observing the reflection prisms of the survey target erected at the peak from the 6 ground stations. The purpose of the intersection and trigonometric height measurements is to provide independent validation dataset for the GNSS derived geodetic coordinates of the peak of MQ.

2 Gravimetric quasigeoid modeling in the area of Mount Qomolangma

83803 points of airborne gravity disturbances, 3570 points of terrestrial gravity anomalies and the 3"×3" Shuttle Radar Topography Mission (SRTM) elevation data (Farr et al. 2007) are used for the determination of gravimetric quasigeoid models. The quasigeoid model is computed on a $1'\times1'$grid in the area bounded by $27.75° \leq \varphi \leq 28.9°$ and $86.4° \leq \lambda \leq 87.7°$ (Figure 1, purple rectangle).

Three computation schemes are used for gravimetric quasigeoid modeling. The scheme 1 computes the quasigeoid model using EIGEN-6C4 model and terrestrial gravity data, no airborne gravity data are used. The scheme 2 computes the quasigeoid model using EIGEN-6C4 model, terrestrial and airborne gravity data. The scheme 3 is based on the spectral combination approach, which combines airborne gravity disturbances and terrestrial gravity anomalies to compute the quasigeoid in one step, the explicit downward continuation of airborne gravity data is not needed (Sjöberg 1981; Wenzel 1982; Jiang and Wang 2016; Jiang 2018).

We validate the gravimetric quasigeoid models using the GNSS leveling derived height anomalies at the 61 benchmarks. Table 1 presents the statistics of the differences between the quasigeoid models based on three computation schemes and the GNSS leveling measured height anomalies.

Table 1. Statistics of the differences between gravimetric quasigeoid models and GNSS leveling measured height anomalies at 61 benchmarks (m)

Computation scheme	Min	Max	Mean	Std
Scheme 1 (EIGEN-6C4 + Terrestrial)	-0.129	0.270	0.169	0.078
Scheme 2 (EIGEN-6C4 +Terrestrial+ Airborne)	0.166	0.371	0.314	0.048
Scheme 3 (EIGEN-6C4 + Terrestrial + Airborne)	0.148	0.333	0.270	0.038

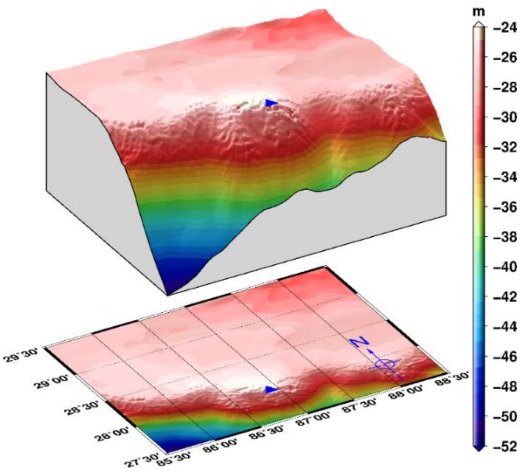

Figure 18. Gravimetric quasigeoid model based on the scheme 3. (Blue triangle: MQ)

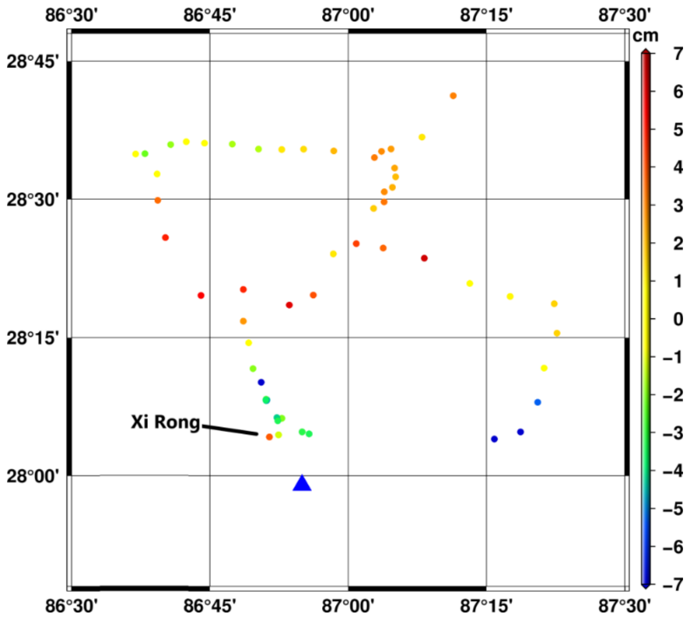

Figure 19. Differences between gravimetric quasigeoid model based on the scheme 3 and GNSS leveling derived height anomalies at 61 benchmarks. (blue triangle: MQ)

3 Determination of the IHRS based orthometric height of the peak of Mount Qomolangma

The orthometric height H of the peak of MQ can be written as follows:

$$H(\varphi,\lambda) = h(\varphi,\lambda) - N(\varphi,\lambda) \tag{1}$$

where (φ,λ,h) are the geodetic latitude, longitude and height of the peak point, which are precisely determined from GNSS measurements at the peak. N is the geoid undulation of the peak point, which is derived from the gravimetric quasigeoid model.

Determination of the geodetic coordinates of the peak of Mount Qomolangma

The software packages of GAMIT/GLOBK developed by Massachusetts Institute of Technology and GPAS (GNSS Processing and Analysis Software) developed by the Chinese Academy of Surveying and Mapping are used to process the BDS and GPS data of the peak GNSS network. Firstly, 14 GNSS reference stations from IGS (International GNSS Service), iGMAS (International GNSS Monitoring & Assessment System), MGEX (Multi-GNSS Experiment) and China BDS reference station network are selected as control stations for the baseline processing of the peak GNSS network, the relaxation constraints are applied to the station coordinates and satellite orbits, yielding the baseline results based on BDS and GPS observations, respectively. Secondly, 116 globally distributed IGS stations are selected as constraints for the adjustment of network consisting of the BDS and GPS derived baselines, the geodetic coordinates of the peak point in the ITRF2014 (International Terrestrial Reference System 2014) based on BDS, GPS and the combination of both systems are obtained, respectively. Table 2 lists the precisions of geodetic coordinates of the peak point derived from BDS, GPS and the combination of two systems. The standard error of the final geodetic coordinates of the peak point based on the combination of BDS and GPS observations is ±13.2 mm in the horizontal direction (north and east) and ±9.4 mm in the vertical direction.

Table 2. Precisions of geodetic coordinates of the peak point (mm)

GNSS data	**Horizontal direction**		**Vertical direction**
	North	**East**	
BDS	8.6	20.3	13.2
GPS	6.5	14.7	13.3
BDS + GPS	5.2	12.1	9.4

The intersection and trigonometric height measurements also provide the geodetic coordinates of the peak point, which is an independent validation for the GNSS derived solution. By taking the weighted average of geodetic height values $h_i (1 \le i \le 6)$ of the peak point measured from the 6 ground stations, the geodetic height h for the peak point with a standard error of ±4.2 cm is finally obtained. Comparing the GNSS derived solution and the intersection derived solution, it is shown that the differences between the geodetic coordinates based on the two independent techniques are 4.2 cm for horizontal component, and 2.6 cm for geodetic height.

Determination of geoid undulation of the peak of Mount Qomolangma

The geoid undulation of the peak of MQ is computed by

$$N = \zeta + \Delta + N_0 \tag{2}$$

where N is the geoid undulation of the peak, ζ is the height anomaly of the peak interpolated from the local gravimetric quasigeoid model, Δ is the geoid to quasigeoid separation, N_0 is the zero-degree term of geoid undulation.

The interpolation of the height anomaly from quasigeoid model is tricky because of large topographic height differences in the area of MQ, the influence of height differences needs to be corrected. Considering the rugged terrain and strong variations in gravity field in this region, we use the rigorous model to compute the geoid to quasigeoid separation term Δ (Flury and Rummel 2009, 2011). Δ is determined to be -1.302 m using the observed gravity value at the peak and 3"×3" SRTM data in this area. The computation of the zero-degree term of geoid undulation N_0 in Equation (2) involves the definition and selection of the specific height datum. Based on the IHRS and the GRS80 reference ellipsoid (Moritz 2000), N_0 for the peak point is determined to be -0.177 m.

As a result, the final orthometric height on the snow surface of the peak of MQ in the IHRS is determined to be 8848.86 m with a precision of ±0.06 m, while the precision is estimated from the errors in the geoid undulation and the geodetic height of the peak.

Bibliography

Dang, Y., Jiang, T., Guo, C., Chen, B., Zhang, C., Yang, Q., Wang, Z. (2023). Determining the new height of Mount Qomolangma based on the International Height Reference System. Geo-spatial Information Science, DOI: 10.1080/10095020.2022.2128901 (SCI).

Dang, Y., Guo, C., Jiang, T., Zhang, Q., Chen, B., Jiang, G. (2020). Height measurement and determination of Mount Qomolangma. Acta Geodaetica et Cartographica Sinica, 50(4): 556-561.

Flury, J., and R. Rummel. 2009. "On the geoid–quasigeoid separation in mountain areas." Journal of Geodesy 83: 829-847

Flury, J., and R. Rummel. "On the computation of the geoid–quasigeoid separation." Journal of Geodesy 85: 185–186. doi:10.1007/s00190-011-0447-1.

Förste, C., S. Bruinsma, O. Abrikosov, J. M. Lemoine, J. C. Marty, F. Flechtner, G. Balmino, F. Barthelmes, and R. Biancale. 2014. "EIGEN-6C4 The latest combined global gravity field model including GOCE data up to degree and order 2190 of GFZ Potsdam and GRGS Toulouse." GFZ Data Services, Potsdam, Germany. doi: 10.5880/icgem.2015.1.

Hofmann, W. B., and H. Moritz. 2005. Physical geodesy. Wien New York: Springer.

Ihde, J., L. Sánchez, R. Barzaghi, H. Drewes, C. Förste, T. Gruber, G. Liebsch, U. Marti, R. Pail, and M. Sideris. 2017. "Definition and proposed realization of the International Height Reference System (IHRS)." Surveys in Geophysics 38 (3): 549-570.

International Association of Geodesy. 2015. "IAG Resolutions Adopted by the IAG Council at the XXVIth IUGG General Assembly." Prague, Czech Republic. https://iag.dgfi.tum.de/en/iag-and-iugg-resolutions/.

International Association of Geodesy. 2019. "IAG Resolutions Adopted by the IAG Council at the XXVIIth IUGG General Assembly." Montreal, Canada. https://office.iag-aig.org/iag-and-iugg-resolutions.

Jiang, T., and Y. M. Wang. 2016. "On the spectral combination of satellite gravity model, terrestrial and airborne gravity data for local gravimetric geoid computation." Journal of Geodesy 90 (12): 1405-1418

Jiang, T. 2018. "On the contribution of airborne gravity data to gravimetric quasigeoid modelling: a case study over Mu Us area, China." Geophysical Journal International 215 (2): 1308.

Jiang, T., Dang, Y., Guo, C., Chen, B., Zhang, C. (2022). Realization of the international height reference system in the region of Mount Qomolangma. Acta Geodaetica et Cartographica Sinica, 51(8): 1757-1767.

Moritz, H. 2000. "Geodetic Reference System 1980." Journal of Geodesy 74: 128-133.

Sánchez, L., J. Ågren, J. Huang, Y. Wang, J. Mäkinen, R. Pail, R. Barzaghi, G. S. Vergos, K. Ahlgren, and Q. Liu. 2021. "Strategy for the realisation of the International Height Reference System (IHRS)." Journal of Geodesy 95. doi: 10.1007/s00190-021-01481-0.

Sjöberg, L. 1981. "Least squares combination of satellite and terrestrial data in physical geodesy." Annales Geophysicae 37 (1): 25-30.

Sánchez, L., and M. G. Sideris. 2017. "Vertical datum unification for the International Height Reference System (IHRS)." Geophysical Journal International 209 (2): 570-586.

Wenzel, H. G. 1982. "Geoid computation by least-squares spectral combination using intergral kernels."The General IAG Meeting, Tokyo, 438-453.

Recent Advance in Geodetic Data Processing

Jianjun Zhu[1], *Leyang Wang*[2], *Jun Hu*[1], *Bofeng Li*[3], *Haiqiang Fu*[1], *Yibin Yao*[4]

[1] *School of Geosciences and Info-physics, Central South University, Changsha, China*

[2] *School of Geomatics, East China University of Technology, Nanchang, China*

[3] *College of Surveying and Geo-informatics, Tongji University, Shanghai, China*

[4] *School of Geodesy and Geomatics, Wuhan University, Wuhan, China*

1 Data processing method

The classical hypothesis testing and reliability theory is only based on single alternative hypothesis, which is inconsistent with the practices. Yang et al. (2013) first extend the original outlier separability theory based on two alternative hypotheses to the general case where there are multiple alternative hypotheses, and then propose the new internal reliability index-minimal separability bias (MSB) that can control both the probability of missed detection and of wrong exclusion (Yang et al. 2017). Recently, Yang et al. (2021) further formulate the complete quality control indices and their algebraic estimation method for the unifying DIA estimators, by taking the uncertainty of the combined estimation-testing procedure into account and performing the propagation of uncertainty. Li et al. (2021) extent the hypothesis testing theory to ill-posed models, in which the overall-test statistics, *w*-test statistics and minimal detectable bias are all reformulated. Then, the bias-corrected w-test and overall-test statistics are both developed, so as to be approximated by a standard normal distribution and two non-central chi-square distributions, respectively.

In addition to the outlier, there is another important source of abnormal error, i.e., unmodeled error. Due to the spatiotemporal complexity of, and limited knowledge on systematic errors such as in GNSS signals, some residual observation errors cannot be eliminated or easily mitigated by differencing and combination of observations, model correction, and parameterization (Li et al. 2018; Zhang et al. 2019). Li et al. (2018) first propose a procedure to examine the significance of unmodeled errors based on a combined use of hypothesis tests. Zhang el al. (2019) propose a real-time site-specific unmodeled error detection method by using dual-frequency C/N0. Based on this, the stochastic model compensation approaches like composite model (Zhang et al. 2022) and functional model compensation approaches like multi-epoch partial parameterization (Zhang and Li 2020) are proposed. The results show that the theory and method for processing the unmodeled errors can further improve the precision and reliability of GNSS positioning and navigation.

For robust estimation problems, Yang et al. (2019) first prove that the traditional median variance estimate is biased when the sample number is small and then propose an unbiased median variance estimate to calibrate for the bias of the variance estimate. Using the unbiased median variance estimate, the M-estimator with IGGIII reduction factor is constructed to mitigate for the biases caused by the variance estimate. Liu et al. (2019) first deduce the weighted least-squares solution of partial errors-in-variables (PEIV) model, and a new RWTLS algorithm of correlated observation is proposed to solve the initial values of robust iterations by using the median parameter method. Then the median parameter method is used to determine the initial value, and on this basis we propose a new robust estimated method, which is based on the standardized residual error and considered the influence of gross error both on observation and structure spaces. Yang and Shen (2020) develop a robust M estimation approach applied for three-dimensional (3D) correlated vector observations. A modified IGGIII bifactor reduction model is constructed, where the weight shrinking factor of the 3D vector observation is determined by a new test statistic that coincides with the estimated direction of the outlier vector. With the proposed bifactor reduction model, the outlying vector observation is down-weighted directly along a specific direction, rather than separately at the three components. Lü et al. (2020) proposes a new robust total least trimmed squares (TLTS) estimator without exhaustive evaluation for the EIV model, but the cofactor matrix of the independent variables needs to have a certain block structure. Tao et al. (2021) introduced the robust estimation into the total least-squares algorithm, developing a new robust weighted total least-squares algorithm, to eliminate the effect of outliers.

For variance component estimation (VCE) problems, Lü et al. (2019) introduced the variable projection principle and derived alternative formulae for the structured EIV model by applying Lagrange multipliers. Then, they applied least-squares variance component estimation (LS-VCE) is applied to estimate different (co)variance components in a structured EIV model. Liu et al. (2019) develop a VCE method termed the least-square variance-covariance component estimation method based on the equivalent conditional misclosure (LSV-ECM). Shi et al. (2020) proved that the maximum likelihood method cannot be used to estimate variance components for some stochastic models of routine measurement systems under some conditions, because the likelihood function is unbounded for such stochastic models. To further improve the quality of estimated values based on variance component estimation of the partial errors-in-variables (EIV) model, Wang et al. (2020) introduced the jackknife resampling method to perform bias calculation and bias correction. Wang et al. (2021) proposed a total solution based on EIV model, taking into account the observation errors of all variables. The variance covariance component estimation method is introduced into the solution of regression prediction model to correct the prior cofactor matrix of the random model and the non-common points to be predicted. To solve the problem of variance component estimation problem with large-scale observations, Nie et al. (2022) proposed an efficient VCE algorithm with rigorous trace calculation based on the local–global parameters partition scheme in satellite geodesy, which is directly applicable to both the simplified yet common case where local parameters are unique to a single observation group and the generalized case where local parameters are shared by different groups of observations.

For accuracy analysis of nonlinear function problems, Wang and his research group systematically researched the theories and methods of nonlinear adjustment precision estimation based on Sigma point. From the perspective of probability distribution of approximate function, Wang and his research group proposed the unscented transformation method based on deterministic Sigma point (Wang et al., 2020), the Sterling interpolation method based on deterministic Sigma point (Wang et al., 2019, 2021, 2022), the adaptive Monte Carlo method based on random Sigma point (Wang et al., 2019, 2021), Jackknife method based on resampled Sigma point (Wang et al., 2021), and Bootstrap method based on resampled Sigma point (Wang et al., 2021). These new theories and method of nonlinear adjustment precision estimation are constructed to solve the problem that the traditional approximate function expression method relies on complex derivative operations. These theories and methods have been applied and proved in seismic fault parameter inversion, volcano Mogi model parameter inversion, volcano CDM model parameter inversion, GNSS baseline vector solution, digital elevation model, coordinate conversion, forward intersection, Gauss projection coordinate forward calculation, satellite clock error prediction, spatial straight line fitting, ellipse fitting and other measurement data processing fields. These researches are of great significance in both theory and application, which further improves and develops the geodetic data processing theory. In addition to this, Qu et al. (2019) proposes an adaptive relaxation algorithm based on the regularization method for stabilizing the nonlinear parameter estimation. Han et al. (2021) proposed a new first-order approximate (NFOA) precision estimation method to evaluate the posterior precision of weighted total least-squares estimates in an errors-in-variables model. A separable nonlinear least squares algorithm based on Moore-Penrose generalized inverse and solid matrix is proposed to solve the special structure of linear combination of nonlinear functions in the field of surveying and mapping.

For ill-posed problems, Song (2019) proposed a new iterative algorithm for rank-deficient adjustment models with inequality constraints, and proved its convergence. Wang et al. (2019) proposed the virtual observation method for solving the ill-posed problem of the PEIV model and the precision estimation method based on a second-order derivative approximate function method. Based on the mean square error (MSE) criterion, the regularization method reduces the parameter estimation variances of ill-posed models through introducing biases. When the uncertainty adjustment model is ill-posed, it is more seriously affected by the error of the coefficient matrix and the observation, Lu et al. (2019) applies ridge estimation method to ill-posed uncertainty adjustment model, derives an iterative algorithm to improve the stability and reliability of the result. To reduce the biases, Lin et al. (2020) proposed a bias reduction method. Based on this method, they proposed a bias-reduced regularization method to improve the MSE of regularized model parameter estimations. Truncated Singular Value Decomposition (TSVD) is an effective method commonly used in solving ill-posed geodetic problems. Lin et al. (2022) truncates small singular values in turn based on TSVD to acquire the changes of the variance and parameter estimation and analyzes the changes to determine the effects of the biases, which can avoid the calculation biases in the use of the true value of the parameters. Thereby, based on the theory of the minimum mean square error, the truncation parameter can be determined. In order to make the adjustment results unique and stable. Zhao et al. (2022) built a function model to solve inequality constraints, and based on the linear complementarity theory, proposed to use the potential function descent interior point algorithm to solve the rank deficient problem. Song et al. (2022) proposed a new ridge estimation method for solving rank-deficient least squares problems, in which a rank-deficient matrix is regarded as an almost rank-deficient. they gave an algebraic derivation that the optimal solution can in fact be obtained by solving a related regularized problem on the optimal worst-case residual. Then, they gave a new iterative algorithm to solve ridge parameter and prove its convergence.

For the total least squares problems, Wang et al. (2019) deduced the formulae of parameter solution for the MEIV model based on the principle of maximum likelihood estimation, and proposed two iterative algorithms. Zeng et al. (2019) proposed an ICTLS solution based on direct observation with constraints, which can restrict both independent and dependent variables. Making using of statistical properties of observations errors and coefficient matrix error, Zhao et al. (2019) deduces a new computational formula of WTLS estimation for PEIV model based on Fisher Score algorithm. Meng et al. (2020) investigated the condition number of the minimum Frobenius norm solution of the multidimensional TLS problem, and provided a tight and computable upper bound estimation method. Sun et al. (2020) proposed the Frozen-Barycentre iteration method, which applies Samaski to the barycenter iteration method, realizes the conversion of internal iteration and external iteration, saves operation time by reducing derivative calculation, and improves the convergence efficiency of the barycenter iteration method. Based on the structural characteristics of the EIV model, Wang et al. (2020) divided the design matrix into a constant matrix and a random matrix, then rewrited the EIV model as a general structured model and reformulated it as an efficient WTLS algorithm, which only attaches a weight matrix to the random matrix to reduce the size of the matrices involved in the iterative process. Zeng et al. (2021) incorporated the second-order term into the constant term of the model based on the EIV model, thus representing the nonlinear general EIV model as a linear Gauss Helmert model, and deduced the linearized total least squares algorithm and approximate precision estimation formula of the general EIV model. Hu et al. (2021) put orthogonal geometric information as constraint conditions into weighted total least squares, and proposed a nonlinear equality constrained total least squares adjustment method with unknown corrected errors for constraint function. Based on the EIV model, Lü et al. (2021) construct an affine function by using the augmented matrix composed of coefficient matrix and observation vector, reconstruct the function model by using the variable projection method, and deduce a minimum double estimation algorithm for the structure population by using the Lagrangian method. Shi et al. (2021) proposed the uncertain total least squares estimation of linear regression model based on the least squares estimation and uncertainty theory. Based on the equality constrained nonlinear Gauss-Helmert (GH) model, Wang et al. (2020) used the Euler Lagrangian method to obtain the least squares solution of the nonlinear GH model with equality constraints, and then expressed it as the standard constrained least squares problem, introducing a unique sensitivity analysis method. Under the total least squares criterion, Xie et al. (2021) transformed the calculation of inequality constrained total least squares solution into a quadratic programming problem according to the Kuhn-Tucker condition of the optimal solution, and proposed an improved Jacobian iterative method to solve the quadratic programming problem. Xie et al. (2022) proposed the optimality conditions for inequality constrained weighted total least squares (ICWTLS) solution in inequality constrained PEIV model. Then they modified the existing linear approximation (LA) approach to make it suitable for cross-correlated data. The sequential quadratic programming (SQP) method is proposed based on the optimality conditions. Since the Hessian matrix is difficult to compute in the SQP algorithm and it converges slowly or even not converges when the Hessian matrix is indefinite positive, the damped quasi-Newton (DQN) SQP method is proposed. Considering coordinate errors of both control points and non-control points, and different weights between control points and non-control points, Zeng et al. (2022) proposed an extended weighted total least squares (WTLS) iterative algorithm of 3D similarity transformation based on Gibbs vector.

For multiplicative error model and mixed additive and multiplicative error model, Wang et al. (2020) and Wang et al. (2022) obtained the second-order accuracy information of the parameters of the multiplicative error model and the mixed additive and multiplicative error model by using Stering method and SUT method without derivative calculation, respectively. For ill-posed multiplicative error model, Wang et al. (2021) proposed to use the A-optimal design method to determine the regularization parameters of the ill-posed model, and established a more reliable parameter estimation method by combining the virtual observation iterative method. For mixed additive and multiplicative error model with constraints, Wang et al. (2022) constructed an exhaustive method for parameter estimation of ill-posed model with inequality constraints, and proved the effectiveness of the method in dealing with related problems. Shi et al. (2020) extended mixed additive and multiplicative error model to a more general generalized mixed additive and multiplicative error model with deterministic trend.

For most of the geodetic applications, the observables are real number and least squares-based adjustment has been widely used to reduce the error and obtain the optimal estimation. However, the observable of InSAR is recorded by a complex number which is related to interferometric phase and correlation. In such a case, complex least squares-based adjustment is needed. To develop the complex least squares-based adjustment, the critical problem is how to establish the least squares criteria and stochastic model for the complex number. Zhu et al. (2019) proposed a non-linear least squares adjustment method whose least squares criteria is the sum of squares of the module of the residual of complex observations is minimal. With this criterion, the adjustment should be conducted in complex domain. Cao et al. (2022) proposed that the complex observation can be divided into real and imaginary parts and complex least squares adjustment is then a joint adjustment of real and real and imaginary. As a result, the existing adjustment theory for real number can also be used to process the complex observable. For the stochastic model, Zhu et al. (2019) and Cao et al. (2022) suggested that standard deviation of the module of complex can be regarded as the weight of the complex observable.

2 Geodetic inversion

The geodetic inversion method has been further developed. To determine the smoothing coefficient (also known as the regularization parameter) in the inversion of the coseismic slip distribution, a compromise curve between the model roughness and the residuals of the data fit is generally used (Wang et al., 2020). Based on the L-curve, the Eclectic Intersection curve was proposed as a new method to determine the smoothing coefficients by Wang et al. (2020). Compared with the L-curve method, the Eclectic Intersection curve method has the advantage of high computational efficiency, no dependence on data fit, and more suitable smoothing coefficients. In Zang et al. (2022), the performance of high-rate single GNSS and multi-GNSS fusion in early warning magnitude calculation, fast mass moment tensor inversion and static fault slip inversion is thoroughly investigated using data related to the Mw 7.4 magnitude earthquake in Mado County, Qinghai Province, China. Zhao et al. (2022) proposed a new method to determine coseismic slip distribution inversion for multi-observation types, which can simultaneously determine the relative weight ratio and regularization parameters of multiple observations.

At the same time, intelligent algorithms have been widely used in seismic inversion problems. Xu et al. (2015) proposed a Bayesian estimation-based method for fault parameter inversion, which can quantify the uncertainty of optimal model parameters through the posterior probability distribution of the parameter space. Yin et al. (2019) proposed a fault parameter inversion method based on the combination algorithm of a genetic algorithm and iterative least squares algorithm, which can give consideration to the sensitivity and correlation of fault parameters. Wang et al. (2020) introduced a scale-free trace transformation (SUT) method based on a deterministic sampling strategy for nonlinear inversion and accuracy estimation of seismic fault parameters. Zhao et al. (2020) proposed an adaptive multi-start Gauss-Newton method (AMGNA) to invert seismic source parameters using multiple geodetic datasets. Wang et al. (2021) proposed a particle swarm optimization algorithm (BH-PSO) incorporating a black hole strategy. The BH-PSO method is less time-consuming than the simulated annealing (SA) method and has higher accuracy than the genetic algorithm (GA). Traditional genetic algorithm (GA) inversion results are unstable and easily fall into local optimum in an inversion of fault parameters (Wang et al., 2021). Wang et al. (2021) proposed a genetic Nelder-Mead neural network algorithm (GNMNNA). GNMNNA outperforms GA and NNA in terms of inversion accuracy and computational stability, and GNMNNA has greater potential for application in complex seismic environments. Zhang et al. (2022) introduced a general variational inference algorithm, Automatic Differential Variational Inference (ADVI) to Bayesian slip inversion, and compares it to the classical Metropolis-Hastings (MH) sampling method. Zhao et al. (2021) proposed a deep learning approach of Earthquake Source Parameters Inversion using ResNet (abbreviated as ESPI-ResNet) from satellite InSAR data. Wang et al. (2021) introduced the Sterling interpolation method to estimate the accuracy of parametric nonlinear inversions in earthquakes and applied it to the Lushan and L'Aquila earthquakes.

The joint inversion of multiple data is still the trend of geodetic inversion. Interferometric synthetic aperture radar (InSAR) has become an important technique to study seismic cyclic deformation. To obtain the complete and accurate three-dimensional (3-D) surface displacements from heterogenous InSAR displacement observations, Liu et al. (2018) proposed a strain model and variance component estimation-based method (SM-VCE), in which the robust variance component estimation (RVCE) algorithm is used to weight different InSAR observations. It has been proved that the SM-VCE method is obviously superior to the traditional InSAR empirical weighting method for obtaining 3-D displacements. In addition to the co-event 3-D displacements, Liu et al. (2022a) proposed a novel Kalman filter-based InSAR method (KFInSAR) to combine multiple InSAR time series observations to estimate the time-series 3-D displacements, in which each InSAR time series dataset is optimized with an iterative weighted least square (IWLS)-based error correction procedure (Liu et al., 2021a), and the decorrelation noise and atmospheric delay can be significantly decreased. Wang et al. (2019) used interferometric synthetic aperture radar data to analyze the isoseismic and postseismic displacement fields associated with the 2016 Central Petermann Ranges earthquake in Australia. Liu et al. (2019) developed a logarithmic model-based approach (LogSIM) for joint inversion of co-seismic and post-earthquake fault sliding using InSAR data from multiple platforms with different tracks. Wang et al. (2019) used GPS and InSAR coseismic deformation fields to jointly invert the sliding distribution model of the Koshien earthquake; analyzed the relationship between the Koshien earthquake and the Mino earthquake based on static Coulomb stress alteration in conjunction with previous research results; and also constructed a fault grid for seven major faults in southwestern Taiwan and obtained their stress alteration models. He et al. (2020) used rising and falling Sentinel-1 satellite interferometric synthetic aperture radar (InSAR) images to construct isoseismic displacements associated with the Mw 7.1 Anchorage earthquake, which showed a sub-circular deformation pattern with -4 cm of subsidence in the line of sight direction. Wang et al. (2020) used three-dimensional co-seismic displacement fields from spatial imaging geodesy to invert the Mw7.8 Kaikoura, New Zealand earthquake. Yang et al. (2021) provided a new interpretation of the 2016 Mino earthquake based on synthetic aperture radar (SAR) satellite, high-speed GPS, and strong motion data. Yan et al. (2022a, b) proposed the improved spatiotemporal random effects (STRE) model and the multiresolution segmentation fusion (MRSF) method for InSAR and GNSS fusion, which can better reveal the spatial heterogeneity of deformation data and the slip distribution in Cascadia Subduction Zone and San Francisco Bay region, California. Liu et al. (2021b, 2022b, 2022c) estimate the 3-D co-seismic displacements of the 6th July 2019 Ridgecrest earthquake, California, the 22nd May 2021 Maduo earthquake, the 9th Janurary 2022 Menyuan earthquake, China, etc. from InSAR and pixel-offset tracking observations based on the SM-VCE method, providing the valuable and accurate datasets for constraining the fault movements. Zhu et al. (2019) and Cao et al. (2022) estimated the forest height and sub-canopy topography with the complex least squares adjustment method from polarimetric InSAR data.

Antarctic basal water storage variation (BWSV) is the mass variation of liquid water under the Antarctic ice cap (Kang et al., 2021). Kang et al. (2021) proposed a stratified gravity density forward/inverse Antarctic BWSV estimation method and associated model based on multi-source satellite observation data. Many recent mass balances using the Gravity Recovery and Climate Experiment (GRACE) and satellite altimetry (including both radar and laser sensors) have used a large number of forward models with uncertainties (Gao et al., 2019). To minimize the considerable sources of error associated with the use of forward models, Gao et al. (2019) used multiple geodetic observations to estimate mass changes in the ice cap and present-day GIA, including GRACE and the Ice, Cloud, and Land Elevation Satellite (ICESat), and the Global Positioning System (GPS), using an improved Joint Inverse Estimation (JIE) method to solve for Antarctic GIA and ice trends simultaneously.

Shi et al. (2022) Analysis of land water reserves using GRACE time-varying gravity field data inversion and periodic characteristics of GLDAS and CPC results. By taking the Yellow River Basin as the study area to obtain the deficient equivalent water height and find that the water reserves in the study area as a whole decreased at a rate of -0.51±0.03cm·a-1 from 2002 to 2020. The lag time of equivalent water height retrieved by GRACE is 2 ~ 3 months relative to precipitation, evapotranspiration, and soil temperature. It was verified by experiments that GRACE has a strong correlation with equivalent water height calculated by GLDAS and CPC, and both have obvious annual resonance periods.

Bibliography

Cao S, Fu H, Zhu J et al (2022) A Forest Height Joint Inversion Method Using Multibaseline PolInSAR Data. IEEE Geoscience and Remote Sensing Letters, 19: 2508105

Gao C, Lu Y, Zhang Z et al (2019) A joint inversion estimate of Antarctic ice sheet mass balance using multi-geodetic data sets. Remote Sensing 11(6) 653.

Han J, Zhang S, Li J (2021) New first-order approximate precision estimation method for parameters in an errors-in-variables model. Journal of Surveying Engineering 147(1):04020023.

Hu C, Fang X, Zhao L (2020) Nonlinear equality constrained total least squares adjustment combined with orthogonal geometry information and its iterative algorithm. Acta Geodaetica et Cartographica Sinica 49(7):816-823.

He P, Wen Y, Chen Y et al (2020) Coseismic rupture geometry and slip rupture process during the 2018 Mw 7.1 Anchorage, south-central Alaska earthquake: Intraplate normal faulting by slab tear constrained by geodetic and teleseismic data. Earth and Space Science 7(1): e2019EA000924.

Kang J, Lu Y, Li Y et al (2021) Basal Water Storage Variations beneath Antarctic Ice Sheet Inferred from Multi-source Satellite Data. The Cryosphere Discussions 1-28.

Li B., Zhang Z., Shen Y., Yang L. (2018) A procedure for the significance testing of unmodeled errors in GNSS observations. Journal of Geodesy, 92(10):1171-1186.

Li B, Wang M, Shen Y (2021) The hypothesis testing statistics in linear ill-posed models. Journal of Geodesy 95(1):1-19.

Lin D, Yao Y, Zheng D et al (2022) Determination of truncation parameter based on the differences of TSVD parameter estimates for ill-posed problems in geodesy. Acta Gedaetica et Cartographica Sinica 51(8):1787-1796.

Lin D, Zhu J, Li C, et al (2020) Bias reduction method for parameter inversion of ill-posed surveying model. Journal of Surveying Engineering 146(3):04020011.

Liu J, Hu J, Li Z, et al (2018) A method for measuring 3-d surface deformations with InSAR based on strain model and variance component estimation. IEEE Transactions on Geoscience and Remote Sensing 56(1):239–250.

Liu J, Hu J, Bürgmann R, et al (2021a) A strain-model based InSAR time series method and its application to the Geysers geothermal field, California. Journal of Geophysical Research: Solid Earth 126(8):e2021JB021939.

Liu J, Hu J, Li Z, et al (2021b) Estimation of 3D coseismic deformation with InSAR: an improved SM-VCE method by window optimization. Acta Geodaetica et Cartographica Sinica 50(9):1222-1239.

Liu J, Hu J, Li Z, et al (2022a) Dynamic estimation of multi-dimensional deformation time series from InSAR based on Kalman filter and strain model. IEEE Transactions on Geoscience and Remote Sensing 60:1–16.

Liu J, Hu J, Li Z, et al (2022b) Complete three-dimensional coseismic displacements due to the 2021 Maduo earthquake in Qinghai Province, China from Sentinel-1 and ALOS-2 SAR images. SCIENCE CHINA Earth Sciences 65:687–697.

Liu J, Hu J, Li Z, et al (2022c) Three-dimensional surface displacements of the 8 January 2022 Mw6.7 Menyuan earthquake, China from Sentinel-1 and ALOS-2 SAR observations. Remote Sensing 14(6):1404.

Lu T, Wu G, Zhou S (2019) Ridge estimation algorithm to ill-posed uncertainty adjustment model. Acta Geodaetica et Cartographica Sinica 48(4):403-411.

Lü Z, Sui L (2021) Structured Total Least Squares Method Based on Variable Projection. Geomatics and Information Science of Wuhan University 46(3):388-394.

Lü Z, Sui L (2020) The BAB algorithm for computing the total least trimmed squares estimator. Journal of Geodesy 94(12):1-

14.

Lü Z, Sui L (2019) Variance-covariance component estimation for structured errors-in-variables models with cross-covariances. Studia Geophysica et Geodaetica 63(4):485-508.

Liu X, Xu W (2019) Logarithmic model joint inversion method for coseismic and postseismic slip: Application to the 2017 Mw 7.3 Sarpol Zahāb earthquake, Iran. Journal of Geophysical Research: Solid Earth 124(11):12034-12052.

Liu Y, Wang J, Wang B et al (2019) Robust Weight Total Least Squares Algorithm of Correlated Observation Based on Median Parameter Method. Geomatics and Information Science of Wuhan University 44(03):378-384.

Liu Z, Zhu D, Yu H et al (2019) Least-square variance-covariance component estimation method based on the equivalent conditional adjustment model. Acta Geodaetica et Cartographica Sinica 48(9);1088-1095.

Meng L, Zheng B, Wei Y (2020) Condition numbers of the multidimensional total least squares problems having more than one solution. Numerical Algorithms 84(3):887-908.

Nie Y, Shen Y, Pail R, et al (2022) Efficient variance component estimation for large-scale least-squares problems in satellite geodesy. Journal of Geodesy 96(2):1-15.

Qu G, Sun Z, Su X et al (2019) Adaptive Relaxation Regularization Algorithm for Nonlinear Parameter Estimation. Geomatics and Information Science of Wuhan University 2019,44(10):1491-1497.

Shi Y, Xu P (2020) Adjustment of Measurements with Multiplicative Random Errors and Trends. IEEE Geoscience and Remote Sensing Letters 18(11):1916-1920.

Shi Y, Xu P (2020) Nonexistence of Maximum Likelihood Estimation of Variance Components in Some Stochastic Models. Journal of Surveying Engineering 146(2):06020001.

Song Y, Li W, Deng C, et al (2022) A new ridge estimation method on rank-deficient adjustment model. Acta Geodaetica et Geophysica, 57(1):1-22.

Song Y (2019) A new iterative algorithm for a rank-deficient adjustment model with inequality constraints. Journal of geodesy 93(12):2637-2649.

Song Z, Fang T, Schonfeld P, et al (2021) Effect of point configurations on parameter estimation analysis of circles. Journal of Surveying Engineering 147(3):04021010.

Shi H, Sun X, Wang S et al (2022) Total least squares estimation model based on uncertainty theory. Journal of Ambient Intelligence and Humanized Computing 1-7.

Shi T, Liu X, Mu D et al (2022) Reconstructing gap data between GRACE and GRACE-FO based on multi-layer perceptron and analyzing terrestrial water storage changes in the Yellow River basin. Chinese Journal of Geophysics 65(7):2448-2463.

Sun Z, Qu G, Su X et al (2020) Frozen-Barycentre Algorithm for Solving Distance Equations.Geomatics and Information Science of Wuhan University 45(9):1478-1484.

Tao W, Hua X, Li P, et al (2021) An iterated reweighting total least squares algorithm formulated by standard least-squares theory. Survey Review 53(380):454-463.

Wang B, Fang X, Liu C et al (2020) Data Snooping for the Equality Constrained Nonlinear Gauss–Helmert Model Using Sensitivity Analysis. Journal of Surveying Engineering 146(4):04020015.

Wang J, Yan W, Zhang Q, et al (2021) Enhancement of Computational Efficiency for Weighted Total Least Squares. Journal of Surveying Engineering 147(4):04021019.

Wang L, Chen T (2021) Virtual Observation Iteration Solution and A-Optimal Design Method for Ill-Posed Mixed Additive and Multiplicative Random Error Model in Geodetic Measurement. Journal of Surveying Engineering 147(4):04021016.

Wang L, Chen T (2022) The SUT method for precision estimation of mixed additive and multiplicative random error model. Acta Geodaetica et Cartographica Sinica 51(11):2303-2316.

Wang L, Chen T (2022) A method for mixed additive and multiplicative random error models with inequality constraints in geodesy. Earth, Planets and Space 74(1):1-15.

Wang L, Ding R (2020) A parameter determination method of unscented transformation and its approximate ability analysis in the precision estimation of nonlinear measurement adjustment. Measurement 166:108065.

Wang L, Ding R (2020)Inversion and precision estimation of earthquake fault parameters based on scaled unscented transformation and hybrid PSO/Simplex algorithm with GPS measurement data. Measurement, 153: 107422.

Wang L, Gao H, Feng G (2019) Triggering relations and stress effects analysis of two Mw> 6 earthquakes in southwest Taiwan based on InSAR and GPS data. Acta Geodaetica et Cartographica Sinica 48(10):1244-1253.

Wang L, Jin X, Xu W et al (2021) A black hole particle swarm optimization method for the source parameters inversion: application to the 2015 Calbuco eruption, Chile. Journal of Geodynamics 146:101849.

Wang L, Li Z (2021) Bootstrap method for inversion and precision estimation of earthquake source parameters. Chinese Journal of Geophysics, 64(6): 2001-2016.

Wang L, Li Z (2021) Bootstrap method and the modified method based on weighted sampling for nonlinear model precision estimation. Acta Geodaetica et Cartographica Sinica, 50(7): 863-878.

Wang L, Luo X (2021) Adaptive Quasi-Monte Carlo method for nonlinear function error propagation and its application in geodetic measurement. Measurement 186:110122.

Wang L, Sun J (2021) Variance Components Estimation for Total Least-Squares Regression Prediction Model. Geomatics and Information Science of Wuhan University 46(2):280-288.

Wang L, Xu R, Yu F (2022) Genetic Nelder-Mead neural network algorithm for fault parameter inversion using GPS data. Geodesy and Geodynamics 13(4):386-398.

Wang L, Yu F, Li Z, et al (2020) Jackknife method for variance components estimation of partial EIV model. Journal of Surveying Engineering, 146(4):04020016.

Wang L, Yu F(2021) Jackknife Resample Method for Precision Estimation of Total Least Squares. Communications in Statistics - Simulation and Computation, 50(5):1272-1289.

Wang L, Zhao X (2020) Determination of Smoothing Factor for the Co-seismic Slip Distribution Inversion. Acta Geodaetica et Cartographica Sinica 3(1):25-35.

Wang L, Zhao Y (2019) Adaptive Monte Carlo Method for Precision Estimation of Nonlinear Adjustment. Geomatics and Information Science of Wuhan University, 44(2): 206-213, 220.

Wang L, Zou C (2019) Accuracy analysis and applications of the Sterling interpolation method for nonlinear function error propagation. Measurement 146:55-64.

Wang L, Zou C (2021)Accuracy estimation of earthquake source geometry parameters by the Sterling interpolation method in the nonlinear inversion. Journal of Surveying Engineering, 147(1): 04020019.

Wang L, Zou C (2022)Sterling Interpolation Method for Parameter Estimation and Precision Estimation in Multiplicative Error Model. Geomatics and Information Science of Wuhan University, 47(2): 219-225.

Wang L, Wen G, Zhao Y (2019) Virtual observation method and precision estimation for ill-posed partial EIV model. Journal of Surveying Engineering, 145(4):04019010.

Wang T, Jiao L, Tapponnier P, Shi X, & Wei S (2020) Space imaging geodesy reveals near circular, coseismic block rotation during the 2016 Mw 7.8 Kaikōura earthquake, New Zealand. Geophysical Research Letters 47(22), e2020GL090206.

Wang S, Xu W, Xu C, Yin Z, Bürgmann R, Liu L, & Jiang G (2019) Changes in groundwater level possibly encourage shallow earthquakes in central Australia: The 2016 Petermann Ranges earthquake. Geophysical Research Letters 46: 3189–3198.

Wang Q, Hu Y, Wang B (2019) The maximum likelihood estimation for multivariate EIV model. Acta Geodaetica et Geophysica 54(2):213-224.

Xie J, Long S, Zhou C (2021) Classical Least Squares Method for Inequality Constrained PEIV Model. Geomatics and Information Science of Wuhan University 46(9):1291-1297.

Xie J, Lin D, Long S (2022) Total least squares adjustment in inequality constrained partial errors-in-variables models: optimality conditions and algorithms. Survey Review 54(384):209-222.

Xu W, Dutta R, Jónsson S (2015) Identifying active faults by improving earthquake locations with InSAR data and Bayesian estimation: the 2004 Tabuk (Saudi Arabia) earthquake sequence. Bulletin of the Seismological Society of America 105(2A): 765-775.

Yan H, Dai W, Xie L, Xu W (2022a) Fusion of GNSS and InSAR time series using the improved STRE model: applications to the San Francisco Bay Area and Southern California. Journal of Geodesy 96(7):47.

Yan H, Dai W, Liu H, Gao H, Neely WR, Xu W (2022b) Fusion of Spatially Heterogeneous GNSS and InSAR Deformation Data Using a Multiresolution Segmentation Algorithm and Its Application in the Inversion of Slip Distribution. Remote Sensing 14(14): 3293.

Yin J, Xu C (2019) Inversion of Fault Parameters Based on Combinational Algorithm for Spherical Layered Model. Geomatics and Information Science of Wuhan University 44(9):1320-1327.

Yang L., Wang J., Knight N.L., & Shen Y. (2013) Outlier separability analysis with a multiple alternative hypotheses test. Journal of Geodesy, 87(6): 591-604.

Yang L, Li B, Shen Y, Rizos C (2017) Extension of internal reliability analysis regarding to separability analysis. Journal of Surveying Engineering, 143(3):04017002.

Yang L, Shen Y, Li B (2019) M-estimation using unbiased median variance estimate. Journal of Geodesy 93(6):911-925.

Yang L, Shen Y (2020) Robust M estimation for 3D correlated vector observations based on modified bifactor weight reduction model. Journal of Geodesy, 94: 31.

Yang L, Shen Y, Li B, Rizos C (2021) Simplified algebraic estimation for the quality control of DIA estimator. Journal of Geodesy, 95:14.

Yang, Y, Chen Q, Diao X, et al (2021) New interpretation of the rupture process of the 2016 Taiwan Meinong Mw 6.4 earthquake based on the InSAR, 1-Hz GPS and strong motion data. Journal of Geodesy 95: 1-21.

Zeng H, He H, Chen L, et al (2022) Extended WTLS iterative algorithm of 3D similarity transformation based on Gibbs vector. Acta Geodaetica et Geophysica 57(1):43-61.

Zhao X, Wang C, Zhang H et al (2021) Inversion of seismic source parameters from satellite InSAR data based on deep learning. Tectonophysics 821:229140.

Zhao Y, Xu C (2020) Adaptive multistart Gauss–Newton approach for geodetic data inversion of earthquake source parameters. Journal of Geodesy 94(2):1-18.

Zeng W, Fang X, Lin Y, et al (2019) On the errors-in-variables model with inequality constraints of dependent variables for geodetic transformation. Survey Review 51(365):166-171.

Zeng W, Liu Z, Fang X et al (2021) Linearization Estimation Algorithm for Universal EIV Adjustment Model. Geomatics and Information Science of Wuhan University 46(9):1284-1290.

Zhao J, Guo F, Li Q (2019) Fisher-Score Algorithm of WTLS Estimation for PEIV Model. Geomatics and Information Science of Wuhan University 44(02):214-220.

Zhao S, Song Y, Li W (2022) A new algorithm for rank-deficient problems with inequality constraints. Survey Review 54(384):223-232.

Zhao X, Xu C, Zhou L, Wen Y, Wang J, Zhao Y (2022) A new method applied for the determination of relative weight ratios under the TensorFlow platform when estimating coseismic slip distribution. Journal of Geophysical Research: Solid Earth 127, e2022JB024843.

Zhang C, Chen T (2022) Bayesian slip inversion with automatic differentiation variational inference. Geophysical Journal International Pages 546–565.

Zang J, Wen Y, Li Z, et al (2022) Rapid source models of the 2021 Mw 7.4 Maduo, China, earthquake inferred from high-rate BDS3/2, GPS, Galileo and GLONASS observations. Journal of Geodesy 96(9): 1-13.

Zhang Z, Li B. Unmodeled error mitigation for single-frequency multi-GNSS precise positioning based on multi-epoch partial parameterization. Measurement Science and Technology, 2020, 31(2): 025008.

Zhang Z, Li Y, He X, Chen W, Li B. A composite stochastic model considering the terrain topography for real-time GNSS monitoring in canyon environments, Journal of Geodesy, 2022, 96: 79.

Zhang Z, Li B, Gao Y, Shen Y. Real-time carrier phase multipath detection based on dual-frequency C/N0 data. GPS Solutions, 2019, 23: 7.

Zhu J, Xie Q, Zuo T et al (2019) Complex least squares adjustment to improve tree height inversion problem in PolInSAR. Journal of Geodesy and Geoinformation Science 2(1): 1-8

Scientific Computation Platform for Geophysical Geodesy

Chuanyin Zhang, Tao Jiang, Wei Wang, Baogui Ke
[1] *Chinese Academy of Surveying and Mapping, Beijing, China*

Large scientific computing platform for geophysical geodesy the high-precision gravity field approximation and geoid calculation system PAGravf4.5 (steady state) and earth tide load effect and deformation monitoring and calculation system ETideLoad4.5 (time-varying) was developed by the gravity field and vertical datum team of the Chinese Academy of Surveying and Mapping, integrating 20 years of research results. Based on public welfare purposes, the scientific computing platform is committed to improving the technology and education environment where there is a severe shortage of such computing resources in domestic and foreign academic fields, showcasing the charm and potential of geodesy, reconstructing collaborative heterogeneous geodetic benchmarks (a geodetic system with deep fusion of multi-source heterogeneous Earth data and a geodetic framework with multiple heterogeneous Earth observation technologies), consolidating the effectiveness of geodetic applications, and supporting the intelligence of massive Earth observations.

1 Precise Approach of Earth Gravity Field and Geoid (PAGravf4.5)

PAGravf4.5 is a large Windows package for scientific computation rigorously based on stationary gravity field theory. Strictly according to physical geodesy, PAGravf4.5 constructs the unified analytical algorithm system of various terrain effects on various gravity field elements on the geoid or in the outer space outside the geoid to improve the geophysical gravity exploration and gravity field data processing. Scientifically constructs the gravity field approach system with the spatial domain integration algorithm based on boundary value theory and spectral domain radial basis function approach algorithm to realize the full element modelling on gravity field in full space outside geoid and fine gravity prospecting from various heterogeneous observations. And develops some ingenious physical geodetic algorithms to improve and unify the regional height datum, so as to consolidate and expand the applications of Earth gravity field.

User can design own schemes and processes, then organize flexibly the related programs and functions in PAGravf4.5, perform some scientific computations for various terrain effects outside geoid, full element modelling on gravity field, refinement of 1cm stationary geoid, fine gravity prospecting from heterogeneous observations, improvement of regional height datum and application of Earth gravity field.

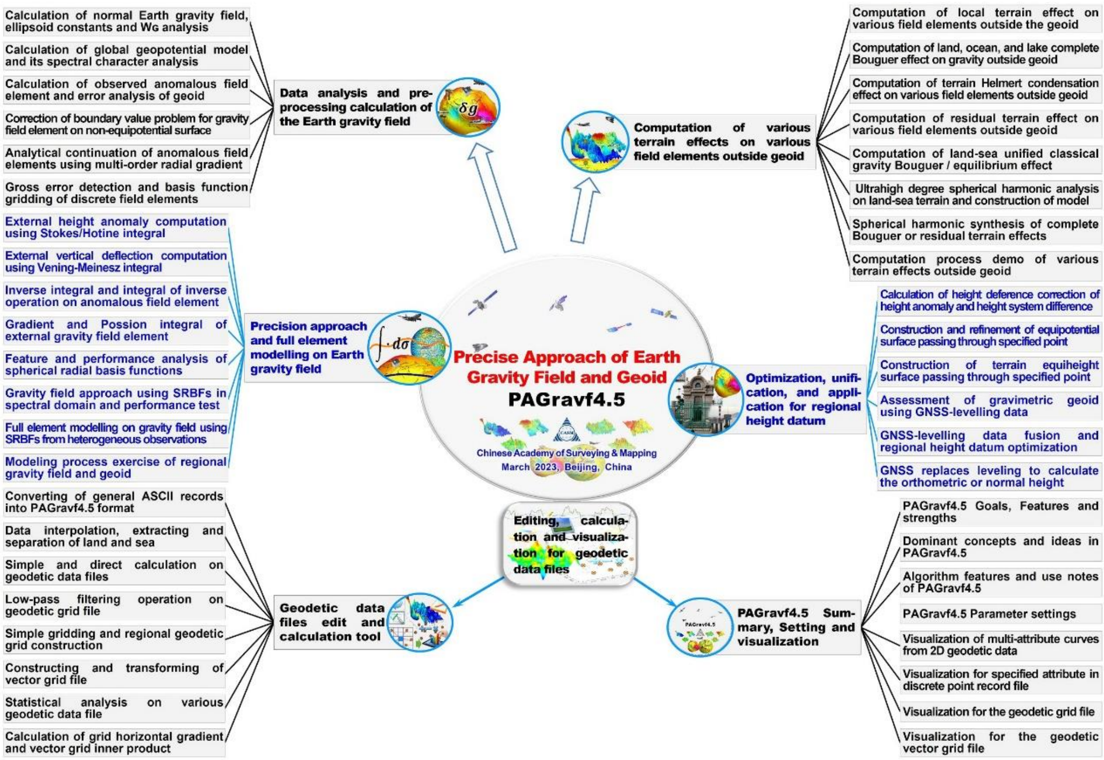

Figure 1. PAGravf4.5 Scientific Computing System Architecture

PAGravf4.5 has five subsystems, which includes data analysis and preprocessing calculation of Earth gravity field, computation of various terrain effects on various field elements outside geoid, precision approach and full element modelling on Earth gravity field, optimization, unification, and application for regional height datum as well as editing, calculation and visualization tools for geodetic data files. The scientific objectives of PAGravef4.5 mainly include the following three points:

(1) Solves the analytical compatibility and rigorous unified computation problems of various modes of terrain effects on various types of field elements, to fulfill the requirements of gravity field data processing in various cases and comprehensively improve the geophysical gravity exploration.

(2) Sets up the scientific and complete gravity field approach system with the positive-inverse integral in spatial domain and SRBF approach in spectral domain, to realize the full element analytical modelling in full space outside geoid from heterogeneous observations.

(3) Develops some ingenious physical geodetic algorithms based on the analytical relationship between Earth gravity field and height datum, to improve and unify the regional height datum, and consolidate and expand the applications of Earth gravity field.

2 Earth Tide, Load Effects and Deformation Monitoring Computation (ETideLoad4.5)

ETideLoad4.5 is a large scientific computing package for geophysical geodetic monitoring, which adopts the scientific uniform numerical standards and analytic compatible geophysical algorithms accurately to compute various tidal and non-tidal effects on various geodetic variations outside the solid Earth, approaches the load deformation field and temporal gravity field from heterogeneous geodetic data, and then quantitatively monitors the land water, geological environment and ground stability variations, in order to support the deep fusion of heterogeneous geodetic data and collaborative monitoring of multi-geodetic technologies.

User can design own schemes and processes, then organize flexibly the related programs and functions from ETideLoad4.5, perform some scientific computations for various tidal or non-tidal effects, ground deformation field or temporal gravity field approach, land water, ground stability, or surface dynamic environment monitoring, and multi-source heterogeneous geodetic data deep fusion.

Figure 2. ETideLoad4.5 Scientific Computing System Architecture

ETideLoad4.5 is mainly composed of five subsystems: computation of various tidal effects on various geodetic variations, processing and analysis on non-tidal geodetic variation time series, load deformation field approach and monitoring from heterogeneous variations, CORS/InSAR collaborative monitoring and ground stability estimation, and geodetic data files edit and calculation tools, The scientific goals of ETideLoad4.5 mainly include the following three points:

(1) Using the consistent geophysical models and uniform numerical standards, accurately compute the various tidal and non-tidal effects on various geometric and physical geodetic variations on the ground and outside the solid Earth by constructing analytic compatible

geodetic and geodynamic algorithms.

(2) Calculate and analyze the global and regional non-tidal load effects, and deeply fuse heterogeneous geodetic and surface load observations according to the theory of solid earth deformation, to realize the collaborative monitoring and high-precision approach of land water variations, load deformation field and time-varying gravity field.

(3) Provide a set of scientific and practical geodetic geodynamic computation tools for construction of heterogeneous spatiotemporal geodetic frames, and deep fusion of heterogeneous Earth observations, collaborative monitoring of multi-geotechnologies, computation of solid Earth deformation, monitoring of surface hydrology environment, and surveying of geological disasters.

3 Typical Applications of Software

The scientific computing platform integrates classroom teaching, self-study exercises, applied computing and scientific research, and is suitable for senior undergraduate, graduate, scientific research and engineering technicians in geodesy and geosciences, geology and geophysics, surveying and mapping engineering and geographic information, aerospace and satellite dynamics, and earthquake and geodynamics. Mainly including several typical applications:

1.Seamless and continuous monitoring of regional land water, ground deformation field, and gravity field changes.

From 2015 to 2016, using data from 26 CORS stations, 8 gravity stations, and 1 tilt station in the Three Gorges region and its surrounding areas (point distribution as shown in the figure), combined with daily average data from river hydrological stations and meteorological stations, as well as observation data from various satellite altimetry, Resource 3 satellite remote sensing, and GRACE satellite gravity, the load dynamics assimilation method was used to comprehensively determine the period from January 2010 to June 2015 in the Three Gorges region 2′×2′ Vertical deformation of the ground (a), ground gravity (b), ground tilt (c), and monthly variation of groundwater (d) grid time series.

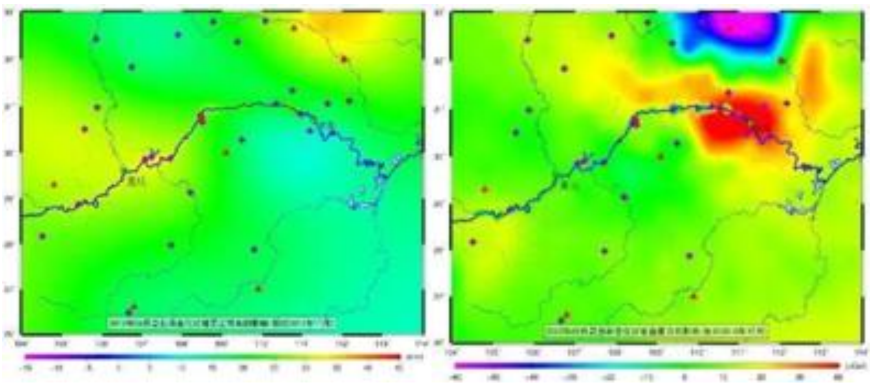

(a) (b)

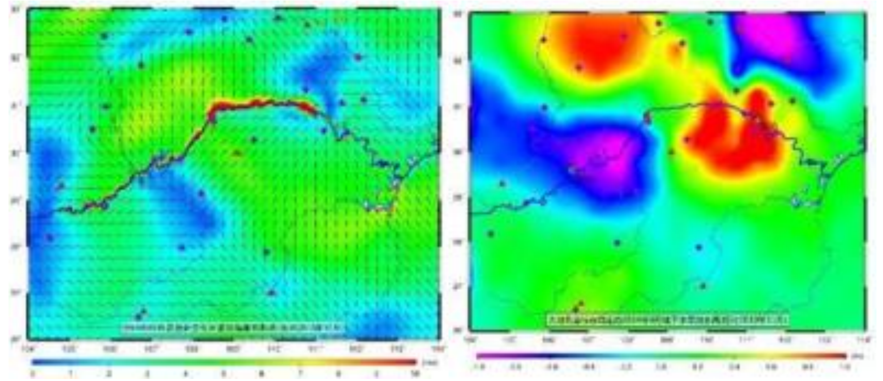

(c) (d)

Figure 3. Three Gorges Region 2′× 2′ Vertical ground deformation (a), ground gravity (b), ground tilt (c), and monthly variation of groundwater (d) grid time series

The results show that:

(1) the monitoring accuracy of ground vertical deformation is 5mm, and the monitoring accuracy of ground gravity change is 10 μGal. The comprehensive monitoring method of multiple elements of surface dynamic environment through multiple geodetic surveys is feasible.

(2) The annual variation amplitude of vertical ground deformation in the Three Gorges area is 36mm, the annual variation amplitude of geoid is 28mm, and the annual variation amplitude of ground gravity is 117 μGal.

(3) After the closure of the Yangtze River, the groundwater variation in the entire reservoir area has increased by nearly 0.5m3 per square meter, and the impact area has expanded by over 150km from the centerline of the Yangtze River to both sides of the area.

2. Evaluation of Ground Stability Changes and Geological Disaster Monitoring and Warning Capability.

From 2017 to 2018, using continuous GNSS observation data from 38 CORS stations in and around Wenzhou, Lishui, Zhejiang Province from 2015 to 2017, combined with daily average atmospheric pressure data from 39 meteorological stations, using load deformation theory as dynamic constraints combined with known load removal recovery plans, calculated 1′×1′ Grid time series of monthly changes in ground vertical deformation, ground gravity, and ground stability in the Wenzhou area of Lishui from January 2015 to December 2017. Evaluate the ability of CORS station network to capture geological hazard precursors by quantitatively tracking changes in ground stability (as shown in the Figure 4).

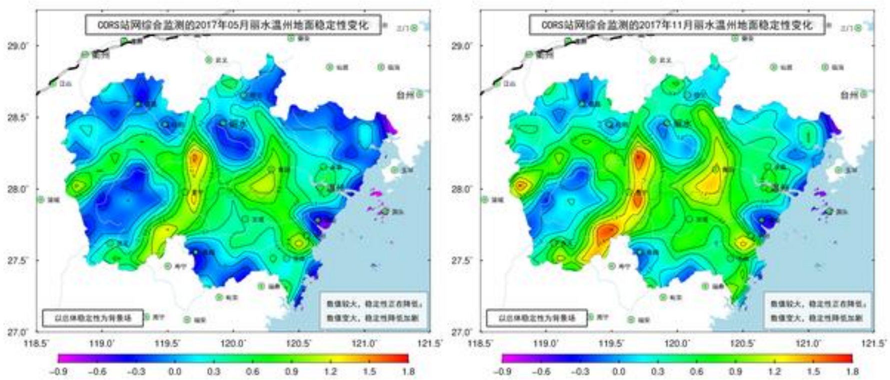

(a)2017.05 (b)2017.11

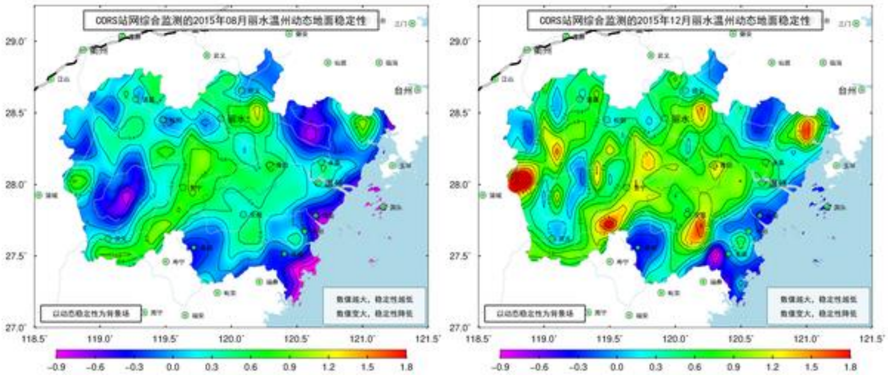

(c)2015.08 (d)2015.12

Figure 4. Comprehensive monitoring of dynamic ground stability in Lishui Wenzhou using CORS station network

The results show that:

(1) CORS network has the ability to continuously and quantitatively track and monitor the time and location of ground stability reduction, the duration of action, and the spatial impact distribution, as well as the ability to track and capture geological disaster processes and precursors.

(2) Before geological disasters occur, the CORS network can detect stability reduction signals in advance by continuously monitoring ground vertical deformation, ground gravity, and ground tilt changes, thereby capturing disaster precursors.

(3) The early capture rate of geological disaster precursors in the CORS station network in the Wenzhou area of Lishui can reach 92.5%.

3. Ground subsidence and elevation benchmark monitoring and maintenance

In 2016, a vertical benchmark monitoring and maintenance demonstration work was carried out in Shandong Province, combining CORS network, gravity satellite, and leveling network.

In 2017, a seamless and continuous monitoring of regional time-varying gravity field and groundwater reserve changes was carried out in the Hanzhong region of Shaanxi Province, in conjunction with the CORS network and gravity satellites.

In 2018, a comprehensive monitoring of land subsidence and regional elevation benchmark stability was carried out in Tianjin through multi-source and multiple geodetic surveys.

In 2019, land subsidence monitoring was carried out in Taizhou City, Zhejiang Province, using a joint time-series InSAR and CORS network.

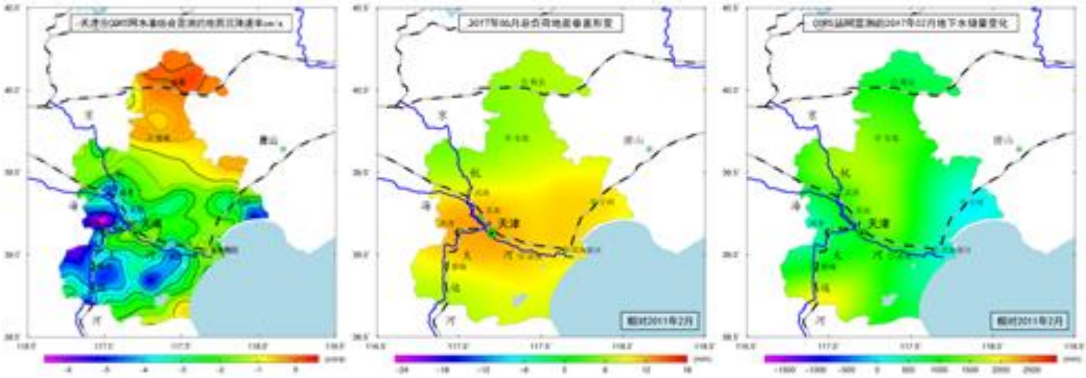

Figure 5. (a) Land subsidence rate of Tianjin CORS network leveling comprehensive monitoring(b) Vertical deformation of the load ground in June 2017(c) Monitoring changes in lunar groundwater reserves using CORS network

The results show:

(1) CORS station can not only directly and continuously monitor ground vertical deformation with millimeter level accuracy, but also, like the principle of monitoring global gravity field changes using GRACE satellite tracking satellites, can monitor small changes in regional gravity field with higher spatiotemporal resolution and sensitivity. Integrating various ground and satellite geodetic measurements can effectively improve the level of multi element monitoring of surface dynamic environment.

(2) In the vicinity of coastal zones and urban roads, InSAR monitoring is severely disturbed by surface non deformation information. After being unified with the CORS network's spatiotemporal monitoring benchmark, it can repair atmospheric delay errors, compensate for the impact of vertical deformation of load tides, and improve the ground's nonlinear and time-varying monitoring ability

4. Regional linkage monitoring and numerical prediction of geological hazards

In 2021, 72 CORS stations, 44 groundwater monitoring stations, 41 river hydrological stations, as well as daily monitoring data of soil water and meteorology (with a time span from January 1, 2018 to December 31, 2020) were used in Baoshan and Dali cities in Yunnan Province (with an area of approximately 60000 square kilometers). The CORS network was used as a control to constrain assimilation of hydrological and meteorological observations and quantitatively monitor regional stability changes based on deformation dynamics and gravity field laws, Quantitative evaluation of geological hazard susceptibility has achieved numerical prediction of geological hazard risk (similar to meteorological and geological hazard trend prediction, replacing changes in meteorological elements with changes in ground stability).

(1) We have established a regional ground stability change and prediction grid time series model (with a spatial resolution of 1km and a time interval of 1 week), continuously monitoring the spatial distribution and temporal evolution trend of the entire region's hazardous areas, and achieving numerical prediction of geological hazard risk.

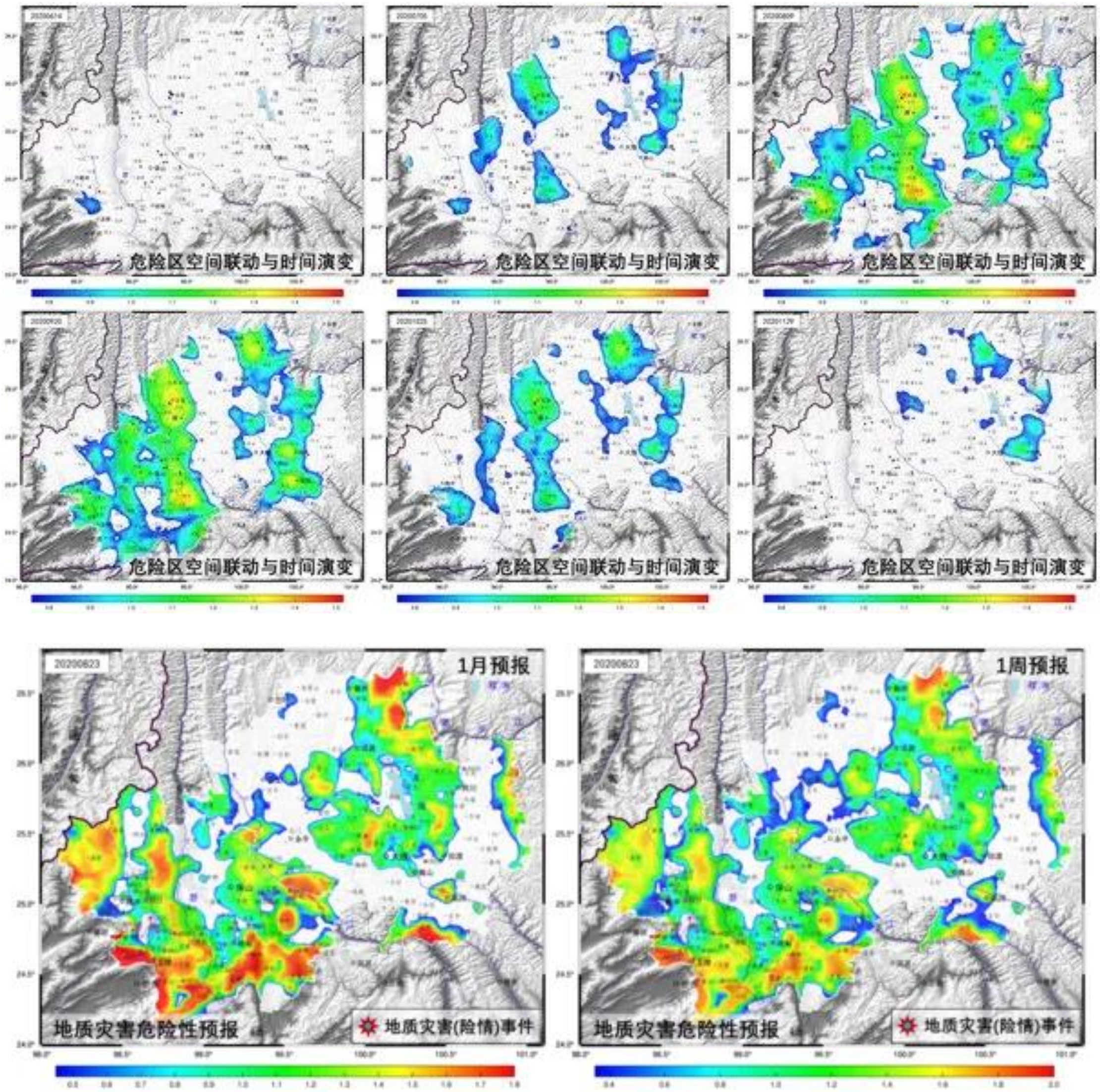

Figure 6. Spatial distribution and temporal evolution trend of hazardous areas and numerical prediction of geological hazard risk

The time of accelerated reduction of ground stability was used as the precursor of disasters, and the monitoring performance of ground stability changes was tested and verified using 197 actual disasters (dangerous situations) from 2018 to 2020. The results showed that 186 disasters showed precursor signals of accelerated ground stability reduction more than 2 days in advance, with a coincidence rate of 94.4%. Using 90 actual geological disasters (dangerous situations) that occurred in 2020 as verification, the 1-week, 2-week, and 1-month prediction rates were 92.2%, 83.3%, and 75.6%, respectively, as shown in Figure 6 (the color in the figure represents the geological hazard danger zone with rock and soil layers as the object. The bottom color scale is dimensionless, and the larger the value, the faster the stability decreases, and the greater the risk of geological disasters occurring here.)

(2) A numerical model for overall ground stability in the region was constructed to quantitatively evaluate the susceptibility of the entire region to geological hazards, and multiple potential geological hazard prone areas were identified.

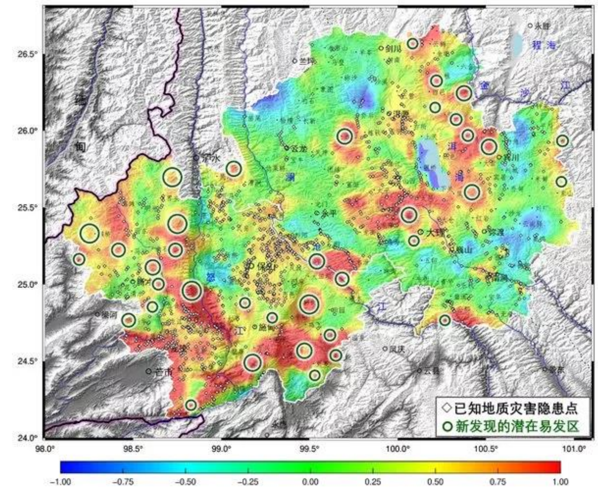

Figure 7. Numerical Model for Overall Ground Stability of Baoshan and Dali Cities in Yunnan Province

A comparative analysis was conducted between the overall stability model and the distribution of known geological hazard hazard points (as of December 2016). The results showed that 83% of known hazard points had poor stability in their basement; About 11% of areas with poor stability have no hidden danger points, and based on this, 37 new potential geological hazard prone areas have been interpreted.

Seafloor Geodetic Positioning and Subsea Navigation Application

Shuqiang Xue[1], Tianhe Xu[2], Yanxiong Liu[3], Xianping Qin[4]

[1] *Chinese Academy of Surveying and Mapping, Beijing.*

[2] *Institute of Space Science, Shandong University, Weihai City, Shandong Province.*

[3] *First Institute of Oceanography, MNR, Qingdao City, Shandong Province.*

[4] *Xian Research Institute of Surveying and Mapping, Xian City, Shanxi Province.*

1 Seafloor Geodetic positioning

The GNSS-A positioning accuracy of seafloor geodetic point is influenced by the trajectory of the surveying vessel. Circle trajectory is a commonly used surveying pattern in determining the position of seafloor geodetic point (Zeng et al. 2021). Compared with the circular measurement pattern for the positioning of seafloor control points, the accuracy of the circular and cross-track measurement pattern can be improved by 1.4 centimeters.

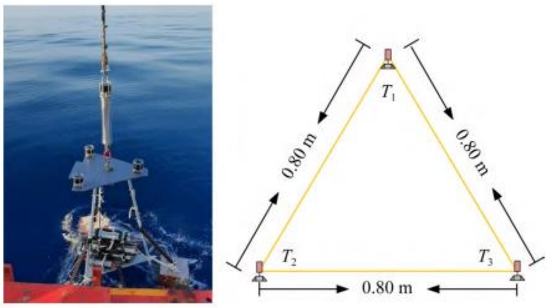

Figure.1 Schematic diggram of seafloor control point and beacon placement position on the station

The acoustic ray tracing algorithm is generally adopted in high-precision underwater positioning. To reduce the acoustic signal delay error and acoustic ray bending error in underwater positioning, the acoustic positioning algorithm based on the ray tracing has been widely applied. The algorithm needs to solve a large number of inverse problems, and therefore efficiently solving the inverse problem becomes critical to improve the whole efficiency of the underwater positioning algorithm.

Chinese scholars have proposed two kinds of p-order secant methods to improve the efficiency of traditional method (Yang et al. 2021), and the methods can be regarded as a generalization of the traditional secant method from two points to *p* points for rapidly solving the inverse problem. In the proposed methods, the calculation information in previous iterations is utilized to fit a polynomial model to speed up the algorithm convergence. The inverse problem is calculated by solving a polynomial equation approximating the function mapping from the emission angle to the radial distance of the ray. In the second-kind method, the inverse problem is however directly solved by approximating the function mapping from the radial distance to the emission angle. As the first-kind method needs to solve a p-order polynomial equation, the practicability of this method is limited to the complexity of solving the high-order equation, while the second-kind method can directly approximate the solution of the inverse problem, which is more practical and flexible.

In order to reduce the influence of sound ray bending and sound velocity variation errors on the submarine station parameters, an observation model considering sound ray bending and sound velocity deviation parameters was established (Qin et al. 2023).

Table 1. Differences in horizontal coordinates between 2 D and 3D adjustments.

Case	Stations		Not estimating acoustic ray bending			Estimating acoustic ray bending		
			Session1	Session2	Session3	Session1	Session2	Session1
1	1	DDN(cm)	6.6	2.5	5.7	0.0	0.0	0.0
		DDE(cm)	7.2	2.7	6.3	0.0	0.0	0.1
	2	DDN(cm)	-2.6	-1.6	-2.5	0.0	0.0	0.0
		DDE(cm)	-7.6	-2.9	-6.6	-0.1	0.0	0.0
	3	DDN(cm)	-6.9	-2.7	-6.0	-0.1	0.0	0.0
		DDE(cm)	-3.3	-1.8	-3.1	0.0	0.0	0.0
	4	DDN(cm)	2.8	1.9	2.7	0.0	0.0	0.1
		DDE(cm)	3.7	2.0	3.4	0.0	0.0	0.0
2	1	DDN(cm)	7.7	3.8	6.6	0.0	0.0	0.1
		DDE(cm)	8.4	4.0	7.1	0.0	0.1	0.0
	2	DDN(cm)	-2.3	-0.3	-1.6	0.0	0.0	0.0
		DDE(cm)	-7.8	-4.2	-7.4	-0.1	0.0	0.0
	3	DDN(cm)	-7.1	-4.1	-6.8	-0.1	0.0	0.0
		DDE(cm)	-3.1	-0.5	-2.1	0.0	0.0	0.0
	4	DDN(cm)	1.7	0.6	1.9	0.0	0.0	0.1
		DDE(cm)	2.5	0.7	2.5	0.0	0.0	0.0

Table 1 shows that, the maximum difference of horizontal coordinates between 2 D and 3 D adjustments is 8.4 cm when the acoustic ray bending parameter is not estimated. If the acoustic ray bending parameter is introduced into the observation model and estimated together with the location parameters, the maximum difference of horizontal coordinates between 2 D and 3 D adjustment is reduced to 0.1 cm.

Table 2. Variations of vertical coordinates before and after adjustment.

Case	Stations		Not estimating acoustic ray bending			Estimating acoustic ray bending		
			Session1	Session2	Session3	Session1	Session2	Session1
(1)	1	DU(cm)	6.6	2.5	5.7	0.0	0.0	0.0
	2	DU(cm)	7.2	2.7	6.3	0.0	0.0	0.1
	3	DU(cm)	-2.6	-1.6	-2.5	0.0	0.0	0.0
	4	DU(cm)	-7.6	-2.9	-6.6	-0.1	0.0	0.0
(2)	1	DU(cm)	-6.9	-2.7	-6.0	-0.1	0.0	0.0
	2	DU(cm)	-3.3	-1.8	-3.1	0.0	0.0	0.0
	3	DU(cm)	2.8	1.9	2.7	0.0	0.0	0.1

4	DU(cm)	3.7	2.0	3.4	0.0	0.0	0.0

As shown in Table 2, after adjustment with a ray bending parameter, the accuracy of vertical coordinates also significantly improved.

However,the traditional acoustic ray tracing method is usually based on the one-way acoustic propagation path without the consideration of the displacement of shipborne transducer during the process of acoustic signal propagation. Therefore,the systematic deviation will be introduced in the positioning for seafloor transponder,which will limit the positioning accuracy of seafloor points. To solve this problem,a layered constant gradient acoustic ray tracing underwater positioning algorithm considering round trip acoustic path is proposed (Yan et al. 2022). Combined with the actual propagation path of underwater acoustic signal,the round trip acoustic path.

Numerous errors are inevitable in marine surveying, including systematic errors and gross errors caused by GNSS dynamic positioning, inaccurate sound velocity profile measurements, and ocean ambient noise, and their interference will be directly reflected in the positioning results (Kuang et al.2023).

Marine geodetic datum positioning is calculated by using the GNSS-A data. Based on the precise round-trip acoustic location model, Chinese scholars model the sound velocity error related to the deviation of sound velocity distribution (SVP) and time-varying error (Sun et al.2023). To reduce the propagation error of the acoustic rays in the ocean, the SVP deviation and seafloor position parameters are resolved simultaneously by the Bayesian estimation using the round-trip acoustic travel time. The time-varying errors of SVP are corrected through symbolic regression using multi-gene genetic programming (MGGP) even without any accurate prespecified mathematical form of marine environmental variations.

First, the position and background SVP deviation is estimated by Bayesian estimation in the precise acoustic positioning model. Next, the time-varying sound velocity errors are modelled by symbolic function and determined by the MGGP approach using the acoustic travel time data. Finally, update the position vector again. These estimation steps are repeated until the position variation is below a convergence criterion.

Based on sound velocity profiles (SVPs) data, the equal gradient acoustic ray- tracing method is applied in high-precision position inversion. However, because of the discreteness of the SVPs used in the forementioned method, it ignores the continuous variation of sound velocity structure in time domain, which worsens the positioning accuracy. Chinese scholars consider the time domain variation of sound velocity structure and the cubic B-spline function is applied to characterize the perturbed sound velocity (Zhao et al.2023).

Based on the ray-tracing theory, an inversion model of “stepwise iteration & progressive corrections” for both positioning and sound speed information is proposed, which conducts the gradual correction of seafloor geodetic station coordinates and disturbed sound velocity.

Robust Bayesian least squares the inversion model of iteration-gradual correction is carried out alternately by "fixed sound velocity - solution position" and "fixed position - estimated sound velocity", and the coordinates and sound velocity structure of the submarine station are modified gradually until the solution results meet the threshold requirements, so as to obtain the time-domain changes of the position of the submarine reference station and sound velocity structure. Quadratic polynomial (QP) method and cubic B-spline (CBS) function method are used to invert the structure of disturbed sound velocity. The spline function used by CBS sound velocity correction method has better smoothness and continuity, so it can obtain a better positioning result.

After modeling the spatio-temporal model of sound velocity disturbance with cubic B-spline curve, Chinese scholars proposed to use the minimum norm condition to select the optimal hyper parameter (Zhuang et al. 2023), and realized the joint estimation of the coordinates of the seabed transponder and the spatio-temporal model of sound velocity. The simplest way to solve the two kinds of parameters of three-dimensional coordinate and sound velocity disturbance is to fix one kind of parameters to solve the other kind of parameters, which cannot guarantee the unbiased parameters. The Bayesian estimation is used to constrain the prior information of the parameters.

Similarly, Chinese scholars have used Bayesian estimation to simultaneously estimate the position of the submarine transponder and the horizontal gradient of sound velocity (Ming et al. 2023). Experimental results show that: at the same time, the method of solving the position of transponder and horizontal gradient of sound velocity is only applicable to the situation where the horizontal gradient of sound velocity changes little. Therefore, if this method is used to locate the seabed transponder, it is recommended to reduce the sailing time as far as possible to meet the assumption that the horizontal sound velocity structure remains approximately unchanged.

All the methods of sound velocity inversion require the constraints such as the real distance or the real terrain, which are often difficult to obtain in underwater positioning. To solve the problem of underwater high-accuracy position under the lack of measured sound velocity profile (SVP), some scholar proposes a self- constraint underwater positioning method without the assistance of measured sound velocity profiles (Zhao et al. 2023). Firstly, the model of incident angle and sound propagation distance is constructed. Then, by fitting the model coefficients, the reference depths of all observation epochs are obtained to be the depth constraint in the SVP inversion. Finally, the coordinates of underwater control points are accurately calculated with the inversion SVP.

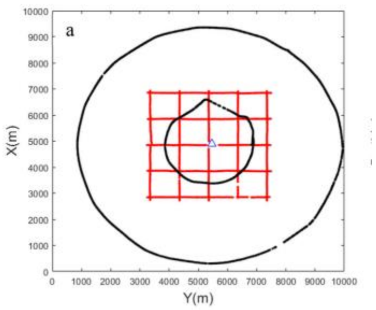

Figure 2. The three sailing routes (a)

Table 3. Variations of vertical coordinates before and after adjustment.

Route	Error(m)	Not estimating acoustic ray bending	Estimating acoustic ray bending

		20m	60m	100m	20m	60m	100m
	dx	0.02	0.02	0.02	0.01	0.01	0.01
Cricle1	dy	0.02	0.01	0.00	0.01	0.03	0.01
	dz	0.91	0.51	0.36	0.45	0.69	0.45
	dx	0.30	0.30	0.30	0.01	0.03	0.01
Cricle2	dy	0.05	0.04	0.03	0.01	0.02	0.01
	dz	0.64	0.24	0.09	0.49	1.40	0.49
	dx	0.01	0.01	0.01	0.00	0.00	0.00
Grid	dy	0.00	0.00	0.00	0.00	0.00	0.00
	dz	1.01	0.83	1.05	0.50	0.53	0.50

The maximum horizontal positioning error is 0.05 m, which benefits from the symmetry of sailing tracks and the accurately retrieved SVP. The maximum vertical positioning error reaches 1.40 m and is larger than the horizontal positioning error, but the relative positioning error is very small in 3000 m depth. The positioning results show that the proposed method achieved high positioning accuracy without the measured SVP.

2 Subsea navigation applications.

Chinese scholars refer to GNSS tropospheric error processing method and propose GNSS acoustic position enhancement service method for underwater vehicle position enhancement service (Chen et al.2023)[错误!未找到引用源。]. The GNSS tropospheric error processing method is used for reference, that is, the signal propagation time is first converted into distance, and then the distance is corrected by the projection function related to height Angle, the zenith tropospheric delay model and parameters, so as to support the high-precision position service. Based on the above method, the acoustic velocity correction information of submarine geodetic control points and surface buoys are used to invert the sea area to support the high-precision navigation calculation of underwater equipment.

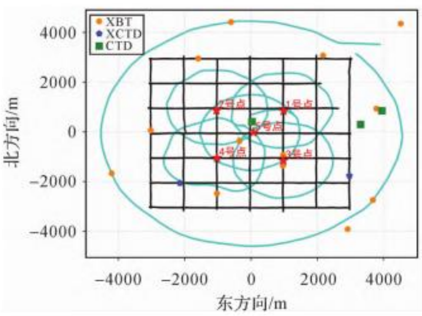

Figure 3. Distribution of seafloor reference stations, measured sound speed profiles and the ship'strack lines

Table 4. Ship's navigation results based on the sound speederror correction model.

Track name (Time sorting)	Mean value of epoch-by-epoch accuracy E	Mean value of epoch-by-epoch accuracy N	Mean value of epoch-by-epoch accuracy U	RMS of mutual difference with GNSS E	RMS of mutual difference with GNSS N	RMS of mutual difference with GNSS U
Circle1	0.098	0.096	0.052	0.635	0.297	0.225

Circle2	0.278	0.267	0.192	0.579	0.438	0.420
Circle3	0.523	0.509	0.356	0.534	0.532	0.379
Circle4	0.299	0.292	0.191	0.482	0.333	0.237
Line	0.865	0.841	0.917	0.831	1.295	0.790
Circle5	0.378	0.367	0.196	0.519	0.343	0.200
Big circle	2.021	1.983	2.890	1.092	1.944	1.503

It can be seen that the accuracy of navigation results away from 3000m horizontal distance to the center of the submarine control network is decimeter level. In the test, the navigation and positioning data (about 16000m in length) of a pilot line crossing the seabed control network on the sea surface were processed, and the mutual difference between the acoustic navigation result and GNSS positioning result was output. It shows that, with the increase of the horizontal distance between the survey ship and the center of the submarine control network, the accuracy of the three-dimensional results of acoustic navigation gradually increases within the range of 6000m, while it increases rapidly outside the range of 6000m. The accuracy of the results in the horizontal direction is about 10m and that in the vertical direction is greater than 40m at 10,000 m.

A rigorous method incorporates the time varying term of the sound velocity ranging error into the coefficient matrix of the underwater observation equation, and the transducer position error should be considered. Therefore, a Gauss-Helmert (GH) model is used for seafloor control point positioning . On this basis, considering the gross errors polluting of the observations, the robust estimation principle is introduced.

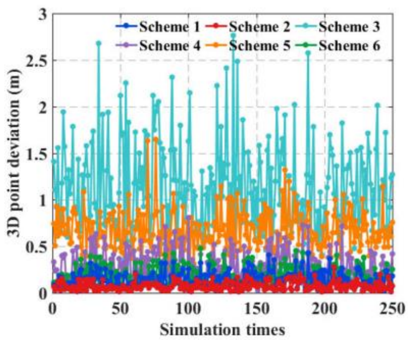

Figure 4. The 3D point deviations of each scheme.

Table 5. The statistical results of each scheme.

Statistics Method	Max	Min	RMS	STD
Scheme1	0.429	0.012	0.166	0.080
Scheme2	0.279	0.012	0.087	0.045
Scheme3	2.763	0.273	1.253	0.485
Scheme4	0.808	0.022	0.331	0.156
Scheme5	1.647	0.244	0.709	0.210
Scheme6	0.477	0.028	0.213	0.101

Scheme 1: When gross errors are not added, the general model is constructed, and the estimation is carried out based on the LS algorithm. Scheme 2: When gross errors are not added, the nonlinear GH model is constructed, and the estimation is carried out based on the WTLS

algorithm. Scheme 3: When gross errors are added, the general model is constructed, and the estimation is carried out based on the LS algorithm. Scheme 4: When gross errors are added, the nonlinear GH model is constructed, and the estimation is carried out based on the WTLS algorithm. Scheme 5: When gross errors are added, the general model is constructed, and the estimation is carried out based on the robust LS algorithm. Scheme 6: When gross errors are added, the nonlinear GH model is constructed, and the estimation is carried out based on the robust WTLS algorithm.

In Scheme 6, the nonlinear GH model is adopted to address several kinds of error factors, and the transducer position error and the time-varying term of the sound velocity ranging error are combined into one unified error vector. The robust WTLS algorithm of the proposed model accounts the anti-interference ability in both the structure and the observation spaces and can construct the equivalent covariance matrix of each observation independently. Hence, the influences of abnormal transducer position information and gross errors can be effectively resisted. Besides, Chinese scholars take into account the effect of transceiver separation (Xin et al. 2022), have suggested that based on the constant gradient sound ray tracing method,the optimal target coordinates can be obtained by searching according to the principle of minimum roundtrip delay difference. A Newton iterative solution algorithm based on round-trip time assignment according to sound distance is proposed to improve the computational efficiency.

Bibliography

Chen G X，Gao K F，Zhao J H, et al. 2023. The method of sound speed errors correction in GNSS-acoustic location service. Acta Geodaetica et Cartographica Sinica. (in chinese), 52(4);536-549.

Kuang Y C, Lu Z P, Wang F C, et al. 2023, A Nonlinear Gauss-Helmert Model and Its Robust Solution for Seafloor Control Point Positioning, Marine Geodesy, 46:1, 16-42.

Ma Y Y, Yang Y X, Zeng A M. 2022. GNSS-A straight-line survey pattern and trajectory combination optimization analysis. Chinese Journal of Geophysics. (in Chinese),65(10):3797-3808.

Ming F，Yang Y X, Zeng A M. 2023. Positioning accuracy of GNSS-A in deep sea based on Bayesian estimation. Chinese Journal of Geophysics. (in Chinese),66(3):951-960.

Qin X P, Yang Y X, Sun B J. 2023. A Robust Method to Estimate the Coordinates of Seafloor Stations by Direct-Path Ranging, Marine Geodesy, 46:1, 83-98.

Sun D J, Yu M, Zheng C I, et.al. 2023. Improved Seafloor Geodetic Positioning via Sound Velocity Correction Based on the Precise Round-Trip Acoustic Positioning Model, Marine Geodesy, 46:1, 43-61.

Xin M Z, Ge M R，Yang F L, et al. 2022. A sound ray tracing positioning method for marine geodetic datum considering the effect of transceiver separation. Chinese Journal of Geophysics. (in Chinese),65(10):3809-3817.

Yang W L, Xue S Q, Liu Y X. 2021. P-order secant method for rapidly solving the ray inverse problem of underwater acoustic positioning. Marine Geodesy, 1-13.

Yan F C, Wang Z J, Zhao S, et al. 2022. A layered constant gradient acoustic ray tracing underwater positioning algorithm considering round trip acoustic path .Acta Geodaetica et Cartographica Sinica. (in chinese),51(1);31-40.

Zeng A M, Yang Y X, Ming F, et al. 2021. Positioning model and analysis of the sailing circle mode of seafloor geodetic datum points. Acta Geodaetica et Cartographica Sinica (in chinese) , Zhao S, Wang Z J，Nie Z X, et al.2023. Precise positioning method for seafloor geodetic stations based on the temporal variation of sound speed structure. Acta Geodaetica et Cartographica Sinica. (in chinese),52(1);41-50.

50(07):939-952.

Zhao J H, Liang W B, Ma J Y, et.al.2023. A Self-Constraint Underwater Positioning Method without the Assistance of Measured Sound Velocity Profile, Marine Geodesy, 46:1, 62-82.

Zhang S Q, Yang Y X, Xu T H. 2023.Estimation of ocean sound velocity variation based on GNSS-A and its influence on positioning. Chinese Journal of Geophysics (in Chinese), 66(3);961-972.

Progress on Hydrogeodesy

Wei Feng[1], Shuang Yi[2], Bo Zhong[3], Qiujie Chen [4], Xiaodong Chen[5], Yulong Zhong[6], Yuanjin Pan[3], Lin Liu[7], Wei Wang[8]

[1] School of Geospatial Engineering and Science, Sun Yat-sen University, Zhuhai, China

[2] University of Chinese Academy of Sciences, Beijing, China

[3] School of Geodesy and Geomatics, Wuhan University, Wuhan, China

[4] College of Surveying and Geo-informatics, Tongji University, Shanghai, China

[5] Innovation Academy for Precision Measurement Science and Technology, Chinese Academy of Sciences, Wuhan, China

[6] School of Geography and Information Engineering, China University of Geosciences, Wuhan, China

[7] The Chinese University of Hong Kong, China

[8] Chinese Academy of Surveying and Mapping, Beijing, China

1 Satellite Gravity

Since the launch of Gravity Recovery and Climate Experiment (GRACE) and its successor, GRACE-Follow on (GRACE-FO), satellite gravimetry has revolutionized our understanding of mass transport and redistribution in the Earth system. Global observations of water and ice mass redistribution in the Earth system at monthly to decadal time scales are essential for understanding the climate variability and changes. GRACE and GRACE-FO have provided unprecedented insights into the Earth's water cycle, ice mass balance, and solid Earth deformation.

Data processing

Low degree spherical harmonic coefficients are proved to be important to accurately estimated the changes in the Earth’s surface mass, which however are missing or corrupted in GRACE/GRACE-FO gravity field models. The time variations of the three degree-1 coefficients, representing geocenter motions, do not exist as satellites always orbit around the center-of-mass of the Earth’s system and insensitive to its motion with respect to the center-of-figure of the solid Earth. The time variations of the C_{20} coefficients (J2), representing the changes in the Earth’s dynamic oblateness, are contaminated by large noise, partially originating from thermo-dependent systematic errors in the accelerometers. The time variations of the C_{30} coefficients are degraded during the end of the GRACE and so far the entire period of the GRACE-FO. To overcome these limitations, Sun et al. (2019, 2020, 2023) have developed and improved several methods to estimate these coefficients separately or simultaneously. The GRACE-OBP approach has been improved by identifying the optimal implementation parameters and considering the self-attraction and loading effects.

There are two major difficulties in the data processing of GRACE/GRACE-FO gravity satellites, namely, how to effectively filter out the strip noise and how to fill the 11 months of missing data between two generations of gravity satellites. For the filtering problem, Yi & Nico (2021) propose a new spatial filter based on autocorrelation in longitude direction and cross-correlation in latitude direction, using the singular spectrum analysis (SSA) technique, which can effectively remove the strip noise while maintaining the orthogonality with the physical signal. For the gap-filling problem, Yi & Nico (2022) propose a method to fill the spherical harmonic coefficients based on SSA and cross-validation, which can extract the long-term and oscillatory variations from the available observations to obtain the gap-filling data with error estimates. Improved multichannel SSA was also used to fill the gap reliably between the two missions (Wang F. et al., 2021). Zhang et al. (2021) used the mass anomaly observed by Swarm mission to fill this gap.

GRACE intersatellite geopotential differences (GPD), as the gravimetric observables, can more directly reflect the surface mass changes compared with the geometric KBR range-rate observations. Based on the remove-compute-restore technique and improved energy balance equation, the precise GPD observations are estimated from GRACE Level-1B data (Zhong B. et al., 2020, 2022). The regional mass concentration (mascon) solutions over South America are estimated from the GPD data using a priori constraints (Zhong B. et al., 2020), and the influence of different external constraints on the estimation of regional mascon solutions are investigated (Zhong B. et al., 2021). Furthermore, to improve the reliability of regional mascon solutions and avoid the influence of external constraints, basin-scale terrestrial water storage anomalies (TWSA) in the Yangtze River Basin of China are estimated by using spatio-temporal constraints with the unconstrained spherical harmonic (SH) solutions (estimated from GPD data) as the a priori information (Zhong B. et al., 2023). In addition, Ferreira et al. (2020) also proposed a parameterization of TWSA based on the so-called improved point mass, which adopts the synthesized residual gravitational potential as observations. The approach allows the basis functions to be represented locally rather than globally, as well as the use of geophysical data constraints.

Terrestrial Water Storage Variations

GRACE/GRACE-FO satellites have played a crucial role in studying the water cycle and water balance of various river basins in China. Zhong et al. (2020a, 2020b) used GRACE-derived terrestrial water storage change (TWSC) data and in-situ precipitation and runoff data to estimate evapotranspiration (ET) in West Liaohe River Basin (WLRB) and nine exorheic basins of China, respectively, based on the water balance equation. The results show that neglecting TWSC in the water balance leads to larger uncertainties in ET estimates, highlighting the importance of GRACE satellites in water balance studies. Bai et al. (2022) proposed a daily TWSA reconstruction framework and used it to improve the accuracy of TWSC estimates, which further led to better estimates of ET in nine exorheic basins of China. Qu et al. (2022) also employed WBE to estimate ET in the Yellow River Basin and investigate the annual, seasonal, and interannual variability of ET.

GRACE and GRACE-FO satellite data have also shown great potential in flood monitoring. Xiao et al. (2022) used GRACE and daily precipitation observations to reconstruct the daily water storage for the first time based on a statistical model to monitor the changes in terrestrial water storage during the "Henan 7.20 rainstorm" of China in 2021. The reconstructed daily TWSA has better potential for near-real-time flood monitoring for short-term events in a small region. Xie et al. (2022) reconstructed daily TWSA based on machine learning models to monitor flood events in the Yangtze River basin, which provides new opportunities for investigating submonthly water storage signals using GRACE and GRACE-FO satellite data. Furthermore, Xiong et al. (2022) established a novel standardized drought and flood potential index based on the ITSG-Grace2018 daily solution, which successfully detected 22 submonthly exceptional floods and droughts in the Yangtze River basin. The index uses standardized anomalies of daily TWSA and daily precipitation to evaluate the potential of floods and droughts in a region.

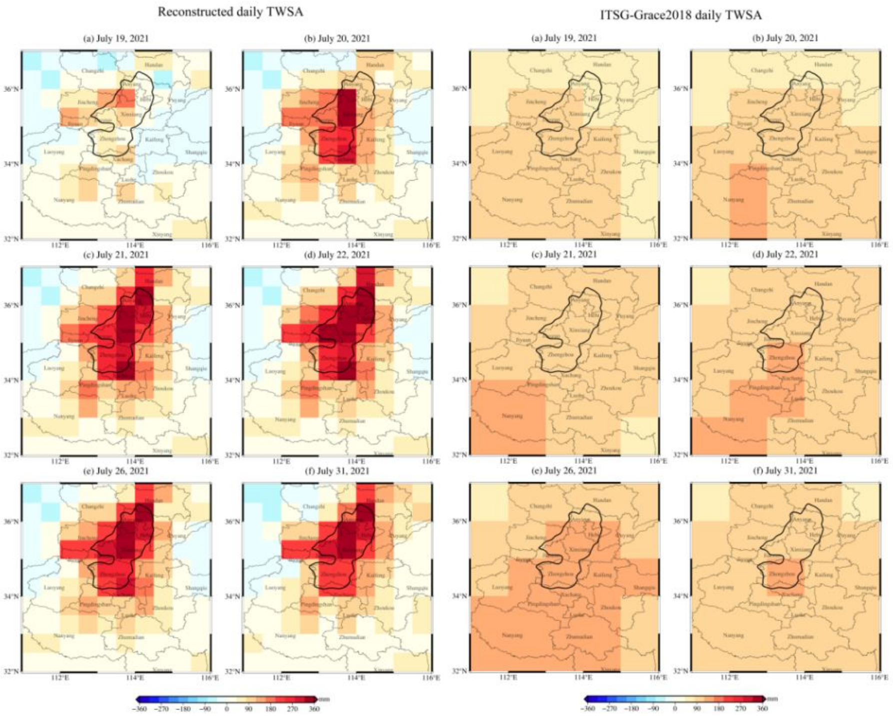

Figure 1 The left panels are the spatial distributions of reconstructed daily TWSA (0.5° × 0.5°), while the right panels are ITSG-Grace2018 daily TWSA (1° × 1°) with the seasonal cycle and the linear trend removed (Xiao et al. 2022).

Cryosphere

Geodetic observations of cryospheric changes have continued to be advanced diversified in both methodological development and applications. Chinese geodesists have made growingly important contributions to the polar studies, with a strong focus on the Tibetan Plateau and its surrounding high-altitude regions, collected known as High Mountain Asia or the third pole, and the Greenland and Antarctica Ice Sheets.

Zhang et al. (2020) improved the estimates of secular variation of Greenland ice mass by introducing a stochastic process described using a forward-backward Kalman Filter into the time series analysis of GRACE data. They obtained an accelerated loss of Greenland ice mass of 1.6 Gt/yr^2 during 2003-2017 and showed that this seemingly smaller acceleration than the reported ones from some of the previous studies was attributed to their better separation of acceleration from irregular interannual variations. Su et al. (2020) found that low-degree spherical harmonic coefficients, including degree-one terms and degree-two/three zonal terms, have a significant impact on estimating mass changes of the Greenland and Antarctic ice sheets using GRACE gravimetry. Ran et al. (2021) compared mascon products with mascon solutions computed in-house using a varying regularization parameter. They found that the observed discrepancies are likely dominated by differences in the applied regularization. They proposed an improved regularization scheme to estimate the mass change of the Greenland ice sheet. Liu et al. (2022) further developed the method and proposed a statistical model suitable for the reconstruction of GRACE-like high mountain glaciers (HMG) mass anomalies. Precipitation and temperature are the only inputs. They reconstructed and evaluated the HMG mass anomaly time series in 14 HMG regions, and the results show high consistent with GRACE/GRACE−FO observations. Li et al., (2020), and Wang et al. (2023) reported that the inter-annual mass variations of Greenland and their spatial characteristics as observed from GRACE and GRACE-FO were correlated with large-scale atmospheric-ocean oscillations and warranted further investigations into the physical mechanisms.

2 Satellite Altimetry

Traditional altimetry has successfully been used to measure global and regional sea level changes (e.g., Li et al., 2021; Chen et al. 2022; Wang et al. 2022). The large footprint limited its application on the alpine glacier. The ice tracking satellites ICESat & ICESat-2 and CryoSat-2 were the dominant approach to derive time-dependent elevation over glacier surfaces, due to their small footprint size.

Recently, Chinese scholars have estimated glacier mass balance in mountain regions by altimetry. Wang et al., (2021) combined ICESat and ICESat-2 data to survey the glacier thickness change in High Mountain Asia (HMA) over 2003-2019 and use independent gravity satellite data to fill the gap of ICESat. Shen et al., (2022) developed an elevation-aspect bin from elevation bin to estimate glaciers' inter-annual and intra-annual elevation changes based on ICESat & ICESat-2 over 2003-2020. Fan et al., (2022) calculated the elevation difference between ICESat-2 and NASA DEM to represent glacier mass balance over 2000-2021. Zhao et al., (2022) integrate ICESat, CryoSat-2, and ICESat-2 to provide high spatiotemporal glacier mass balance in southeastern Tibet. Wang and Sun (2022) used a new approach to obtain the complete seasonal cycle of glacier thickness changes in HMA.

3 GNSS/InSAR

Mass loading and deformation

GNSS data provides high precision measurements of the Earth’s surface displacements, which can be used to study various geophysical phenomena, including mass loading. To solve the ill-posed problem of GNSS inversion for regional mass loading based on loading Green's function theory, some improved estimation strategies (e.g., construction of regularization constraint matrix, estimation of optimal regularization parameter) are presented to improve the reliability and stability of GNSS-derived TWS changes (Li et al., 2022a, 2022b, 2023). The GNSS-derived TWS changes present higher temporal (daily) and spatial (dozens of kilometers) resolution than the GRACE/GFO estimates where GNSS stations are densely distributed, and the GNSS-inferred TWSA can well bridge the data gap of GRACE/GFO estimates (Li et al., 2023; Jiang et al., 2021).

Wang et al. (2017) used the GNSS station network to monitor the changes in groundwater reserves in the Three Gorges area. The results were then compared with the water level from groundwater monitoring wells. Li et al. (2023) proposed a fusion method for inverting regional GWS changes by integrating GNSS and GRACE data. Regional GWSA are inverted by using loading Green's function method and the spherical harmonic function method, which use GNSS and GRACE data, respectively. On this basis, the remove–restore theory in Earth's gravity field is introduced to fuse the two results from GNSS and GRACE, thus obtaining more reliable spatiotemporal changes in regional GWS in the Shaanxi–Gansu–Ningxia of China.

Wang et al. (2022) examined mass load inversion using a combination of both horizontal and vertical GNSS displacements and found that including horizontal displacements led to approximately a 10% improvement in mass inversion for the current precision level of GNSS. Moreover, through synthetic experiments, they predicted a further improvement of approximately 20% to 30% with a higher GNSS precision level.

Pan et al. (2019) proposed a joint inversion method of GNSS and GRACE to estimate the partitioning of vertical deformation to glacial and tectonic sources. The results showed that the elastic effects of glacier melting accounted for 0.39 mm/year of the average ground uplift rate of 0.72 ± 0.12 mm/year. In another study, Pan et al. (2023) found that the continuous water deficit throughout Tianshan and Pamir mainly located in glacier-covered areas, leading to spatial surface uplifting at rates of approximately 0.2–0.5 mm/yr. For Mainland China, Pan et al. (2021) used the GRACE/GRACE-FO products to isolate tectonic deformation signals at GPS sites within mainland China from 2002 to 2019. The results revealed the long-term spatial patterns of vertical tectonic motion in different blocks in mainland China. For the Tibetan Plateau, Jiao et al. (2019) found a rather poor correlation between satellite gravimetry and hydrological data in the interior basin. They separated the hydrological signal from satellite gravimetry using GNSS and other space geodesy data and concluded that the residual signals in the Tibetan Plateau should be attributed to deep tectonics.

Land Subsidence and Groundwater Depletion

The InSAR technique, together with GNSS and GRACE, has been frequently used in quantifying land subsidence and investigating groundwater depletion. Tang et al. (2022) evaluated the effects of the water transfer from the Yellow River to Taiyuan basin and suggested that subsidence rates in the subsidence areas of the Taiyuan Basin reduced by up to ~70% in the period of 2017–2020 with respect to the period of 2007–2010. Similar studies were performed in SuZhou (Shi et al., 2021), Tianjin-Langfang (Shi et al., 2022), and Wuhan (Zhao et al., 2022). These studies provide crucial information for sustainable groundwater management practices.

Deep groundwater (confined groundwater) is the major water source in the North China Plain (NCP). Long-term deep groundwater overexploitation has resulted in substantial groundwater storage (GWS) depletion, which has been detected by GRACE (Feng et al. 2013, 2018). Quantifying the influence of long-term overexploitation on deep groundwater resources is extremely important to maintain the sustainability of the confined aquifer system. Bai et al. (2021) presented a new method to estimate the total exploitable GWS and the total GWS depletion since the 1960s, by combining use of the InSAR deformation, hydraulic head observations and hydrogeological data. The total exploitable GWS in Cangzhou was 26.1±21.3 km^3 and decreased by 13.0±8.1 km^3~13.6±8.5 km^3 until 2010, accounting for 49.8%~52.2% of the total amount. It is worth noting that 87.4%~87.9% of the total GWS depletion is irreversible, leading to a substantial permanent loss of groundwater storage capacity.

Cryosphere

Frozen ground, defined by subsurface temperature, is not a typical target for geodesy but has been recently tackled using InSAR and GNSS Reflectometry. Chen J. et al. (2022) combined InSAR ground deformation with an independent multivariate statistical method to isolate the cyclic seasonal com-ponent of the surface displacements related to active layer freeze and thaw from other signal components. Their results suggested a net increase of active layer water content of about 8 cm equivalent water thickness and widespread intensification of the surficial water cycle in central Tibet. By equaling the multi-year trends in surface subsidence as the volume change of ground ice, Wang L. et al. (2022) estimated a ground ice loss rate from permafrost degradation in the Selin Co basin, which contributed about 12% of the observed increase of lake volume in Selin Co.

GNSS-Interferometric Reflectometry (GNSS-IR), an unconventional method using reflected GNSS signals, enables estimates of snow depth around numerous geodetic-level continuous GNSS sites with a typical footprint of 1000 m^2. Zhang Z.Y. et al. (2020) conducted the first comprehensive data mining study in which we screened seven major open-data GNSS networks to identify what sites are suitable for using GNSS-IR for permafrost studies. From the 186 continuously operating sites located in the Arctic permafrost areas, they identified 23 usable ones, the majority of which are located in northern Canada and Alaska. Applying GNSS-IR to 80 GNSS sites across northern China, Wan et al. (2022) generated the GSnow-CHINA product that includes snow depth time series at 2-to-24-hour intervals spanning 2013 to 2022. Such a new dataset is complementary to the current point measurements and remote sensing products, opening new opportunities for water resource management and regional climate modeling.

4 Surface Gravimetry

Estimation of regional water storage with superconducting gravimetry

He et al. (2022) proposed a new method for implementing the quantitative separation of the vadose zone water storage changes with superconducting gravimetry. The new method is validated with observations from a superconducting gravimeter (GWR-C032) at the National Geodetic Observation Station in Wuhan, China, and also with theoretical results computed by the local hydrological modeling method. Xing et al. (2022) assessed the local deep groundwater storage changes in a karst aquifer by using a more than 4-year record (2017–2021) of the superconducting gravimeter OSG-066 located at the Lijiang station.

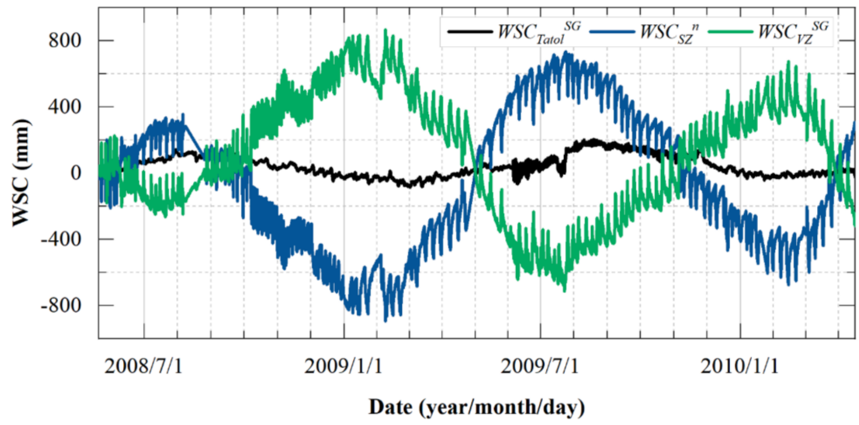

Figure2. Water storage changes at Wuhan SG Station quantitatively separated using the superconducting gravity technique. (He et al., 2022)

Large Reservoirs and Basins

Wang et al. (2021) investigated the 2020 flood events and the spatio-temporal variations of Yangtze River of China using multiscale combination of GRACE and gPhone data. Wang et al. (2019) estimated the TWSA of China's Three Gorges Reservoir (TGR) using GRACE data and global hydrology models, and presented the main contribution of seepage variability to the difference between GRACE-based estimation and in-situ volume measurements. Ma et al. (2020) used Gaofen-1 (GF-1) satellite data and in-situ water level observations to developed a high-resolution dynamic model of TGR water storage. Wang et al. (2020) presented a framework to evaluate GRACE mascon products based on in-situ GPS measurements from the Yangtze River Basin (YRB) in China, and found more consistency between CSR mascon and in-situ observations.

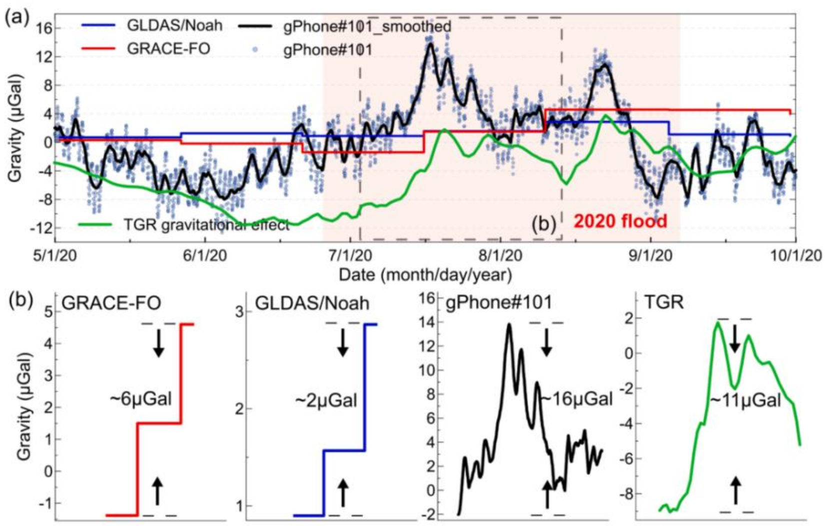

Figure3. The different gravity sensors and model, at gPhone#101 location, response to TWS changes in TGR during 2020 flood season (Wang et al., 2021).

Bibliography

Bai L, Jiang L, Zhao Y et al (2022). Quantifying the influence of long-term overexploitation on deep groundwater resources across Cangzhou in the North China Plain using InSAR measurements. Journal of Hydrology 605: 127368

Bai H, Ming Z, Zhong Y et al (2022). Evaluation of evapotranspiration for exorheic basins in China using an improved estimate of terrestrial water storage change. Journal of Hydrology 610: 127885

Chen Q, Wang F, Shen Y et al (2022). Monthly gravity field solutions from early LEO satellites' observations contribute to global ocean mass change estimates over 1993~2004. Geophysical Research Letters 49(21): e2022GL099917

Chen J, Wu T, Liu L et al (2022). Increased Water Content in the Active Layer Revealed by Regional-Scale InSAR and Independent Component Analysis on the Central Qinghai-Tibet Plateau. Geophysical Research Letters 49(15): e2021GL097586

Feng W, Shum C K, Zhong M et al (2018). Groundwater storage changes in China from satellite gravity: An overview. Remote Sensing 10(5): 674

Feng W, Zhong M, Lemoine J M et al (2013). Evaluation of groundwater depletion in North China using the Gravity Recovery and Climate Experiment (GRACE) data and ground-based measurements. Water Resources Research 49(4): 2110-2118

Ferreira V G, Yong B, Tourian M J et al (2020). Characterization of the hydro-geological regime of Yangtze River basin using remotely-sensed and modeled products. Science of the Total Environment 718: 137354

Fan Y, Ke C Q, Zhou X et al (2023). Glacier mass-balance estimates over High Mountain Asia from 2000 to 2021 based on ICESat-2 and NASADEM. Journal of Glaciology 69(275): 500-512

He Q, Chen X, Sun H et al (2022). Quantitative separation of the local vadose zone water storage changes using the superconductive gravity technique. Journal of Hydrology 609: 127734

Jiang Z, Hsu Y J, Yuan L et al (2021). Characterizing spatiotemporal patterns of terrestrial water storage variations using GNSS vertical data in Sichuan, China. Journal of Geophysical Research: Solid Earth 126(12): e2021JB022398

Jiao J, Zhang Y, Yin P et al (2019). Changing Moho Beneath the Tibetan plateau revealed by GRACE observations. Journal of Geophysical Research: Solid Earth 124(6): 5907-5923

Li Z, Zhang Z, Scanlon B R et al (2022). Combining GRACE and satellite altimetry data to detect change in sediment load to the Bohai Sea. Science of The Total Environment 818: 151677

Li W, Shum C K, Li F et al (2020). Contributions of Greenland GPS observed deformation from multisource mass loading induced seasonal and transient signals. Geophysical Research Letters 47(15): e2020GL088627

Li W, Zhang C, Wang W et al (2023). Inversion of Regional Groundwater Storage Changes Based on the Fusion of GNSS and GRACE Data: A Case Study of Shaanxi–Gansu–Ningxia. Remote Sensing 15(2): 520

Li X, Zhong B, Li J et al (2022). Analysis of terrestrial water storage changes in the Shaan-Gan-Ning Region using GPS and GRACE/GFO. Geodesy and Geodynamics 13(2): 179-188

Li Xianpao, Zhong Bo, Liu Tao (2022). Simulation Analysis of Inverting Regional Surface Mass Variations Using GNSS Vertical Displacement. Geomatics and Information Science of Wuhan University 47(1): 45-54

Li X, Zhong B, Li J et al (2023). Inversion of terrestrial water storage changes from GNSS vertical displacements using a priori constraint: A case study of the Yunnan Province, China. Journal of Hydrology : 129126

Liu B, Zou X, Yi S et al (2022). Reconstructing GRACE-like time series of high mountain glacier mass anomalies. Remote Sensing of Environment 280: 113177

Ma X, Wang L, Chen C et al (2020). Simulation of the dynamic water storage and its gravitational effect in the head region of three gorges reservoir using imageries of gaofen-1. Remote Sensing 12(20): 3353

Pan Y, Chen R, Yi S et al (2019). Contemporary mountain-building of the Tianshan and its relevance to geodynamics constrained by integrating GPS and GRACE measurements. Journal of Geophysical Research: Solid Earth 124(11): 12171-12188

Pan Y, Hammond W C, Ding H et al (2021). GPS Imaging of Vertical Bedrock Displacements: Quantification of Two-Dimensional Vertical Crustal Deformation in China. Journal of Geophysical Research: Solid Earth 126(4): e2020JB020951

Pan Y, Jiang W, Ding H et al (2023). Intradecadal Fluctuations and Three-dimensional Crustal Kinematic Deformation of the Tianshan and Pamir derived from Multi-Geodetic Imaging. Journal of Geophysical Research: Solid Earth 128(1):e2022JB025325

Qu W, Jin Z, Zhang Q et al (2022). Estimation of evapotranspiration in the yellow river basin from 2002 to 2020 based on GRACE and GRACE follow-on observations. Remote Sensing 14(3): 730

Ran J, Ditmar P, Liu L et al (2021). Analysis and mitigation of biases in Greenland ice sheet mass balance trend estimates from GRACE mascon products. Journal of Geophysical Research: Solid Earth 126(7): e2020JB020880

Shen C, Jia L, Ren S. (2022). Inter-and intra-annual glacier elevation change in high mountain Asia region based on ICESat-1&2 data using elevation-aspect bin analysis method. Remote Sensing 14(7): 1630

Shi G, Ma P, Hu X et al (2021). Surface response and subsurface features during the restriction of groundwater exploitation in Suzhou (China) inferred from decadal SAR interferometry. Remote Sensing of Environment 256: 112327

Shi X, Zhu T, Tang W et al (2022). Inferring decelerated land subsidence and groundwater storage dynamics in Tianjin–Langfang using Sentinel-1 InSAR. International Journal of Digital Earth 15(1): 1526-1546

Su X, Guo J, Shum C K et al (2020). Increased low degree spherical harmonic influences on polar ice sheet mass change derived from GRACE Mission. Remote Sensing 12(24): 4178

Sun Y, Li Y, Guo X et al (2023). Estimating C30 coefficients for GRACE/GRACE-FO time-variable gravity field models using the GRACE-OBP approach. Journal of Geodesy 97(3): 20

Sun Y, Riva R (2020). A global semi-empirical glacial isostatic adjustment (GIA) model based on Gravity Recovery and Climate Experiment (GRACE) data. Earth System Dynamics 11(1): 129-137

Sun Y, Riva R, Ditmar P et al (2019). Using GRACE to explain variations in the Earth's oblateness. Geophysical Research Letters 46(1): 158-168

Tang W, Zhao X, Motagh M et al (2022). Land subsidence and rebound in the Taiyuan basin, northern China, in the context of inter-basin water transfer and groundwater management. Remote Sensing of Environment 269: 112792

Wan W, Zhang J, Dai L et al (2022). A new snow depth data set over northern China derived using GNSS interferometric reflectometry from a continuously operating network (GSnow-CHINA v1. 0, 2013–2022). Earth System Science Data 14(8): 3549-3571

Wang F, Shen Y, Chen Q et al (2021). Bridging the gap between GRACE and GRACE follow-on monthly gravity field solutions using improved multichannel singular spectrum analysis. Journal of Hydrology 594: 125972

Wang F, Shen Y, Chen Q et al (2022). Revisiting sea-level budget by considering all potential impact factors for global mean sea-level change estimation. Scientific Reports 12(1): 10251

Wang L, Kaban M K, Thomas M, et al (2019). The challenge of spatial resolutions for GRACE-based estimates volume changes of larger man-made lake: the case of China’s Three Gorges Reservoir in the Yangtze River. Remote Sensing 11(1): 99

Wang L, Chen C, Ma X et al (2020). Evaluation of GRACE mascon solutions using in-situ geodetic data: The case of hydrologic-induced crust displacement in the Yangtze River Basin. Science of the Total Environment 707: 135606

Wang L, Peng Z, Ma X et al (2021). Multiscale gravity measurements to characterize 2020 flood events and their spatio-temporal evolution in Yangtze river of China. Journal of Hydrology 603: 127176

Wang L, Zhao L, Zhou H et al (2022). Contribution of ground ice melting to the expansion of Selin Co (lake) on the Tibetan Plateau. The Cryosphere 16(7): 2745-2767

Wang Q, Sun W. (2022). Seasonal Cycles of High Mountain Asia Glacier Surface Elevation Detected by ICESat-2. Journal of Geophysical Research: Atmospheres 127(23), e2022JD037501

Wang Q, Yi S, Sun W. (2021). Continuous estimates of glacier mass balance in high mountain Asia based on ICESat-1, 2 and GRACE/GRACE follow-on data. Geophysical Research Letters, 48(2): e2020GL090954

Wang S Y, Li J, Chen J et al (2022). On the improvement of mass load inversion with GNSS horizontal deformation: a synthetic study in Central China. Journal of Geophysical Research: Solid Earth 127(10): e2021JB023696

Wang W, Zhang C, Liang S et al (2017). Monitoring of the temporal and spatial variation of groundwater storage in the Three Gorges area based on the CORS network. Journal of Applied Geophysics 146: 160-166

Wang Z, Zhang B, Yao Y et al (2023). GRACE and mass budget method reveal decelerated ice loss in east Greenland in the past decade. Remote Sensing of Environment 286: 113450

Xiao C, Zhong Y, Feng W et al (2022). Monitoring the Catastrophic Flood With GRACE-FO and Near-Real-Time Precipitation Data in Northern Henan Province of China in July 2021. IEEE Journal of Selected Topics in Applied Earth Observations and Remote Sensing 16: 89-101

Xie J, Xu Y P, Yu H et al (2022). Monitoring the extreme flood events in the Yangtze River basin based on GRACE and GRACE-FO satellite data. Hydrology and Earth System Sciences 26(22): 5933-5954

Xing L, Niu X, Bai L et al (2022). Monitoring groundwater storage changes in a Karst aquifer using superconducting gravimeter OSG-066 at the Lijiang station in China. Pure and Applied Geophysics 179(5): 1853-1870

Xiong J, Yin J, Guo S (2021). Integrated flood potential index for flood monitoring in the GRACE era. Journal of Hydrology 603: 127115

Yi S, Sneeuw N. (2021). Filling the data gaps within GRACE missions using singular spectrum analysis. Journal of Geophysical Research: Solid Earth 126(5): e2020JB021227

Yi S, Sneeuw N. (2022). A novel spatial filter to reduce north–south striping noise in GRACE spherical harmonic coefficients. Journal of Geodesy 96(4): 23

Zhang Z, Guo F, Zhang X. (2020). Triple-frequency multi-GNSS reflectometry snow depth retrieval by using clustering and normalization algorithm to compensate terrain variation. GPS Solutions 24: 1-18

Zhang C, C.K. Shum, Ales B et al (2021). Rapid Mass Loss in West Antarctica Revealed by Swarm Gravimetry in the Absence of GRACE, Geophys. Res. Lett. 48, e2021GL095141. https://doi.org/10.1029/2021GL095141

Zhang B, Liu L, Yao Y et al (2020). Improving the estimate of the secular variation of Greenland ice mass in the recent decades by incorporating a stochastic process, Earth and Planetary Science Letters 549, 116518

Zhao F, Long D, Li X et al (2022). Rapid glacier mass loss in the Southeastern Tibetan Plateau since the year 2000 from satellite observations, Remote Sensing of Environment 270, 112853

Zhao Y, Zhou L, Wang C et al (2022). Analysis of the spatial and temporal evolution of land subsidence in Wuhan, China from 2017 to 2021. Remote Sensing 14(13), 3142

Zhong B, Li Q, Chen J, Luo Z (2022). A dataset of GRACE intersatellite geopotential differences from April 2002 to July 2016 (Version V2), Science Data Bank

Zhong B, Li Q, Chen J et al (2020). Improved Estimation of Regional Surface Mass Variations from GRACE Intersatellite Geopotential Differences Using a Priori Constraints. Remote Sensing 12(16), 2553

Zhong B, Li Q, Li X et al (2023). Basin-scale terrestrial water storage changes inferred from GRACE-based geopotential differences: A case study of the Yangtze River Basin, China. Geophysical Journal International 233(2): 1318–1338

Zhong B, Tan J, Li Q et al (2021). Simulation analysis of regional surface mass anomalies inversion based on different types of constraints. Geodesy and Geodynamics 12(4): 298–307

Zhong Y, Zhong M, Feng W et al (2020). Evaluation of the Evapotranspiration in the West Liaohe River Basin Based on GRACE Satellite and in Situ Measurements. Geomatis and Information Science of Wuhan University 45: 173-178

Zhong Y, Zhong M, Mao Y et al (2020). Evaluation of Evapotranspiration for Exorheic Catchments of China during the GRACE Era: From a Water Balance Perspective. Remote Sens. 12(3): 511